

**OPTICAL CODE-DIVISION MULTIPLE ACCESS SYSTEM
AND
OPTICAL SIGNAL PROCESSING**

Bo Dai

**A Thesis Submitted for the Degree
Of
Doctor of Philosophy
In
Institute of Photonics and Quantum Sciences**

Supervisor: Dr. Xu Wang

Heriot-Watt University

April 2013

Abstract

This thesis presents our recent researches on the development of coding devices, the investigation of security and the design of systems in the optical code-division multiple access (OCDMA) systems. Besides, the techniques of nonlinear signal processing used in the OCDMA systems fire our imagination, thus some researches on all-optical signal processing are carried out and also summarized in this thesis.

Two fiber Bragg grating (FBG) based coding devices are proposed. The first coding device is a superstructured FBG (SSFBG) using $\pm\pi/2$ -phase shifts instead of conventional $0/\pi$ -phase shifts. The $\pm\pi/2$ -phase-shifted SSFBG en/decoders can not only conceal optical codes well in the encoded signals but also realize the reutilization of available codes by hybrid use with conventional $0/\pi$ -phase-shifted SSFBG en/decoders. The second FBG based coding device is synthesized by layer-peeling method, which can be used for simultaneous optical code recognition and chromatic dispersion compensation.

Then, two eavesdropping schemes, one-bit delay interference detection and differential detection, are demonstrated to reveal the security vulnerability of differential phase-shift keying (DPSK) and code-shift keying (CSK) OCDMA systems.

To address the security issue as well as increase the transmission capacity, an orthogonal modulation format based on DPSK and CSK is introduced into the OCDMA systems. A 2 bit/symbol 10 Gsymbol/s transmission system using the orthogonal modulation format is achieved. The security of the system can be partially guaranteed.

Furthermore, a fully-asynchronous gigabit-symmetric OCDMA passive optical network (PON) is proposed, in which a self-clocked time gate is employed for signal regeneration. A remodulation scheme is used in the PON, which let downstream and upstream share the same optical carrier, allowing optical network units source-free. An error-free 4-user 10 Gbit/s/user duplex transmission over 50 km distance is realized.

A versatile waveform generation scheme is then studied. A theoretical model is established and a waveform prediction algorithm is summarized. In the demonstration, various waveforms are generated including short pulse, trapezoidal, triangular and sawtooth waveforms and doublet pulse.

In addition, an all-optical simultaneous half-addition and half-subtraction scheme is achieved at an operating rate of 10 GHz by using only two semiconductor optical amplifiers (SOA) without any assist light.

Lastly, two modulation format conversion schemes are demonstrated. The first conversion is from NRZ-OOK to PSK-Manchester coding format using a SOA based Mach-Zehnder interferometer. The second conversion is from RZ-DQPSK to RZ-OOK by employing a supercontinuum based optical thresholder.

TO MY FAMILY

Acknowledgements

I am deeply indebted to my supervisor, **Dr. Xu Wang**, for his enthusiastic guidance, consistent support and sincere encouragement throughout my research and considerate care of my life. With his strong recommendation, I was awarded a lot of incredible opportunities, including the Internship Research Fellowship from National Institute of Information and Communications Technology (NICT), Japan.

I would like to thank **Dr. Naoya Wada** for providing me the internship and research opportunities in NICT. I am very grateful to **Dr. Nobuyuki Kataoka**, **Dr. Satoshi Shimizu**, **Dr. Benjamin J. Puttnam**, **Dr. J. M. Delgado Mendinueta**, **Mr. Hiroyuki Sumimoto**, **Mr. Takeshi Makino** and **Mr. Takahiro Hashimoto** for their invaluable suggestions and numerous technical supports.

I express my sincere thanks to **Prof. Ken-ichi Kitayama** and **Dr. Takahiro Kodama** of Osaka University for their various help, invaluable advices and fruitful discussion.

I appreciate **Prof. Jianming Tang** of Bangor University for his encouragement.

My warm thanks also go to all members in our Optical Communication and Photonic Networks Group for being my close friends and colleagues. **Dr. Zhensen Gao**, **Mr. Xuhua Wang**, **Mr. Mumtaz Ali** and **Mr. Yu Liang** deserve a special acknowledgement for their patient assistance and productive collaboration.

Many thanks to **all friends** for their selfless helps.

Finally, I would express my special appreciation to **my parents** and my wife, **Ms. Yuekang Wu**, for their endless love and support.

ACADEMIC REGISTRY

Research Thesis Submission



Name:	Bo Dai		
School/PGI:	School of Engineering and Physical Sciences Institute of Photonics and Quantum Sciences		
Version: <i>(i.e. First, Resubmission, Final)</i>	Final	Degree Sought (Award and Subject area)	Doctor of Philosophy (Optical communication)

Declaration

In accordance with the appropriate regulations I hereby submit my thesis and I declare that:

- 1) the thesis embodies the results of my own work and has been composed by myself
- 2) where appropriate, I have made acknowledgement of the work of others and have made reference to work carried out in collaboration with other persons
- 3) the thesis is the correct version of the thesis for submission and is the same version as any electronic versions submitted*.
- 4) my thesis for the award referred to, deposited in the Heriot-Watt University Library, should be made available for loan or photocopying and be available via the Institutional Repository, subject to such conditions as the Librarian may require
- 5) I understand that as a student of the University I am required to abide by the Regulations of the University and to conform to its discipline.

* *Please note that it is the responsibility of the candidate to ensure that the correct version of the thesis is submitted.*

Signature of Candidate:		Date:	
-------------------------	--	-------	--

Submission

Submitted By <i>(name in capitals)</i> :	BO DAI
Signature of Individual Submitting:	
Date Submitted:	

For Completion in the Student Service Centre (SSC)

Received in the SSC by <i>(name in capitals)</i> :			
Method of Submission <i>(Handed in to SSC; posted through internal/external mail):</i>			
E-thesis Submitted (mandatory for final theses)			
Signature:		Date:	

Table of Contents

Abstract	i
Acknowledgements	iii
List of Figures	viii
List of Tables	xv
List of Abbreviations	xvi
List of Publications	xix
 Chapter 1 Introduction	 1
1.1 Overview of OCDMA systems	1
1.2 Background of FBG	3
1.2.1 Theoretical analysis of FBG	3
1.2.2 Synthesis method of FBG	6
1.3 Nonlinear effects of SOAs	8
1.4 Objectives and outlines	9
 Chapter 2 Novel FBG based Coding Devices	 11
2.1 Coding principle of SSFBG	11
2.2 $\pm\pi/2$ -phase-shifted SSFBG en/decoder	13
2.2.1 Security vulnerability of $0/\pi$ -SSFBG en/decoders	13
2.2.2 Security improvement using $\pm\pi/2$ -SSFBG en/decoders	16
2.2.3 Coding performance of $\pm\pi/2$ -SSFBG en/decoders	21
2.2.4 $\pm\pi/2$ -SSFBG en/decoders in the OCDMA systems	25
2.3 FBG based decoder for simultaneous optical code recognition and chromatic dispersion compensation	29
2.3.1 Derivation of the target reflection spectrum	30
2.3.2 Synthesis and performance of DC-FBG decoder	31
2.3.3 Tolerance to phase shift error	36
2.4 Summary	37

Chapter 3 Eavesdropping in the OCDMA Systems	39
3.1 Eavesdropping by one-bit delay interference detection	39
3.2 Eavesdropping by differential detection	42
3.3 Summary	45
 Chapter 4 Orthogonal Modulation Format Based on DPSK and CSK	 46
4.1 Overview of optical orthogonal modulation formats	47
4.2 A system with orthogonal DPSK/CSK modulation	50
4.2.1 Principle of orthogonal DPSK/CSK modulation	50
4.2.2 Experimental demonstration	51
4.2.3 Investigation on the security of the system	55
4.3 Summary	58
 Chapter 5 Fully-Asynchronous Gigabit-Symmetric OCDMA-PON	 59
5.1 Overview of remodulation schemes	60
5.2 Overview of nonlinear signal processing in the OCDMA systems	62
5.2.1 Optical thresholding	64
5.2.2 Optical time gating	67
5.3 All-optical self-clocked time gate	68
5.3.1 Operation principle	69
5.3.2 Application of self-clocked time gate in the DPSK-OCDMA system ...	71
5.4 Source-free-ONU DPSK/OOK OCDMA-PON	74
5.4.1 OCDMA-PON architecture	74
5.4.2 Experimental demonstration and results	76
5.4.3 Power budget of the OCDMA-PON	80
5.5 Summary	82

Chapter 6 Versatile Waveform Generation	83
6.1 Overview of optical Fourier synthesis	83
6.2 Theoretical model of the waveform generation system	88
6.3 Algorithm of waveform generation	91
6.4 Experimental demonstration of waveform generation	92
6.4.1 Generation of short pulse	93
6.4.2 Generation of trapezoidal waveform	95
6.4.3 Generation of triangular waveform	97
6.4.4 Generation of doublet pulse	98
6.4.5 Generation of sawtooth waveform	99
6.5 Summary	100
 Chapter 7 All-Optical Half-Adder and Half-Subtractor	 101
7.1 Overview of all-optical half-addition and half-subtraction schemes	101
7.2 Simultaneous half-adder and half-subtractor	108
7.2.1 Operation principle	109
7.2.2 Experimental demonstration	110
7.3 Summary	114
 Chapter 8 All-Optical Modulation Format Conversion	 115
8.1 NRZ-OOK to PSK-Manchester format conversion	115
8.1.1 Operation principle	116
8.1.2 Experimental demonstration	118
8.1.3 Improvement in operating speed	120
8.2 DQPSK to OOK format conversion	121
8.2.1 Operation principle	122
8.2.2 Experimental demonstration	123
8.3 Summary	126

Chapter 9	Conclusions and Future Research Directions	128
9.1	Conclusions	128
9.2	Future research directions	131
List of References		133

List of Figures

- Figure 1.1 Flow chart of the DLP method.
- Figure 2.1 Schematic diagram of encoding and decoding using SSFBG.
- Figure 2.2 Reflected-pulse model.
- Figure 2.3 Demonstration of code extraction technique for $0/\pi$ -SSFBG using a waveform encoded by 31-chip Gold code.
- Figure 2.4 Encoded waveforms of $0/\pi$ -SSFBG and $\pm\pi/2$ -SSFBG encoders with different chip durations (a) CG1 and (b) NG1.
- Figure 2.5 Reflected temporal response of 3-chip $\pm\pi/2$ -SSFBG with different or same adjacent phase shifts.
- Figure 2.6 Demonstration of code extraction technique for the $\pm\pi/2$ -SSFBG encoders (a) NG1 and (b) NG2.
- Figure 2.7 The disparity of raised and decayed peak (I_R/I_D) with different chip duration and input pulse width ratios (T_C/T_W).
- Figure 2.8 Autocorrelation of the $0/\pi$ -SSFBG and $\pm\pi/2$ -SSFBG en/decoders with 31-chip, 63-chip and 127-chip Gold code.
- Figure 2.9 Cross-correlation of the $0/\pi$ -SSFBG and $\pm\pi/2$ -SSFBG en/decoders and the hybrid use with (a) 31-chip, (b) 63-chip and (c) 127-chip Gold code.
- Figure 2.10 Measured and calculated correlation of $0/\pi$ -SSFBG and $\pm\pi/2$ -SSFBG en/decoders.
- Figure 2.11 Experimental setup of 2-user OOK-OCDMA system and measured waveforms and eye diagrams.
- Figure 2.12 BER performances of the $0/\pi$ -SSFBG and $\pm\pi/2$ -SSFBG en/decoders in the OOK-OCDMA system.
- Figure 2.13 Experimental setup of 4-user OOK-OCDMA system with hybrid use of en/decoders and measured waveforms and eye diagrams.
- Figure 2.14 Experimental setup of 4-user DPSK-OCDMA system with hybrid use of en/decoders and measured waveforms and eye diagrams.
- Figure 2.15 Measured waveforms and eye diagrams in the 4-user DPSK-OCDMA

system.

Figure 2.16 BER performances of the $0/\pi$ -SSFBG and $\pm\pi/2$ -SSFBG en/decoders in the DPSK-OCDMA system.

Figure 2.17 (a) Coupling coefficient and (b) spatial relative phase of the DC-FBG with -170 ps/nm dispersion.

Figure 2.18 Target and synthesized spectra of DC-FBG decoder and synthesized error. R_{Target} and $R_{Synthesized}$: Reflectivity of target and synthesized spectra.

Figure 2.19 (a) Encoded waveform and (b) dispersed encoded waveform after transmission.

Figure 2.20 Decoded waveform using the SSFBG decoder (dashed line) and the DC-FBG decoder (solid line).

Figure 2.21 Shape of the input pulse (solid line, FWHM 4 ps), the autocorrelation pulse back-to-back decoded by the SSFBG decoder (dotted line, FWHM 5.3 ps), and the autocorrelation pulse decoded by the DC-FBG decoder after 10 km dispersive transmission (dashed line, FWHM 5.9 ps).

Figure 2.22 Single-user OOK-OCDMA model. PG: Optical pulse generator. EOM: Electro-optic modulator. PD: Photodetector. Th: Threshold.

Figure 2.23 (a) BER evaluation for different transmission distances and data rates. Eye diagrams for 5 Gbit/s 10 km transmission using (b) SSFBG decoder and (c) DC-FBG decoder.

Figure 2.24 The superimposed normal density of P/W and P/C with phase-shift error.

Figure 3.1 Experimental setup of security attack on DPSK-OCDMA system.

Figure 3.2 BER performances and corresponding eye diagrams for security attack on the DPSK-OCDMA system.

Figure 3.3 Experimental setup of security attack on CSK-OCDMA system.

Figure 3.4 BER performances and corresponding eye diagrams for security attack on the CSK-OCDMA system.

Figure 3.5 Experimental setup of CSK-OCDMA system with differential detection.

Figure 3.6 Lookup table for differential detection.

Figure 3.7 (a) Measured original electrical data sequence and (b) extracted data

sequence using differential detection. (c) Eye diagram after differential detection.

Figure 4.1 4-dimensional orthogonality of the characteristics of optical signals.

Figure 4.2 Schematic diagram of (a) IM-payload/FSK-label and (b) IM-payload/DPSK-label transmission link.

Figure 4.3 Constellation maps for (a) 16 QAM and (b) OOK.

Figure 4.4 Constellation maps for (a) DPSK, (b) CSK, and (c) DPSK/CSK modulation scheme and associated symbols (b_P , $b_{C(n)}$).

Figure 4.5 Experimental setup of the DBPSK/binary-CSK system.

Figure 4.6 Waveforms measured at different positions of the system.

Figure 4.7 (a) Measured BER performance and eye diagrams for both (b) binary-CSK data and (c) DBPSK data transmission.

Figure 4.8 Simulated received power of DBPSK data transmission with different code lengths at BER of 10^{-9} .

Figure 4.9 Security investigation of the system using orthogonal DBPSK/binary-CSK modulation.

Figure 4.10 Eye diagram for (a) one-bit delay interference detection and (b) differential detection.

Figure 5.1 Network structure of a WDM-PON using FP laser based transmitter for remodulation [142].

Figure 5.2 Schematic diagram of a DWDM-PON using DPSK in downstream and upstream remodulated signals [144].

Figure 5.3 Network structure of a WDM-PON employing 16-QAM intensity modulated OFDM downstream and OOK modulated upstream signals [145].

Figure 5.4 (a) Decoding process and the principles of (b) thresholder and (c) time gate.

Figure 5.5 Transfer function of the optical thresholder using a HF. Inset: Signal spectrum before and after the HF [147].

Figure 5.6 Spectral plot demonstrating how the thresholder discriminates between the target decoded signal and the interfering users' signals [148].

Figure 5.7 Transfer function of SC based optical thresholder [116].

Figure 5.8 NOLM based time gating scheme [150].

Figure 5.9 Setup of the self-clocked time gate.

Figure 5.10 Operation principle of the self-clocked time gate.

Figure 5.11 Experimental setup of multi-user DPSK OCDMA system.

Figure 5.12 The waveforms after (a) decoding and (b) time gate for the case of four MAIs and 63-chip coding.

Figure 5.13 (a)–(c) Eye diagrams for DPSK signal without coding, target user with and without time gate.

Figure 5.14 (a) and (b) BER performances for 31-chip and 63-chip coding multi-user DPSK-OCDMA system with and without time gate.

Figure 5.15 Experimental measurement of system improvement by using the time gate.

Figure 5.16 Diagram of the proposed OCDMA-PON architecture.

Figure 5.17 Experimental setup of the duplex multi-user OCDMA system: a 50 km 4-user 10 Gbit/s/user DPSK downstream link and a 50 km 4-user 10 Gbit/s/user OOK upstream link.

Figure 5.18 Downlink waveforms of (a) 4-user multiplexing encoded signal, (b)–(c) signals after decoding, and (f)–(i) signals after time gate.

Figure 5.19 Uplink waveforms of (a) 4-user multiplexing encoded signal and (b) signal after decoding.

Figure 5.20 Eye diagrams of (a)–(d) downstream signals after decoding, (e)–(h) downstream signals after time gate and (i)–(k) upstream signals without coding, for single user and 4-user.

Figure 5.21 BER performances in the situations of (a) back-to-back and (b) 50 km uplink and 50 km downlink.

Figure 5.22 Power budget model.

Figure 5.23 Relationship between transmission distance and total number of users.

Figure 6.1 Schematic diagram of Fourier synthesis in [161].

Figure 6.2 Schematic diagram of optical spectral comb generator in [162].

- Figure 6.3 Schematic diagram of optical spectral comb generator in [163].
- Figure 6.4 Schematic diagram of optical spectral comb generator in [164].
- Figure 6.5 Schematic diagram of Fourier synthesis in [165].
- Figure 6.6 Schematic diagram of dispersion-free pulse shaping in [169].
- Figure 6.7 Schematic diagram of waveform generation scheme.
- Figure 6.8 Generated optical spectral comb.
- Figure 6.9 Flowchart of the waveform generation algorithm.
- Figure 6.10 (a) Calculated and (b) measured short pulses under the flat spectrum conditions. (c) Calculated normalized gradient and instantaneous frequency corresponding to short pulse intensity profile.
- Figure 6.11 Influence of RF phase noise and bias drift.
- Figure 6.12 (a) The target trapezoidal waveform and the gradient and instantaneous frequency of the calculated waveform. (b) Calculated and (c) measured trapezoidal waveforms. (d) Measured optical spectrum.
- Figure 6.13 (a) The target triangular waveform and the gradient and instantaneous frequency of the calculated waveform. (b) Calculated and (c) measured triangular waveforms. (d) Measured optical spectrum.
- Figure 6.14 (a) Calculated and (b) measured doublet pulses. (c) Measured optical spectrum. (d) Calculated power spectrum of the 1 Gbit/s doublet pulses. Red dashed line: FCC spectral mask for indoor applications. Inset diagram: the waveform of the generated 1 Gbit/s doublet pulse.
- Figure 6.15 (a) The target sawtooth waveform and the gradient and instantaneous frequency of the calculated waveform. (b) Calculated and (c) measured sawtooth waveforms. (d) Measured optical spectrum.
- Figure 7.1 Logic diagrams of half-adder and half-subtractor.
- Figure 7.2 Logic diagram of the half-adder in [188].
- Figure 7.3 Schematic diagram of two SOAs based an XOR logic gate and an MZI and an AND logic gate in [190].
- Figure 7.4 Schematic diagram of the half-adder in [191].

Figure 7.5 Schematic diagram of four SOAs based an XOR and an AND logic gates in [192].

Figure 7.6 Schematic diagram of a PPLN and an SOA based two AND logic gates in [193].

Figure 7.7 Logic diagram of simultaneous half-addition and half-subtraction scheme.

Figure 7.8 Schematic diagram of single-PPLN based half-adder and half-subtractor in [194].

Figure 7.9 Schematic diagram of two SOAs and a PPLN based three AND logic gates in [186].

Figure 7.10 Schematic diagram of two SOAs based three AND logic gates.

Figure 7.11 The operation principle of the proposed scheme.

Figure 7.12 The experiment setup of 10 Gbit/s half-adder and half-subtractor.

Figure 7.13 (a) and (b) The input and output spectra, measured before and after SOA 1 and SOA 2. (Resolution: 0.01 nm).

Figure 7.14 Waveforms of (a) and (b) input signals and (c)–(f) output signals. (g)–(l) Corresponding eye diagrams. (Output signals are measured at point ξ).

Figure 7.15 BER performances for the input and output signals.

Figure 8.1 Operation principle of NRZ-OOK to PSK-Manchester modulation format conversion.

Figure 8.2 Experimental setup of the proposed scheme.

Figure 8.3 Experimental setup of the proposed sheme. (a) and (b) Input clock and NRZ-OOK signals. (c) Converted PSK-Manchester signal. (d) and (e) Interference outputs.

Figure 8.4 (a) Measured BER performances. (b) and (c) Eye diagrams of NRZ-OOK and PSK-Manchester signals without transmission at $\text{BER}=10^{-9}$.

Figure 8.5 (a) Calculated phase recovery of the SOAs. (b) and (c) Eye diagrams of calculated 40 Gbit/s NRZ-OOK and converted PSK-Manchester signals.

Figure 8.6 Proposed scheme in the network structure.

Figure 8.7 The operation principle of DQPSK to OOK modulation format conversion.

Figure 8.8 (a) Measured spectra of A: demodulated DQPSK signal, B: filter response at 1545 nm, C: filter response at 1555nm and D: generated SC. (b) Power transfer function of the SC based optical thresholder.

Figure 8.9 Experiment setup of DQPSK to OOK modulation format conversion.

Figure 8.10 (a) Demodulated signals and (b) eye diagram for I-channel. (c) Signals after optical thresholder and (d) eye diagram for I-channel. (e) Demodulated signals and (f) eye diagram for Q-channel. (g) Signals after optical thresholder and (h) eye diagram for Q-channel.

Figure 8.11 BER performances for DQPSK and OOK data using different filters with and without 50 km transmission.

List of Tables

- Table 2.1 Different SSFBG en/decoders used in the experiment.
- Table 2.2 Average values of autocorrelation and cross-correlation for different en/decoder and chip length.
- Table 4.1 Summary of the security investigation on DPSK-OCDMA, CSK-OCDMA and DPSK/CSK-OCDMA systems.
- Table 5.1 Power contribution of each component.
- Table 7.1 Truth table of half-adder and half-subtractor.
- Table 7.2 Truth table of the single-rail half-adder.
- Table 8.1 Output of probe light with a set of representative parameters.

List of Abbreviations

ATT	attenuator
ASE	amplified spontaneous emission
ASK	amplitude-shift keying
AWG	arrayed waveguide grating
BER	bit-error rate
BPD	balanced photodetector
BPF	bandpass filter
CH	carrier heating
CSK	code-shift keying
CW	continuous-wave
DCF	dispersion-compensation fiber
DD-MZM	dual-drive Mach-Zehnder modulator
DFB	dispersion flattened fiber
DFG	difference frequency generation
DLP	discrete layer-peeling
DPSK	differential phase-shift keying
DQPSK	differential quadrature phase-shift keying
EDFA	erbium doped fiber amplifier
ER	extinction ratio
FBG	fiber Bragg grating
FDM	frequency-division multiplexing
FIR	finite impulse response
FODL	fiber optical delay line
FP	Fabry–Pérot
FSK	frequency-shift keying
FWM	four-wave mixing
FWHM	full width at half maximum
GbE	gigabit ethernet
HNLF	highly nonlinear fiber

IM	intensity modulator
ISI	inter-symbol interference
LN-SW	lithium niobate optical switch
MAI	multiple-access interference
MAN	wide area network
MLLD	mode-locked laser diode
MRR	micro-ring resonator
MZI	Mach-Zehnder interferometer
NG-PON	next-generation passive optical network
NOLM	nonlinear optical loop mirror
NRZ	non-return-to-zero
OCDMA	optical code-division multiple access
OFDM	orthogonal frequency-division multiplexing
OLT	optical line termination
ONU	optical network unit
OOK	on-off keying
PC	polarization controller
PD	photodetector
PDM	polarization-division multiplexing
PM	phase modulator
PolSK	polarization-shift keying
PON	passive optical network
PPG	pulse pattern generator
PPLN	periodically poled lithium niobate
PRBS	pseudorandom bit sequence
PSK	phase-shift keying
QAM	quadrature amplitude modulation
RMS	root-mean-square error
RZ	return-to-zero
SC	supercontinuum

SFG	sum frequency generation
SGM	self-gain modulation
SHB	spectral hole burning
SLPM	spatial light phase modulator
SMF	single mode fiber
SNR	signal-to-noise ratio
SOA	semiconductor optical amplifier
SPM	self-phase modulation
SSFBG	superstructured fiber Bragg grating
TDMA	time-division multiplexing access
TOAD	terahertz optical asymmetric demultiplexer
TODL	tunable optical delay line
VBS	variable-bandwidth spectrum shaper
VOA	variable optical attenuator
WAN	wide area network
WDMA	wavelength-division multiplexing access
XGM	cross-gain modulation
XPM	cross-phase modulation

List of Publications

Journal papers

- [1] **B. Dai** and X. Wang, "Security improvement using $\pm\pi/2$ -phase-shifted SSFBG en/decoder in time-spreading OCDMA," *Photon. Technol. Lett.*, vol. 22, no. 12, pp. 881–883, Jun. 2010.
- [2] **B. Dai** and X. Wang, "Novel FBG decoder for simultaneous time domain coherent optical code recognition and chromatic dispersion compensation," *Photon. Technol. Lett.*, vol. 22, no. 22, pp. 1671–1673, Nov. 2010.
- [3] **B. Dai**, Z. Gao, X. Wang, N. Kataoka and N. Wada, "Demonstration of differential detection on attacking code-shift-keying OCDMA system," *Electron. Lett.*, vol. 46, issue. 25, pp. 1680–1682, Dec. 2010.
- [4] **B. Dai**, Z. Gao, X. Wang, N. Kataoka and N. Wada, "Versatile waveform generation using a single-stage dual-drive Mach-Zehnder modulator," *Electron. Lett.*, vol. 47, issue. 5, pp. 336–338, Mar. 2011.
- [5] Z. Gao, **B. Dai**, X. Wang, N. Kataoka and N. Wada, "Transparent transmission of a secure time domain spectral phase encoding/eecoding DPSK–OCDM signal over a DWDM network," *J. Opt. Commun. Netw.*, vol. 3, issue 5, pp. 404–410, May 2011.
- [6] Z. Gao, **B. Dai**, X. Wang, N. Kataoka and N. Wada, "Rapid programmable/code-length-variable, time-domain bit-by-bit code shifting for high-speed secure optical communication," *Opt. Lett.*, vol. 36, no. 9, pp. 1623–1625, May 2011.
- [7] **B. Dai**, Z. Gao, X. Wang, N. Kataoka and N. Wada, "Performance comparison of $0/\pi$ - and $\pm\pi/2$ -phase-shifted superstructured fiber Bragg grating En/decoder," *Opt. Express*, vol. 19, no. 13, pp. 12248–12260, Jun. 2011.
- [8] **B. Dai**, Z. Gao, X. Wang, N. Kataoka and N. Wada, "A novel optical orthogonal modulation format based on differential phase-shift keying and code-shift keying," *Photon. Technol. Lett.*, vol. 23, no. 17, pp. 1210–1212, Sep. 2011.
- [9] Z. Gao, **B. Dai**, X. Wang, N. Kataoka and N. Wada, "40 Gb/s, secure optical communication based upon fast reconfigurable time domain spectral phase en/decoding with 40 Gchip/s optical code and symbol overlapping," *Opt. Lett.*, vol. 36, no. 22, pp. 4326–4328, Nov. 2011.

- [10] Z. Gao, **B. Dai**, X. Wang, N. Kataoka and N. Wada, “10-Gbit/s, reconfigurable time domain SPE-OCDMA system with code shifting and pulse overlapping,” *Microwave and Opt. Technol. Lett.*, vol. 54, issue 3, pp. 808–810, Mar. 2012.
- [11] **B. Dai**, S. Shimizu, X. Wang and N. Wada, “All-optical modulation format conversion from NRZ-OOK to PSK-Manchester using SOA-MZI,” *Electron. Lett.*, vol. 48, issue. 19, pp. 1221–1222, Sep. 2012.
- [12] **B. Dai**, S. Shimizu, X. Wang and N. Wada, “Full-asynchronous gigabit-symmetric DPSK downstream and OOK upstream OCDMA-PON with source-free ONUs employing all-optical self-clocked time gate,” *Opt. Express*, vol. 20, no. 26, pp. B21–B31, Nov. 2012.
- [13] **B. Dai**, Z. Gao, X. Wang, H. Chen, N. Kataoka and N. Wada, “Generation of versatile waveforms from CW light by using dual-drive Mach-Zehnder modulator and employing chromatic dispersion,” *J. Lightw. Technol.*, vol. 31, no. 1, pp. 145–151, Jan. 2013.
- [14] **B. Dai**, S. Shimizu, X. Wang and N. Wada, “Simultaneous all-optical half-adder and half-subtractor based on two semiconductor optical amplifiers,” *Photon. Technol. Lett.*, vol. 25, no. 1, pp. 91–93, Jan. 2013.

Conference papers

- [1] **B. Dai**, Z. Gao, X. Wang, N. Kataoka and N. Wada, “Experimental investigation on security of temporal phase coding OCDMA system with code-shift keying and differential phase-shift keying,” Asia Communications and Photonics Conference and Exhibition (*ACP '10*), Shanghai, China, Dec. 2010, Paper FO1.
- [2] **B. Dai**, Z. Gao, X. Wang, N. Kataoka and N. Wada, “Experimental demonstration of $\pm\pi/2$ -phase-shifted SSFBG encoder for security improvement in time-spreading OCDMA,” Asia Communications and Photonics Conference and Exhibition (*ACP '10*), Shanghai, China, Dec. 2010, Paper FU2.
- [3] **B. Dai**, Z. Gao, X. Wang, N. Kataoka and N. Wada, “Generation of versatile optical waveforms from CW laser using a single-stage dual-drive Mach-Zehnder modulator,” Asia Communications and Photonics Conference and Exhibition (*ACP '10*), Shanghai, China, Dec. 2010, Paper P123.

- [4] Z. Gao, **B. Dai**, X. Wang, N. Kataoka and N. Wada, “2-D time domain spectral phase encoding/wavelength hopping coherent DPSK-OCDMA system using fiber Bragg gratings and phase modulator,” Asia Communications and Photonics Conference and Exhibition (*ACP '10*), Shanghai, China, Dec. 2010, Paper FO7.
- [5] Z. Gao, **B. Dai**, X. Wang, N. Kataoka and N. Wada, “Ultrafast optical pulse repetition rate multiplication based on time domain spectral amplitude/phase filtering,” Asia Communications and Photonics Conference and Exhibition (*ACP '10*), Shanghai, China, Dec. 2010, Paper SuG3.
- [6] **B. Dai**, Z. Gao, X. Wang, N. Kataoka, N. Wada, “Demonstration of hybrid using $\pm\pi/2$ - and $0/\pi$ -phase-shifted SSFBG en/decoders in the 4×10 Gbit/s OCDMA system,” The Optical Fiber Communication Conference and Exposition (*OFC '11*), Los Angeles, USA, Mar. 2011, Paper OWV6.
- [7] X. Wang, Z. Gao, **B. Dai**, X.-H. Wang, N. Kataoka, N. Wada, “Fast optical code reconfigurable technique for secure optical communication,” International Conference on Transparent Optical Networks (*ICTON '11*), Stockholm, Sweden, Jun. 2011, Paper We.B1.4.
- [8] X. Wang, Z. Gao, **B. Dai**, N. Kataoka and N. Wada, “Secure optical communication based on optical code reconfiguration scheme,” Photonics and Optoelectronics Meetings (*POEM '11*), Optical Communication Systems and Networking, vol. Proc. SPIE 8331, pp. 83310F-1–83310F-10, Jan. 2012.
- [9] **B. Dai**, S. Shimizu, X. Wang and N. Wada, “All-optical NRZ-OOK to Manchester modulation format conversion,” The Institute of Electronics, Information and Communication Engineers Photonic Network meeting (*IEICE PN '12*), Yamagata, Japan, Jun. 2012, vol. 112, no. 87, pp. 61–65, Paper PN2012-12.
- [10] **B. Dai**, S. Shimizu, X. Wang and N. Wada, “Supercontinuum based optical threshold assisted all-optical modulation format conversion from RZ-DQPSK to RZ-OOK,” International Conference on Transparent Optical Networks (*ICTON '12*), Coventry, England, Jul. 2012, Paper Tu.P.7.
- [11] **B. Dai**, S. Shimizu, X. Wang and N. Wada, “Full-asynchronous gigabit-symmetric OCDMA-PON with source-free ONUs based on DPSK downstream and remodulated OOK upstream links,” European Conference and Exhibition on Optical Communication (*ECOC '12*), Amsterdam, The Netherlands, Sep. 2012, Paper Mo.1.B.5.

Chapter 1

Introduction

This chapter overviews the development of optical code-division multiple access (OCDMA) systems and reviews the technology of fiber Bragg grating (FBG), which acts as a coding device in the OCDMA systems. In addition, this chapter introduces the nonlinear effects of semiconductor optical amplifiers (SOA). The objectives and outline of the thesis are also included in this chapter.

1.1 Overview of OCDMA systems

Multiple access techniques provide an important way to realize high-speed first/last-mile telecommunications between large-capacity metro networks and customer premises. Time-division multiplexing access (TDMA) and wavelength-division multiple access (WDMA) are two major multi-access techniques. In the TDMA communication systems, the transmission of each customer premise is allocated in a specific time slot, while in the WDMA systems a specific wavelength channel is assigned to each customer premise for transmission. Besides these two conventional multi-access techniques, code-division multiple access (CDMA) technique is an alternative for multi-access communications. CDMA techniques realize the multi-access by assigning each transceiver a unique code, which is orthogonal to other codes, for encoding and decoding signals. An encoded signal is correlated to other encoded signals and can only be correctly decoded by a target transceiver which owns the same code.

The concept of CDMA was firstly introduced into the optical communications from the wireless communications in 1980's [1, 2]. Afterwards, CDMA techniques have been extensively explored in the optical communications [3–24]. Many advantages of optical CDMA (OCDMA) systems were claimed including asynchronous transmission, high network flexibility, low latency, protocol transparency and especially high security. In the OCDMA systems, coding process is a key function, which is realized in the optical domain using various optical signal processing techniques. According to coding

schemes, OCDMA systems can be categorized in two ways.

The first way is based on the coding principle and OCDMA systems can be divided into two groups, incoherent and coherent OCDMA systems. In the incoherent OCDMA systems, the intensity of an optical signal is changed for coding, while in the coherent OCDMA systems, coding process is performed in the bipolar manner, which is similar to that in the wireless CDMA systems, and the phase of an optical signal is manipulated for coding. In comparison, incoherent OCDMA systems are relatively simple but coherent OCDMA systems present better performance due to their better coding correlations [25].

The second way of categorization is based on the coding domain. The coding process can be realized in the spectral domain and temporal domain using 1-dimensional (1D) code sequences [1–3, 12, 17, 22] and in the spatial domain and spectral/temporal domains using 2-dimensional (2D) code sequences [26–31]. 1D coding is mostly used due to the simplicity and can be realized in the both incoherent and coherent systems by different schemes. In the OCDMA systems with temporal coding, each data bit is divided into several short time periods, called chips, and intensities or phases of these chips are changed according to a code sequence. Similarly, spectral coding is done by dividing the spectrum of each data bit into several narrow bandwidths, called frequency bins, and controlling the intensities and phases of these frequency bins. Most 2D coding processes are in incoherent manner and very few coherent 2D coding schemes were reported. Comparing to 1D coding, 2D coding can support more users in a network and significantly improve the system performance because the size of 2D code set is larger and the correlation properties of 2D code sequences are better than 1D code sequences.

To achieve the key function, coding process, in the OCDMA systems, a lot of coding devices have been proposed and demonstrated, including parallel fiber optical delay line (FODL) [32–34], spatial light phase modulator (SLPM) [4, 35, 36], fiber Bragg grating (FBG) [13, 25, 29, 37–49], arrayed waveguide grating (AWG) [50–56], and micro-ring resonator (MRR) [57, 58].

FODL is used to generate a high-speed pulse train and performs as a matched filter

to realize the correlation process of a pulse train, i.e. the functions of encoding and decoding. However, since FODL uses multiple delay lines, it is lack of efficiency for coherent coding. SLPM can provide 1D incoherent and coherent coding and 2D coherent coding, but it is not compact because it consists of bulk optics and is based on the free-space transmission. FBG devices have the advantages of compactness and low cost and can be designed for various coding schemes (both incoherent and coherent and both 1D and 2D). MRR enables programmable and reconfigurable 1D and 2D coding in a compact integrated photonic circuit, while it requires optimized design and fabrication of the ring structure to increase code length, which is proportional to the correlation (coding) performance and system scalability. AWG is a cost-effective device because it can simultaneously generate and recognize a set of optical codes (OC). Among the above coding devices, FBG and AWG coding devices attract a lot of interests and are widely used in the recent OCDMA systems due to their mature design principle and fabrication techniques.

1.2 Background of FBG

FBGs are also called *reflection* or *short-period* grating. A FBG most efficiently couples light between modes travelling in the opposite directions, and it is achieved by creating a periodic perturbation of the refractive index along the fiber length [59–62]. Since the interference occurs during the coupling, light with particular wavelengths are reflected. Based on this fundamental principle, FBGs have been developed into many essential devices for various applications including dispersion compensator [63–66], fiber amplifiers [67–70], fiber lasers [71–76], and strain and temperature sensing devices [77–80].

1.2.1 Theoretical analysis of FBG

In the FBGs, a perturbation to the effective refractive index, n_{eff} , takes the form of a phase and amplitude-modulated periodic waveform as follows.

$$\delta n_{eff}(z) = \overline{\delta n_{eff}}(z) \left\{ 1 + \nu \cos \left[\frac{2\pi}{\Lambda} z + \Phi(z) \right] \right\}$$

where $\overline{\delta n_{eff}}$ is the “dc” index change spatially averaged over a grating period, v is the fringe visibility of the index change, Λ is the nominal period and $\Phi(z)$ describes grating chirp.

The “design wavelength” for Bragg scattering by an infinitesimally weak grating ($\delta n_{eff} \rightarrow 0$) is

$$\lambda_D = 2n_{eff}\Lambda \quad (1.1)$$

while the maximum reflectivity occurs at the wavelength

$$\lambda_{max} = \left(1 + \frac{\overline{\delta n_{eff}}}{n_{eff}}\right) \lambda_D \quad (1.2)$$

The grating causes a coupling between the forward and backward propagating waves and the interaction can be described in terms of the following coupled-mode equations [62].

$$\frac{dR}{dz} = j\hat{\sigma}R(z) + j\kappa S(z) \quad (1.3)$$

$$\frac{dS}{dz} = -j\hat{\sigma}S(z) - j\kappa^* R(z) \quad (1.4)$$

where $R(z) = A(z)\exp(j\delta - \Phi/2)$, $S(z) = B(z)\exp(-j\delta + \Phi/2)$, $A(z)$ and $B(z)$ are the complex envelopes of the forward and backward propagating waves, respectively and δ is the wavenumber detuning defined by

$$\delta = 2\pi n_{eff} \left(\frac{1}{\lambda} - \frac{1}{\lambda_D} \right) \quad (1.5)$$

and $\hat{\sigma}$ is the general dc self-coupling coefficient defined as

$$\hat{\sigma} = 2\pi n_{eff} \left(\frac{1}{\lambda} - \frac{1}{\lambda_D} \right) + \frac{2\pi}{\lambda} \overline{\delta n_{eff}}(z) - \frac{1}{2} \frac{d\Phi}{dz} \quad (1.6)$$

and for a single mode FBG κ is the ac coupling coefficient which is given by

$$\kappa(z) = \kappa^*(z) = \frac{\pi}{\lambda} v \overline{\delta n_{eff}}(z) \quad (1.7)$$

The z -dependent phase term, $(1/2)d\Phi/dz$, describes the chirp of the grating period, which is defined as

$$\frac{1}{2} \frac{d\Phi}{dz} = -\frac{4\pi n_{eff} z}{\lambda_D^2} \frac{d\lambda_D}{dz} \quad (1.8)$$

where $d\lambda_D/dz$ is a measure of the rate of change of the design wavelength with position in the grating.

The coupled-mode equations can be solved in a closed form when appropriate boundary conditions are imposed. The boundary conditions are based on the assumption that there is a forward propagating wave from $z=-\infty$, i.e. $R(0)=I$, and no backward propagating wave for $z \geq L$, i.e. $S(L)=0$. The propagation of waves through the uniform grating can be described by a 2x2 fundamental matrix, F_i .

$$\begin{pmatrix} R(L) \\ S(L) \end{pmatrix} = F_M \cdot F_{M-1} \cdot \dots \cdot F_i \cdot \dots \cdot F_1 \begin{pmatrix} R(0) \\ S(0) \end{pmatrix} \quad (1.9)$$

and

$$F_i = \begin{pmatrix} \cosh(\gamma \Delta z) - j \frac{\hat{\sigma}}{\gamma} \sinh(\gamma \Delta z) & -j \frac{\kappa}{\gamma} \sinh(\gamma \Delta z) \\ j \frac{\kappa}{\gamma} \sinh(\gamma \Delta z) & \cosh(\gamma \Delta z) + j \frac{\hat{\sigma}}{\gamma} \sinh(\gamma \Delta z) \end{pmatrix} \quad (1.10)$$

where Δz is the length of i th uniform section and γ is imaginary at wavelength for which $\hat{\sigma} > \kappa$ and is defined by

$$\gamma = \sqrt{\kappa^2 - \hat{\sigma}^2} \quad (1.11)$$

For phase-shifted gratings, where there are discrete phase shifts or effective phase changes, φ , created by the physical separation between grating sections, the following matrix should be inserted into the grating sections.

$$F_\varphi = \begin{pmatrix} \exp\left(-j \frac{\varphi}{2}\right) & 0 \\ 0 & \exp\left(j \frac{\varphi}{2}\right) \end{pmatrix} \quad (1.12)$$

The reflection, $r(\lambda)$, and transmission, $t(\lambda)$, coefficients can then be calculated from the following equations.

$$r(\lambda) = \frac{S(0)}{R(0)} \quad (1.13)$$

$$t(\lambda) = \frac{R(L)}{R(0)} \quad (1.14)$$

Finally, the reflectivity, $R(\lambda)$, and transmissivity, $T(\lambda)$, are given by $R(\lambda) = |r|^2$ and $T(\lambda) = |t|^2$.

1.2.2 Synthesis method of FBG

Synthesis method of FBG is a useful design tool to find the grating structure (grating amplitude and phase) from a specified complex spectrum. It has been a common view that the synthesis problem is complicated, especially compared to the well-known direct problem of computing the reflection spectrum from a grating structure. This section is to introduce the discrete layer-peeling (DLP) synthesis method proposed by R. Feced *et al.* [81] and improved by J. Skaar *et al.* [82], which is an efficient and stable method to synthesize a grating structure.

The DLP model is based on a discretization of the grating model itself, i.e. the grating is approximated as a series of discrete complex reflector. The discrete model of the entire gratings is thus a series of N discrete complex reflectors with a distance of Δz between all reflectors. The method starts from the first reflector with a physically realizable reflection spectrum $r_I(\delta)$, where δ is the wavenumber detuning compared to a Bragg design wavenumber β_D .

Then, the calculation of complex reflection coefficient, ρ_I , can be achieved by the discrete Fourier transform of $r_I(\delta)$.

$$\rho_I = \frac{1}{M} \sum_{m=1}^M r_I(m) \quad (1.15)$$

where $r_I(m)$ denotes a discrete version of the spectrum $r_I(\delta)$ in the range $|\delta| \leq \pi/2\Delta z$ and

M is the number of wavelengths in the spectrum, which should be larger than N in the calculation.

The coupling coefficient, $\kappa(z)$, is related to the complex reflection coefficient as follows.

$$\rho = -\tanh(|\kappa|\Delta z) \frac{\kappa^*}{|\kappa|} \quad (1.16)$$

By solving Eqt. 1.16, the coupling coefficient of each discrete reflector, the physical characteristic of the grating, can be determined. The reflection spectrum of the next discrete reflector can be obtained by propagating the fields using the transfer matrix or can be described as

$$r_n = \exp(-j2\delta\Delta z) \frac{r_{n-1}(\delta) - \rho_{n-1}}{1 - \rho_{n-1}^* r_{n-1}(\delta)} \quad (1.17)$$

The discrete reflectors are calculated one by one using Eqt. 1.15 to Eqt. 1.17 until the entire grating structure is determined.

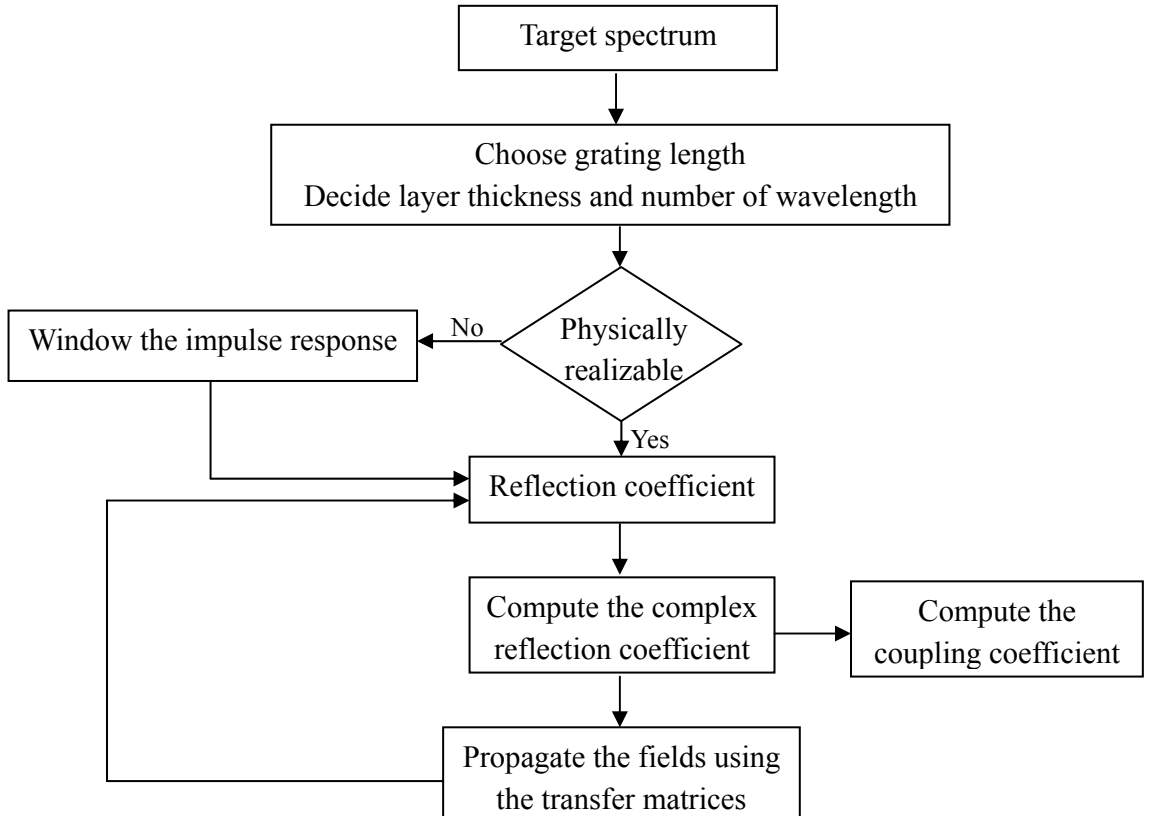


Figure 1.1 Flow chart of the DLP method.

To help understanding the procedure of DLP method, a flow chart is illustrated in Fig. 1.1. It is worth noting that when using the layer-peeling algorithm for synthesis of actual gratings, the desired reflection spectrum is not necessarily realizable for a series of N reflectors or a grating of finite length L . To obtain a realizable reflection spectrum, the apodizing or windowing procedure, which is a common technique in the digital finite-impulse-response (FIR) filter design, can be used. It forces the impulse response to be zero out of a certain window, apodizes the windowed impulse response to cause the tails to approach zero more smoothly and shifts the whole response to start at zero.

1.3 Nonlinear effects of SOAs

Nonlinear effects are powerful tools for all-optical signal processing. To implement all-optical processing, nonlinear effects of SOAs are mostly used including cross-gain modulation (XGM), cross-phase modulation (XPM) and four-wave mixing (FWM). The use of SOAs has been envisioned for the applications of all-optical signal processing such as wavelength conversion [83–91], signal regeneration [92–97] as well as logic operation [98–103].

In the operation of SOAs, there is a variation of the total density of the carriers and their distributions [104]. The variation engenders intraband and interband transitions. The interband transition only changes the carrier density but does not affect the carrier distribution, which is produced by the stimulated emission, the spontaneous emission and the non-radiative recombination. The intraband transition, such as spectral hole burning (SHB) and carrier heating (CH), is at the origin of the fast dynamics of the SOAs. The change of the carrier distribution happens in the conduction band.

The main nonlinear effects of SOAs, as introduced as follows, are caused mainly by the change of the carriers density induced by input signals.

Self-gain modulation (SGM) [105]

SGM is an effect which corresponds to the modulation of the gain induced by the variation of the input signal power.

Self-phase modulation (SPM) [106, 107]

SPM is a nonlinear effect that the output signal of the SOA experiences the phase modulation which is caused by gain saturation due to the input signal power, resulting in intensity dependent changes in the refractive index in response to variations in carrier density.

Cross-gain modulation (XGM) [108–110]

XGM is similar to SGM. The modulation of the gain is induced by another optical signal, known as a control or pump signal, which affects the gain of a probe signal propagating simultaneously in the SOA. XGM can take place in a SOA with a co-propagation or counter-propagation configuration.

Cross-phase modulation (XPM) [110, 111]

XPM is similar to SPM. The phase modulation corresponds to the change of the refractive index induced by another optical signal, known as a control or pump signal, which affects the phase of a probe signal propagating at the same time in the SOA.

Four-wave mixing (FWM) [112, 113]

FWM is a parametric process. It can be explained by the phenomenon of beating between two or several optical signals at different wavelengths propagating in the SOA, which generates signals locating at a new wavelength.

1.4 Objectives and outlines

Since CDMA technology was introduced into the optical communications, OCDMA technology has been explored for more than twenty years. As a candidate to next-generation passive optical network (NG-PON), OCDMA technology is not regarded as competitive as other multiplexing technologies in terms of data rate and scalability. However, OCDMA technology has its own unique feature, i.e. security. OCDMA technology is definitely an excellent player in the field of secure optical

communications. Bearing this point in mind, we carry out some research, including developing novel coding devices, investigating system security and demonstrating advanced modulation format, to improve OCDMA technology. Furthermore, during the research on OCDMA technology, we are inspired by the nonlinear signal processing techniques. Therefore, we also conduct some projects on optical signal processing, such as waveform generation, arithmetic operation and modulation format conversion, which we believe are powerful tools for future photonics community.

In Chapter 2, we introduce FBG based coding devices. Two novel FBG based coding devices are proposed. One is developed for high security and the other is designed for simultaneous coding and chromatic dispersion compensation.

In Chapter 3, we investigate the security of OCDMA systems. Two eavesdropping schemes are used to demonstrate the vulnerability of the systems.

In Chapter 4, we study an advanced orthogonal modulation format based on differential phase-shift keying and code-shift keying.

In Chapter 5, we demonstrate a fully-asynchronous gigabit-symmetric OCDMA-PON.

In Chapter 6, we analyze a versatile waveform generation scheme, in which short pulse, trapezoidal, triangular and sawtooth waveforms and doublet pulse are theoretically and experimentally generated at the repetition rate of 10 GHz.

In Chapter 7, we carry out an experiment on simultaneous all-optical half-addition and half-subtraction.

In Chapter 8, we conduct two schemes on modulation format conversion. One is differential quadrature phase-shift keying (DQPSK) to differential phase-shift keying (DPSK) format conversion and the other is on-off keying (OOK) to phase-shift keying-Manchester (PSK-Manchester) format conversion.

In Chapter 9, we conclude the thesis and present the future research work.

Chapter 2

Novel FBG based Coding Devices

In the OCDMA systems, coding process is a key function and optical coding devices are crucial components for code generation and recognition. Many coding devices are proposed for OCDMA systems, among which FBG can be employed in the both coherent and incoherent OCDMA systems for temporal and spectral phase coding with the advantages of low insertion loss, high compactness, polarization independent performance and low cost.

In this chapter, the coding principle of superstructured FBG (SSFBG) is introduced and then two FBG based coding devices with novel structures are developed. The first FBG en/decoder is superstructured and uses $\pm\pi/2$ -phase shifts instead of conventional $0/\pi$ -phase shifts to improve the security of coding and realize the reutilization of available codes by hybrid use of both $0/\pi$ -phase-shifted and $\pm\pi/2$ -phase-shifted SSFBG en/decoders simultaneously in the same systems. The second proposed FBG coding device has the ability to achieve chromatic dispersion compensation at the same time as optical code recognition.

2.1 Coding principle of SSFBG

An SSFBG is a conventional uniform period FBG onto which an additional slowly varying refractive index modulation profile is imposed. In the design of SSFBG, discrete phase shifts can be added to the grating structure. Within the weak grating limit, the impulse response of the SSFBG has a temporal response which is determined by the slowly varying refractive index profile. When a short optical pulse is reflected from an SSFBG with discrete phase shifts, the output signal comprises a series of coherent pulse whose relative phases are set by those in the grating structure. To work as a temporal phase coding device, a code sequence is used to decide the pattern of discrete phase shifts in the SSFBG. Consequently, the temporal response of such SSFBG contains the code information.

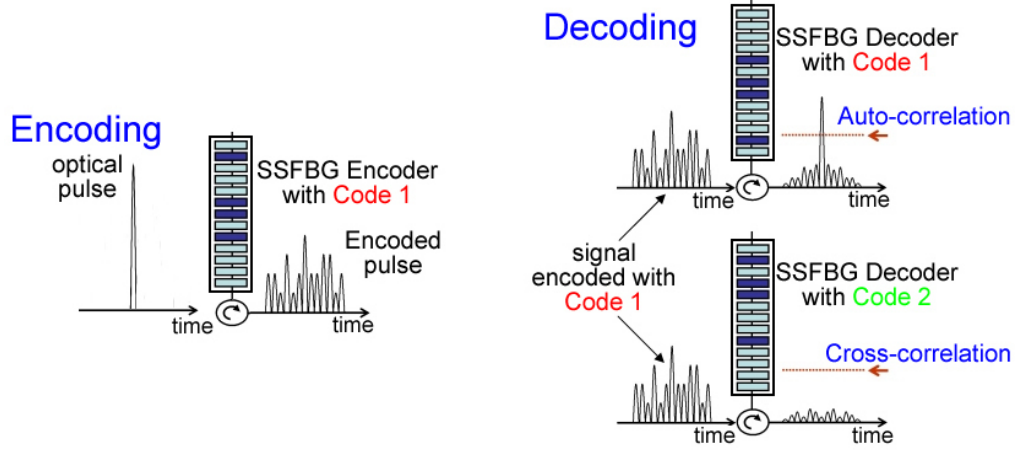


Figure 2.1 Schematic diagram of encoding and decoding using SSFBG.

Graphically, Figure 2.1 illustrates the principle of encoding and decoding using SSFBGs. A short pulse is input into the SSFBG encoder. The SSFBG consists of several subgratings. Each subgrating corresponds to a code chip. Between two adjacent subgratings, a phase shift is added depending on OCs. The output signal has a noise-like encoded waveform. The temporal duration of the encoded waveform is

$$t_{En} = \frac{2N_{chip}n_{eff}L_{chip}}{c} \quad (2.1)$$

where n_{eff} is the effective refractive index of the grating, L_{chip} is the length of subgrating (chip length), N_{chip} is the code length and c is the speed of light. In the decoding section, the encoded signal is injected into SSFBG decoders. An SSFBG decoder, comprising the physically reversed encoder structure, can correctly recover a high-intensity auto-correlation peak. Other SSFBG decoders using different code sequences can only produce low-intensity cross-correlation noise, i.e. multiple-access interference (MAI) noise. The temporal duration of the decoded waveform is

$$t_{De} = \frac{2(2N_{chip}-1)n_{eff}L_{chip}}{c} \quad (2.2)$$

To avoid inter-symbol interference (ISI), the temporal duration of the decoded waveform should be shorter than one bit duration. In other words, the data rate of the

transmission is limited by the code length and the chip length. However, the coding performance is related to the code length. Longer codes can provide better correlation performance, i.e. lower MAI noise, because the energy of improper decoded signal is widely spread along the time intervals. In addition, a shorter chip length, which yields to a shorter temporal duration of decoded signal, is preferred for a higher data rate, while practically the chip length is restricted by the precision of the fabrication.

2.2 $\pm\pi/2$ -phase-shifted SSFBG en/decoder

In this section, we firstly analyze the security vulnerability of conventional binary $0/\pi$ -phase-shifted SSFBG en/decoders. To improve the security, we propose SSFBG en/decoders with a novel structure using $\pm\pi/2$ -phase shifts. We investigate the security enhancement of the novel en/decoders. In addition, we find that the hybrid use of both conventional and novel en/decoders is feasible. Finally, we experimentally test the novel en/decoders with the conventional en/decoders in the various OCDMA systems.

2.2.1 Security vulnerability of $0/\pi$ -SSFBG en/decoders

In the coherent time-spreading OCDMA system, SSFBGs are applied for the phase coding, which are capable to generate ultra-long codes with ultra-high chip rates [44–47, 114]. Typically, $0/\pi$ -phase-shifted SSFBG ($0/\pi$ -SSFBG) en/decoders, which have the structure of 0 or π phase shift between adjacent chips, are used for the temporal binary phase coding. However, the security vulnerability exists in the encoded waveform of $0/\pi$ -SSFBG encoders [48, 115].

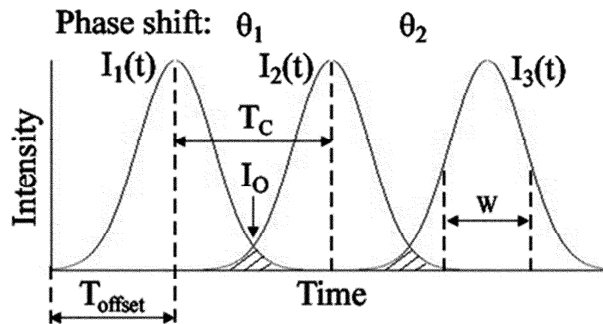


Figure 2.2 Reflected-pulse model.

To investigate the security of the encoded waveform, a reflected-pulse model, as shown in Fig. 2.2, is built to demonstrate a simplified output waveform of an SSFBG encoder. Three pulses reflected from adjacent chips of SSFBG are considered in this model. θ_1 and θ_2 are phase shifts between two chips. W is pulse width, which is full-width-at-half-maximum of pulse. Shaded area is the overlapped part of the two pulses. T_C is chip duration of the grating. Each reflected pulse is assumed to be a Gaussian shaped pulse, whose intensity is

$$I_n(t) = \left| A \exp \left(-\frac{(t - T_{offset} - (n-1)T_C)^2}{2(W/1.665)^2} + i\varphi \right) \right|^2 \quad (2.3)$$

where T_{offset} is the time when first pulse peak appears, A is the amplitude, φ is the phase and $n = 1, 2, \text{ and } 3$.

For a conventional $0/\pi$ -SSFBG, the phase shift is either 0 or π between adjacent chips. When the phase shift is π , two pulses cancel each other in the overlapped part, generating a dip. Such phenomenon can be explained mathematically using the reflected-pulse model. The intensity in the middle of the overlapped part for 0 or π phase shift is

$$\begin{aligned} I_{O,0} &= \left| A \exp \left[-\frac{(T_C/2)^2}{2(W/1.665)^2} + i\theta \right] + A \exp \left[-\frac{(-T_C/2)^2}{2(W/1.665)^2} + i\theta \right] \right|^2 \\ &= 4A^2 \exp^2 \left[-\frac{(T_C/2)^2}{2(W/1.665)^2} \right] \end{aligned} \quad (2.4)$$

or

$$\begin{aligned} I_{O,\pi} &= \left| A \exp \left[-\frac{(T_C/2)^2}{2(W/1.665)^2} + i\theta \right] + A \exp \left[-\frac{(-T_C/2)^2}{2(W/1.665)^2} + i(\theta + \pi) \right] \right|^2 \\ &= 0 \end{aligned} \quad (2.5)$$

When phase shift is π , two pulses cancel each other in the middle of the overlapped part. Compared with non-zero intensity when phase shift is 0, the null intensity for π phase shift can be distinguished clearly. Therefore, the temporal dips in the encoded waveform hint π phase shifts between adjacent chips. An eavesdropper can then easily extract the code sequence from the encoded waveform according to the dips. The code

extraction technique for $0/\pi$ -SSFBG is summarized as follows:

- 1) Examine the potential dip positions to find out the dips.
- 2) Compare the time interval between two dips with the chip duration to locate chip positions.
- 3) Assume the code ('-1' or '1') in the first chip.
- 4) Derive the code in the next chip. If there is a dip, the next code is different from the previous one; otherwise, the next code remains the same.
- 5) Repeat Step 4 until the whole code sequence is figured out.

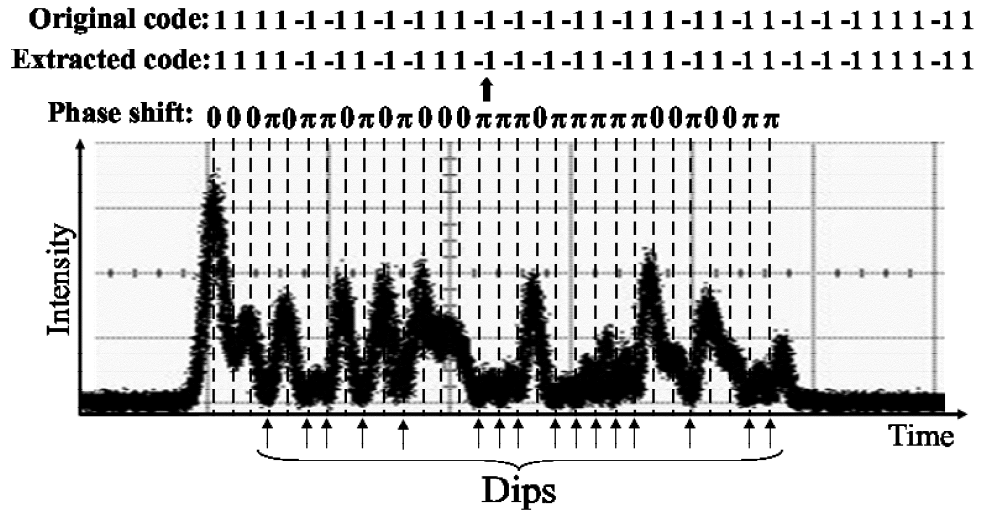


Figure 2.3 Demonstration of code extraction technique for $0/\pi$ -SSFBG using a waveform encoded by 31-chip Gold code.

The extraction approach is demonstrated in Fig. 2.3. The measured waveform is encoded by a $0/\pi$ -SSFBG with a 31-chip Gold code sequence. The chip length is 0.156 mm and the chip rate is 640 Gchip/s. There are 30 potential dip positions for 31-chip code. Within these 30 potential dip positions, the actual dips are found and the chip positions are located. The code sequence can be derived according to the last three steps in the above procedure. Consequently, the extracted code is same as the one fabricated to the $0/\pi$ -SSFBG, as shown on the top of Fig. 2.3. This reveals a security vulnerability of the $0/\pi$ -SSFBG encoded signals that needs to be addressed by exploiting new structure of SSFBG encoders.

2.2.2 Security improvement using $\pm\pi/2$ -SSFBG en/decoders

We propose using $\pm\pi/2$ -SSFBG as encoder to conceal code pattern in the encoded waveform. In the $\pm\pi/2$ -SSFBG structure, the phase shift at the boundary of adjacent chips is either $+\pi/2$ or $-\pi/2$ instead of 0 or π . Theoretically, whatever the phase shift is $+\pi/2$ or $-\pi/2$, each overlapped part of adjacent reflected pulses has identical intensity, which can be expressed using the simplified reflected-pulse model as follow

$$\begin{aligned}
 I_{o,\pm\frac{\pi}{2}} &= \left| A \exp \left[-\frac{(T_c/2)^2}{2(W/1.665)^2} + i\theta \right] + A \exp \left[-\frac{(-T_c/2)^2}{2(W/1.665)^2} + i\left(\theta \pm \frac{\pi}{2}\right) \right] \right|^2 \\
 &= 2A^2 \exp^2 \left[-\frac{(T_c/2)^2}{2(W/1.665)^2} \right]
 \end{aligned} \tag{2.6}$$

We developed a set of gratings with $0/\pi$ - and $\pm\pi/2$ -phase shifts and using two code sequences to test the security, coding and system performances, as tabulated in Table 2.1. The $0/\pi$ -SSFBG and $\pm\pi/2$ -SSFBG en/decoders using two same code sequences have the chip length of 0.156 mm, corresponding to the chip duration of 1.56 ps. Two 31-chip gold codes are used as the code patterns.

Table 2.1 Different SSFBG en/decoders used in the experiment.

Grating	Type	Code Sequence	Chip Length (mm)
CG1:CG1*	$0/\pi$ -SSFBG	Gold code 1	0.156
CG2:CG2*	$0/\pi$ -SSFBG	Gold code 2	0.156
NG1:NG1*	$\pm\pi/2$ -SSFBG	Gold code 1	0.156
NG2:NG2*	$\pm\pi/2$ -SSFBG	Gold code 2	0.156

* indicates the decoder

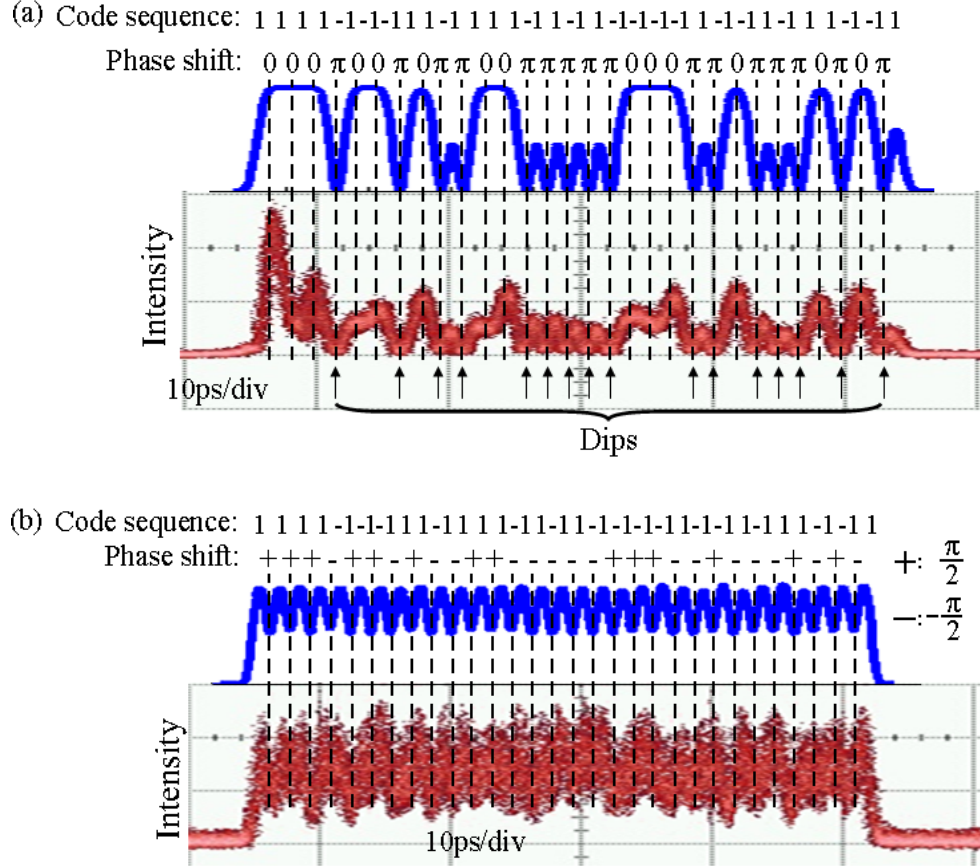


Figure 2.4 Encoded waveforms of $0/\pi$ -SSFBG and $\pm\pi/2$ -SSFBG encoders with different chip durations (a) CG1 and (b) NG1.

In the experiment, we generated the Gaussian shaped optical pulse with the pulse width of 1 ps (FWHM) and launched into the $0/\pi$ -SSFBG and $\pm\pi/2$ -SSFBG encoders (CG1 and NG1) to investigate the security of the encoded waveforms, as shown in Fig. 2.4. The calculated results are also shown above the experimental results. The measured waveforms fit the calculated results well. Dips can be easily found in the waveform encoded by the $0/\pi$ -SSFBG encoder. The existence of the dips hints the π phase shifts in the code pattern and results in the vulnerable regularity, based on which the thirty phase shifts can be determined. Then, the whole code sequence can be extracted accordingly. In the Fig. 2.4(b), 31 chips exhibit same peaks and valleys and no regularity can be found in the encoded waveform. The $\pm\pi/2$ -SSFBG encoder conceals the code sequences well in the uniform encoded waveform, significantly improving the security of encoding.

The vulnerable regularity in the encoded waveform of $0/\pi$ -SSFBG encoders is related to the structure of the encoder. However, it has been found that the input pulse has the influence over the encoded waveform of the $\pm\pi/2$ -SSFBG encoder. The intensity of the pulse reflected from the subgrating is variable with the change of the input pulse width, since the neighboring reflected pulses on the two sides have some influence over the middle one, as shown in Fig. 2.5. When the chip duration of the $\pm\pi/2$ -SSFBG is fixed, with the increase of the pulse width, the reflected pulse within two different phase shifts grows, while that within same phase shifts decays relatively.

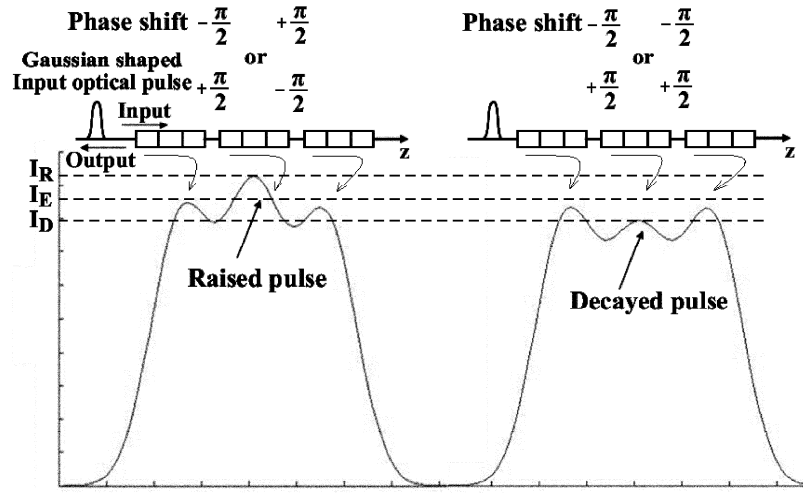


Figure 2.5 Reflected temporal response of 3-chip $\pm\pi/2$ -SSFBG with different or same adjacent phase shifts.

Apparently, an eavesdropper can utilize the relationship between the disparity of reflected pulse and phase shift to find out the code pattern. We summarize the code extraction technique for the $\pm\pi/2$ -SSFBG encoder as follows.

- 1) Partition the encoded waveform into N_{chip} sections.
- 2) Determine the intensity levels for the raised and decayed pulses, I_R and I_D , and set the extraction level, $I_E = (I_R + I_D)/2$.
- 3) Assume the first phase shift to be $+\pi/2$ or $-\pi/2$. The assumption will result in two non-equivalent code sequences extracted from the waveform.
- 4) Derive the next phase shift. If the intensity of next reflected pulse is above the extraction level, the next phase shift is different from the previous one, and vice

versa.

- 5) Repeat Step 4 until all phase shifts are found.
- 6) Set the code in the first chip as '1'.
- 7) Find out the code in the next chip. If the phase shift is $+\pi/2$, the next code is same as the previous one, and it is different when the phase shift is $-\pi/2$
- 8) Repeat Step 7 until the whole code sequence is found.
- 9) Two code sequences are obtained due to the different assumption of the first phase shift. To ascertain the real code sequence, decode the encoded signal with one code sequence. If the trial code sequence is the correct one, an autocorrelation peak can be observed.

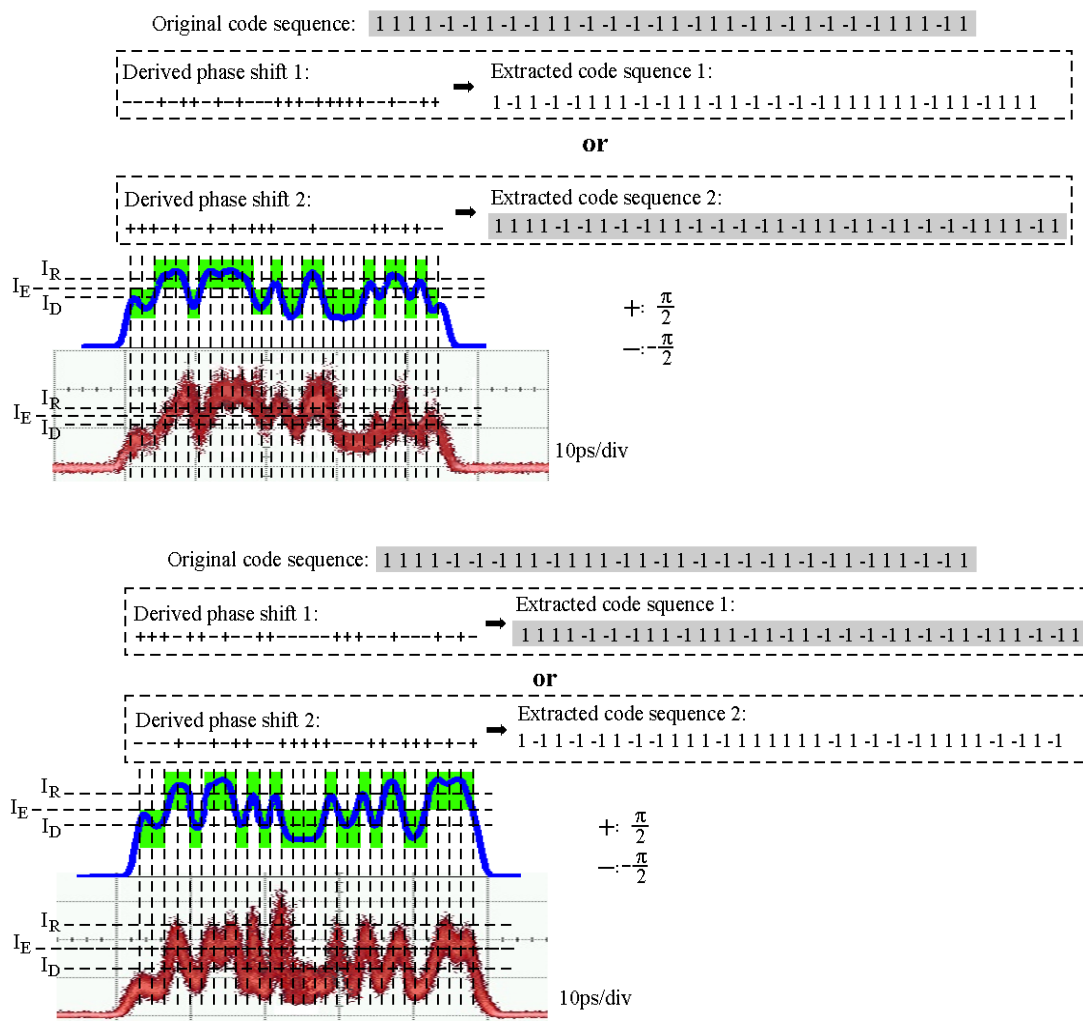


Figure 2.6 Demonstration of code extraction technique for the $\pm\pi/2$ -SSFBG encoders (a) NG1 and (b) NG2.

To demonstrate the code extraction technique for the $\pm\pi/2$ -SSFBG encoder, we launched a 1.7 ps (FWHM) Gaussian shaped optical pulse into the encoders (NG1 and NG2). In the encoded waveforms, as illustrated in Fig. 2.6, the reflected pulses have different intensities. In the code extraction process, the chip positions are firstly determined and the intensity levels of the raised and decayed pulses are estimated, based on which the extraction level I_E is calculated. Then two groups of phase shift can be obtained. According to the two groups of phase shift, two non-equivalent code sequences are found. Since the two code sequences will generate the same waveform, it is impossible to tell the real code sequence only by calculation. To confirm the real code sequence, the eavesdropper has to fabricate an SSFBG decoder to perform autocorrelation. Only the decoder using the real code sequence can generate the autocorrelation.

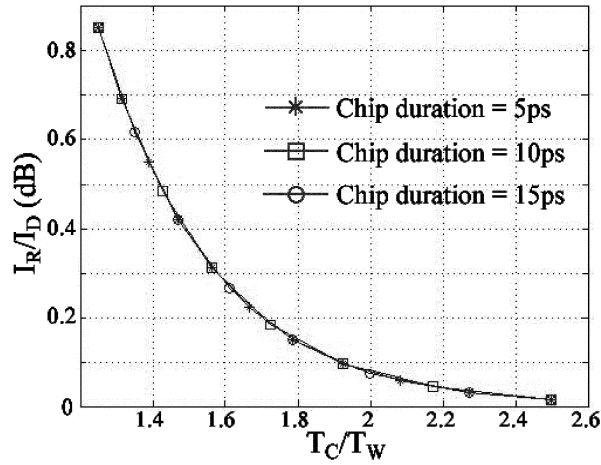


Figure 2.7 The disparity of raised and decayed peak (I_R/I_D) with different chip duration and input pulse width ratios (T_C/T_W).

The distinction of raised and decayed pulses is a premise for the security of $\pm\pi/2$ -SSFBG, so the ratio of raised and decayed peak intensities (I_R/I_D) can be used to quantitatively evaluate the security performance. If I_R/I_D is small enough, it is hard to tell the difference between reflected pulses. Once the disparity of reflected pulses is unmeasurable, eavesdroppers are unable to decide the extraction level and extract the

code from the encoded waveform. I_R/I_D is determined by the ratio of chip duration and pulse width (T_C/T_W). The relation between I_R/I_D and T_C/T_W is depicted in Fig. 2.7. Three different chip durations are considered with T_C/T_W ranging from 1.25 to 2.5, and the results are identical for different chip durations. I_R/I_D decreases with the increase of T_C/T_W . It indicates that shorter input pulse results in less disparity of reflected pulses, improving the uniformity of the encoded waveform. When the chip duration is twice as large as the pulse width, i.e. T_C/T_W is 2, I_R/I_D is smaller than 0.1 dB, so that an eavesdropper can hardly determine the extraction level and extract the code sequence. Therefore, short input pulses are desirable for security improvement.

By comparison, the $0/\pi$ -SSFBG encoder can not provide security in substance, since the eavesdropper can always find the dips in the encoded waveform and extract the code sequence, while the $\pm\pi/2$ -SSFBG encoder can conceal the code pattern well in the encoded waveform and guarantee the security by nature.

2.2.3 Coding performance of $\pm\pi/2$ -SSFBG en/decoders

Besides the security performance, we also investigate the coding performance of both $0/\pi$ -SSFBG and $\pm\pi/2$ -SSFBG en/decoders by evaluating the ratio of autocorrelation intensity peak over the maximum autocorrelation wing level (P/W) and to the maximum cross-correlation level (P/C). In our calculation, the SSFBG en/decoder has the chip duration of 1.56 ps and the input pulse has the pulse width of 1 ps. Subsets of 31-chip, 63-chip and 127-chip Gold codes are used.

Table 2.2 Average values of autocorrelation and cross-correlation for different en/decoder and chip length.

En/decoder	31-chip		63-chip		127-chip	
	P/W	P/C	P/W	P/C	P/W	P/C
$0/\pi$ -SSFBG	13.02	8.17	16.63	11.81	32.25	29.10
$\pm\pi/2$ -SSFBG	13.05	8.34	16.58	12.03	32.46	29.36
Hybrid use		10.79		20.42		32.27

Fig. 2.8 illustrates the superimposed normal density of P/W for three different code lengths and the average values are listed in the Table 2.2. The $\pm\pi/2$ -SSFBG en/decoder has the similar autocorrelation performance as the $0/\pi$ -SSFBG en/decoder. With the increase of the code length, the autocorrelation performance of both en/decoders improves and the code capacity expands. Compared to the 31-chip and 63-chip cases, the en/decoders using 127-chip Gold code has much better performance.

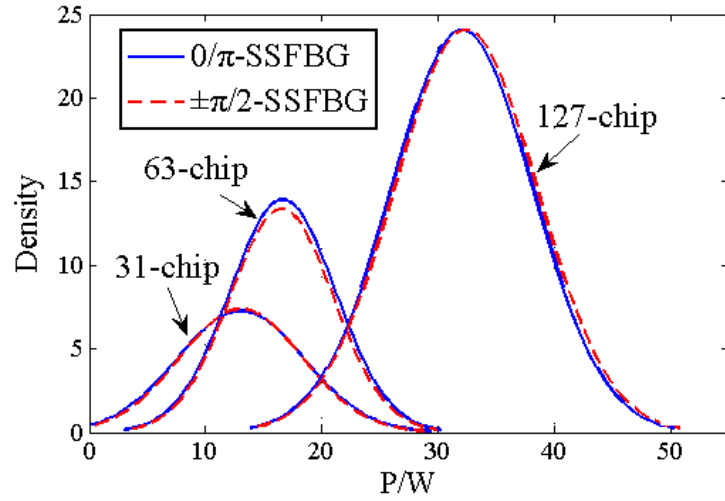


Figure 2.8 Autocorrelation of the $0/\pi$ -SSFBG and $\pm\pi/2$ -SSFBG en/decoders with 31-chip, 63-chip and 127-chip Gold code.

Furthermore, we analyze the hybrid use of both en/decoders, i.e. $0/\pi$ -SSFBG encoder to $\pm\pi/2$ -SSFBG decoder and $\pm\pi/2$ -SSFBG encoder to $0/\pi$ -SSFBG decoder, whose cross-correlation performance is exhibited within the top-left and bottom-right box in Fig. 2.9. The average P/C values are tabulated in the Table 2.2. In the hybrid use, the intensity level of the cross-correlation is low, which results in high P/C values. Due to the good cross-correlation performance of hybrid use, it guarantees that $\pm\pi/2$ -SSFBG en/decoder can be used together with $0/\pi$ -SSFBG en/decoder in the same system.

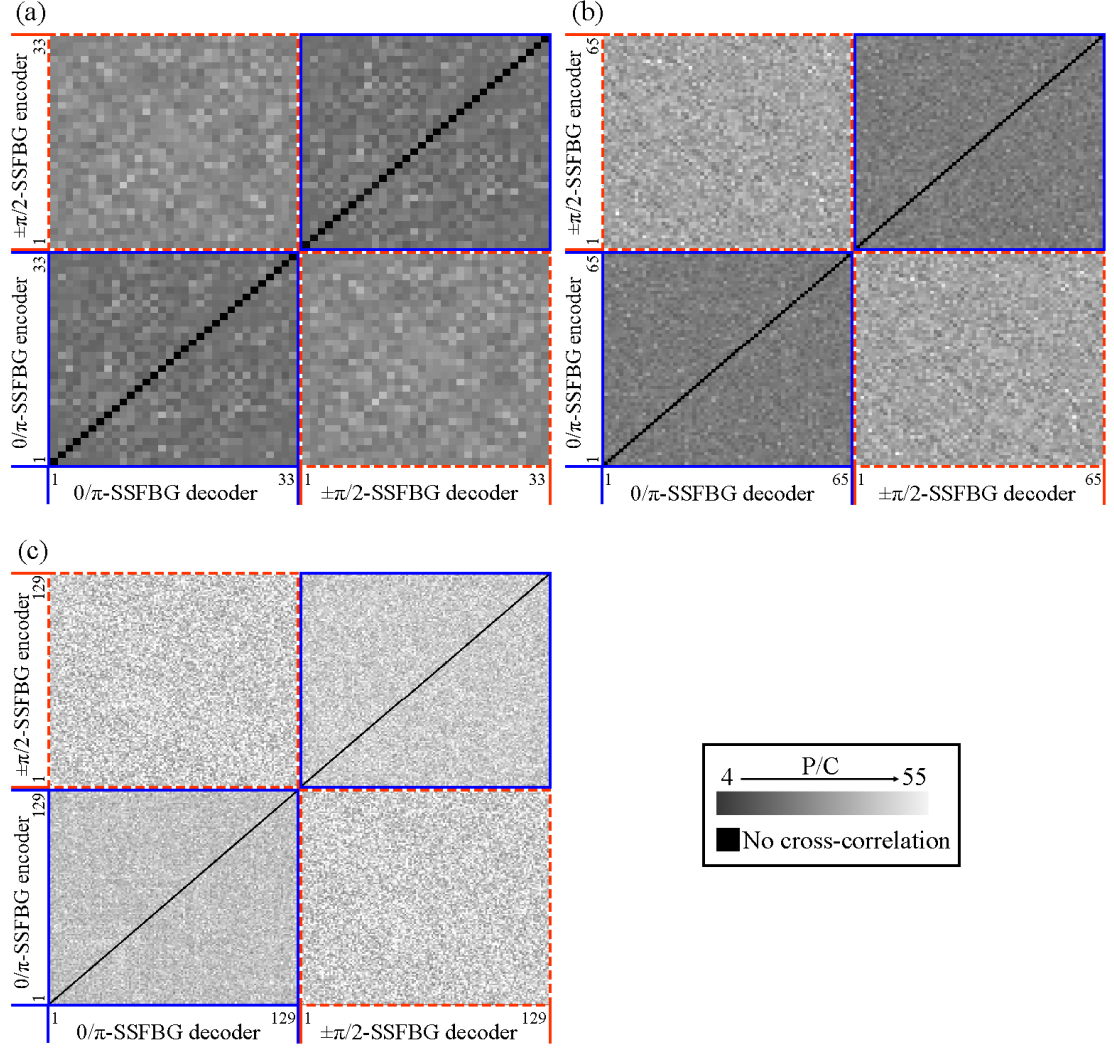


Figure 2.9 Cross-correlation of the $0/\pi$ -SSFBG and $\pm\pi/2$ -SSFBG en/decoders and the hybrid use with (a) 31-chip, (b) 63-chip and (c) 127-chip Gold code.

We measure the coding performance of the fabricated en/decoders. In the experiment, a 1 ps Gaussian shaped optical pulse was launched into the encoder and the decoder followed the encoder directly. Both measured and calculated decoded waveforms are shown in Fig. 2.10. The decoded waveforms of $0/\pi$ -SSFBG and $\pm\pi/2$ -SSFBG en/decoders are in the top-left and bottom-right box and the waveforms of the hybrid use is in the bottom-left and top-right box. An autocorrelation high peak is generated, if the decoder matches the encoder. Otherwise, a cross-correlation low power signal is produced. The hybrid use of the $0/\pi$ -SSFBG and $\pm\pi/2$ -SSFBG en/decoders also leads to the low power level cross-correlation. The P/W and P/C are all larger than 7. The good correlation guarantees the coding performance of both en/decoders and

promises the hybrid use of the $0/\pi$ -SSFBG and $\pm\pi/2$ -SSFBG en/decoders.

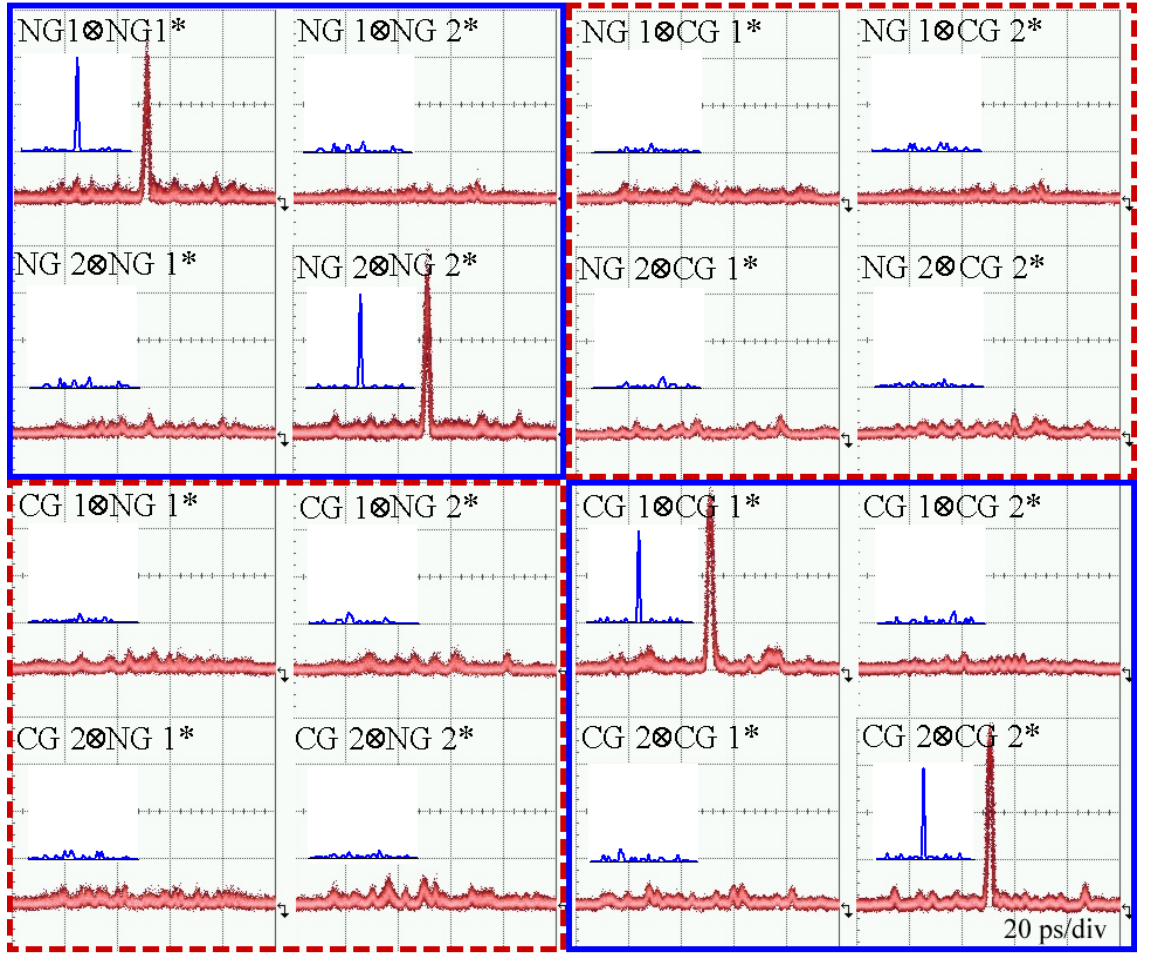


Figure 2.10 Measured and calculated correlation of $0/\pi$ -SSFBG and $\pm\pi/2$ -SSFBG en/decoders.

The code recognition in SSFBG is aperiodic correlation, but the code sets used in the OCDMA system are designed for good periodic correlation properties. The number of codes with good aperiodic correlation is limited [45]. The hybrid use of both kinds of en/decoders is capable of reusing the same codes. According to our calculation and experimental measurement, the signals encoded with the same optical codes by $0/\pi$ -SSFBG and $\pm\pi/2$ -SSFBG en/decoders perform good cross-correlation ($P/C > 10$). It allows the same code being used twice in the same system. Therefore, the hybrid use makes it possible to reuse the available codes from the same code set in the same system.

2.2.4 $\pm\pi/2$ -SSFBG en/decoders in the OCDMA systems

To investigate the performances of $\pm\pi/2$ -SSFBG en/decoders in the OCDMA system, we placed the en/decoders in a 2-user OOK-OCDMA system. The experimental setup is shown in Fig. 2.11. A mode locked laser diode (MLLD) generated a Gaussian shaped pulse train with the pulse width of 2.3 ps (FWHM) at a repetition rate of 10 GHz, spectrally centered at 1563 nm. After a 2 km dispersion flattened fiber (DFF) and a 7.5 nm band-pass filter (BPF), the pulse width was compressed to 1 ps. The pulse train was modulated with the $2^{15}-1$ pseudorandom bit sequence (PRBS) data by an intensity modulator (IM). The modulated pulse train was split into two arms. Two $0/\pi$ -SSFBG encoders (CG1 and CG2) or two $\pm\pi/2$ -SSFBG encoders (NG1 and NG2) were applied for the encoding. A 20 m single mode fiber (SMF) was added for de-coherence and an attenuator was used to balance the power of the encoded signals in the both arms. Then the encoded signals were combined for decoding. In the decoding section, corresponding decoder was used.

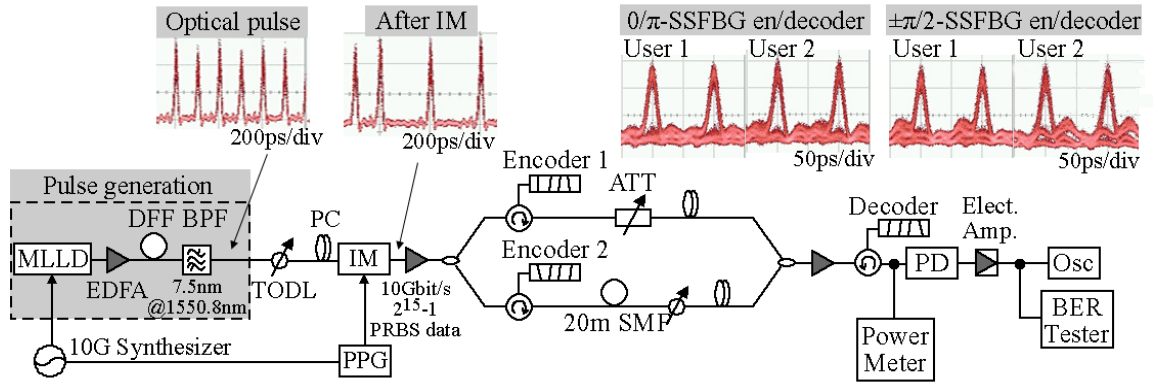


Figure 2.11 Experimental setup of 2-user OOK-OCDMA system and measured waveforms and eye diagrams.

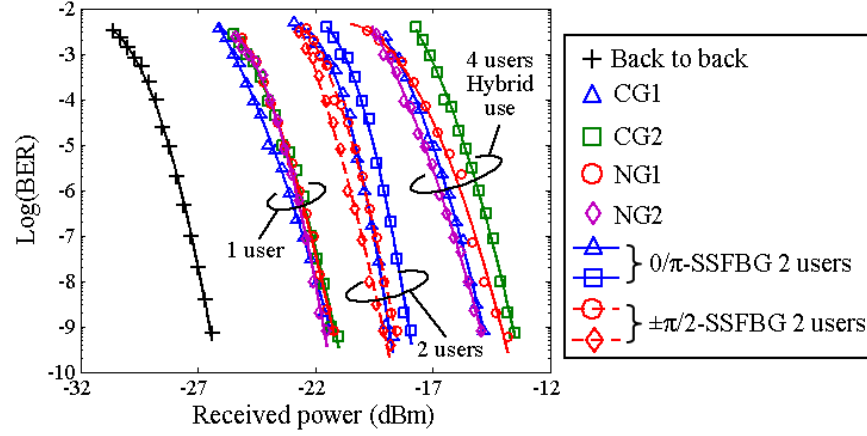


Figure 2.12 BER performances of the $0/\pi$ -SSFBG and $\pm\pi/2$ -SSFBG en/decoders in the OOK-OCDMA system.

The bit-error-rate (BER) measurement against the received power is illustrated in Fig. 2.12. Both $0/\pi$ -SSFBG and $\pm\pi/2$ -SSFBG en/decoders achieve the error-free ($\text{BER} < 10^{-9}$). Relative to the single-user OOK-OCDMA system, the 2-user system has about 3 dB power penalty, which is resulted from the MAI noise. Compared to the $0/\pi$ -SSFBG en/decoder, $\pm\pi/2$ -SSFBG en/decoder has equally good performance in the system.

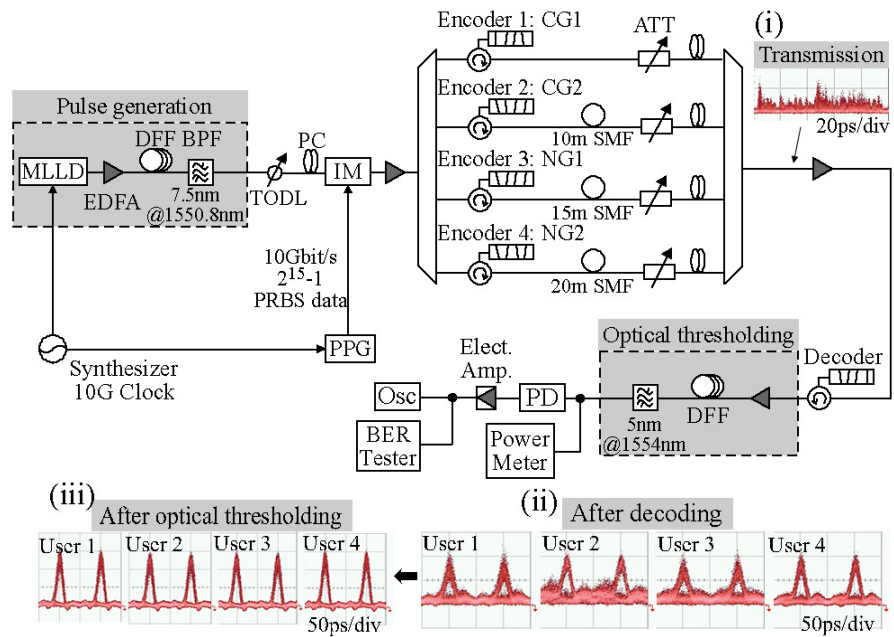


Figure 2.13 Experimental setup of 4-user OOK-OCDMA system with hybrid use of en/decoders and measured waveforms and eye diagrams.

To investigate the hybrid use of the $0/\pi$ -SSFBG and $\pm\pi/2$ -SSFBG en/decoders in the same system, we modified the experimental setup according to Fig. 2.13. Two $0/\pi$ -SSFBG encoders and two $\pm\pi/2$ -SSFBG encoders were simultaneously utilized for the encoding. The encoded signals were multiplexed to generate the 4-user OOK-OCDMA signals, which exhibited as noise-like waveforms, as shown in the inset Fig. 2.13(i). In the receiving side, four decoders were used one by one to decode the multiplexed signal. When the decoder matched the encoder, the target signals were recovered into the high intensity peaks and the signals from other users resulted in the MAI noise, as illustrated in the inset Fig. 2.13(ii). To suppress the interference from other users, the supercontinuum (SC) based optical thresholding was adopted, which consisted of an erbium doped fiber amplifier (EDFA), a 2000 m DFF and a 5 nm BPF with the center wavelength of 1554 nm [116]. The MAI was efficiently removed by the optical thresholding (see inset Fig. 2.13(iii)). Clear eye diagrams for four users could be observed. The BER of four users is also depicted in Fig. 2.12. Compared to the single-user system, the four-user system causes about 7 dB power penalty at the BER of 10^{-9} . The BER of four users confirms the feasibility of the hybrid use of the $0/\pi$ -SSFBG and $\pm\pi/2$ -SSFBG en/decoders.

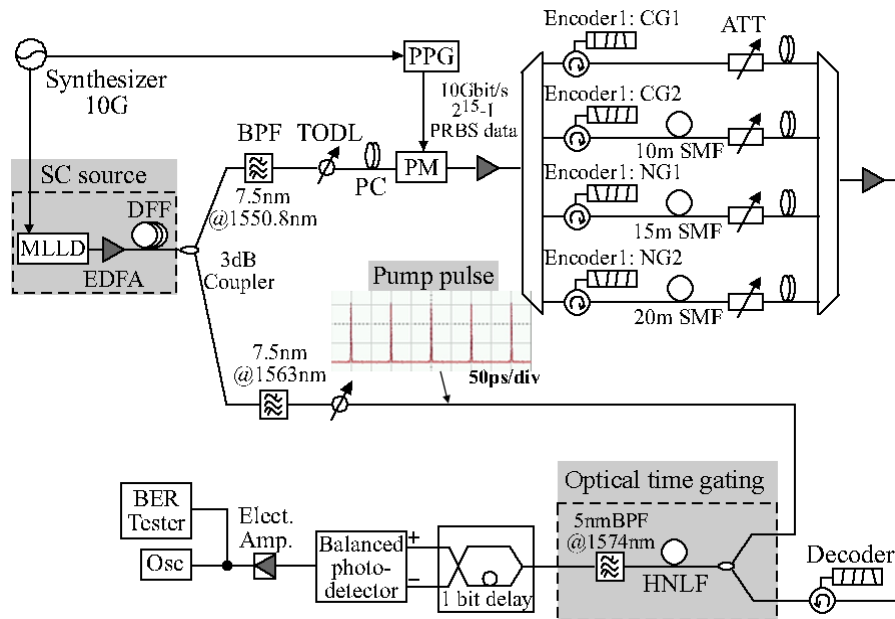


Figure 2.14 Experimental setup of 4-user DPSK-OCDMA system with hybrid use of en/decoders and measured waveforms and eye diagrams.

We also study the performance of the en/decoders in the 4-user 10 Gbps/user DPSK-OCDMA system with the optical time gating detection, whose experimental setup is shown in Fig. 2.14. The pulse train from the SC source was divided into two branches. One was filtered at 1550.8 nm and modulated with the $2^{15}-1$ PRBS data by the phase modulator (PM). The modulated pulse train was divided into four arms for encoding and combined to generate the 4-user DPSK-OCDMA signals. At the receiver, the multiplexed signals were decoded by the corresponding decoders, followed by the optical time gating detection. Optical time gating is capable to efficiently remove the MAI noise in an OCDMA system [117–119]. In the optical time gating section, the decoded signals were combined by a 3 dB coupler with the pump pulses, which were from another branch of the SC source and filtered at 1563 nm. The combined signals were launched into the highly nonlinear fiber (HNLf) for four-wave mixing (FWM). A 5 nm filter centered at 1574 nm was used to let the correctly decoded high-peak signal pass. After the time gating, the MAI was mitigated and the target signals were detected by the balanced photodetector (BPD).

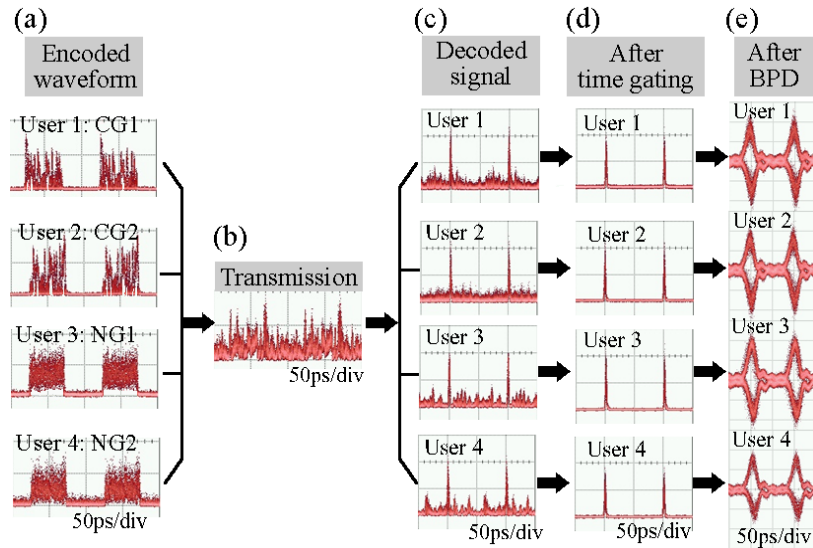


Figure 2.15 Measured waveforms and eye diagrams in the 4-user DPSK-OCDMA system.

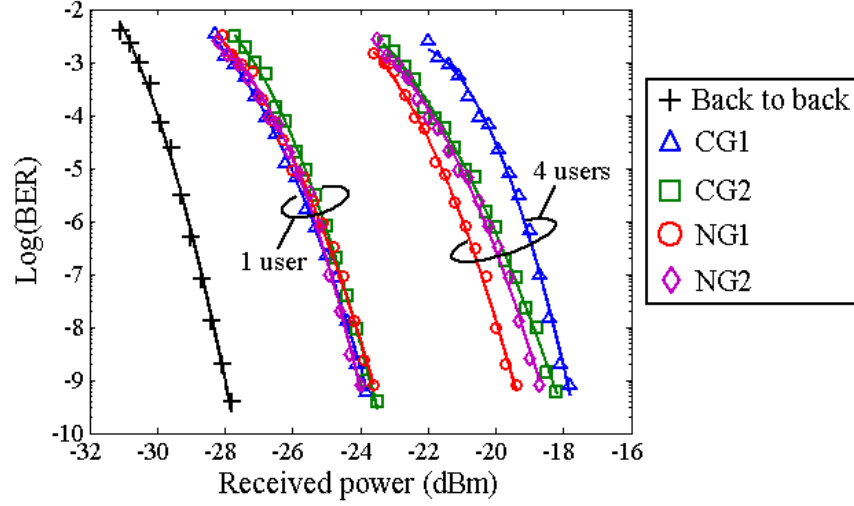


Figure 2.16 BER performances of the $0/\pi$ -SSFBG and $\pm\pi/2$ -SSFBG en/decoders in the DPSK-OCDMA system.

The measured waveforms at different points of the experiment are illustrated in the Fig. 2.15. The encoded waveforms of the $0/\pi$ -SSFBG encoders are distinguishable, while the waveforms encoded by the $\pm\pi/2$ -SSFBG encoders have the uniform shapes, as shown in Fig. 2.15(a). Comparing the waveforms in Fig. 2.15(c) with those in Fig. 2.15(d), we can see that the MAI can be well suppressed by means of the time gating. Clear open eye diagrams can be obtained after the balanced detection, shown in Fig. 2.15(e). Fig. 2.16 shows the BER performance for the hybrid use of the $0/\pi$ -SSFBG and $\pm\pi/2$ -SSFBG en/decoders in the DPSK-OCDMA system. Error-free has been achieved for all the four users and the 4-user system has a 6 dB power penalty compared to the single-user system. The $\pm\pi/2$ -SSFBG en/decoder performs as well as the $0/\pi$ -SSFBG en/decoder. The error-free coding achieved in the experiment promises that the hybrid use of both en/decoders is also feasible in the phase modulated system.

2.3 FBG based decoder for simultaneous optical code recognition and chromatic dispersion compensation

In typical OCDMA systems, compared to the nonlinearity, dispersion is a more significant factor to limit the system performance. Some research work has been carried out to address this issue [120]. After long transmission, due to the chromatic dispersion,

the decoded signal from conventional decoder is spread over time and the autocorrelation peak can not be recovered. Consequently, in the multi-user system with the chip-rate detection or data-rate detection with optical threshold, the system performance degrades with the increase of the number of users because the signal-to-noise ratio (SNR) diminishes [121]. Even in a single user system, the broadened pulses from adjacent bits overlapping with each other causes ISI, especially at high data rate. Therefore, dispersion compensation before decoding is essential in an OCDMA system. It is desirable to use a single FBG for simultaneous optical recognition and dispersion compensation. In this section, we propose a novel dispersion compensation FBG (DC-FBG) decoder, designed by the DLP method [81, 82], for simultaneous OC recognition and dispersion compensation.

2.3.1 Derivation of the target reflection spectrum

When a short pulse is reflected from an SSFBG encoder, it is transformed into a noise-like pulse train, whose frequency response is

$$Y(\omega) = X(\omega) \times H(\omega) \quad (2.7)$$

where $Y(\omega)$ and $X(\omega)$ are the Fourier transform of the output and the incident signal and $H(\omega)$ is the impulse response of the SSFBG encoder. To perform the correct OC recognition, the decoder should be spatially reversed to that of the encoder, i.e. $G(\omega) = H^*(\omega)$. The response can be expressed as follows.

$$Z(\omega) = Y(\omega) \times G(\omega) \quad (2.8)$$

where $Z(\omega)$ is the Fourier transform of the decoded waveform.

In a practical system, the dispersive transmission introduces a dispersive phase, $\Phi_{Disp}(\omega; L)$, which is frequency- and length-dependent. Thus, the frequency response after the transmission is

$$Y_T(\omega) = Y(\omega) \times \exp[i\Phi_{Disp}(\omega; L)] \quad (2.9)$$

where $\exp[i\Phi_{Disp}(\omega; L)]$ is the dispersion phase coefficient. Then, the decoded waveform after the transmission is

$$\begin{aligned} Z_{Disp_T}(\omega) &= Y_T(\omega) \times G(\omega) \\ &\neq Z(\omega) \end{aligned} \quad (2.10)$$

The existence of the dispersion phase coefficient leads to incorrect OC recognition. To compensate and decode the signal concurrently, we derive the target impulse response of the DC-FBG decoder, which contains an opposite signed dispersive phase, given by

$$G_{DC-FBG}(\omega) = G(\omega) \times \exp[-i\Phi_{Disp}(\omega; L)] \quad (2.11)$$

Therefore, the decoded signal from this DC-FBG decoder is same as that without transmission, i.e.

$$\begin{aligned} Z_T(\omega) &= Y_T(\omega) \times G_{DC-FBG}(\omega) \\ &= Z(\omega) \end{aligned} \quad (2.12)$$

2.3.2 Synthesis and performance of DC-FBG decoder

We adopt the DLP method [81, 82] to synthesize the structure of DC-FBG decoder. We use a 63-chip conventional SSFBG decoder as an example to demonstrate the synthesis method. The chip length is 0.5 mm, corresponding to temporal chip duration of 5 ps.

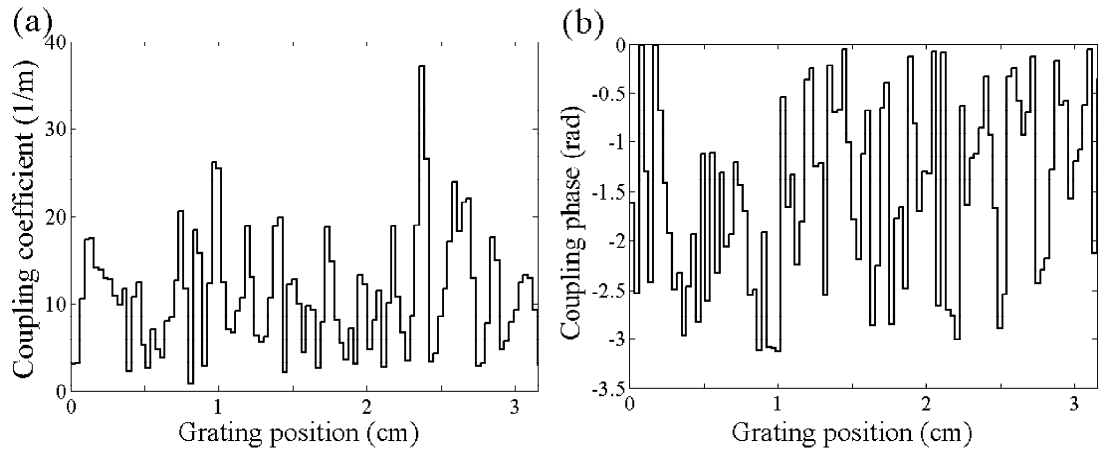


Figure 2.17 (a) Coupling coefficient and (b) spatial relative phase of the DC-FBG with -170 ps/nm dispersion.

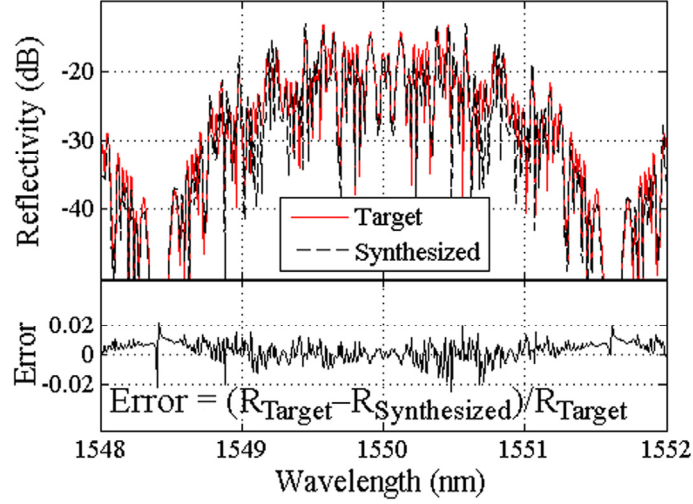


Figure 2.18 Target and synthesized spectra of DC-FBG decoder and synthesized error.

R_{Target} and $R_{\text{Synthesized}}$: Reflectivity of target and synthesized spectra.

A group delay per unit length of -170 ps/nm is considered in the synthesis of grating for compensating the chromatic dispersion caused by a 10 km transmission over a single mode fiber (SMF) with dispersion of $+17$ ps/nm·km. In the calculation, the DC-FBG decoder consists of 100 subgratings and its length is 3.15 cm. A longer grating is required for larger dispersion. The synthesized coupling coefficient and relative phase are illustrated in Fig. 2.17. The synthesized spectrum is shown in Fig. 2.18 together with the target spectrum and synthesized error. The synthesized error is no more than $\pm 2\%$, which indicates a good similarity of the synthesized spectrum.

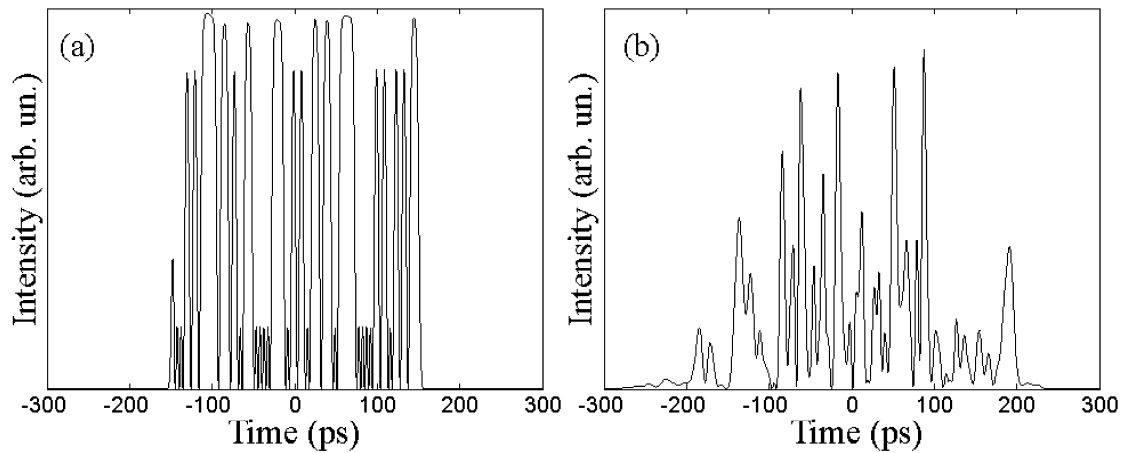


Figure 2.19 (a) Encoded waveform and (b) dispersed encoded waveform after transmission.

The encoded waveform of the 63-chip SSFBG encoder with 4ps Gaussian shape input pulse is shown in Fig. 2.19(a). The temporal duration of the encoded waveform is about 300 ps. After transmitting through a 10 km SMF with dispersion of +17 ps/nm·km, the waveform is broadened to more than 400 ps as shown in Fig. 2.19(b).

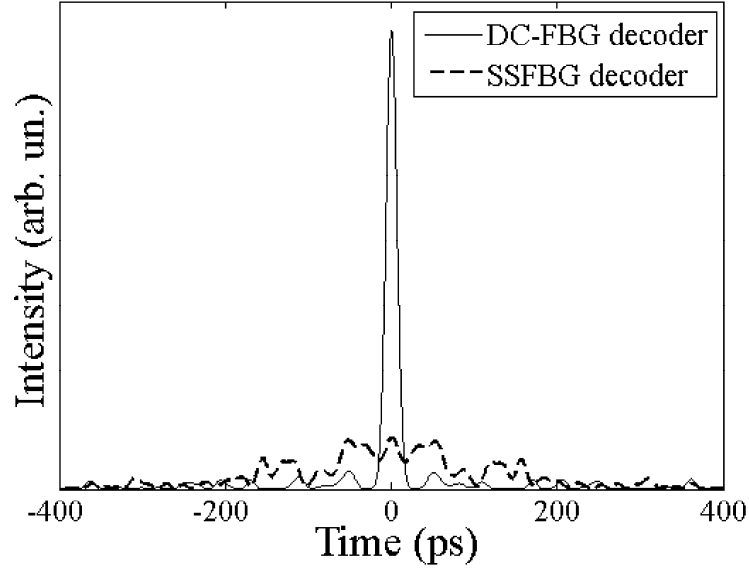


Figure 2.20 Decoded waveform using the SSFBG decoder (dashed line) and the DC-FBG decoder (solid line).

On the receiving side, the conventional SSFBG decoder and the DC-FBG decoder are used to compare the OC recognition performance. Fig. 2.20 shows the resultant waveforms generated by these two decoders. The signal from the SSFBG decoder presents a relatively low intensity and spreads over a long time duration (dashed line). On the contrary, the signal from the synthesized DC-FBG decoder (solid line) shows a good autocorrelation spike with low sidelobes.

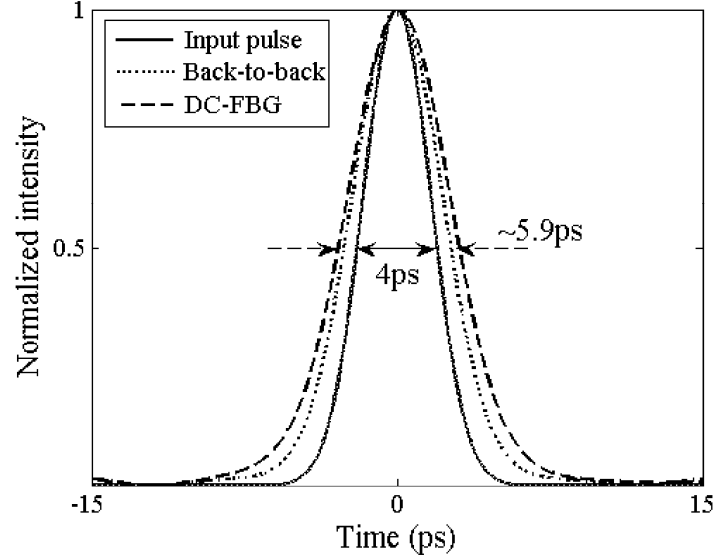


Figure 2.21 Shape of the input pulse (solid line, FWHM 4 ps), the autocorrelation pulse back-to-back decoded by the SSFBG decoder (dotted line, FWHM 5.3 ps), and the autocorrelation pulse decoded by the DC-FBG decoder after 10 km dispersive transmission (dashed line, FWHM 5.9 ps).

We also compare the pulse width of the initial transform limited input pulse and decoded signals, as illustrated in Fig. 2.21. The FWHM pulse width of the input pulse is 4 ps and the autocorrelation pulse directly decoded by the SSFBG decoder without transmission has the pulse width of 5.3 ps, while the autocorrelation pulse decoded from dispersed encoded waveform by the DC-FBG decoder has the pulse width of 5.9 ps.

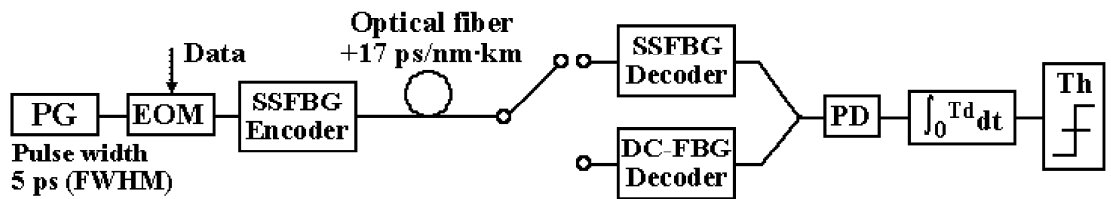


Figure 2.22 Single-user OOK-OCDMA model. PG: Optical pulse generator. EOM: Electro-optic modulator. PD: Photodetector. Th: Threshold.

To analyze the performance of the DC-FBG decoder in the system, we study the single-user OOK-OCDMA system. The signal detection is at a data-rate level. The system model is shown in Fig. 2.22. The design and synthesis of the gratings are same

as those in the previous section. The dispersive transmission has first-order dispersion of $+17$ ps/nm·km. The effects of higher-order dispersion are neglected. In the analysis, we change the transmission distance and calculate the BER with the same energy per bit for different data rates. The calculated results are shown in Fig. 2.23 (a).

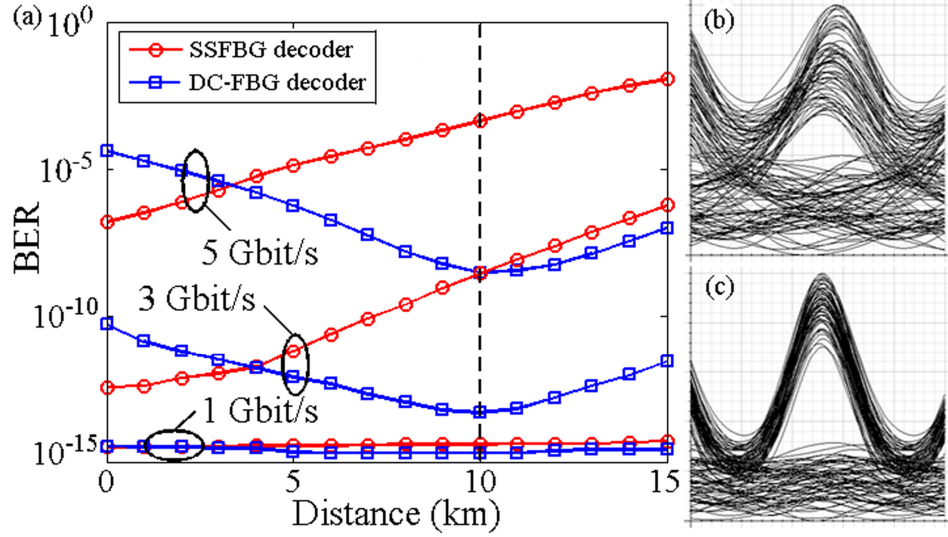


Figure 2.23 (a) BER evaluation for different transmission distances and data rates. Eye diagrams for 5 Gbit/s 10 km transmission using (b) SSFBG decoder and (c) DC-FBG decoder.

Generally, with the increase of the distance, the DC-FBG decoder performs better than the SSFBG decoder does, since the incorrect decoding by the SSFBG decoder diminishes SNR. When the data rate is 3 Gbit/s or 5 Gbit/s, the dispersed signal overlaps each other, causing serious ISI noise, and the superiority of the DC-FBG decoder over the SSFBG decoder is obvious. The BER performance for the DC-FBG decoder keeps at a relatively low level and the optimum results appear at the distance of 10 km. Two eye diagrams for 5 Gbit/s 10 km transmission using both the SSFBG and the DC-FBG decoders are illustrated in Fig. 2.23(b) and (c). The eye diagram for the SSFBG decoder is blurry and interference from adjacent bits can be observed, while the eye is clearly open in Fig. 2.23(c), which verifies that the DC-FBG decoder improves the system performance significantly. As for multi-user system without dispersion compensation process, it is predictable that the performance of the SSFBG decoder will be even worse,

because the target decoded signal can not be distinguished from MAI noises introduced by other users. However, the transmission system supporting multiple users can be realized if the DC-FBG decoder is used, due to its good dispersion compensation and code recognition performances.

2.3.3 Tolerance to phase shift error

The DC-FBG decoder is superstructured and it can be fabricated in the same way as the conventional SSFBG decoder. However, it is hard to ensure that the fabricated phase shift between two subgratings is exactly same as that in the theoretical design. To evaluate the degradation of decoding performance, we introduce the phase shift error deliberately and randomly and investigate the decoding performance by calculating the ratio of autocorrelation intensity peak over the maximum wing level (P/W) and the ratio of autocorrelation intensity peak to the cross-correlation level (P/C).

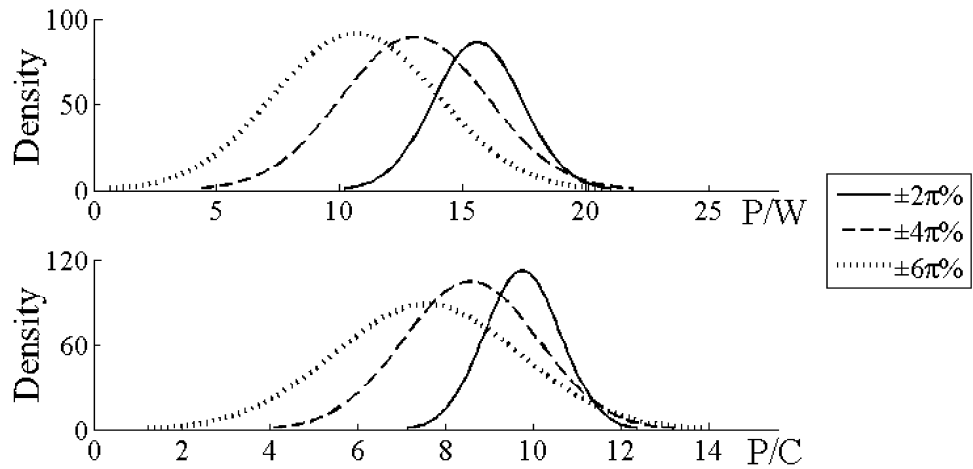


Figure 2.24 The superimposed normal density of P/W and P/C with phase-shift error.

Statistically, we calculate the superimposed normal density of P/W and P/C for 1000 cases when the phase-shift error is within the range from $\pm 2\pi\%$ to $\pm 6\pi\%$, as shown in Fig. 2.24. With the increase of the phase-shift error, the decoding performance degrades. Most cases are within the acceptable range. When the phase-shift error is $\pm 6\pi\%$, for more than 80% of the cases, P/W and P/C are larger than 8 and 6, respectively.

2.4 Summary

In this chapter, the improvement in security and the development in functionality of FBG based coding devices are presented.

As a coding device, a SSFBG encoder should provide security for encoded signals. However, the existence of dips in the encoded waveforms of conventional $0/\pi$ -SSFBG encoders makes it easy for an eavesdropper to extract code sequences from the encoded signals. Thus, $\pm\pi/2$ -SSFBG en/decoders are proposed to generate uniform encoded waveforms, which significantly improve the security. The influence of the input pulse over the encoded waveform of the $\pm\pi/2$ -SSFBG encoder is analyzed and the code extraction technique is discussed when the input pulse has large pulse width. Using short input pulses is a key point to guarantee the security.

In the aspect of the coding performance, the correlation performances of both en/decoders with 31-chip, 63-chip and 127-chip Gold codes are theoretically calculated. The $\pm\pi/2$ -SSFBG en/decoder exhibits as good performance as the $0/\pi$ -SSFBG en/decoder does. Importantly, the hybrid use of both en/decoders is proposed based on their good correlation performances. Furthermore, the coding performances of four fabricated 31-chip 640 Gchip/s $0/\pi$ -SSFBG and $\pm\pi/2$ -SSFBG en/decoders are demonstrated. The good correlation performance of the hybrid use ensures the reutilization of the available codes in the same code space.

In addition, proof of principle experiments are carried out to investigate the performances of the $0/\pi$ -SSFBG and $\pm\pi/2$ -SSFBG en/decoders in the multi-user OOK- and DPSK-OCDMA systems. The achieved error-free transmissions in different systems confirm the acceptable performances of the $\pm\pi/2$ -SSFBG en/decoder and the hybrid use of the both en/decoders.

To combine the functions of OC recognition and chromatic dispersion compensation, a DC-FBG decoder is proposed. The DC-FBG decoder with -170 ps/nm dispersion is synthesized from a derived target reflection spectrum by the DLP method. The synthesized DC-FBG decoder can correctly decode the dispersed encoded signal. In the single-user OOK-OCDMA system, DC-FBG presents a better performance,

especially within the range near the optimum distance and at high data rates. Furthermore, the performance of the DC-FBG decoder is tolerable to phase shift errors in the fabrication. This multi-functional FBG based coding device has been realized in the later research work [122], which achieves the chromatic dispersion compensation and coding tasks at the same time. Furthermore, it also reveals that the FBGs can be designed into the high-reflectivity regime employing synthesis method, reducing 9 dB insertion loss of each device.

Chapter 3

Eavesdropping in the OCDMA Systems

Secure transmission is a special feature of OCDMA systems comparing to other optical transmission systems. However, this plausible fact is worth much deeper discussion [123]. For example, OOK-OCDMA systems have no security at all for single-user situations [124]. Even though the data is encoded as noise-like signals, an eavesdropper can use a simple energy detection to break the security without the knowledge of the code. Thus, the security can not be guaranteed before the multiplexing in the OOK-OCDMA systems. DPSK-OCDMA and code-shift keying (CSK) OCDMA systems were proposed for superior privacy of data [125, 126]. DPSK-OCDMA utilizes the phase modulation for the data instead of intensity modulation so that both bit '1' and bit '0' of the data have same energy in the transmission. In the CSK-OCDMA system, bit '1' and bit '0' are encoded by two different codes with same energy. Compared to the OOK-OCDMA system, DPSK- and CSK-OCDMA systems resolve the vulnerability of simple energy detection and enhance the privacy of data.

In this chapter, the security vulnerability of the coherent time-spreading DPSK- and CSK-OCDMA systems is investigated by using two eavesdropping methods to attack the systems.

3.1 Eavesdropping by one-bit delay interference detection

Security vulnerability has been experimentally demonstrated in the spectral phase coding CSK-OCDMA [127]. The security vulnerability is from one-bit delay interference detection using a DPSK demodulator. This kind of attack is based on the constructive and deconstructive interference of adjacent bits with like and unlike spectral phase coding. In this section, we experimentally demonstrate the attack from the one-bit delay interference detection against time-spreading phase coding single-user DPSK- and CSK-OCDMA systems.

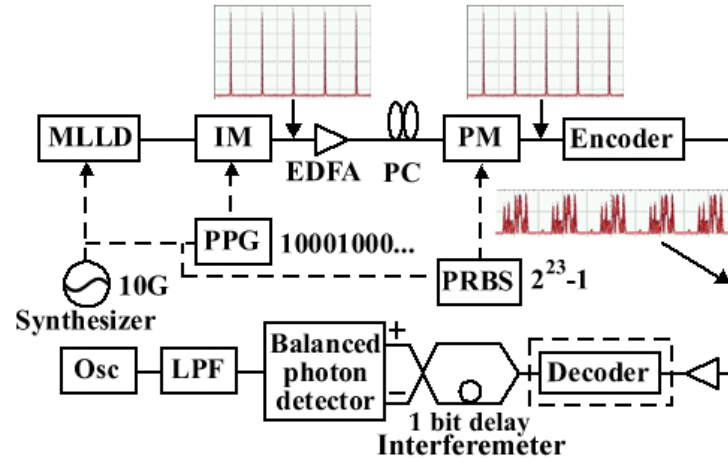


Figure 3.1 Experimental setup of security attack on DPSK-OCDMA system.

Figure 3.1 shows the experimental setup of a typical temporal phase coding DPSK-OCDMA system. A 10 GHz optical pulse train with pulse width of 2.8 ps was generated by an MLLD. An IM was used to convert the data rate to 2.5 GHz. Then, the optical pulse train was modulated by the phase modulator with a $2^{23}-1$ PRBS at data rate of 2.5 Gbit/s. A time-spreading phase encoding device followed the PM. In our experiments, the encoders were two 31-chip 640 Gchip/s SSFBG. To have an in-depth analysis of the coding dependence, both SSFBG encoders were used in this experiment. The modulated and encoded optical pulses had same energy but different phases, shown in Fig. 3.1. In the receiving section, the decoder was removed and the encoded signals were directly detected by a DPSK demodulator, which was a one-bit delay interferometer, followed by a BPD without decoding.

The BER performances and the eye diagrams were measured, as illustrated in Fig. 3.2. The error-free BER performances could be obtained for both encoders. The clear open eyes can be observed, which were measured when $\text{BER}=10^{-9}$. Therefore, it indicates that eavesdropping is possible even if time-spreading phase coding process is adopted in the DPSK-OCDMA systems.

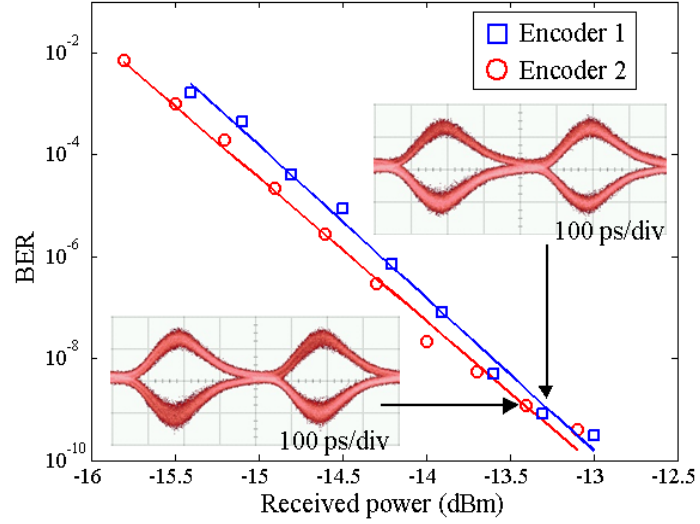


Figure 3.2 BER performances and corresponding eye diagrams for security attack on the DPSK-OCDMA system.

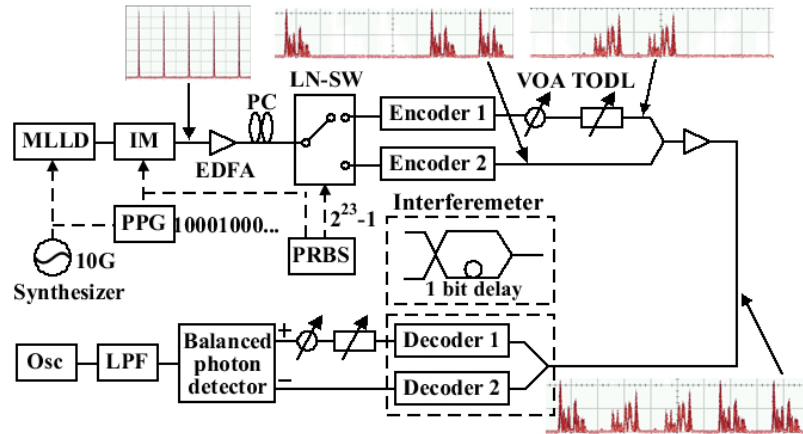


Figure 3.3 Experimental setup of security attack on CSK-OCDMA system.

Then, we investigate the security vulnerability of time-spreading phase coding CSK-OCDMA system using one-bit delay interference detection. The experimental setup is depicted in Fig. 3.3. A 2.5 GHz optical pulse train was generated by an MLLD and an IM. In the encoding section, a lithium niobate optical switch (LN-SW) was driven by a $2^{23}-1$ PRBS at data rate of 2.5 Gbit/s. The optical pulses were separated to upper and lower branches according to bit '0' and '1' in the PRBS. The optical pulses in two branches were encoded by two different SSFBG encoders. After the combination of two branches, the optical pulses of bit '0' and '1' presented as noise-like waveforms with equal energy. In the decoding section of a typical CSK-OCDMA system, the

encoded data stream was divided into two branches and decoded by two corresponding decoders. In our demonstration, the decoding section was replaced by a 2.5 Gbit/s DPSK demodulator. After that, a BPD was used for balanced detection.

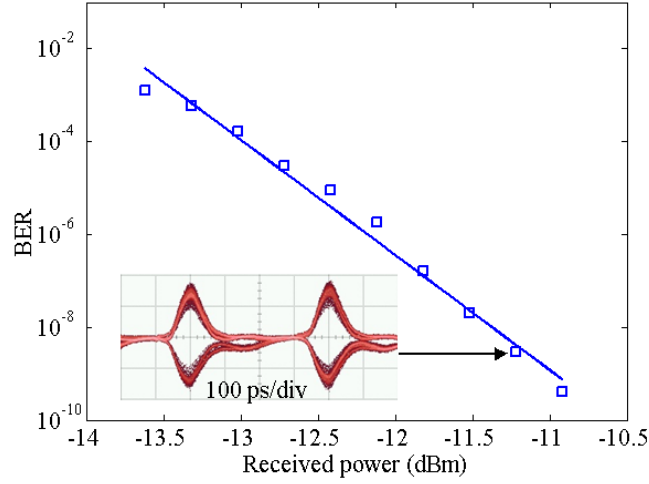


Figure 3.4 BER performances and corresponding eye diagrams for security attack on the CSK-OCDMA system.

The measured BER performance and the corresponding eye diagram were shown in Fig. 3.4. We could get error-free BER performance and open eyes in the measurement. With the help of the one-bit delay interference detection, an eavesdropper can detect the encoded signal directly and obtain the original data without any knowledge of the code. Thus, the security vulnerability occurs in this typical time-spreading phase coding single-user CSK-OCDMA system.

3.2 Eavesdropping by differential detection

In this section, we use another eavesdropping method, differential detection, to attack CSK-OCDMA systems.

The differential detection is to compare two encoded signals and distinguish the difference in their waveforms. The schematic diagram of the differential detection module is shown in Fig. 3.5. A 3 dB coupler divides the encoded signal into two arms. In the one arm, a tunable optical delay line (TODL) is added to generate one-bit delay. In the other arm, a variable optical attenuator (VOA) is used to balance the power.

These two arms are connected to a BPD, where there are two PDs converting the optical signals into electrical signals and a subtracter detecting the difference between the two electrical signals.

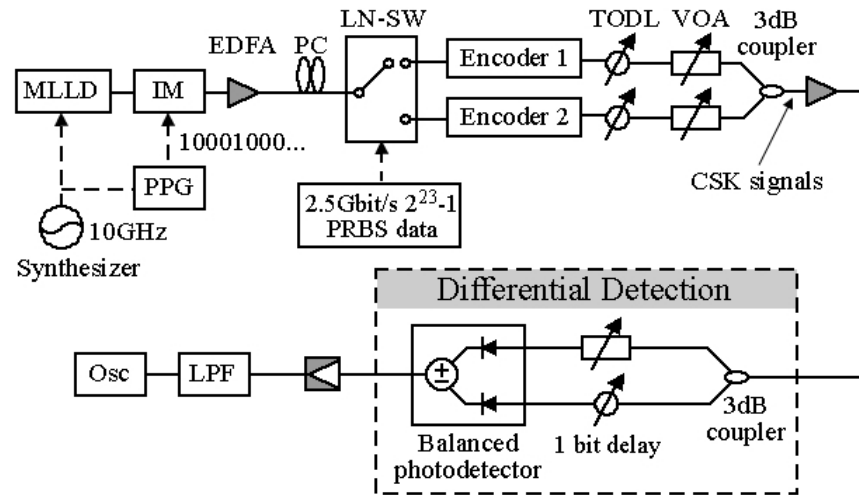


Figure 3.5 Experimental setup of CSK-OCDMA system with differential detection.

Encoded data		After balanced photodetector
Previous bit	Current bit	
'0' → OC1	'0' → OC1	Time
'0' → OC1	'1' → OC2	Time OR Time
'1' → OC2	'0' → OC1	Time OR Time
'1' → OC2	'1' → OC2	Time

Figure 3.6 Lookup table for differential detection.

According to the different combinations of the consecutive bits, the resultant waveforms from the BPD are illustrated in Fig. 3.6. If the symbols of consecutive bits are same, they are encoded by the same code, resulting in the cancellation between each other in the differential detection and no output; while if the symbols of consecutive bits

are different, it leads to either positive or negative output. Using Fig. 3.6 as a lookup table, the symbol of each data bit can then be derived one by one from the output of the differential detection: a null output indicates that the current data bit is same as the previous one, and non-zero outputs hint the difference between current and previous data bits. Furthermore, by adjusting the TODL to generate multi-bit delay, it is possible to compare any two encoded bits at any two different time slots, which is very flexible.

The experimental setup of the CSK-OCDMA system with the differential detection is shown in Fig. 3.5. A 10 GHz optical pulse train with pulse width of 2 ps was generated by an MLLD. An intensity modulator, driven by a pulse pattern generator (PPG) with the data pattern of 10001000..., was used to convert the data rate to 2.5 Gbit/s. Then, the optical pulses were separated into two branches by means of a LN-SW, according to the data bit '0' and '1' of the $2^{23}-1$ PRBS data. The optical pulses in the two branches were encoded with two different 31-chip Gold codes by two 640 Gchip/s SSFBG encoders, respectively. The TODLs and VOAs were used to align the pulses and balance the power in both branches. Then the signals from two branches were combined using a 3 dB coupler generating the CSK signal, where the signals for both bits '0's and '1's presented as noise-like waveforms with equal power.

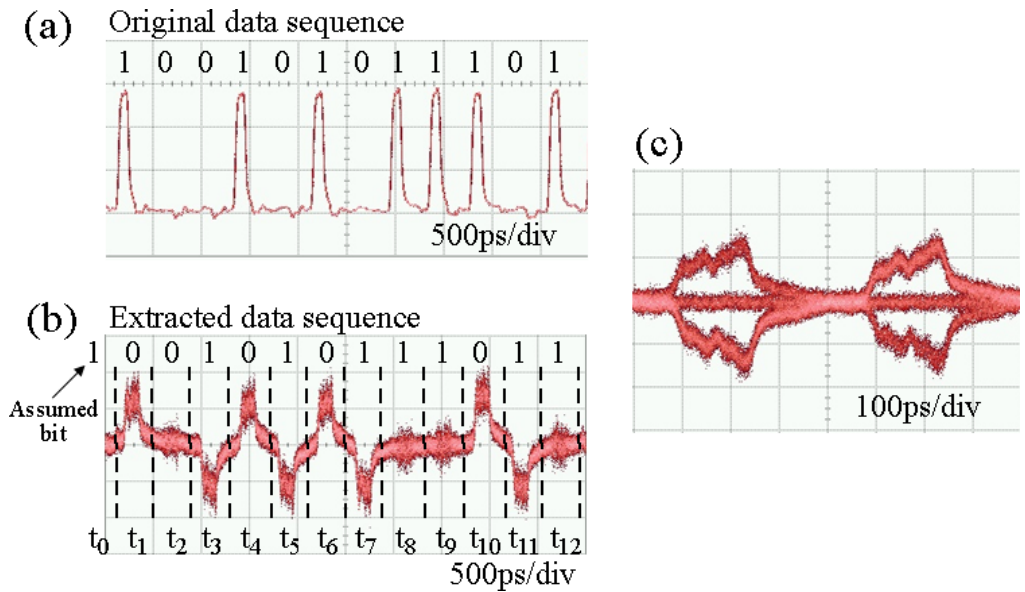


Figure 3.7 (a) Measured original electrical data sequence and (b) extracted data sequence using differential detection. (c) Eye diagram after differential detection.

In the receiving side, the differential detection was implemented directly without the decoding process. In our experiment, the response rate of the BPD was 45 GHz. Fig. 3.7 shows the original data sequence, the detected waveform from the differential detection and the measured eye diagram. We can attempt to extract the data sequence from the detected waveform in Fig. 3.7(b). Firstly, we assume the first bit at t_0 is '1' (assuming it is '0' will result in a complementary data sequence). Then, we can derive the second bit based on the lookup table in Fig. 3.6. Non-zero output at t_1 exposes the second bit is different from the first one, so the second bit is '0'. The third bit is '0' as well due to the null output at t_2 . The negative output at t_3 hints the fourth bit is '1'. The following data sequence can be similarly derived one by one. Finally, the whole data sequence can be extracted from the detected waveform by means of the differential detection. The extracted data sequence is exactly same as the original data sequence, as shown in Fig. 3.7(a). Fig. 3.7(c) shows the measured eye diagram after the differential detection. In the eye diagram, three levels, null and non-zero (positive and negative) outputs, can be clearly distinguished, which accords with the analysis and verifies the feasibility of the eavesdropping scheme.

3.3 Summary

In this chapter, two eavesdropping methods are proposed investigate the security of the coherent time-spreading single-user OCDMA systems. The one-bit delay interference detection can detect the phase difference between two adjacent data bits and thus can be used to attack time-spreading phase coding single-user DPSK- and CSK-OCDMA systems. The differential detection can detect the intensity difference between any two data bits and can be used to attack single-user CSK-OCDMA systems. Due to the flexibility of the bit-to-bit comparison, the differential detection has the potential to be implemented in other complex systems. The research work is to give a suggestion that future secure communication systems should be immune to these two eavesdropping methods.

Chapter 4

Orthogonal Modulation Format based on DPSK and CSK

In the coherent OCDMA system, the coherent optical codes are based on the phase and amplitude of the optical field. Therefore, the optical codes are compatible with the phase modulation, based on which DPSK-OCDMA system was proposed and successfully demonstrated^{*}. DBPSK-OCDMA system with the balanced detection has the advantages of the improved receiver sensitivity and the better tolerance to beat noise and MAI [125]. Furthermore, multi-level modulation format can be adopted to improve the transmission capacity. DQPSK-OCDMA system has been experimentally demonstrated in the synchronous condition [128]. Meanwhile, optical coding provides another domain for the modulation. Binary-CSK-OCDMA system with balanced detection can significantly improve the multi-user capability [126]. The multi-level CSK modulation format, M-ary CSK-OCDMA system, was demonstrated for high capacity and enhanced privacy [129, 130]. Both DPSK and CSK modulation formats are good candidates in the OCDMA systems. However, as demonstrated in Chapter 3, since data can be simply detected from the encoded signals by either one-bit delay interference detection or differential detection, both DBPSK- and binary-CSK-OCDMA systems are lack of security

To increase the transmission capacity and address the security issue, the concept of orthogonal modulation is introduced into the OCDMA systems. In this chapter, some orthogonal modulation format schemes are briefly introduced. A novel orthogonal modulation format based on DPSK and CSK is demonstrated to improve transmission capacity of the optical code based communication system. Importantly, the privacy of data in the OCDMA system using orthogonal DPSK/CSK modulation is enhanced, which is completely immune to one-bit delay interference detection and partially resistant to differential detection.

^{*} Only in this chapter, the term ‘DPSK’ refers to the general concept of differential phase-shift keying and ‘DBPSK’ stands for differential binary-phase-shift keying. Similarly, ‘CSK’ refers to the general concept of code-shift keying instead of binary-code-shift keying.

4.1 Overview of optical orthogonal modulation formats

An optical field has several characteristics such as amplitude, phase, polarization and frequency. Fig. 4.1 illustrates that each characteristic of optical signals is in a distinct dimension and orthogonal to each other. In the conventional optical modulation, the data is expressed by a certain form using one of the characteristics. For example, in the ASK modulation, different data is represented by different amplitudes. Other dimensional characteristics are not utilized, or in other words, they are not efficiently used. An orthogonal modulation scheme can efficiently increase the total capacity by using more than one dimensional characteristic of the optical carrier. The orthogonal modulation schemes are based on the good orthogonality of the modulation formats, which are related to the characteristics of the optical signals. Several orthogonal modulation schemes have been employed in the optical-label-controlled packet switching systems and the transmission systems with high spectral efficiency.

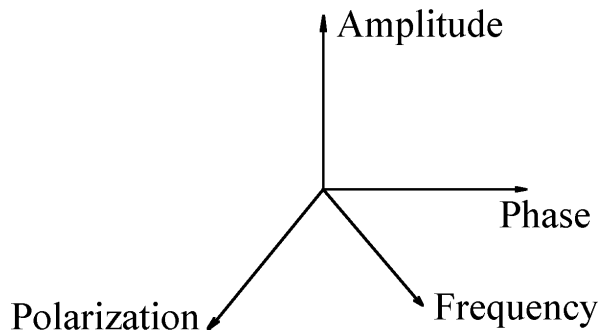


Figure 4.1 4-dimensional orthogonality of the characteristics of optical signals.

In the optical-label-controlled packet switching, all-optical orthogonal labeling allows simultaneous detection and recovery of label and payload and requires less-precise timing control and alignment.

An orthogonally modulated label, which was encoded using either frequency-shift keying (FSK) or DPSK with respect to intensity-modulated (IM) payload, was used in the generalized multiprotocol label switched (GMPLS)-based optical networks [131–133]. The orthogonal label defined the switched path. The schematic diagram of

the transmission links is shown in Fig. 4.2. The payload data were transmitted using intensity modulation, while moderate-speed label data were transmitted on the same optical carrier by phase or frequency modulation. FSK labeling could be obtained by direct current modulation of the laser, whereas an external phase modulator was required in the case of DPSK labeling. Then the payload information and label information could be separately detected using different demodulation techniques at the receiving end.

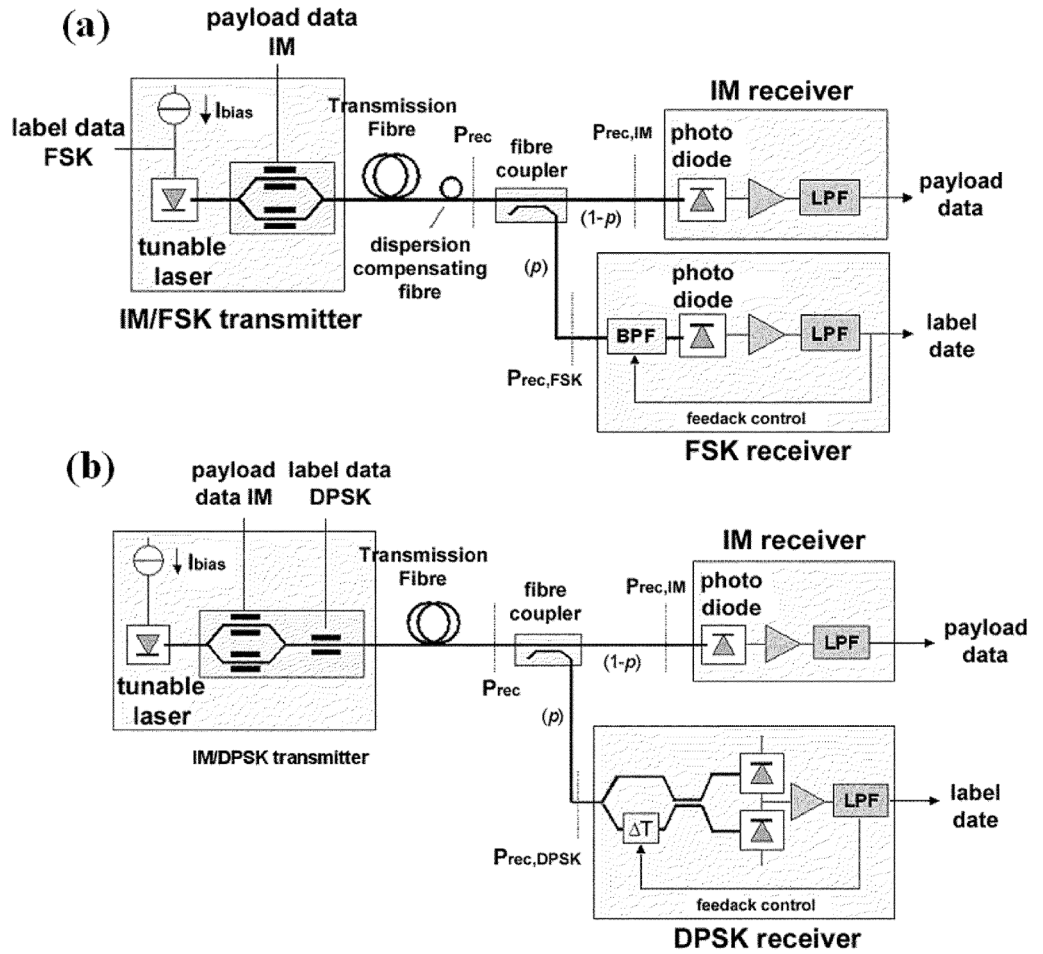


Figure 4.2 Schematic diagram of (a) IM-payload/FSK-label and (b) IM-payload/DPSK-label transmission link.

An orthogonal modulation scheme was applied to an orthogonally labeled packet by using a ASK payload and a polarization-shift keying label [134]. Comparing to the labeling using DPSK/ASK orthogonal modulation, PolSK/ASK labeling eliminates the need for DPSK pre-coding circuitries and complicated decoding and demodulation at

each intermediate node, thus reducing the equipment costs and packet processing latency. Besides, PolSK modulation format does not suffer from excess frequency chirp, as in the DPSK and FSK, which would result in a transmission penalty and spectral broadening at the bit boundaries of the DPSK label impressed onto the ASK payload.

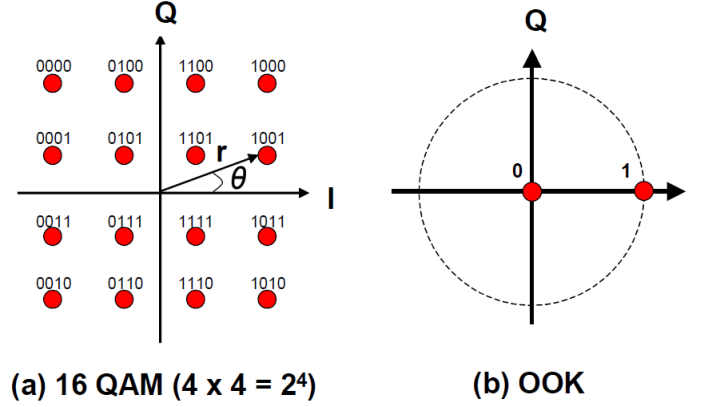


Figure 4.3 Constellation maps for (a) 16 QAM and (b) OOK.

The coherent quadrature amplitude modulation (QAM) using ASK and PSK orthogonal modulation has been employed in the coherent transmission system, which is one of the most effective formats for increasing spectral efficiency. In the generation of QAM, two optical carriers are combined whose amplitudes are modulated independently with the same optical frequency and their phases are shifted by 90 degrees. These carriers are called in-phase carrier (I) and quadrature-phase carrier (Q). The QAM can assign 2^N state by using I - and Q -carriers, which is called 2^N -QAM. Fig. 4.3 shows constellation maps for a 16-QAM and a conventional OOK. 2^N -QAM signal processes N bits in a single channel, so it can realize N times spectral efficiency compared with OOK. A lot of researches challenged high spectral efficiency to approach Shannon limit. 14 Gbaud polarization-division multiplexed (PDM) 16-QAM transmission system was demonstrated, which achieved the spectral efficiency beyond 4 bit/s/Hz [135]. Furthermore, 1 Gbaud frequency-division multiplexed (FDM) 128-QAM coherent transmission system achieved the spectral efficiency as high as 10 bit/s/Hz [136].

4.2 A system with orthogonal DPSK/CSK modulation

4.2.1 Principle of DPSK/CSK orthogonal modulation

The concept of orthogonal modulation has not been applied to the OCDMA systems yet. By combining DPSK with CSK, which is a special modulation format in the optical code based systems, it can not only increase the transmission capacity but also achieve a multi-bit per symbol optical communication. Figure 4.4 illustrates the constellation maps of DPSK modulation, CSK modulation and DPSK/CSK orthogonal modulation.

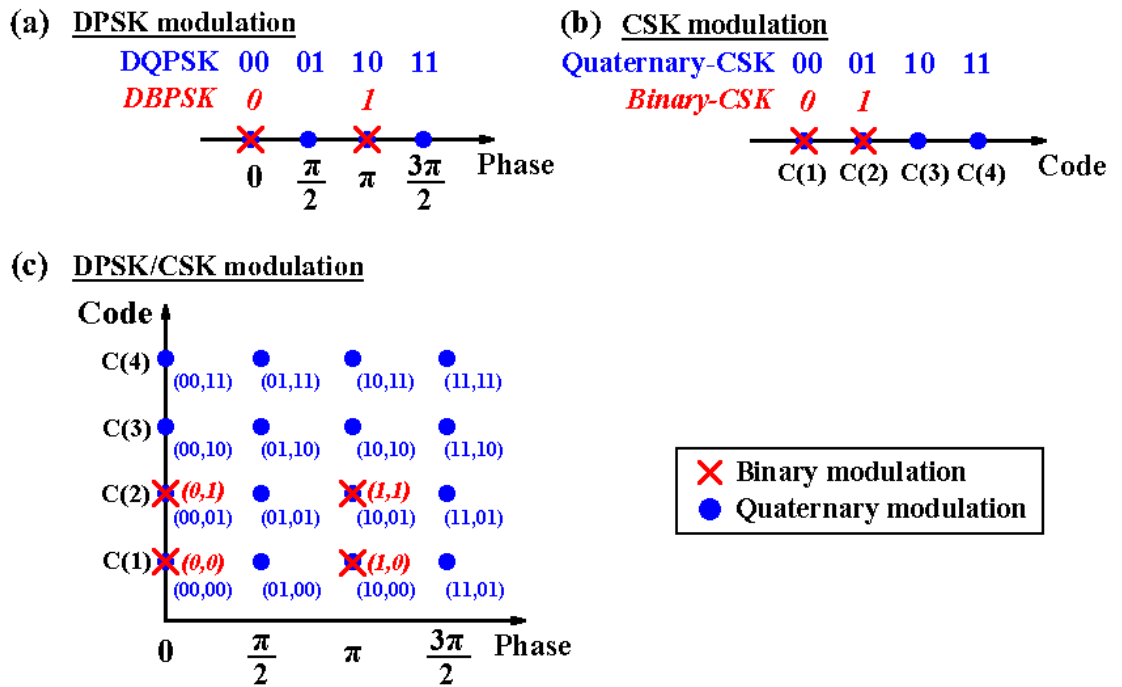


Figure 4.4 Constellation maps for (a) DPSK, (b) CSK, and (c) DPSK/CSK modulation scheme and associated symbols (b_P , $b_{C(n)}$).

In the DPSK modulation, different phases are used to represent different symbols as shown in Fig. 4.4(a). The two crosses on the phase-axis with possible phases of 0 and π , representing the symbols (b_P) ‘0’ and ‘1’, are for the DBPSK modulation, while the four dots (0, $\pi/2$, π and $3\pi/2$) are for the four symbols in the DQPSK modulation.

The CSK modulation processes the data transmission by means of the codes. Fig. 4.4(b) depicts the constellation map of the CSK modulation. The position of the code on the code-axis is not related to the scale of magnitude, but only to the order of the code in

the code set. Two codes ($C(1)$ and $C(2)$), marked with two crosses, are used for the symbols ($b_{C(n)}$) '0' and '1' respectively in the binary-CSK modulation. In the quaternary-CSK modulation, four codes are used (four dots) to represent four different symbols.

Due to the fact that coding is coherent, the coding and the phase modulation can be realized simultaneously in a coherent code based system. Thus, the CSK modulation can provide another dimension of the orthogonal modulation with DPSK modulation. The proposed DPSK/CSK modulation scheme is to realize the coexistence of two orthogonal modulation formats in the same system.

Fig. 4.4(c) shows the constellation map for the proposed DPSK/CSK modulation scheme. Considering the differential binary-phase shift keying (DBPSK)/binary-CSK modulation, two possible phases (0 and π) and two codes ($C(1)$ and $C(2)$) are used to represent the different symbols. Compared to the single DBPSK or binary-CSK modulation, the DBPSK/binary-CSK modulation scheme has one more dimension of the modulation to support the twofold transmission capacity (2-bits/symbol).

Generally, the proposed scheme can be extended to the multi-level modulation formats. The constellation map for orthogonal DQPSK/Quaternary-CSK modulation is also shown in Fig. 4.4(c). In this case, four possible phases and four codes are used, marked with sixteen dots, which results in 4-bits/symbol transmission. If the higher-level DPSK and CSK modulation formats are adopted, the transmission capacity can be significantly improved.

4.2.2 Experimental demonstration of DPSK/CSK orthogonal modulation

Figure 4.5 shows the experimental setup of the proposed orthogonal modulation scheme. The architecture can be divided into several sections. In the pulse generation section, a 10 GHz Gaussian shaped pulse train was generated by an MLLD. A 2000 m DFF and a 7.5 nm band-pass filter centered at 1550.8 nm were used to compress the pulse to 1 ps (FWHM). The pulse train was modulated by a phase modulator driven by the 10 Gbit/s 2^7-1 PRBS DBPSK data. Then, the DPSK modulated pulse train was switched into two branches by an optical switch, which was driven by another 2^7-1

PRBS data at a data rate of 10 Gbit/s. The optical switch had an extinction ratio of 30 dB, which could suppress the untargeted signals well. The pulses switched into the upper and lower branches represented bits '0' and '1' of the binary-CSK data respectively. In the experiment, the encoders and decoders were two pairs of 63-chip 640 Gchip/s SSFBGs. The signals carrying DBPSK data and the binary-CSK data were simultaneously encoded in this stage. The encoded signals presented as noise-like waveforms and were combined into one path after the precise adjustment of delay and the balance of power.

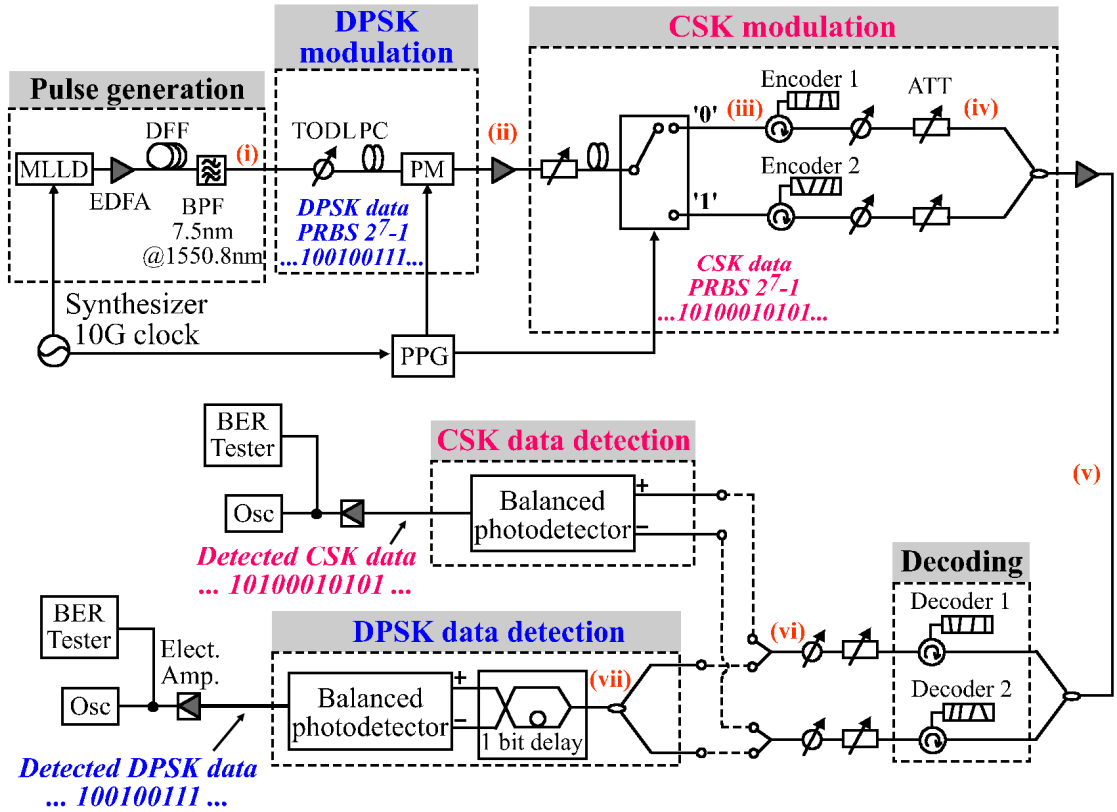


Figure 4.5 Experimental setup of the DBPSK/binary-CSK system.

In the decoding section, the multiplexed encoded signals were split into two branches. The SSFBG decoders for bits '0' and '1' were placed on each branch and recovered the corresponding encoded signals into autocorrelation high peaks. The autocorrelation signal had the pulse width of about 3 ps and would be detected by binary-CSK and DBPSK detection modules respectively, while the incorrectly decoded

cross-correlation signals become the interference to the target signals. Due to polarization independence of the coding devices, the signals in the two decoding branches had the same polarization and polarization controls were not necessary before DBPSK demodulation. The encoding and decoding blocks were placed in the temperature-stabilized environment to improve the phase-stabilization of the DBPSK transmission. Considering the further improvement of long-term phase-stabilization, either integrated components or active stabilization techniques could be used in the future work. The waveforms for the binary-CSK modulation with the data pattern after switching, encoding, multiplexing and decoding are depicted in Fig. 4.6.

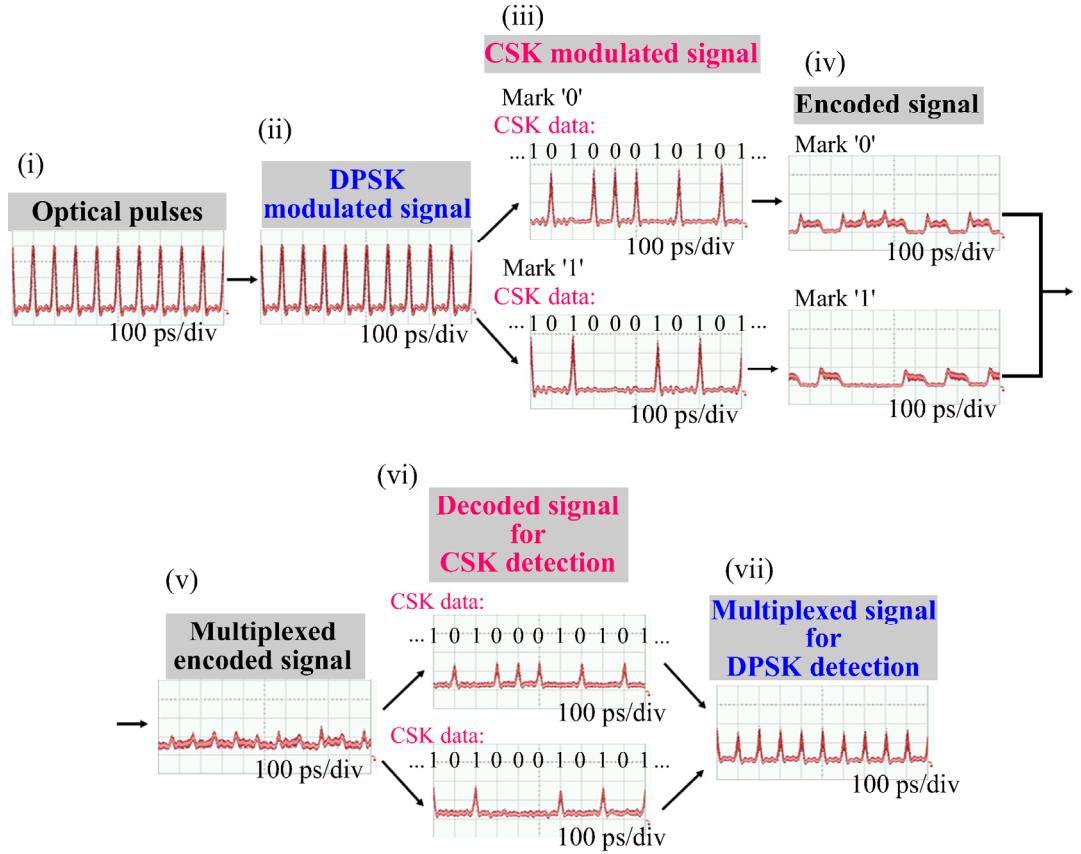


Figure 4.6 Waveforms measured at different positions of the system.

In the receiving side, the encoded signals were divided into two branches for decoding before detection. Then, in the detection section, two different modules were used to detect the DBPSK data and the binary-CSK data, respectively. In the DBPSK

data detection module, the decoded signals were firstly combined into one path and then detected by a DPSK demodulator, which was a one-bit delay interferometer, and a BPD. As for the binary-CSK data detection module, it only contained a BPD. The binary-CSK data could be directly detected from the decoded signals by the BPD.

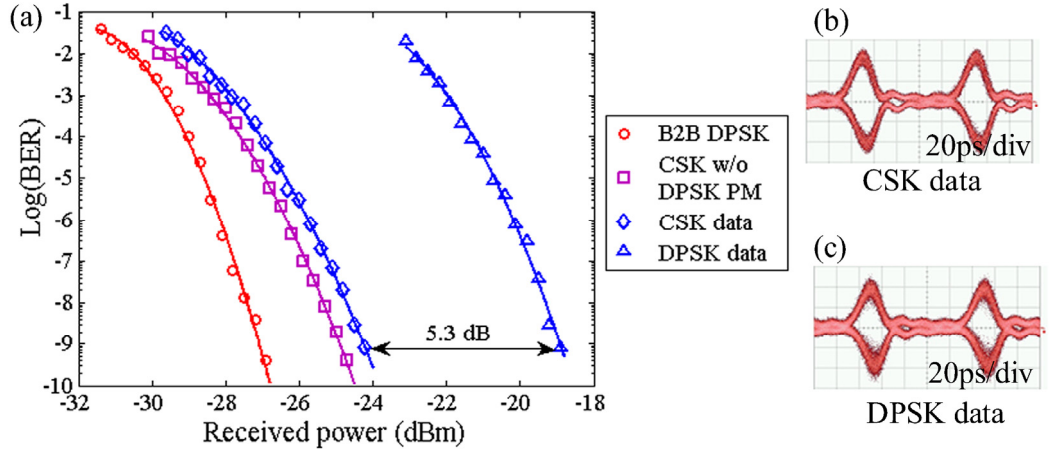


Figure 4.7 (a) Measured BER performance and eye diagrams for both (b) binary-CSK data and (c) DBPSK data transmission.

To verify the feasibility of the proposed system and investigate the orthogonality between the binary-CSK modulation and DBPSK modulation, we measured the eye diagram and the BER performance for both binary-CSK and DBPSK data. In Fig. 4.7(a), the DBPSK back-to-back transmission and the binary-CSK transmission without DBPSK modulation are used as the references. The diamond and triangular marked curves are for the binary-CSK data and DBPSK data, respectively. Compared to the binary-CSK transmission without DBPSK modulation, the power penalty at the BER of 10^{-9} for the binary-CSK data transmission in the proposed system is less than 1 dB, which indicates that the existence of the DBPSK modulation has the subtle influence on the binary-CSK data transmission. The DBPSK data transmission suffers more power penalty, about 5.3 dB to the binary-CSK data transmission, which are resulted from the beat noise due to the cross-correlation signals. Fig 4.7(b) and (c) show the eye diagrams for both binary-CSK and DBPSK data transmission. The clear open eyes can be observed for the binary-CSK data transmission, while the eyes for the DBPSK data transmission have some degradation.

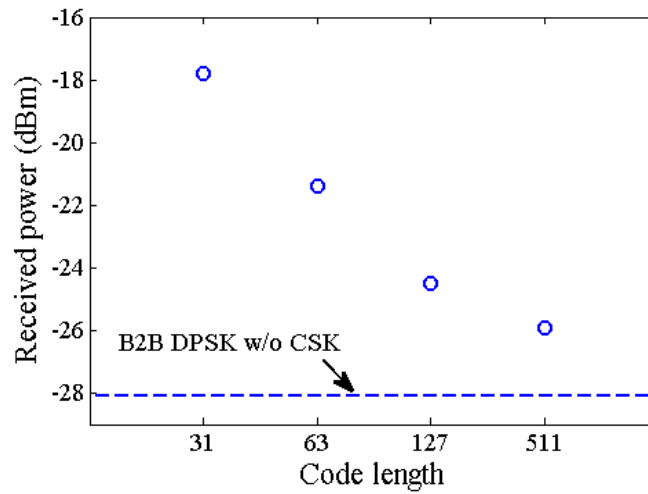


Figure 4.8 Simulated received power of DBPSK data transmission with different code lengths at BER of 10^{-9} .

The cross-correlation signals from another decoder introduce the noise to the DBPSK data transmission. Therefore, in this orthogonal modulation system, the coding with low cross-correlation is necessary to eliminate the noise and optimize the system. When longer codes are used, both correlation performance and privacy of data can be improved. Fig. 4.8 illustrates the simulated result of the received power for DBPSK data transmission with different code lengths at the BER of 10^{-9} . The decrease of the received power indicates that less power penalty can be achieved if longer codes are used. In addition, if codes are well designed to minimize cross-correlation, the DBPSK data will suffer lower power penalty.

4.2.3 Investigation on the security of the system

It has been demonstrated that both DBPSK and binary-CSK OCDMA systems have security vulnerability. Using one-bit delay interference detection can directly obtain the data from the encoded signals in the DBPSK and binary-CSK OCDMA systems without knowing codes, while differential detection can easily attack the binary-CSK OCDMA system according to the difference of the encoded signals. The security of the system using DBPSK/binary-CSK orthogonal modulation is also investigated.

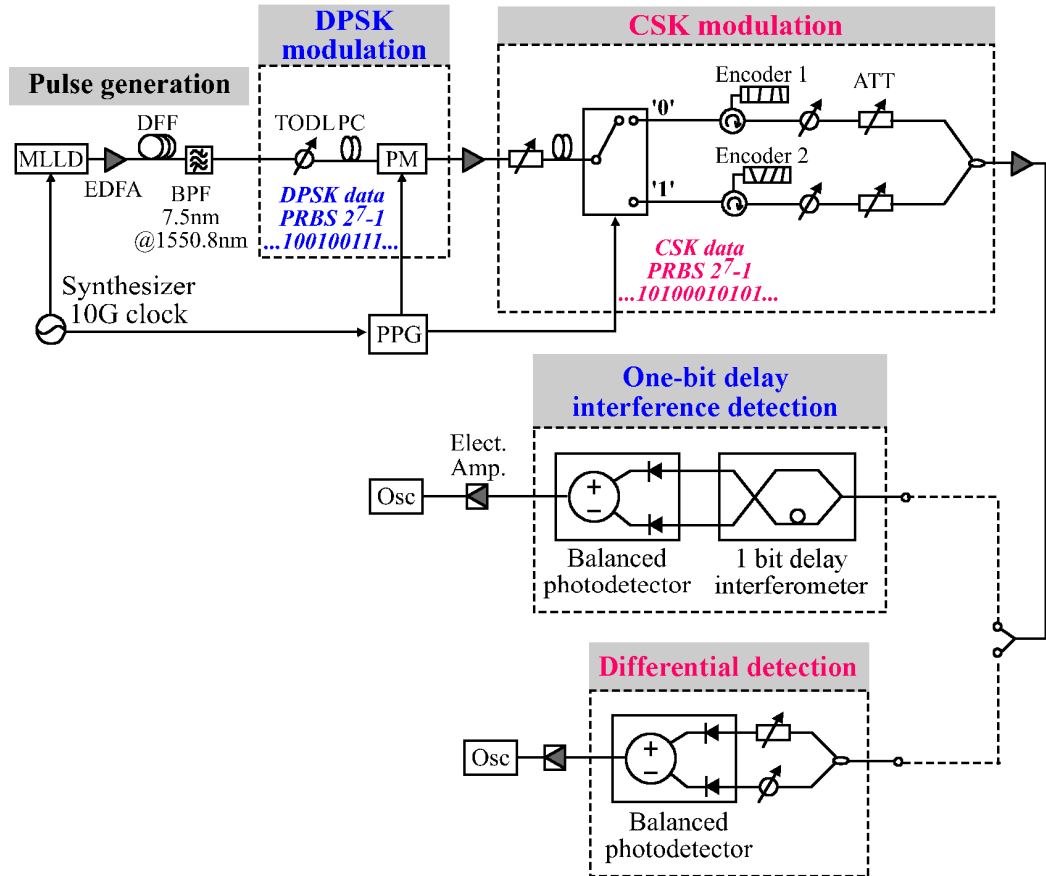


Figure 4.9 Security investigation of the system using orthogonal DBPSK/binary-CSK modulation.

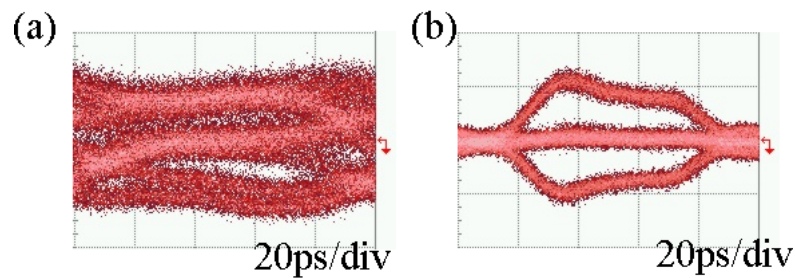


Figure 4.10 Eye diagram for (a) one-bit delay interference detection and (b) differential detection.

In the experimental investigation, two decoders were removed and one-bit delay interference detection and differential detection modules were connected to CSK modulation section directly to detect the encoded signals, as shown in Fig. 4.9. The detected eye diagrams are illustrated in Fig. 4.10. When one-bit delay interference

detection is used, no clear open eyes can be observed, because the phase of each encoded bit is not purely the phase modulated by DPSK data or the phase induced by CSK codes. Thus, the system using orthogonal DPSK/CSK modulation has immunity to the one-bit delay interference detection.

Differential detection can be used to detect the difference of waveforms between two bits. In the DPSK/CSK system, even though the phase of each data bit is mixed by DPSK data and CSK codes, the waveform of each bit is only determined by the codes representing different CSK data. Hence, differential detection is still workable to figure out the CSK data in the DBPSK/binary-CSK systems. The eye diagram in Fig. 4.10 is obtained by using differential detection. Three levels can be clearly distinguished. By using the lookup table and the principle in Chapter 3, the CSK data can be derived from the detected signals.

Table 4.1 Summary of the security investigation on DPSK-OCDMA, CSK-OCDMA and DPSK/CSK-OCDMA systems.

		One-bit delay interference detection	Differential detection
DPSK-OCDMA system		Insecure	Secure
CSK-OCDMA system		Insecure	Insecure
System using orthogonal DPSK/CSK modulation	DPSK data	Secure	Secure
	CSK data	Secure	Insecure

Table 4.1 summarizes the results of security investigation on DPSK-OCDMA system, CSK-OCDMA system and the system using orthogonal DPSK/CSK modulation. DPSK-OCDMA and CSK-OCDMA systems are not secure, where data can be detected from the encoded signals by an eavesdropper. Although the system using orthogonal DPSK/CSK modulation can not guarantee the privacy of the CSK data, it is able to keep

the privacy of the DPSK data. There is no doubt that comparing to using only one dimensional DPSK or CSK modulation in the optical code based system, using orthogonal DPSK/CSK modulation can enhance the security.

4.3 Summary

In this chapter, a novel orthogonal modulation format based on DPSK and CSK modulations is proposed and a coherent OCDMA system using DBPSK/binary-CSK orthogonal modulation format is experimentally demonstrated, which achieves 2-bit/symbol 10 Gsymbol/s transmission. The proposed modulation format can increase the transmission capacity in the optical code based communication system. It also implies a further enhancement with the replacement of the DBPSK and binary-CSK by using multi-level modulation formats in the phase and code domains. Furthermore, the privacy of the system using orthogonal DPSK/CSK modulation is enhanced, comparing to those of the one-dimensional DPSK-OCDMA and CSK-OCDMA systems. This research could set an important precedent for applying orthogonal modulation schemes into the optical code based systems.

Chapter 5

Fully-Asynchronous Gigabit-Symmetric OCDMA-PON

In the PON, downstreams are broadcast to all end users, so it is necessary to encrypt the transmitted signals to guarantee information privacy and prevent eavesdropping. OCDMA systems can provide an attractive feature on security enhancement to address this information privacy issue. Besides, OCDMA systems have the advantage of asynchronous transmission and are suggested to be applied for new-generation PONs, where secure gigabit-symmetric transmissions are required to meet the needs of future bidirectional high data-rate applications such as telediagnosis services and video conference services

Many researches have proposed and demonstrated OCDMA systems in the PONs. El-Sahn et al. demonstrated an architecture consisting of a standalone uplink burst-mode receiver in a 622 Mbit/s/user 7-user incoherent spectral amplitude coded (SAC) OCDMA-PON with local sources or centralized sources [137]. A fully-asynchronous 10 Gigabit Ethernet (GbE) interface OCDMA prototype architecture was demonstrated in a field trial of duplex 10 Gbit/s/user 8-user DPSK-OCDMA system over 100 km by using hybrid multi-port AWG and SSFBG encoders/decoders [138]. In addition, an OCDMA-PON with optical network units (ONUs) inter-networking was demonstrated using gain-switched Fabry-Pérot (FP) lasers with external dual-wavelength injection [139]. In [140], an incoherent OCDMA-PON was proposed. All wavelength channels including downstream and upstream channels were generated in the central office. Only half wavelength channels were used for incoherent OCDMA downstream and the other half un-modulated and non-coded wavelength channels were sent to ONUs for encoding and modulation with uplink data for upstream transmission. A 10 Gbit/s fully-duplex coherent OCDMA-PON was demonstrated to realize source-free ONUs by sending a seed pulse train, which was at the same wavelength as the downlink signals, from the optical line termination (OLT) to ONUs for the use of upstream transmission [141]

In this chapter, a fully-asynchronous gigabit-symmetric DPSK-downstream and remodulated OOK-upstream OCDMA-PON, in which ONUs are source-free, is experimentally demonstrated. The power budget of the OCDMA-PON is analyzed. In addition, an all-optical self-clocked time gate employed for signal regeneration is introduced and its performance is evaluated.

5.1 Overview of remodulation schemes

In the PON, an ONU processes the conversion between optical signals and electrical signals at a user's premise. The complexity of ONUs should be mitigated to reduce the cost of end users. The technique of remodulation is a good way to simplify the structure of ONUs. Several remodulation schemes have been proposed in the different PONs.

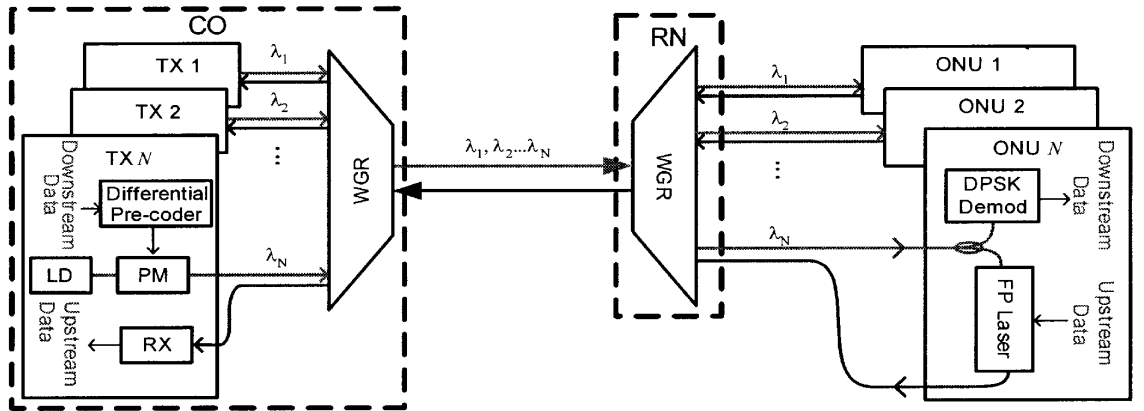


Figure 5.1 Network structure of a WDM-PON using FP laser based transmitter for remodulation [142].

An OOK upstream transmitter, which consisted of a Fabry–Pérot (FP) laser diode, was proposed for remodulation in a WDM-PON [142, 143], as shown in Fig. 5.1. An FP laser diode located at an ONU was injection locked by a portion of the received optical power of either NRZ-OOK or DPSK downstream signal and directly modulated to produce the upstream signal. Injection locking enhanced the sidemode suppression ratio of the FP laser, enabling long-reach upstream transmission. Compared with using NRZ downstream, using DPSK downstream could not only reduce costs by employing

LiNbO₃ PM instead of Mach-Zehnder IM but also mitigate various nonlinear phenomena due to constant-intensity nature of the DPSK modulation format. A 10 Gbit/s DPSK downstream and 2.5 Gbit/s OOK upstream over 50 km transmission was achieved in the demonstration.

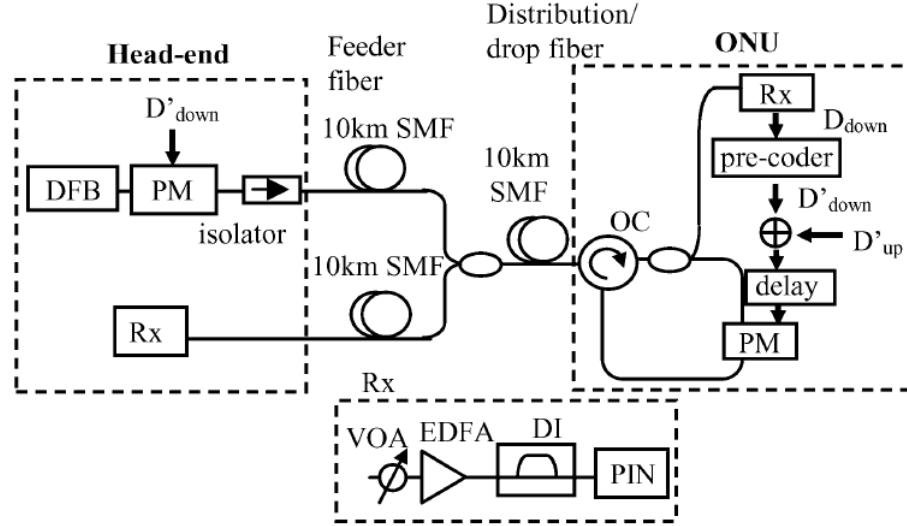


Figure 5.2 Schematic diagram of a DWDM-PON using DPSK in downstream and upstream remodulated signals [144].

A wavelength remodulation scheme using DPSK formats in both downstream and remodulated upstream was demonstrated in a 10 Gbit/s DWDM-PON [144]. The experimental setup of the system is shown in Fig. 5.2. The remodulation was realized by rewriting the phase information onto the downstream signal. The output of the exclusive-OR (XOR) logic operation of differential pre-coded downstream data and upstream data was applied to a PM to modulate the phase of the downstream DPSK signal, producing the upstream signal. It was pointed out that strict synchronization was required because the alignment between the downstream and the applied electrical signals to the PM is crucial. In the experiment, a 10 Gbit/s DPSK downstream and remodulated upstream over 20 km transmission was demonstrated.

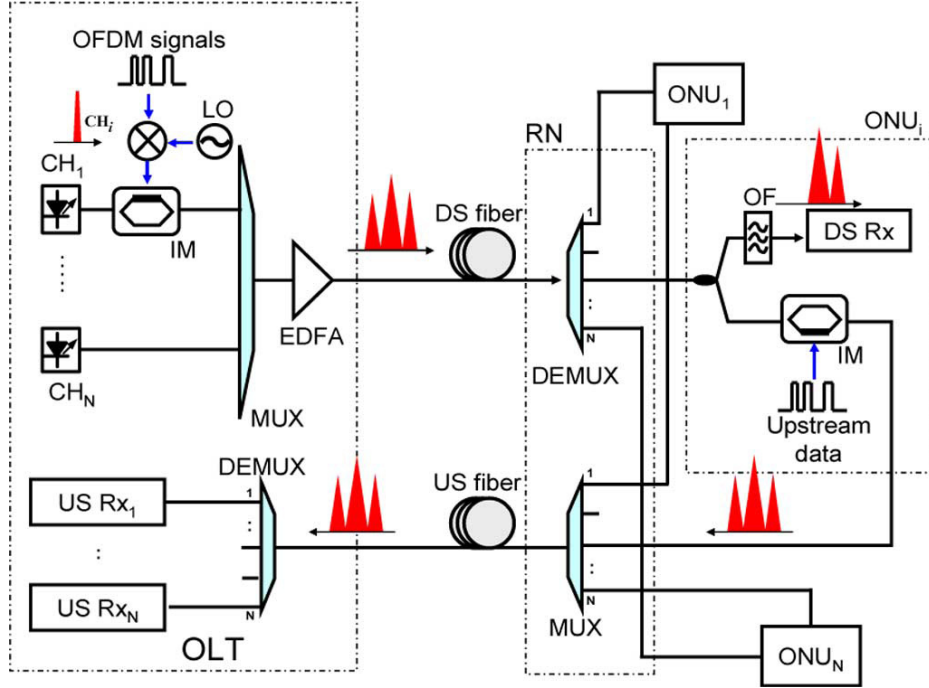


Figure 5.3 Network structure of a WDM-PON employing 16-QAM intensity modulated OFDM downstream and OOK modulated upstream signals [145].

In [145], a centralized lightwave remodulation scheme was used in the WDM-PON, as shown in Fig. 5.3. In this scheme, a 16-QAM intensity-modulated orthogonal frequency-division multiplexing (OFDM) signal was used for downstream transmission. A remodulation scheme based on wavelength-reuse was employed to carry the upstream data to reduce the cost at the ONU. By using one intensity modulator, the downstream OFDM signal was remodulated for upstream OOK data based on its RZ shape waveform. Consequently, the centralized lightwave was realized because there was no additional light source in the ONU. In the demonstration, 10 Gbit/s 16-QAM downstream and a remodulated 2.5 Gbit/s OOK upstream were successfully transmitted over 25 km.

5.2 Overview of nonlinear signal processing in the OCDMA systems

In the OCDMA systems, encoded signals are broadcast to all receivers. In each receiver, an optical decoder is used to recover the encoded signal into an auto-correlation high-intensity signal. Other encoded signals are spread in the time domain, remaining cross-correlation low intensity, which are MAI noises. In the

coherent OCDMA systems, an original signal before encoding as well as a correctly decoded signal is in a format of short pulse (sub-ps). After decoding, recovered short pulses are superposed with low-intensity noises, as shown in Fig. 5.4(a). Then, a photodetector is employed to transform optical intensity into electrical current. However, the bandwidth (B_{PD}) of a practical photodetector is usually at a level of data rate (~ 10 GHz). The rise time response (t_r) is approximately equal to $0.35/B_{PD}$ (several tens ps). Due to the relatively low response of the photodetector, almost same energy is detected from both the correctly decoded signal and the MAI noises in the multi-user situations. Hence, it is hard to distinguish the correctly decoded signal from the detected signals, leading to a serious degradation of the system performance. To obtain a good SNR, it is necessary to remove the MAI noises or regenerate the correctly decoded signal before detection.

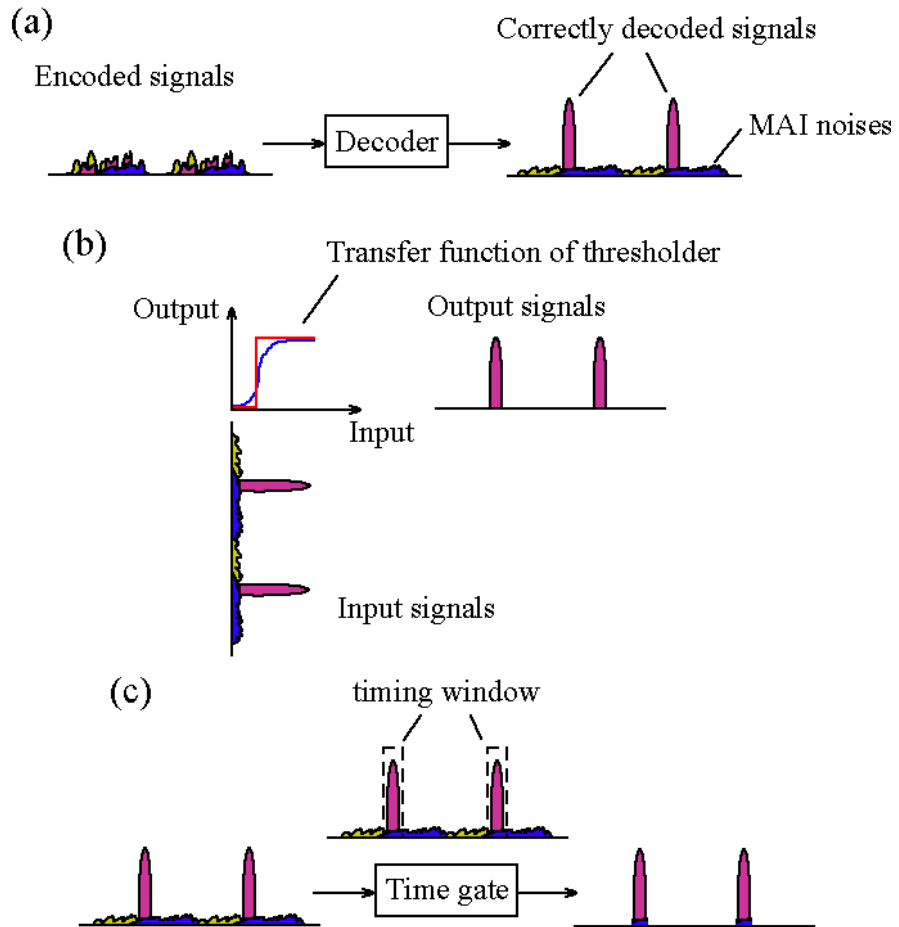


Figure 5.4 (a) Decoding process and the principles of (b) thresholder and (c) time gate.

Various nonlinear signal processing techniques have been proposed to suppress the MAI noises or extract correctly decoded signal from the superposition of decoded signals. Optical thresholding and time gating are two major techniques used in the OCDMA systems to improve signal quality. Fig. 5.4(b) and (c) show the working principle of optical thresholding and time gating.

5.2.1 Optical thresholding

Fig. 5.4(b) shows the working principle of an optical thresholder. When a low-intensity signal is input into an optical thresholder, there is no output. Once the intensity of input signal is above a certain level, the thresholder outputs a signal with large intensity. In practice, an optical thresholder with a transfer function of a sudden, discrete change at the thresholding level (red curve in Fig. 5.4(b)) does not exist. Alternatively, an optical thresholder with a dramatic change at the thresholding level (blue curve in Fig. 5.4(b)) is preferred. According to the working principle of optical thresholding, the high-intensity correctly decoded signal can pass through the optical thresholder but there are no outputs when the low-intensity MAI noises are input into the thresholder. Besides, optical thresholding does not require any synchronization, which is suitable for asynchronous transmission systems, such as OCDMA systems. Due to the essentiality and suitability of optical thresholding, a variety of OCDMA systems have adopted such techniques to improve transmission quality. Some fiber-based optical thresholders are overviewed in this section.

In [146], a nonlinear thresholder was built by a 500 m dispersion shifted fiber (DSF) followed by a longpass filter (a filter that attenuates the signal at short wavelength and passes the signal at long wavelength). Nonlinear propagation effects caused the spectrum of the high-intensity correctly decoded signal to spread to both side of the center wavelength. The low-intensity MAI noises propagated through the same length of the fiber but exhibited negligible spectral shifts. A wavelength pass filter only allows the spectrally broadened signal to pass so that only the correctly decoded signal can pass the thresholder and the MAI noises are attenuated.

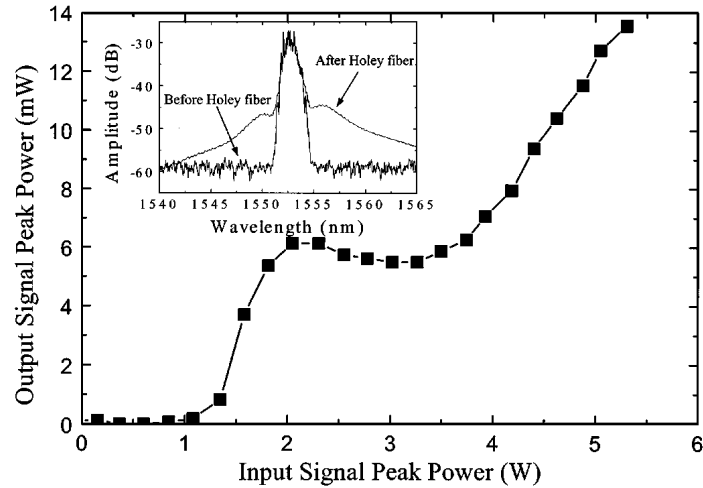


Figure 5.5 Transfer function of the optical thresholder using a HF. Inset: Signal spectrum before and after the HF [147].

A nonlinear thresholder using a holey fiber (HF) was used in [147]. Self-phase modulation (SPM) accompanied by Raman scattering in a 8.7 m highly nonlinear HF due to the high-intensity spike of the correctly decoded signal resulted in spectral broadening as shown in Fig. 5.5. The optical thresholder has a transfer function which allows the high-intensity signal to pass only. This HF based optical thresholder owns an excellent characteristic of steep change at the thresholding level, but the thresholding power is extremely high, which is not energy efficient.

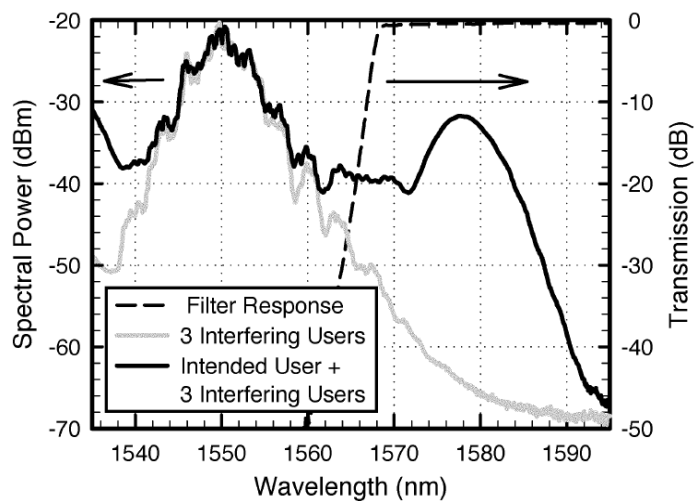


Figure 5.6 Spectral plot demonstrating how the thresholder discriminates between the correctly decoded signal and the interfering users' signals [148].

Another fiber based thresholder was proposed in [148]. In this scheme, a 500 m highly nonlinear fiber (HNLF) and a fiber-based longpass filter was employed in the thresholder which proved strikingly effective in the presence of MAI noises. Fig. 5.6 illustrates the transmission characteristics of the longpass filter overlaid with the spectra generated by the correctly decoded signal plus three interfering users and just the three interferers alone. The high peak power of the correctly decoded signal in the HNLF shifted spectral power into longer and shorter wavelengths due to SPM and other nonlinearities. The longer wavelengths were passed to the photodetector through the longpass filter. The HNLF increases the sensitivity of the thresholding by more than five-fold compared to the DSF-based thresholder in [146].

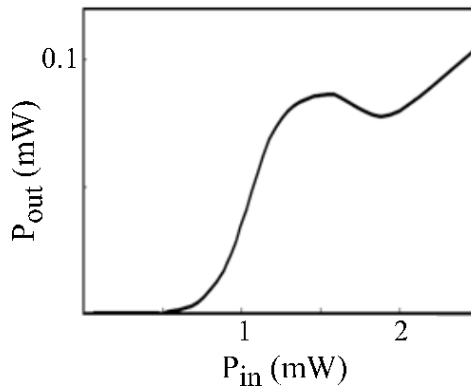


Figure 5.7 Transfer function of SC based optical thresholder [116].

In [116], a supercontinuum (SC) based optical thresholder was demonstrated. The thresholder consisted of an EDFA, a 2 km dispersion-flattened fiber (DFF) and a 5 nm BPF. The EDFA firstly boosted the decoded signals to a proper level. The correctly decoded signal, which had a well defined shape with 2 ps pulse width and high peak power, was able to generate SC in the DFF, while the MAI noises was unable to generate SC. The BPF only allowed the SC signal passing through. Consequently, the correctly decoded signal could be recovered without MAI noises. A steep transfer function was shown in Fig. 5.7. Compared with other techniques, the SC based optical thresholder was characterized by polarization independency, rather low insertion loss, steep transfer function as well as pulse reshaping capability.

5.2.2 Optical time gating

The working principle of an optical time gating is depicted in Fig. 5.4(c). An optical time gating allows signals passing through only during a short time period, i.e. timing window, and rejects signals out of the timing window. Usually, a control signal or sometimes called pump signal, which is a sequence of short pulses with high-intensity, is needed to trigger the time gate to turn on the timing window. A desired signal, which contains information to be extracted, is coincident with the control signal. Once the control signal turns on the timing window, the desired signal can pass the time gate. A precise control is required to align the desired signal exactly within the timing window. In the OCDMA systems, optical time gates have been widely used for extraction of the correctly decoded signal. Two major time gating schemes used in the OCDMA systems, FWM based optical time gate and NOLM based time gate, are overviewed in this section.

FWM based optical time gates employing either semiconductor optical amplifier (SOA) or HNLF were employed in the phase-modulated OCDMA systems [49, 149]. These schemes are very simple to manipulate. Firstly, the decoded signal is temporally adjusted to ensure the autocorrelation pulses overlap with the pulses in the control signal. Secondly, when control and decoded signals, which are at two different wavelengths, are injected into a nonlinear element (NLE), either SOA or HNLF, a signal at a new wavelength, an idler signal, is generated by FWM. Thirdly, an optical bandpass filter is then used to filter out the new generated signals. The advantage of this scheme is that phase information can be preserved during the FWM process.

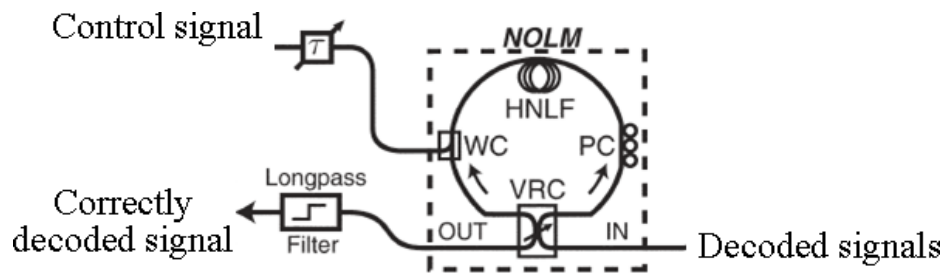


Figure 5.8 NOLM based time gating scheme [150].

Fig. 5.8 shows the nonlinear optical loop mirror (NOLM) based time gating scheme, which was used in the 8-user spectral phase-encoded time-spreading OCDMA system [150]. The NOLM consisted of a variable ratio coupler (VRC), a wavelength coupler (WC) and a span of 500 m HNLF. A control pulse train was at a wavelength other than the decoded signals and the control pulses had pulse width of 3 ps corresponding to the timing window. The decoded signal entered the VRC and was split into clockwise and counter-clockwise propagating signals. Without the presence of the control pulse, both clockwise and counter-clockwise propagating signals travelled around the loop experiencing the same phase shift and recombined at the VRC. Since the net phase shift was zero, the entire signal would exit the input port of the VRC, thus acting as a mirror. To operate as a time gate, a control pulse was coupled into the loop through a WC and temporally aligned with the clockwise correctly decoded signal. As the control pulse co-propagated with the clockwise signal in the HNLF, it imparted a phase shift to the signal via XPM. If the net phase shift was π , that portion of the signal exited from the output port of the VRC. Then, the control pulse could be separated from the correctly decoded signal by a longpass filter at the output port of the NOLM.

5.3 All-optical self-clocked time gate

Optical time gates, widely used for wavelength conversion, optical signal regeneration, and demultiplexing, are essential devices in the optical communication networks [151]. Besides, time gates are also widely used in the optical code based technologies for signal extraction and MAI noise suppression [21, 49, 149, 150]. However, in a time gate, a synchronous clock signal is needed to extract a target signal from a data stream, which increases the complexity of systems and obliges systems to abandon the advantage of asynchronous transmission. To avoid using an additional clock signal, self-clocked time gates have been proposed, where a clock signal can be obtained and used to extract a target signal from an original data stream [152, 153].

An all-optical self-clocked time gate is proposed, which can provide an advantage of asynchronous up/downstream transmission in the OCDMA-PON, for signal extraction and MAI suppression.

5.3.1 Operation principle

The proposed self-clocked time gate consists of two stages, as shown in Fig. 5.9. The first stage is to obtain a clock signal from an original signal, which consists of data and MAIs, and the second stage is to extract the data from the original signal.

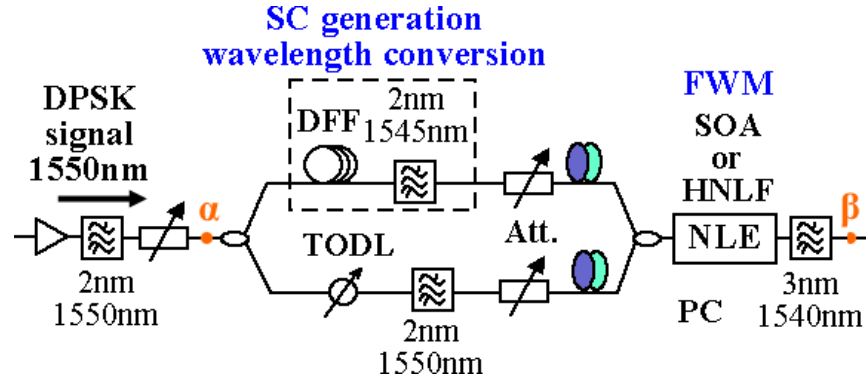


Figure 5.9 Setup of the self-clocked time gate.

In the first stage, an input signal is separated into two branches. In the upper branch, a SC based threshold, which consists of a DFF and a BPF, is used to generate a clock signal. In the DFF, only high-intensity pulses can generate SC, while low-intensity noises can not generate SC. The following filter centered at another wavelength only allows the generated SC pass through. As a result, a train of high-intensity pulses with the same repetition rate of the data, i.e. a clock signal, is obtained. The SC based threshold is widely used for MAI suppression in the OOK-OCDMA system [116], but it is not suitable for DPSK systems, because the phase information can not be preserved during the SC generation [154]. Thus, this technique is used for the extraction of clock signal instead of the reshaping of DPSK signals. The signal in the lower branch is adjusted by a TODL to ensure that the pulses are temporally overlapped with the pulses of the clock signal after a 3-dB coupler.

In the second stage, the coupled signals are injected into a NLE for FWM, which is a time gating process. In the FWM process, a phase-conjugate replica of the target signal is generated. A following filter is to filter out the generated replica.

The characteristics of the self-clocked time gate are experimentally investigated. In

the experiment, a 10 GHz 1.5 ps (FWHM) Gaussian shaped pulse train is used as an input, whose center wavelength is at 1550 nm. The input operating power (at point α) is 14 mW, which means that the required peak power is 0.86 W. A span of 2 km DFF is used for SC generation and a 2 nm BPF centered at 1545 nm is to filter out the clock signal. In the two branches, two attenuators (ATT) and two polarization controllers (PC) are placed before coupling to optimize the FWM condition. In the second stage, a SOA or a span of 100 m HNLF is used as an NLE.

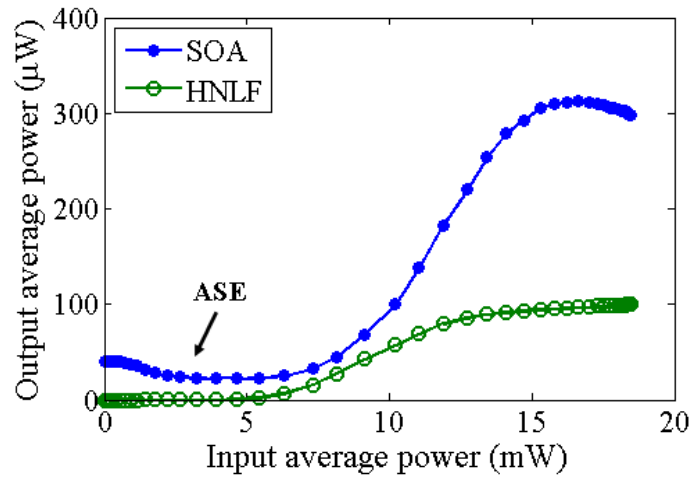


Figure 5.10 Operation principle of the self-clocked time gate.

The transfer function is illustrated in Fig. 5.10. The input average power (P_α) and output average power (P_β) are measured at the points α and β in Fig. 5.9. When input power is low, there is no output if the HNLF is used, while there are some very low outputs if the SOA is used, resulted from amplified spontaneous emission (ASE). When high power is input, high outputs can be obtained for both cases and the output power in the case of SOA is three times as that in the case of HNLF. Thus, the time gate can be applied to remove low-intensity noises, such as MAI noises. Insertion loss ($10\log(P_\beta/P_\alpha)$) of the time gate using the SOA and the HNLF are about -16 dB and -21 dB at the operating points. Besides, the time gate using the HNLF is more polarization-sensitive. Therefore, the time gate using the SOA is used in the further experiments.

5.3.2 Application of self-clocked time gate in the DPSK-OCDMA system

To acquire the potential properties of the time gate, the influence over the system improvement resulted from the time gate is experimentally investigated.

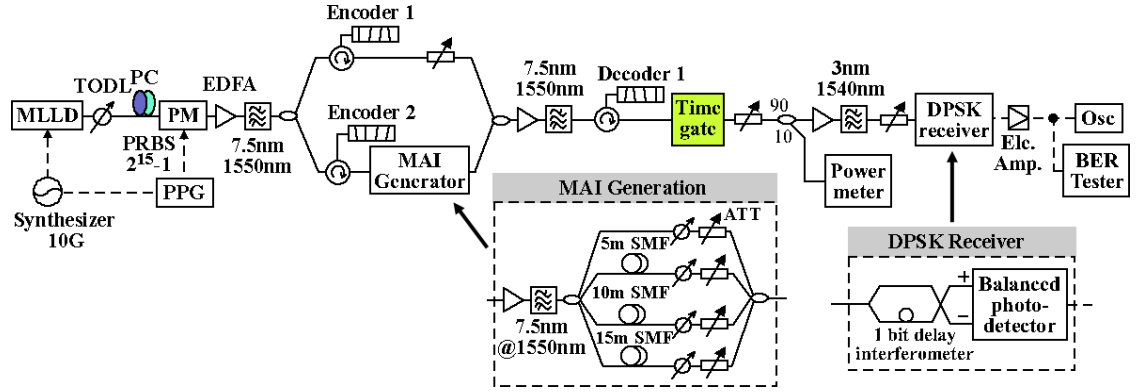


Figure 5.11 Experimental setup of multi-user DPSK-OCDMA system.

The time gate was tested in a multi-user DPSK-OCDMA system. Fig. 5.11 shows the experimental setup of a DPSK-OCDMA system. A train of 10 Gbit/s Gaussian shaped optical pulses was modulated with a $2^{15}-1$ PRBS by a phase modulator. Then, the modulated pulse train was split into two branches and encoded by Encoder 1 and Encoder 2, respectively. The en/decoders were 640 Gchip/s SSFBGs. The SSFBG en/decoders using either 31-chip or 63-chip Gold codes were employed to evaluate performances under different coding situations. In the lower branch, the encoded pulse train was input into an MAI generator, which was to generate up to four MAIs by temporal misalignment and power balance of the signal encoded by Encoder 2. Then, all encoded signals were multiplexed and transmitted to the receiving side.

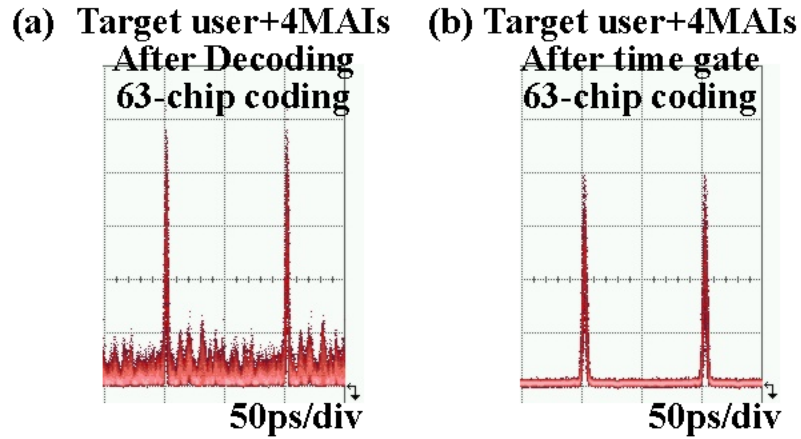


Figure 5.12 The waveforms after (a) decoding and (b) time gate for the case of four MAIs and 63-chip coding.

In the receiving side, Decoder 1 was used to decode the signal encoded by Encoder 1. Only correctly decoded signals could be recovered to high-intensity pulses, and incorrectly decoded signals remained low intensity, which was MAI noises, as shown in Fig. 5.12(a). The followed time gate was to extract the high-intensity signals from the decoded signals. After the time gate, the MAI noises were removed and only the correctly decoded signals remained, as shown in Fig. 5.12(b). Then, the signals were detected by a DPSK receiver, which consisted of a one-bit delay interferometer and a BPD.

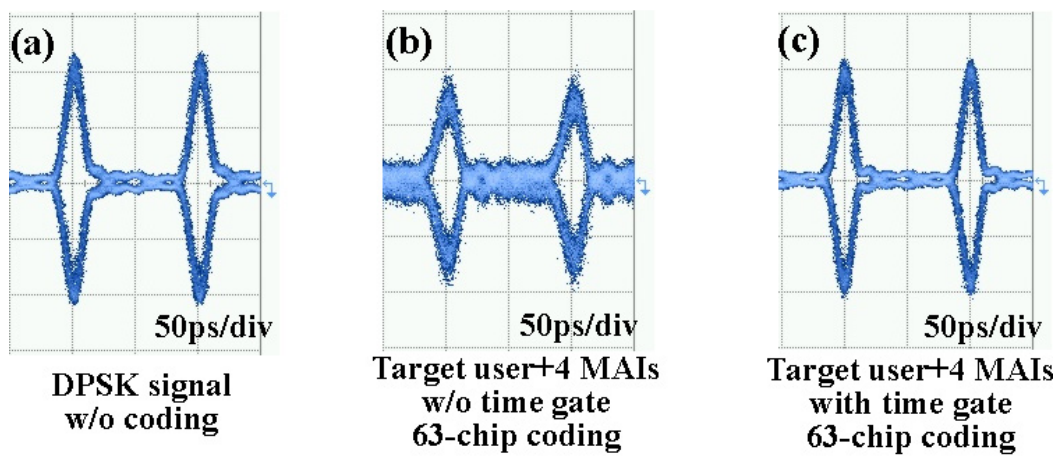


Figure 5.13 (a)–(c) Eye diagrams for DPSK signal without coding, target user with and without time gate.

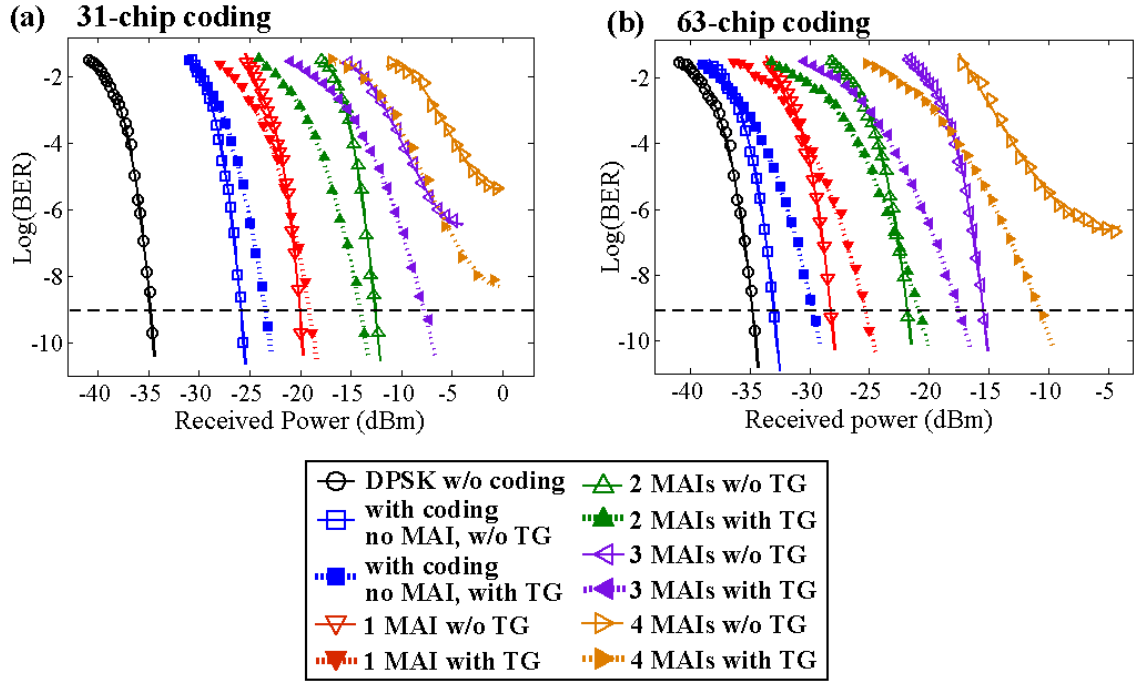


Figure 5.14 (a) and (b) BER performances for 31-chip and 63-chip coding multi-user DPSK-OCDMA system with and without time gate.

Eye diagrams are illustrated in Fig. 5.13(a)–(c). Compared to the four-MAI case without using the time gate, noises in the sidelobes are significantly mitigated and eyes become clearer when using the time gate. Measured BER performances for both 31-chip and 63-chip coding situations are plotted in Fig. 5.14(a) and (b). When the number of interfering users is small, there is some degradation when using the time gate, which is resulted from ASE noises induced by the SOA. However, when the number of interfering users becomes larger, it is obvious that improvement occurs when using the time gate, because the MAI noises are removed and the signal-to-noise ratio is improved.

In addition, the performance analysis is carried out experimentally in the worst and the best situations which are defined as the most and the least MAIs overlapping with the correctly decoded signal in the detection window.

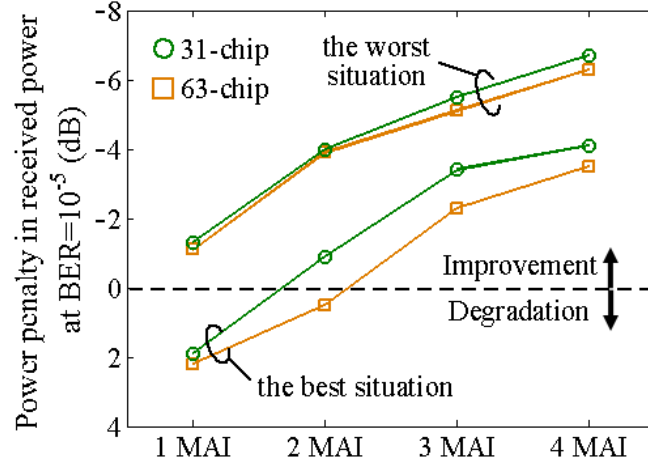


Figure 5.15 Experimental measurement of system improvement by using the time gate.

In the experiment, the worst and the best situations are realized by adjusting the temporal alignment of each interfering user. Figure 5.15 shows the power penalties between the situations with and without the use of the time gate. This comparison is conducted under the conditions when BER is 10^{-5} while the number of interfering users varies. The negative power penalty means the improvement of the performance while the positive values stands for the degradation. The worst and the best situations give upper and lower boundaries of the performance. The time gate can not help the system to improve the performance when few MAIs overlap with the correctly decoded signal, because in these situations the ASE noise from the SOA in the time gate dominates the degradation rather than the MAI noises. When the number of interfering users increases, the time gate has more contributions to performance improvement, due to the efficient elimination of MAI noises, which benefits multi-user systems.

5.4 Source-free-ONU DPSK/OOK OCDMA-PON

5.4.1 OCDMA-PON architecture

The proposed OCDMA-PON architecture is shown in Fig. 5.16. In the OLT which serves as a service provider and processes the coordination of multiplexing, a broadband light source, e.g. a MLLD, is used to generate a train of short optical pulses. This pulse train is split into N branches (where N is the number of total users) and modulated by N PMs. The phase modulation can be any advanced M-ary (D)PSK formats. Then, the

modulated signals are encoded by encoders which could be SSFBG encoders, multi-port AWG encoders, or MRR based encoders. The encoded signals are low-intensity noise-like signals and are multiplexed by a power coupler for downlink transmission.

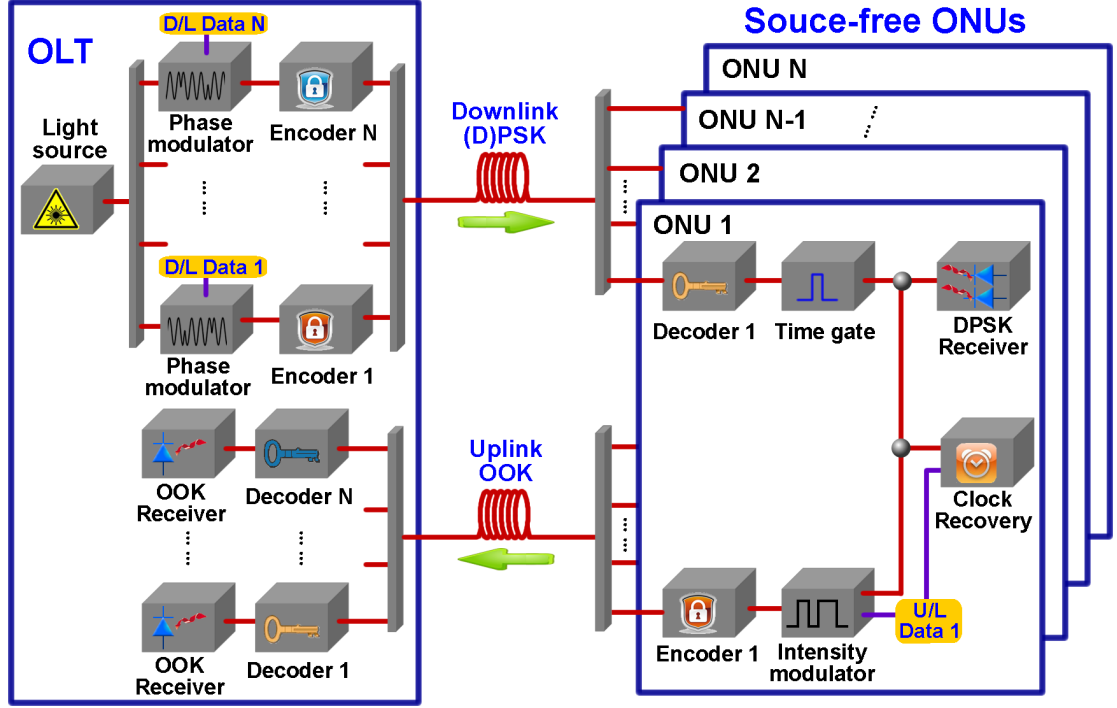


Figure 5.16 Diagram of the proposed OCDMA-PON architecture.

At the ONU side, the multiplexed encoded signals are split into N branches by a power splitter. In each ONU, a corresponding decoder is used for decoding the signal. Correctly decoded signals are recovered into high-intensity peak pulses while incorrectly decoded signals remain low intensity, which produce MAI noises. The following signal regeneration process, where a time gate or a phase-preserved thresholder can be used, is to extract the correctly decoded signals and to suppress the MAI noises. Then, the signals are separated into two branches. In one branch, the signal is demodulated and detected in the receiver. In the other branch, the signal is used for the upstream transmission. This upstream signal is further split into two. One is input into a clock-recovery device for clock extraction and the other is input into an IM whose input electrical data are synchronized by the extracted clock. The intensity-modulated signal is encoded and multiplexed with the encoded signals from other ONUs for the transmission to the OLT, where the upstream signal is split into N branches for decoding

and detection.

An efficient network control is needed for this OCDMA-PON. Since downstream and upstream transmissions use the same optical carrier, the light source in the OLT generates the optical carrier once it requires data transmissions between the OLT and ONUs. The status of PM and IM shifts between operating and idle mode depending on whether there is data to transmit. Thus, upstream transmissions are not affected even if there is no downlink data to transmit.

In the proposed OCDMA-PON, the data rate in the uplink can be as high as that in the downlink, because the upstream modulation is a direct intensity modulation of the downstream signal and the coding mechanisms for both downlink and uplink are same. Thus, gigabit-symmetric transmissions can be achieved. Besides the contribution to the high data rate of uplink, the remodulation scheme can simplify the ONUs by omitting light sources, which agrees the intention of the network design. In this network, synchronization is only needed during the remodulation in the ONUs locally and is not necessary for the duplex transmission. Therefore, the proposed OCDMA-PON can provide fully-asynchronous transmission for both downlink and uplink and use the Tell-and-Go (TaG) protocol [155]. Comparing to other source-free-ONU OCDMA-PONs [140, 141], the proposed scheme does not require additional non-modulated and non-coded optical carriers from OLT for upstream transmission.

5.4.2 Experimental demonstration and results

Figure 5.17 shows the experimental setup of a 4-user downlink and 4-user uplink OCDMA-PON. In the downlink, a train of Gaussian shaped optical pulses generated from a MLLD was modulated with a $2^{15}-1$ PRBS data by a PM and then split into four branches. On each branch, the modulated pulse train was encoded by a 640 Gchip/s $0/\pi$ -phase-shift SSFBG encoder. Four 31-chip Gold codes were used in the encoders. After power balance and decoherence, the encoded signals were coupled and transmitted to the ONU side through a span of SMF and dispersion-compensation fiber (DCF) with a total length of 50 km. The waveform of 4-user multiplexing signals is shown in Fig. 5.18(a). In the ONU, the encoded signal was decoded and passed through

the time gate. The waveforms of the decoded signals and the signals after the time gate are illustrated in Fig. 5.18(b)–(i). After that, the signal was separated into two branches. In the upper branch, the signal was demodulated by a DPSK demodulator which was an asymmetric one-bit delay interferometer and detected by a BPD. The signal in the lower branch was for the uplink.

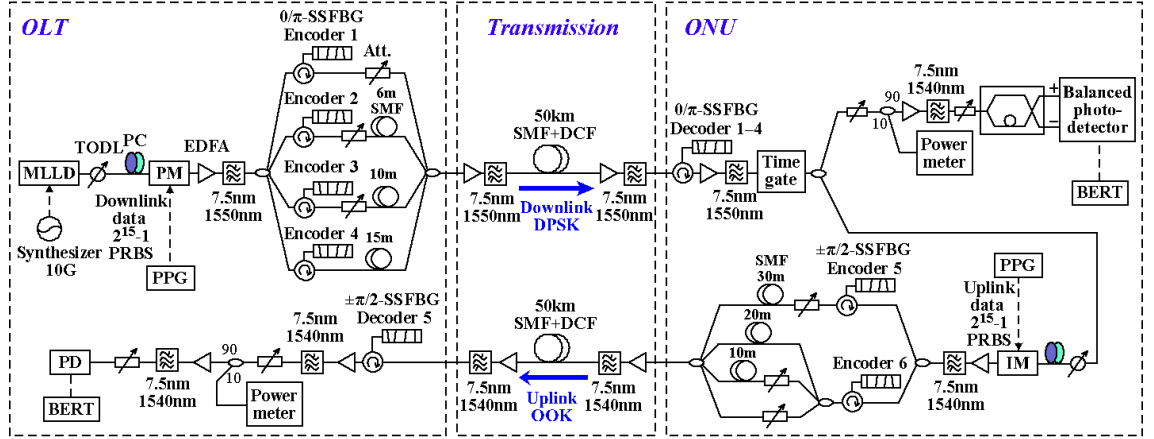


Fig. 5.17 Experimental setup of the duplex multi-user OCDMA system: a 50 km 4-user 10 Gbit/s/user DPSK downstream link and a 50 km 4-user 10 Gbit/s/user OOK upstream link.

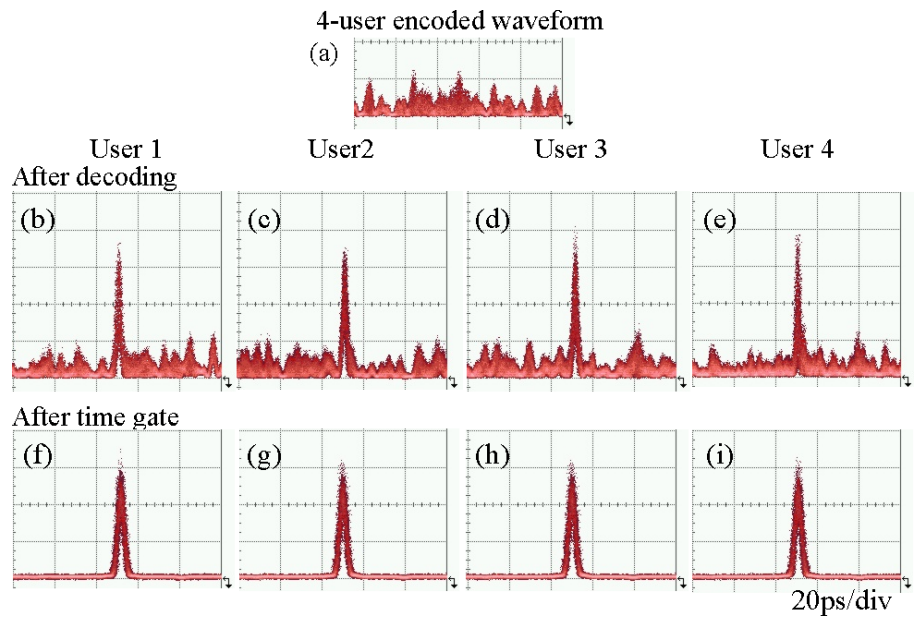


Figure 5.18 Downlink waveforms of (a) 4-user multiplexing encoded signal, (b)–(e) signals after decoding, and (f)–(i) signals after time gate.

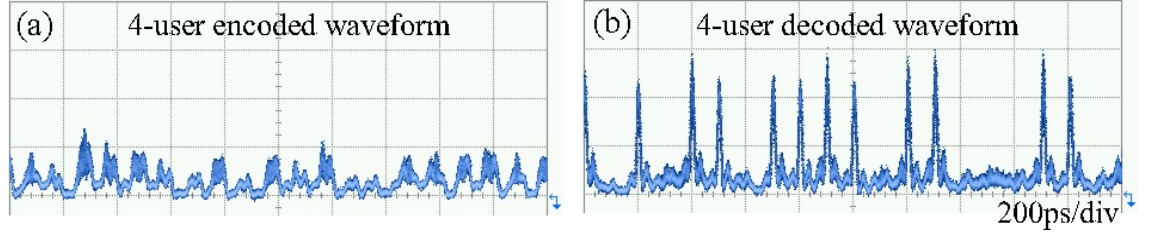


Figure 5.19 Uplink waveforms of (a) 4-user multiplexing encoded signal and (b) signal after decoding.

In the uplink, the signal was modulated by an IM. The clock recovery section was omitted in the experiment. The modulated signal was then split into two branches and encoded by two 31-chip 640 Gchip/s $\pm\pi/2$ -phase-shift SSFBG encoders. The signal encoded by Encoder 6 was divided into three replicas to represent three MAI-users. After power balance and pattern decorrelation, the encoded signals were combined by a power coupler and transmitted to the OLT through a span of 50 km fiber (SMF+DCF), as shown in Fig. 5.19(a). In the OLT, the encoded upstream is decoded by Decoder 5 and detected by a photodetector. The decoded waveform is shown in Fig. 5.19(b).

Eye diagrams for both uplink and downlink are shown in Fig. 5.20, where clear open eyes can be observed. Compared with the eye diagram in Fig. 5.20(e)–(h), the noises in Fig. 5.20(a)–(d) are efficiently removed after the time gate. In the uplink, MAIs can be observed in the 4-user situation, as shown in Fig. 5.20(k), but the eyes are widely and clearly opened. BER performances with and without transmission are plotted in Fig. 5.21, where error-free ($\text{BER} < 10^{-9}$) measurements are achieved for all cases. The DPSK downlink has better performance than the OOK uplink, where the power penalty is about 2–5 dB. It is worth noting that there is a 3 dB difference between the DPSK and OOK receiver sensitivity. Thus, the degradation resulted from the remodulation is not serious.

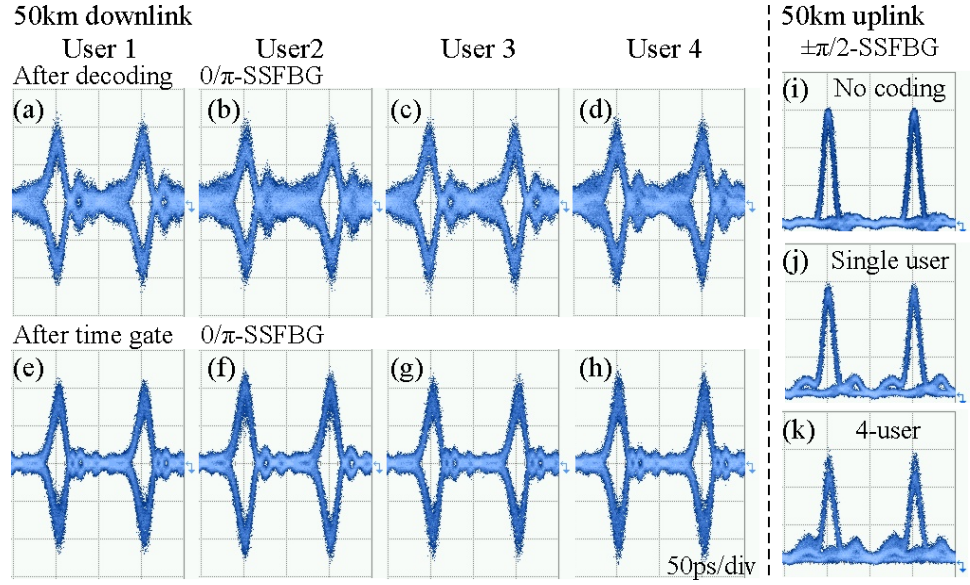


Figure 5.20 Eye diagrams of (a)–(d) downstream signals after decoding, (e)–(h) downstream signals after time gate and (i)–(k) upstream signals without coding, for single user and 4-user.

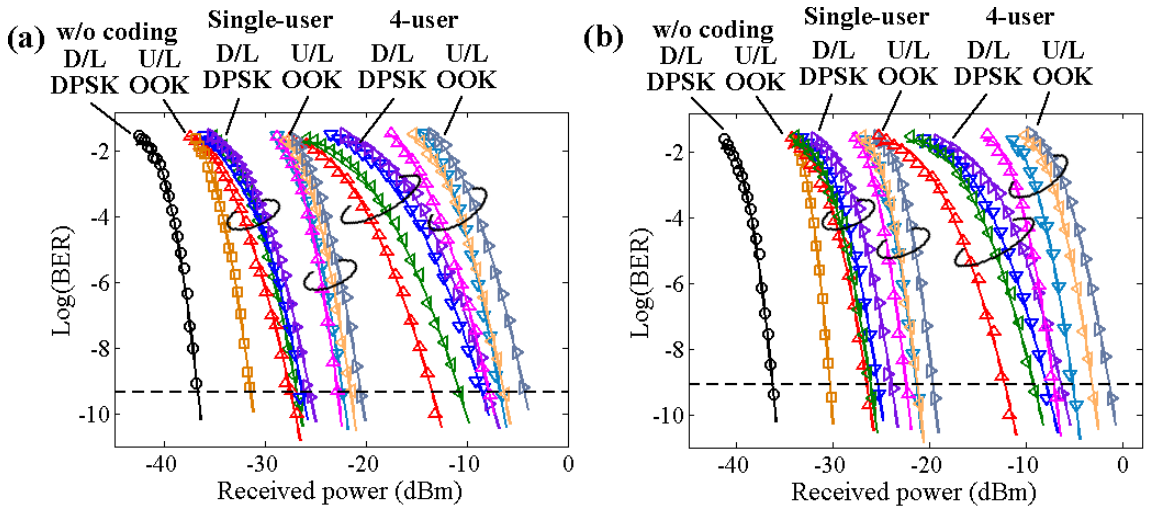


Figure 5.21 BER performances in the situations of (a) back-to-back and (b) 50 km uplink and 50 km downlink.

The experimental demonstration is only to show the feasibility of the proposed OCDMA-PON. It has potential to further improve the system performance by applying a thresholder or a time gate in the OLT to remove MAI noises in the upstream. Besides that, like some other hybrid systems for next-generation PON stage 2 (NG-PON2) such as time/wavelength-division multiplexing (TWDM) systems [140, 156], large scalability

of the network can be achieved by introducing WDM techniques into the OCDMA-PON [16].

5.4.3 Power budget of the OCDMA-PON

In the proposed scheme, there are no light sources in the ONUs. To ensure the transmission quality, especially for the uplink transmission, power consumption in the each stage should be well planned. Thus, a power budget of the proposed duplex transmission system is evaluated. In the analysis of power budget, specific conditions, such as special characteristics of coding devices and optical codes, are not taken into the consideration and only power consumptions are used for calculation.

Table 5.1 Power contribution of each component.

Item	Power	Loss/Gain
Light source	0 dBm	
PM modulator		−5 dB
IM modulator		−5 dB
En/decoder		−15 dB
Transmission fiber		−0.2 dB/km
Multiplexing/Demultiplexing		L_C dB
Time gate		−16 dB
Erbium doped fiber amplifier (EDFA)		+14 dB
System margin	8 dB	
DPSK receiver sensitivity	−40 dBm	
OOK receiver sensitivity	−37 dBm	

Table 5.1 lists the power consumption of each component used in the duplex transmission. There are two factors affecting the power budget, the total number of users, K , and the transmission distance, L . The total number of users is related to multiplexing/demultiplexing loss, $L_C = -3 \lceil \log_2^K \rceil$ where $\lceil u \rceil$ denotes the smallest integer larger than or equal to u . A power budget model is illustrated in Fig. 5.22. Components used in the duplex transmission are depicted in the model and their loss and gain are listed. In the analysis, the maximum transmission distance is investigated

without in-line amplifications. Besides, an 8 dB system margin is considered in the both downlink and uplink for a high tolerance of deterioration in the transmission.

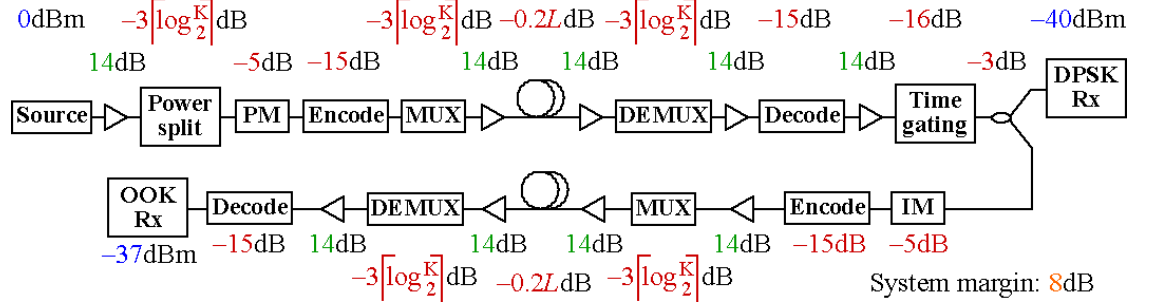


Figure 5.22 Power budget model.

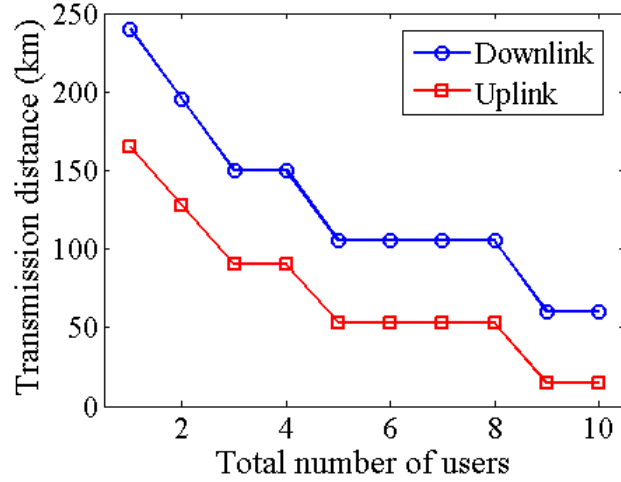


Figure 5.23 Relationship between transmission distance and total number of users.

According to the power budget model, the relationship between the transmission distance and the number of users for both downlink and uplink are calculated and depicted in Fig. 5.23. The transmission distance descends with the increase of the number of total users, which is mainly resulted from the coupling loss. Since the uplink experiences more power loss, the duplex transmission is mainly limited by the performance of the uplink. For a 50 km duplex transmission, the total number of users can be up to 8. Furthermore, employing en/decoders with low insertion-loss can significantly reduce the power consumption. For example, the proposed SSFBG en/decoders in [45] adopting apodization technique have insertion loss of only -1 dB.

By using these kinds of en/decoders, there will be 28 dB and 56 dB improvements in the downlink and uplink respectively. The improved power efficiency ensures a higher signal-to-noise ratio (SNR) and a better system performance, which allows a longer transmission. To obtain a large number of users in the OCDMA system, optical codes with good aperiodic correlation should be used.

5.5 Summary

In this chapter, a fully-asynchronous gigabit-symmetric OCDMA-PON is demonstrated. The duplex transmission is based on remodulating DPSK downstream signals into OOK format for upstream transmission, which realizes the centralized light source in the OLT and makes ONUs source-free. An experimental demonstration of an asynchronous 4-user 10 Gbit/s/user 50 km OCDMA-PON is conducted. Error-free transmissions are achieved both in the uplink and downlink.

In addition, a self-clocked time gate is proposed and analyzed. In this time gate, a clock signal is extracted from an original input signal and there is no need to use additional clock signals from other extra light sources. Therefore, it has the potential to be applied to an asynchronous system. Furthermore, the time gate functions like a phase-preserved threshold and consequently it is used in a DPSK-OCDMA system for signal regeneration. The system performance is improved when the time gate is used, especially in the multi-user situation.

The self-clocked time gate is also applied to the OCDMA-PON. With the help of the time gate, the downstream signal qualities are significantly improved, thus making it possible to remodulate the downstream signals for further upstream transmission. Furthermore, a power budget model is built to evaluate the power consumption of the OCDMA-PON. Since ONUs are source-free, it is upstream transmission that limits the transmission distance, which is shortened by increasing the total number of users. To enhance the energy efficiency and extend the transmission distance, en/decoders with low insertion-loss are suggested to be employed. The demonstrated OCDMA-PON is a promising candidate for future miscellaneous networks and the related techniques have potential to be applied to other secure transmission systems.

Chapter 6

Versatile Waveform Generation

Photonic waveform generation techniques have significant impacts on many fields of science and engineering, including optical communication, biomedical optical imaging and microwave transmission. Hence, developing techniques for generating different prospective waveforms is an attractive research area [157–160].

In this chapter, a scheme of versatile waveform generation using a single-stage dual-drive Mach-Zehnder modulator (DD-MZM) and a span of dispersive fiber is investigated. A theoretical model on the process of waveform generation is built and an algorithm on the prediction of the waveform generation is developed. Furthermore, versatile waveforms, such as short pulse, trapezoidal, triangular and sawtooth waveforms and doublet pulse, are theoretically generated under different combinations of the four variables. The generated waveforms are analyzed in terms of the gradient and the instantaneous frequency. Finally, the waveform generation is experimentally demonstrated at the repetition rate of 10 GHz.

6.1 Overview of optical Fourier synthesis

Among numerous photonic waveform generation approaches, the Fourier synthesis approach is a practical method that is widely used, in which the optical spectral comb is firstly generated from an input signal and then is convolved with the Fourier transform of a spectral filter to produce prospective waveforms.

In the Fourier synthesis approach, the first step is to generate optical spectral comb. Many configurations have been proposed to generate optical spectral comb using cascaded modulation of a CW laser.

In [161], the generation of optical spectral comb was realized by means of cascaded intensity modulation. The experimental demonstration was carried out to generate 9 spectral lines by using two cascaded Mach-Zehnder IMs. The schematic diagram is illustrated in Fig. 6.1. The number of optical spectral lines generated by this method

depends on the number of cascaded intensity modulators. When N modulators are cascaded, 3^N spectral lines are generated. However, it is not practical to generate a large number of spectral lines by cascading several modulators.

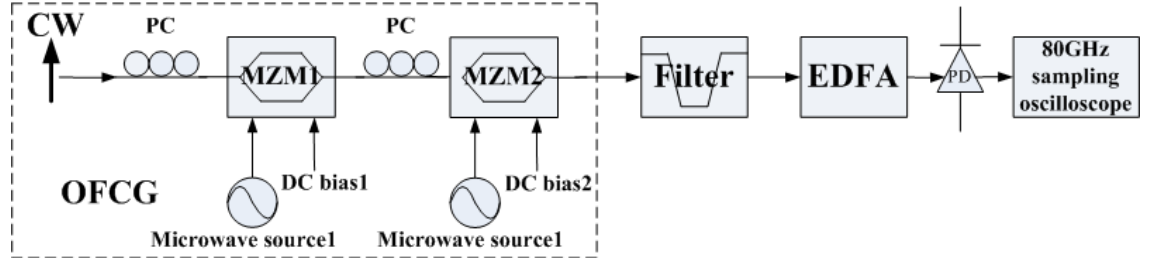


Figure 6.1 Schematic diagram of Fourier synthesis in [161].

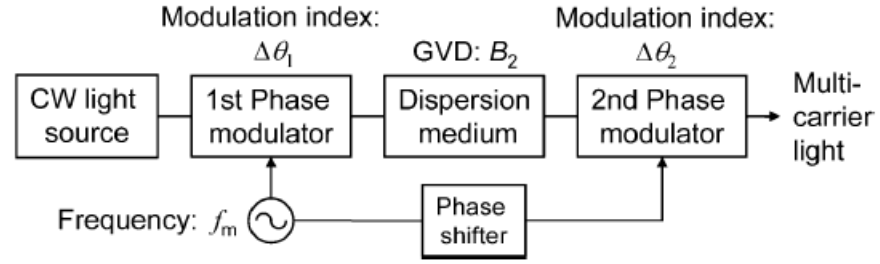


Figure 6.2 Schematic diagram of optical spectral comb generator in [162].

Besides using cascaded intensity modulation, optical spectral comb can be generated by using two cascaded PMs and a chromatic dispersion medium that is inserted in between the two PMs [162]. Fig. 6.2 shows the schematic diagram of this scheme. By applying a sinusoidal phase modulation with a modulation index of $\pi/4$ to the first PM and setting the group velocity dispersion of the dispersion medium at $\pm 1/(4\pi f_m^2)$, where f_m is the modulation frequency, an optical spectral comb could be obtained for any modulation index of the second PM. The number of spectral lines was approximately proportional to the modulation index of the second phase modulator. Compared with the schemes using intensity modulation, this method did not suffer from an intrinsic 3 dB loss caused by Mach-Zehnder IM and required no DC bias control.

It is also possible to generate optical spectral comb by using phase and intensity hybrid modulation. For example, in [163], the optical spectral comb generator was built

by an IM and a PM, as shown in Fig. 6.3. In the demonstration, 9 spectral lines were generated within 3 dB power deviation. However, it was difficult to increase the number of spectral comb meanwhile keeping low power deviation. To obtain a flat spectral comb when generating a large number of spectral lines, a modified version was proposed as shown in Fig. 6.4 [164]. The modulators were driven by specially tailored RF waveforms. An optical spectral comb of 38 spectral lines with power deviation below 1 dB was generated. The number of spectral lines that could be generated is limited by the power handling capability of the phase modulator and this could be scaled without compromising the spectral flatness.

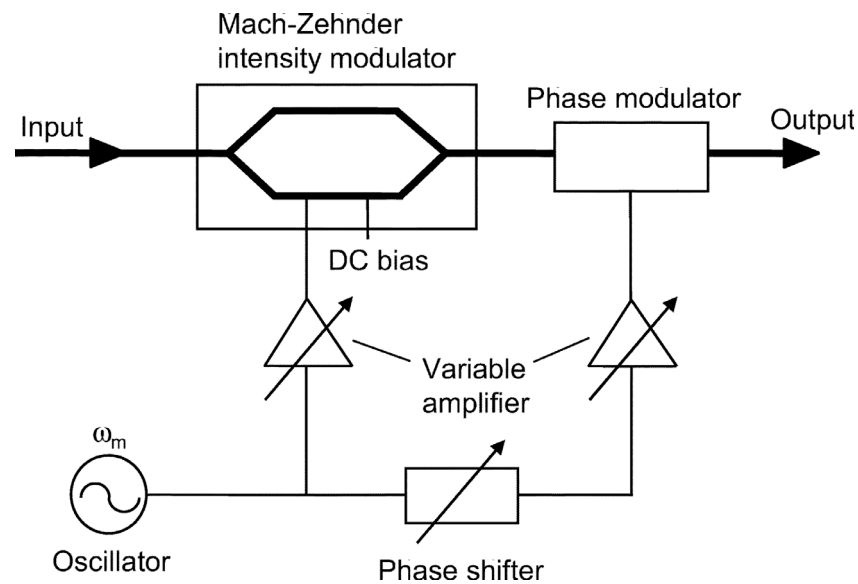


Figure 6.3 Schematic diagram of optical spectral comb generator in [163].

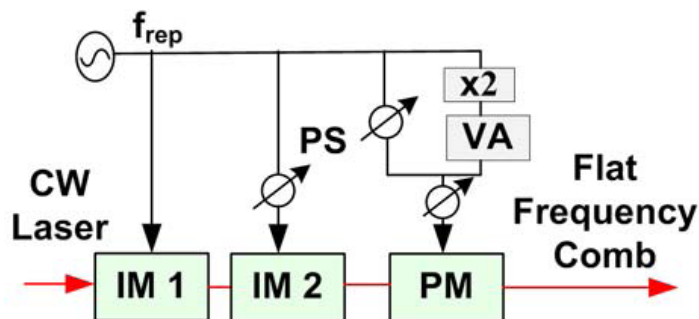


Figure 6.4 Schematic diagram of optical spectral comb generator in [164].

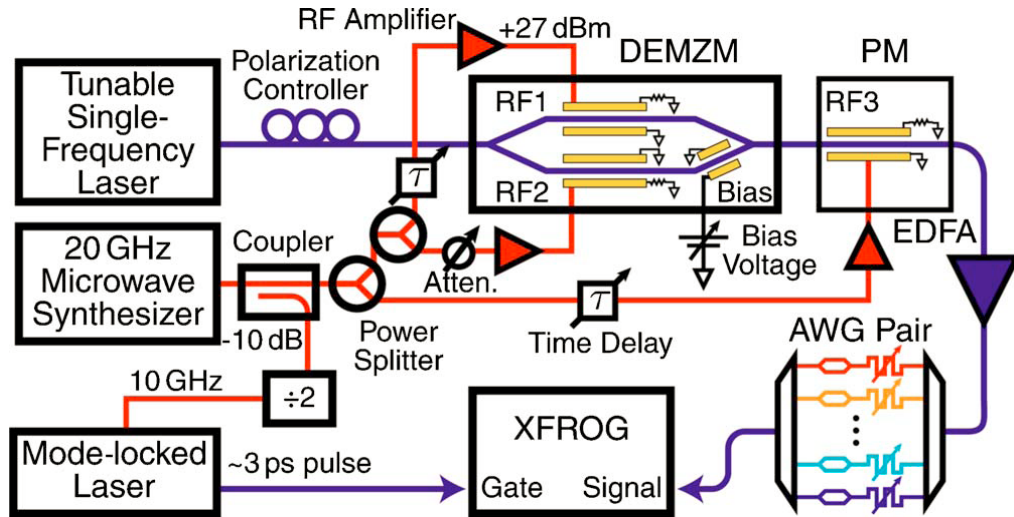


Figure 6.5 Schematic diagram of Fourier synthesis in [165].

In addition to using single-arm modulators, in some configurations, dual-arm modulators were used. In [165], the module for generation of optical spectral comb consisted of a LiNbO₃ dual-electrode Mach-Zehnder modulator (DEMZM) followed by a LiNbO₃ PM, as shown in Fig. 6.5. The PM was driven with a RF power (signal RF3), while other two RF signals (signals RF1 and RF2) drove the DEMZM. The amount of phase modulation and intensity modulation occurring in the DEMZM depended on the relative phase and amplitude between signals RF1 and RF2 and the DC bias. The phase of signal RF3 was adjusted to maximize the number of modes.

Another configuration was to use a DD-MZM to generate a flat spectral comb [166–168]. Due to the good stability and high coherence of the generated spectral comb, the generation of 200 fs (FWHM) ultra-short pulses can be achieved using this approach. In addition to this, as shown in this work, the repetition rate may be widely tunable, ranging from 5 GHz to 17 GHz. Furthermore, compared to the cascaded modulations, the single-stage dual-drive modulation can not only reduce the number of components but also simplify the system.

The second step of the Fourier synthesis approach is to manipulate the generated spectral comb. Traditionally, spectral patterned masks are applied to the composition of spectral components [169], shown schematically in Fig. 6.6. A pair of gratings was placed at the focal planes of a unit magnification confocal lens pair. Spatially patterned

amplitude and phase masks were inserted midway between the two lenses at the point where the optical spectral components experienced maximal spatial separation. The pulse shape at the output was the Fourier transform of the pattern transferred by the masks onto the frequency spectrum. However, this free-space optics based system is bulky and not convenient for implementation.

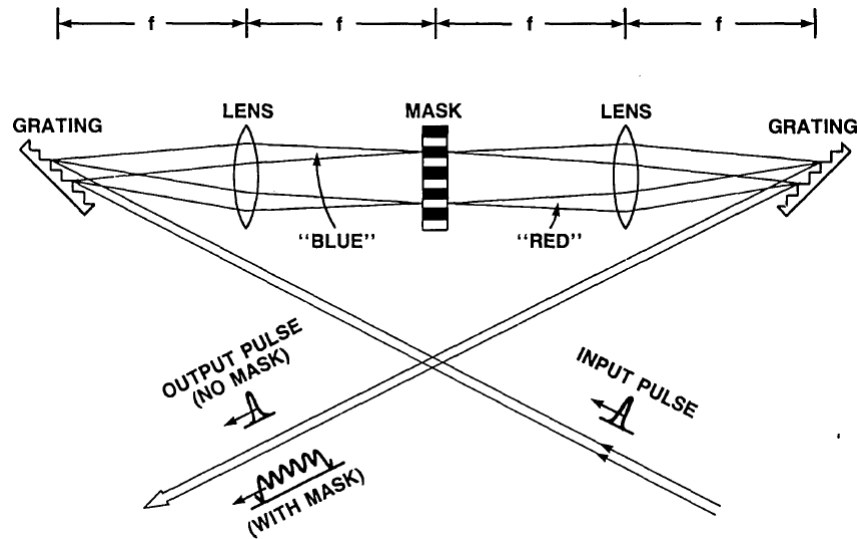


Figure 6.6 Schematic diagram of dispersion-free pulse shaping in [169].

More advanced examples of pulse shaping were reported recently using FBGs [170, 171] and modified AWG [172–174]. These FBG and AWG based schemes were able to provide a wide time window, compatibility with fiber optics, compactness, and integration capabilities.

The implementation of liquid crystal modulator (LCM) arrays leads to a new regime for arbitrary waveform generation by means of line-by-line manipulation of the spectral comb [34, 175, 176]. The schematic diagram is similar to that in Fig. 6.6, but the spectral patterned masks are replaced by a LCM array, which can be programmed for independent grey-level intensity and phase control. The independent programmable control of more than 100 spectral lines at 5 GHz line spacing was obtained, which was a significant step for complex waveform generation.

Another alternative waveform generation approach, which relies on a single transverse spatial mode, can integrate with fiber systems well [177, 178]. The

manipulation of optical spectral comb was successfully achieved in the time domain when spectral decomposition occurs by using chromatic dispersion. Confinement to a SMF removed the time–space interrelation inherent in traditional pulse shaping devices, and it allowed one to envision pulse shaping during propagation over long dispersion-compensated spans. This concept lent itself to new signaling methods including in-line schemes for coherent spectral phase coding OCDMA systems.

6.2 Theoretical model of the waveform generation system

In our proposed waveform generation scheme, the Fourier synthesis, generation and manipulation of the optical spectral comb, is accomplished simultaneously by controlling DD-MZM and chromatic dispersion. Figure 6.7 shows the schematic diagram of the proposed waveform generation scheme. A continuous-wave (CW) laser is used as the light source. The CW light is directed into the LiNbO₃ DD-MZM. A RF sinusoidal signal is generated from a RF synthesizer, divided into two paths (*RF-a* and *RF-b*) by a hybrid coupler and amplified by two microwave amplifiers to drive the DD-MZM. The relative amplitudes (A_1 and A_2) and the phase difference of the two RF signals can be adjusted by controlling two RF attenuators and a tunable delay line. After undergoing the electro-optic modulation, an optical spectral comb with multiple sidebands on both sides of the fundamental component is generated from the CW light, as shown in Fig. 6.8.

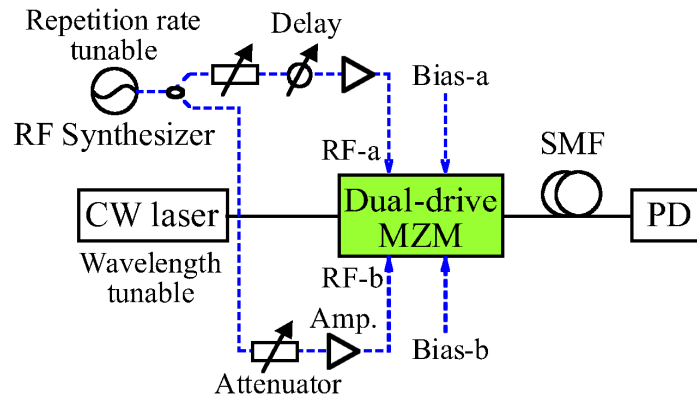


Figure 6.7 Schematic diagram of waveform generation scheme.

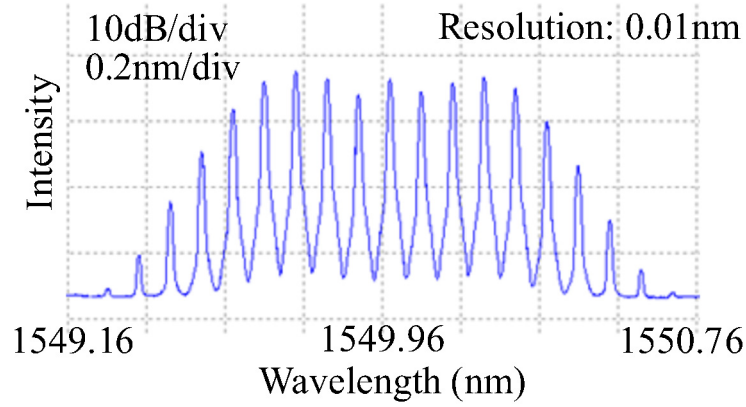


Figure 6.8 Generated optical spectral comb.

The output electrical field from the DD-MZM is given as [179]

$$E_o(t) = \frac{1}{2} E_{in} \exp(j\omega_c t) \left[\exp\left(j\pi \left(\frac{V_1(t)}{V_{\pi RF}} + \frac{V_{Bias1}}{V_{\pi DC}} \right)\right) + \exp\left(j\pi \left(\frac{V_2(t)}{V_{\pi RF}} + \frac{V_{Bias2}}{V_{\pi DC}} \right)\right) \right] \quad (6.1)$$

where E_{in} is the amplitude of CW light electrical field; ω_c is the optical carrier frequency; $V_{\pi RF}$ is the switching voltage; $V_{\pi DC}$ is the switching bias voltage; V_{Bias1} and V_{Bias2} are the DC bias voltages applied to the two arms; and $V_1(t)$ and $V_2(t)$ are the RF modulating electrical voltages. $V_1(t)$ and $V_2(t)$ can be expressed as two sinusoidal functions: $V_1(t) = A_1 \sin(\omega t)$ and $V_2(t) = A_2 \sin(\omega t + \phi)$, where A_1 and A_2 are the amplitudes of the two RF signals; ω is the frequency of the modulating RF signal; and ϕ is the phase shift according to the delay between the two RF signals. In our theoretical analysis, the linewidth of CW light is assumed to be much narrower than the modulation frequency.

After Jacobi Anger expansion, the output electrical field can be written as follows

$$E_o(t) = \frac{1}{2} E_{in} \exp(j\omega_c t) \left\{ \sum_{n=-\infty}^{\infty} J_n \left(\frac{\pi A_1}{V_{\pi RF}} \right) \exp\left(j \left(n\omega t + \frac{\pi}{V_{\pi DC}} V_{Bias1} \right)\right) + J_n \left(\frac{\pi A_2}{V_{\pi RF}} \right) \exp\left(j \left(n\omega t + n\phi + \frac{\pi}{V_{\pi DC}} V_{Bias2} \right)\right) \right\} \quad (6.2)$$

From Eqt. (6.2), it can be seen that the number and the magnitude of generated comb lines are determined by the amplitudes of the two RF signals. After the generation of spectral comb, a span of SMF is used to induce the chromatic dispersion for the

formation of waveform. The chromatic dispersion is obtained from the derivative of the group delay with respect to each spectral comb line [180]. The attenuation and nonlinear effects of SMF are neglected and only the first order chromatic dispersion is considered. Due to the presence of chromatic dispersion, the electrical field with induced chromatic dispersion after SMF can be expressed as

$$E_O(t) = \frac{1}{2} E_{in} \exp(j\omega_c t) \left\{ \sum_{n=-\infty}^{\infty} J_n \left(\frac{\pi A_1}{V_{\pi RF}} \right) \exp \left[j \left(n\omega t + \frac{\pi}{V_{\pi DC}} V_{Bias1} + n^2 \theta \right) \right] \right. \\ \left. + J_n \left(\frac{\pi A_2}{V_{\pi RF}} \right) \exp \left[j \left(n\omega t + n\varphi + \frac{\pi}{V_{\pi DC}} V_{Bias2} + n^2 \theta \right) \right] \right\} \quad (6.3)$$

where θ is the dispersion phase angle and is related to both the length (z in kilometer) and the dispersion characteristic (D in ps/nm·km) of SMF, whose expression is

$$\theta = -\frac{z\lambda_c^2 D \omega^2}{4\pi c} \quad (6.4)$$

where c is velocity of light in a vacuum. The induced chromatic dispersion recomposes the spectral comb, operating the waveform formation. It is worth noting that since the formation of waveforms is based on the chromatic dispersion, it requires a zero-dispersion for a further propagation of the generated waveforms.

For detection, a photodiode (PD) is employed for O/E conversion. The output intensity of the signal is expressed as

$$I = |E_O(t)|^2 \\ = \frac{1}{2} E_{in}^2 \Re \left\{ \sum_{n=-\infty}^{\infty} \left[\left[J_n \left(\frac{\pi A_1}{V_{\pi RF}} \right) \right]^2 + \left[J_n \left(\frac{\pi A_2}{V_{\pi RF}} \right) \right]^2 + J_n \left(\frac{\pi A_1}{V_{\pi RF}} \right) J_n \left(\frac{\pi A_2}{V_{\pi RF}} \right) \cos \left(\frac{\pi}{V_{\pi DC}} (V_{Bias1} - V_{Bias2}) - n\varphi \right) \right] \right. \\ + \sum_{m=1}^{\infty} \sum_{n=-\infty}^{\infty} \left[J_n \left(\frac{\pi A_1}{V_{\pi RF}} \right) J_{n+m} \left(\frac{\pi A_1}{V_{\pi RF}} \right) \cos(m\omega t + (m^2 + 2mn)\theta) \right. \\ + J_n \left(\frac{\pi A_2}{V_{\pi RF}} \right) J_{n+m} \left(\frac{\pi A_2}{V_{\pi RF}} \right) \cos(m\omega t + m\varphi + (m^2 + 2mn)\theta) \\ + J_n \left(\frac{\pi A_1}{V_{\pi RF}} \right) J_{n+m} \left(\frac{\pi A_2}{V_{\pi RF}} \right) \cos \left(m\omega t + (n+m)\varphi - \frac{\pi}{V_{\pi DC}} (V_{Bias1} - V_{Bias2}) + (m^2 + 2mn)\theta \right) \\ \left. \left. + J_{n+m} \left(\frac{\pi A_1}{V_{\pi RF}} \right) J_n \left(\frac{\pi A_2}{V_{\pi RF}} \right) \cos \left(m\omega t - n\varphi + \frac{\pi}{V_{\pi DC}} (V_{Bias1} - V_{Bias2}) + (m^2 + 2mn)\theta \right) \right] \right\} \quad (6.5)$$

where \Re is responsivity of the PD. From Eqt. (6.5), we can see that each harmonic ($m\omega$) is resolved and can be analyzed individually. It is the amplitudes of the modulating RF signals (A_1 and A_2), the phase difference between the two RF signals (φ), the difference of the two bias voltages ($V_{Bias1}-V_{Bias2}$) and the chromatic dispersion of the SMF (θ) that determine the waveform formation. In the generation of the spectral comb, the amplitudes of the two RF signals determine the number of spectral components, which was also mentioned in [168]. Nevertheless, this term is limited by the gain and saturation power of the RF amplifiers and the maximum RF input power of the modulator.

6.3 Algorithm of waveform generation

According to the theoretical analysis, there are four variables that affect the waveform formation, based on which we use the multi-variable control method to search the values of the four variables for the generation of an optimum waveform. The flowchart of the algorithm is depicted in Fig. 6.9.

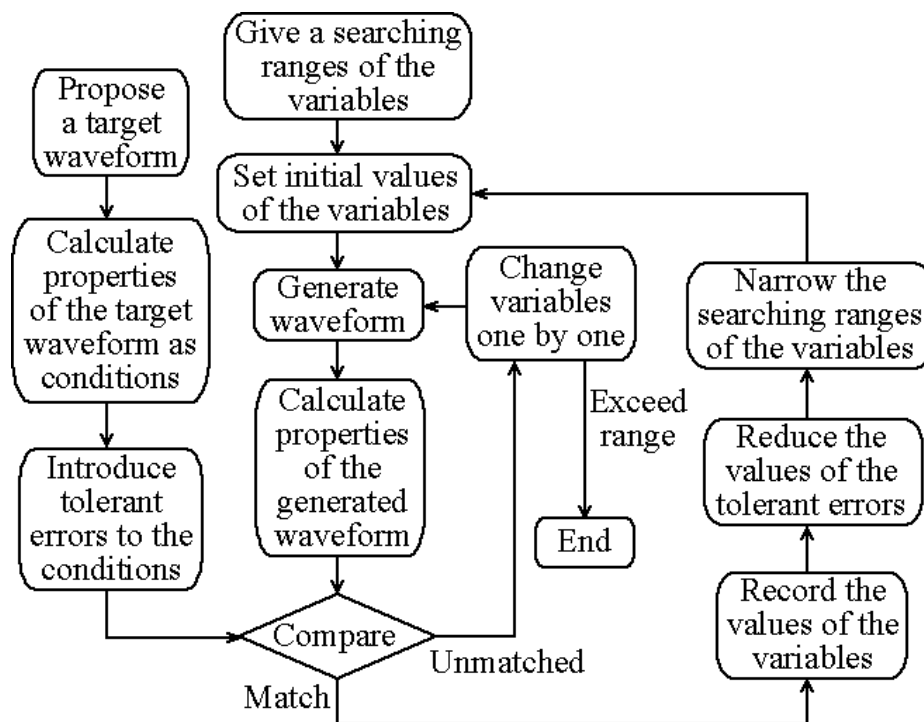


Figure 6.9 Flowchart of the waveform generation algorithm.

Firstly, a target waveform is proposed and the properties of the target waveforms (such as waveform shape, optical spectrum and power spectrum) are calculated. These properties are the conditions of the waveform generation. Besides, tolerant values are introduced into the conditions to relax conditions. Secondly, initial values are assigned to the four variables and the searching ranges of these four variables are also given. By substituting these initial values into Eqt. (6.5), a waveform is generated. Thirdly, the properties of the generated waveform are calculated and compared with the target waveform. If they are unmatched, the values of the variables are changed one by one for another round of waveform generation and condition matching. However, once the comparison is matched, the values of the variables are recorded. Meanwhile, the searching ranges of the variable are narrowed and the tolerant values are reduced to tighten up the restrictions. A new set of initial values within narrowed searching ranges are given to generate waveform. Then, the variable searching procedure continues until all combinations of the four variables within the searching ranges are tested. Finally, after the variable searching finishes, the recording of the four variables is checked. If there is no recording, it indicates that the proposed scheme can not generate the target waveform. Otherwise, the recorded variables are used for waveform generation and the generated waveform is the optimum one for the target waveform.

According to Eqt. (6.5), the output signal is manipulated as a whole by adjusting the four variables and it is not straightforward to generate any arbitrary waveforms by controlling the limited variables individually. However, it is a very simple scheme to set up and control for the generation of versatile meaningful waveforms with acceptable tolerances.

6.4 Experimental demonstration of waveform generation

The experimental setup to verify the proposed scheme is shown in Fig. 6.7. The four variables are controlled by different components. The amplitudes of the two RF signals (A_1 and A_2) are adjusted by two RF attenuators. The control of the phase difference between the two RF signals (φ) is realized by inserting some delay on one branch. The two RF signals are amplified by two RF amplifiers. The gains of the

amplifiers are ~ 30 dB and the saturation powers are ~ 40 dBm. The difference of the two bias voltages ($V_{Bias1} - V_{Bias2}$) is adjusted by the DC voltage controllers and the chromatic dispersion of the SMF (θ) depends on the length of the SMF. The DD-MZM has the optical bandwidth of ~ 18 GHz. The switching voltages ($V_{\pi RF}$) for both electrodes are about 6.5 V, which are measured at 1 GHz with the use of one electrode only. The PD used in the experiment has the bandwidth of 40 GHz, which cuts off the high-order harmonics.

6.4.1 Generation of short pulse

In [166], the authors have demonstrated the generation of short pulses by using a single-stage DD-MZM under the flat-spectrum condition, which is

$$\frac{\pi}{V_{\pi RF}} \frac{A_1 - A_2}{2} = \frac{\pi}{4} \quad (6.6)$$

$$\frac{\pi}{V_{\pi DC}} \frac{V_{Bias1} - V_{Bias2}}{2} = \frac{\pi}{4} \quad (6.7)$$

Firstly, we use Eqt. (6.5) to calculate the signal based on the flat-spectrum condition to examine the feasibility of the derived equation. In our calculation, both switching voltage, $V_{\pi RF}$, and switching bias voltage, V_{Bias2} , are 4V. According to the flat spectrum condition, we set $A_1 = 12$ V, $A_2 = 10$ V, $V_{Bias1} = 2$ V and $V_{Bias2} = 0$ V. There is no delay between the two RF signals, i.e. $\phi = 0$. The chromatic dispersion, D , is 17 ps/nm•km and the length of the SMF is 1.1 km. Besides, it is worth noting that the maximum value of the parameter m in Eqt. (6.5) depends on the bandwidth of the PD. The calculated short pulses are illustrated in Fig. 6.10(a). We also carried out a proof-to-principle experiment. In the experiment, a 10 GHz sinusoidal signal was used as the modulating RF signal. Under the flat-spectrum condition, 4 ps (FWHM) pulses were generated at the repetition rate of 10 GHz, as shown in Fig. 6.10(b).

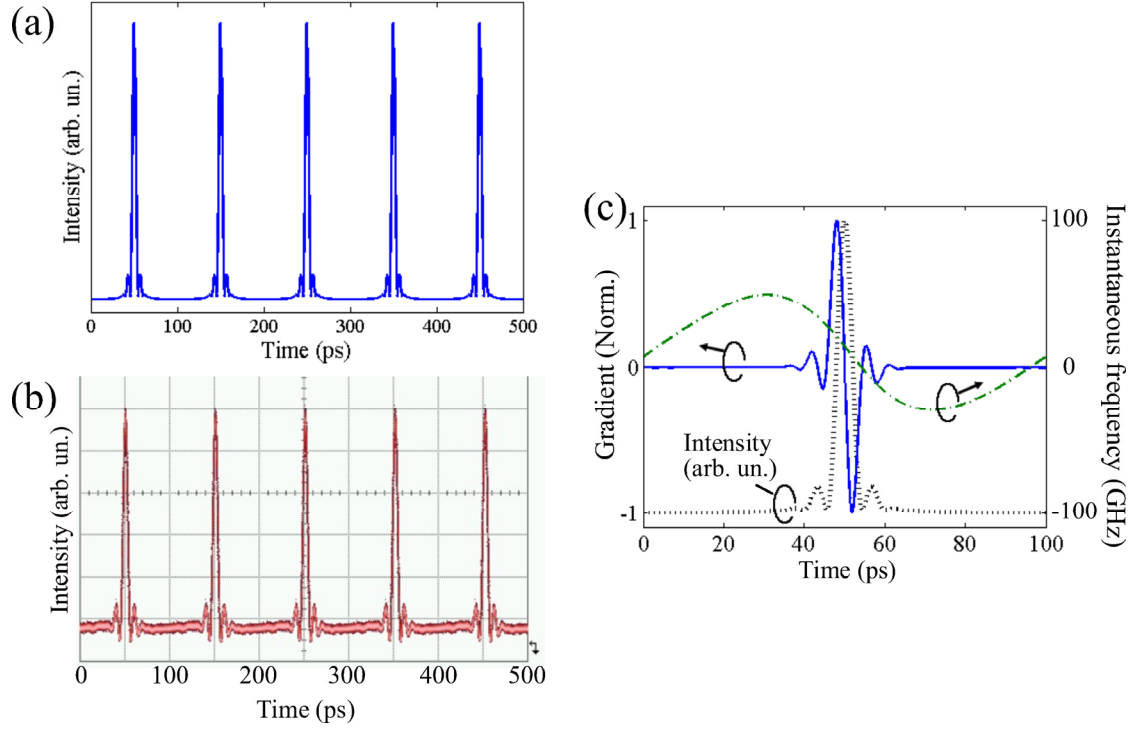


Figure 6.10 (a) Calculated and (b) measured short pulses under the flat spectrum conditions. (c) Calculated normalized gradient and instantaneous frequency corresponding to short pulse intensity profile.

The optical spectrum is shown in Fig. 6.8, which is a flat spectral comb. The detailed waveform for only one pulse is illustrated in Fig. 6.10(c). Since the frequency comb has a rectangular shape, the resultant temporal waveform presents a Sinc^2 function and there are pedestals around the main lobes. The detailed discussion on this phenomenon can be found in [167]. The normalized gradient and the instantaneous frequency are also plotted to show the properties of the waveform. The gradient tells the intensity change and the linearity of the generated waveform, while the instantaneous frequency indicates the phase information and chirp of the waveform. Eqt. (6.5) only provides the intensity synthesis. To show the phase oscillation in the generated pulse, the instantaneous frequency is calculated by Eqt. (6.3). The successful generation of short pulses indicates that the derived equation, Eqt. (6.5), is workable and can be used to predict more waveform generations.

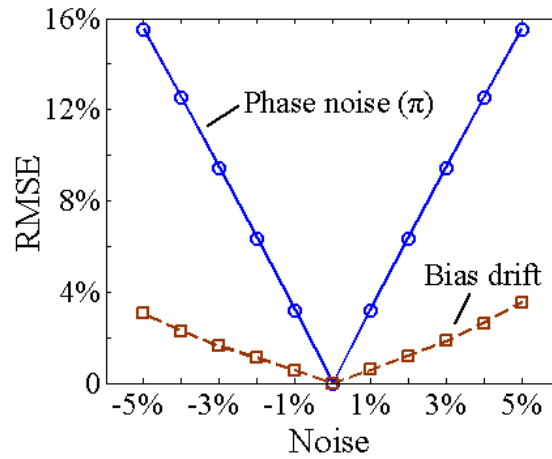


Figure 6.11 Influence of RF phase noise and bias drift.

To analyze the tolerance of the system during the operation, the influences of RF phase noise and DC bias drift over the performance of waveform generation are investigated theoretically. Root-mean-square errors (RMSE) are calculated to evaluate the quality of the waveforms with the induced noises. According to the calculation, the system suffers from the RF phase noise seriously (blue solid line in Fig. 6.11), if the two RF signals from two independent synthesizers are employed without phase locking. In our experiment, the RF phase noise is avoided by using the two RF signals from a single synthesizer. Furthermore, using a single synthesizer can also reduce the complexity of the system. The DC bias drift is an unavoidable issue in this system. According to our analysis, the generated waveforms have less than 3.8% errors compared to the optimum one even when the bias drift is up to $\pm 5\%$ (brown dashed line), which indicates that the system has a high tolerance to the bias drift. In addition, in the experiment, the waveform generation is very stable.

6.4.2 Generation of trapezoidal waveform

Trapezoidal waveforms can deliver the same energy with less dissipation compared to pulses and were suggested to be used in the liquid crystal displays (LCDs) [181]. We can also generate trapezoidal waveform using the proposed scheme. The first step is to calculate the properties of the target waveform. A trapezoidal waveform have a flat top, i.e. a section of zero-gradient, and the intensity in this section is larger than those in the

other sections. The target waveform and normalized gradient are plotted using dashed lines in Fig. 6.12(a). In the calculation, we firstly assume that $\pm 5\%$ ripple is allowed in the flat-top section. Then, we use the algorithm described above to determine the optimum values of the four variables. The variables are obtained when the ripple in the flat-top section converges to $\pm 2.8\%$. $A_1=5$ V, $A_2=3$ V, $V_{Bias1}=0.15$ V and $V_{Bias2}=0$ V. There is no delay between the two RF signals and the length of SMF is 1.1 km.

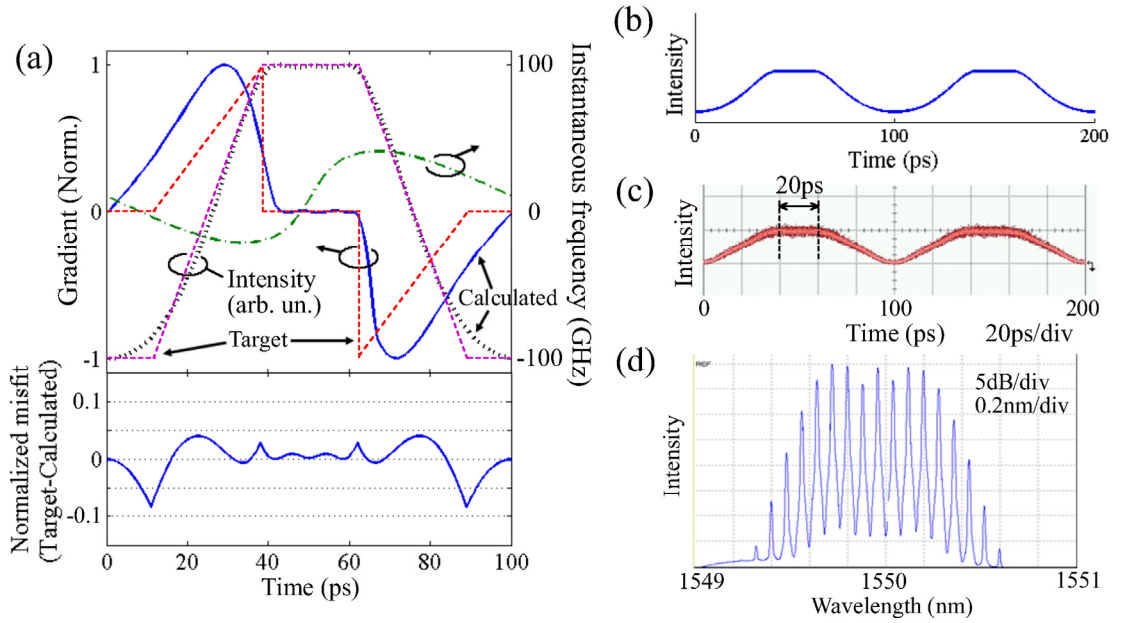


Figure 6.12 (a) The target trapezoidal waveform and the gradient and instantaneous frequency of the calculated waveform. (b) Calculated and (c) measured trapezoidal waveforms. (d) Measured optical spectrum.

The calculated waveform is plotted in Fig. 6.12(b) and a misfit curve comparing the target and calculated waveform is depicted in the subplot of Fig. 6.12(a). Besides, RMSE, calculated to measure the difference between the target and calculated waveforms, is 5.61%. The normalized gradient of the calculated waveform has a zero-level gradient, as shown in Fig. 6.12(a), indicating the flatness of the flat top. An up-chirp occurs within the flat-top section, while on the leading and tailing edges, the instantaneous frequency decreases, i.e. down-chirp. In the experiment, we tried to generate the trapezoidal waveform that was consistent with the calculated waveform. The measured waveform is shown in Fig. 6.12(c), which is symmetric and has a flat top

of 20 ps and smooth leading and tailing edges of 40 ps each. Compared with the target waveform, the measured waveform has the RMSE of 5.96%. The optical spectrum is shown in Fig. 6.12(d).

6.4.3 Generation of triangular waveform

When $V_{BiasI}=2.5$ V and other variables remain the same, the formation of triangular waveforms is achieved, as depicted in Fig. 6.13(b). The calculated waveform is compared with the target waveform in Fig. 6.13(a). The normalized misfit curve is bounded within ± 0.08 , which indicates that the difference between the target and calculated waveforms is very slight. The RMSE of the calculated result is 6.42%. Two horizontal sections in the gradient show the linearity in the leading and tailing sides. The instantaneous frequency is also plotted in Fig. 6.13(a). Two spikes of the instantaneous frequency on the two sides indicate steep changes in the phase. It is clear that the generated triangular waveform is chirped.

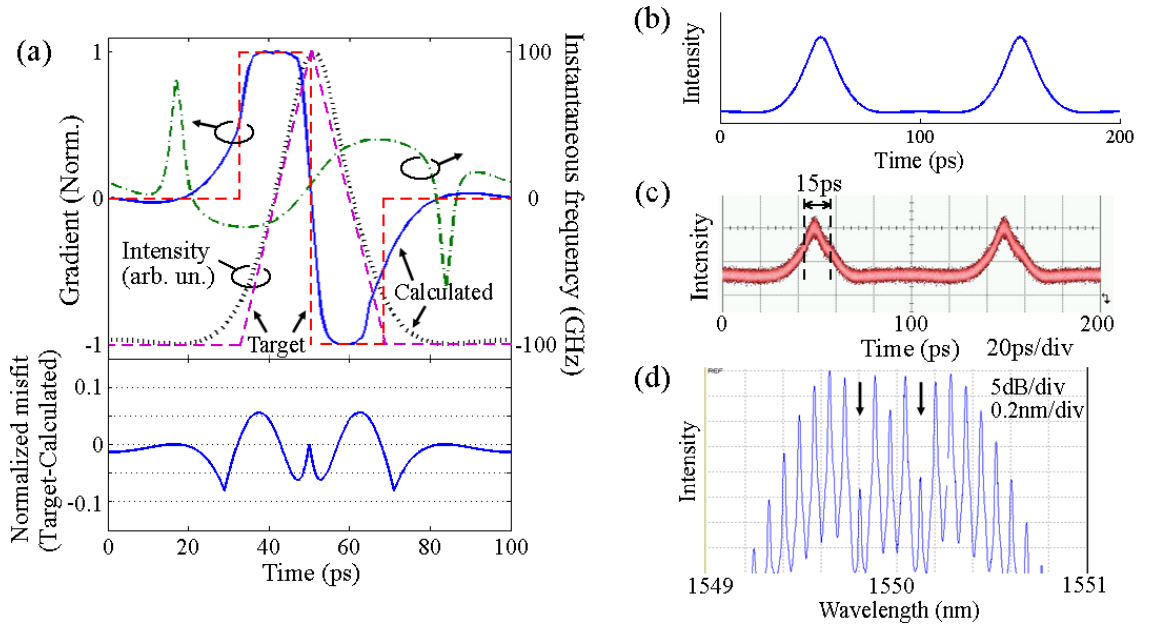


Figure 6.13 (a) The target triangular waveform and the gradient and instantaneous frequency of the calculated waveform. (b) Calculated and (c) measured triangular waveforms. (d) Measured optical spectrum.

The experimentally measured waveform and optical spectrum of the generated triangular waveform are shown in Fig. 6.13(c) and (d), respectively. The width is about 15 ps (FWHM). The RMSE of the measured waveform is 7.03%. Two spectral lines in the frequency comb (highlighted with arrows in Fig. 6.13(d)) are suppressed by the modulation.

6.4.4 Generation of doublet pulse

In the generation of doublet pulses, the amplitudes of the RF signals and the DC bias voltages become $A_1=5$ V, $A_2=5$ V, $V_{Bias1}=4$ V and $V_{Bias2}=0$ V. A 18 ps delay is also added to RF-b, which results in a phase shift between the two RF modulating signals. Fig. 6.14(a) and (b) show the calculated and measured waveforms. The doublet pulses are symmetric and have deep dips in the middle. The peak separation is about 15 ps. In the frequency comb, three spectral lines, including the central spectral line, are suppressed by 20 dB after the modulation, as marked in Fig. 6.14(c).

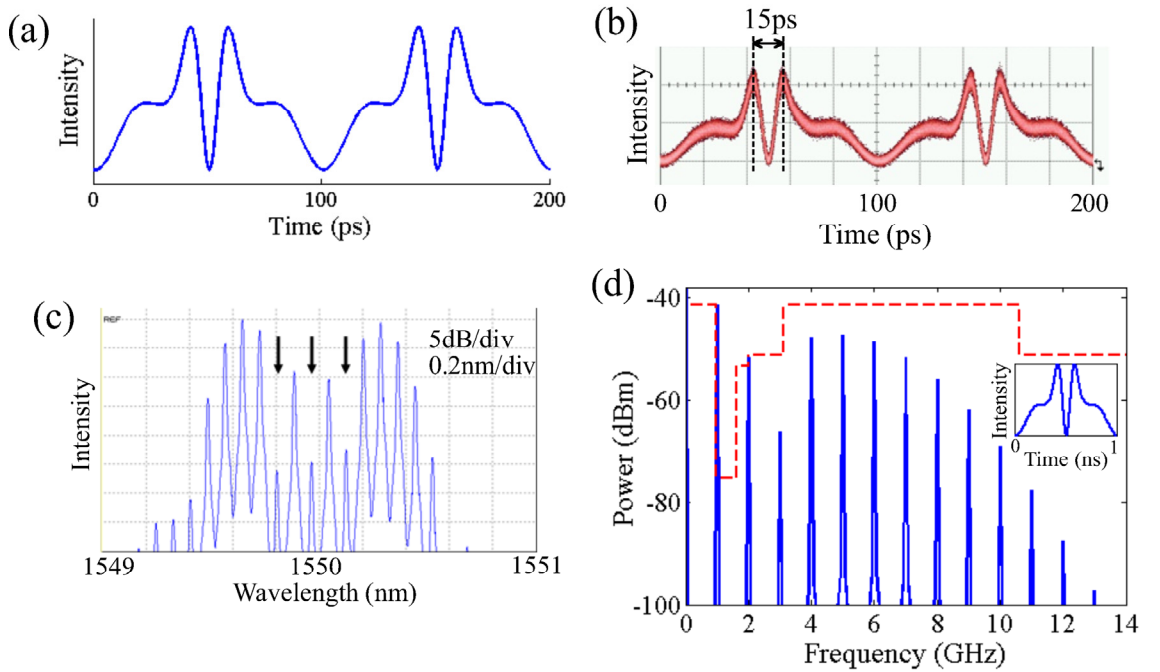


Figure 6.14 (a) Calculated and (b) measured doublet pulses. (c) Measured optical spectrum. (d) Calculated power spectrum of the 1 Gbit/s doublet pulses. Red dashed line: FCC spectral mask for indoor applications. Inset diagram: the waveform of the generated 1 Gbit/s doublet pulse.

In the calculation, we also obtain 1 Gbit/s doublet pulses and investigate the power spectrum. To generate 1 Gbit/s doublet pulses, 1 GHz RF modulating signal is used. The amplitudes of the RF signals and the DC bias are unchanged. The delay of RF-b becomes 175 ps and the length of SMF is shortened to 0.2 km. The calculated power spectrum is illustrated in Fig. 6.14(d). The U.S. Federal Communication Commission (FCC) specified ultra-wideband (UWB) indoor emission mask is also plotted for comparison [182]. The power spectrum of the doublet pulses is centered around 6.5 GHz and has a 10 dB bandwidth of about 6 GHz, which fits well the FCC-specified spectral mask.

6.4.5 Generation of sawtooth waveform

It has been demonstrated that the use of sawtooth (asymmetric triangular) waveform can provide three-fold improvement relative to the use of Gaussian pulses for wavelength conversion due to the asymmetric spectral intensity evolution of sawtooth waveform [170]. Sawtooth waveforms can also be generated by means of the proposed scheme, as shown in Fig. 6.15(b) and (c). Both RF modulating signals are kept at 5 V. 97 ps delay is added to RF-b. The difference of the DC bias voltages is adjusted to 2.7 V. The length of SMF is extended to 1.47 km for larger chromatic dispersion. In Fig. 6.15(a), a negative stationary section of the normalized gradient states that the waveform has a linear tailing side. The instantaneous frequency behaves in a nonlinear fashion and decreases on the tailing edge of the generated sawtooth waveform. A misfit curve is depicted in the subplot to and the difference in the tailing side is within ± 0.05 . The RMSE of the calculated waveform is 9.51%. In the experiment, we also generated the sawtooth waveform as expected. They have sharp leading side and slow downward ramp, whose width is about 30 ps (FWHM). The measured waveform has the RMSE of 11.38%. The frequency comb is asymmetric and the spectral lines on the right side of the center are suppressed gradually, as shown in Fig. 6.15(d).

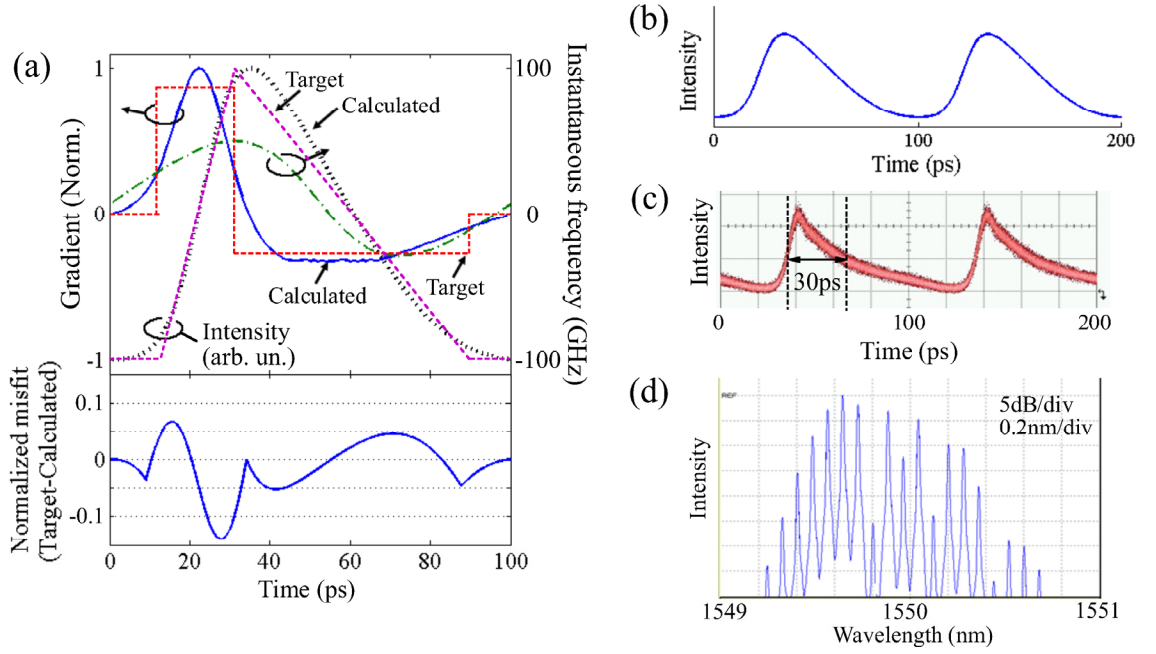


Figure 6.15 (a) The target sawtooth waveform and the gradient and instantaneous frequency of the calculated waveform. (b) Calculated and (c) measured sawtooth waveforms. (d) Measured optical spectrum.

6.5 Summary

In this chapter, a waveform generation model is built based on a single-stage DD-MZM and a SMF employing direct detection, and the mathematical expression for the system is derived. The model can help with the prediction of the waveform generation. In this system, there are four variables affecting the waveform formation. With the different combinations of these four variables, versatile waveforms, short pulse, trapezoidal, triangular and sawtooth waveforms and doublet pulse are obtained. The characteristics of these waveforms are evaluated by investigating the gradient and the instantaneous frequency. Also, the generation of these waveforms is demonstrated at the repetition rate of 10 GHz in the experiment. In addition, the scheme has two potential features, tunable repetition rate and tunable center wavelength, due to the adjustable RF signal and CW light source. This scheme is particularly attractive as a waveform generation source for photonic network applications.

Chapter 7

All-Optical Half-Adder and Half-Subtractor

In the current telecommunications, many essential functions such as packet forwarding, time-to-live (TTL) decrementing and address recognition rely on the electrical operations. However, in the future all-optical networks, all-optical signal processing is required to remedy the speed limitation of electronics, enhance energy efficiency and improve transparency by omitting redundant optical-to-electrical (O/E) and electrical-to-optical (E/O) conversions. A wide range of researches have been conducted on the optical digital logic gates (e.g. AND, OR, NOT and XOR) and optical logical operation modules (e.g. counters, adders, subtractors and shift registers) to achieve the all-optical signal processing [183–185].

In particular, several all-optical half-adder and half-subtractor schemes have been proposed. Both half-adder and half-subtractor can be used for encryption and decryption in the secure networks, arithmetic operation in the arithmetic-logic units (ALU), and optical packet checksum calculation in the packet switching systems [186]. Besides, half-subtractor can be applied to TTL decrementing, routing loop control and dual-direction binary counters [187].

In this chapter, a variety of all-optical half-addition and half-subtraction schemes are overviewed firstly. Then, an all-optical simultaneous 10 Gbit/s half-addition and half-subtraction scheme is demonstrated. The scheme uses only two SOAs and no assist light is needed.

7.1 Overview of all-optical half-addition and half-subtraction schemes

Half-addition and half-subtraction operating on binary numbers are two basic arithmetic functions. A half-adder adds two one-bit binary numbers (A and B) and outputs a sum of these two bits and a carry. In the half-addition module, an AND gate and an exclusive-OR (XOR) gate are implemented, whose outputs are corresponding to the carry and the sum. The XOR gate results in the value of logic ‘1’ if exactly one of

the inputs equals to logic '1', which can be expressed as $\overline{A}B + A\overline{B}$.

A half-subtractor performs the function of subtraction for two bits. In the subtraction module, there are two inputs, which are minuend and subtrahend, and two outputs, difference and borrow. The operation of the difference functions as the XOR gate. The borrow outputs logic '1' only when minuend is logic '0' and subtrahend is logic '1', i.e. (0–1=1). The logical function of the borrow can be represented as $\overline{A}B$ or $A\overline{B}$, depending on whether A is minuend or subtrahend.

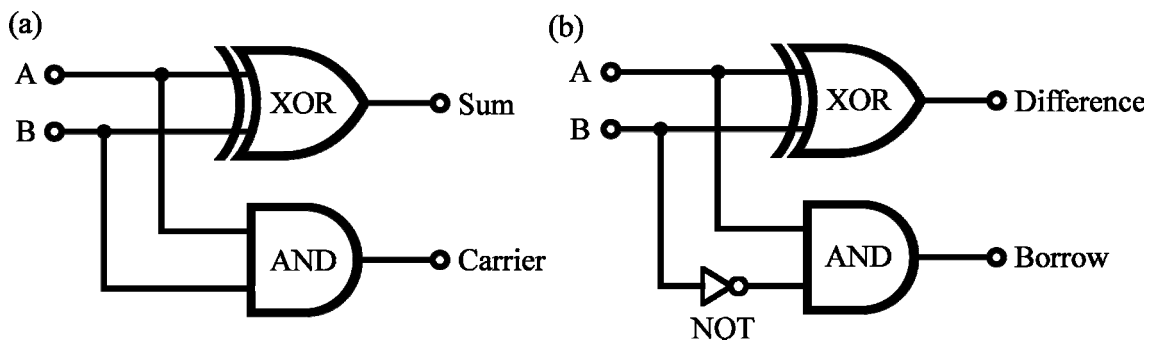


Figure 7.1 Logic diagrams of half-adder and half-subtractor.

Table 7.1 Truth table of half-adder and half-subtractor.

Input signal		Half-adder		Half-subtractor		
A	B	Carry	Sum	Borrow $A - B$	Borrow $B - A$	Difference
0	0	0	0	0	0	0
0	1	0	1	1	0	1
1	0	0	1	0	1	1
1	1	1	0	0	0	0
Logical function		AB AND	$A \oplus B$ XOR	$\overline{A}B$	$A\overline{B}$	$A \oplus B$ XOR

The logic diagrams of half-adder and half-subtractor are shown in Fig. 7.1 and their truth table is listed in Table 7.1. From the logic diagram and truth table, it can be found that there are four logical operations, AND (AB), XOR ($A \oplus B$), $\overline{A}B$ and $A\overline{B}$, in the

half-adder and half-subtractor modules, among which XOR function is a combination of $A\bar{B}$ and $\bar{A}B$ ($A \oplus B = A\bar{B} + \bar{A}B$). The logical operations can be realized by a nonlinear optical device. In the previous researches, all-optical half-addition and half-subtraction schemes were mainly realized by means of SOA and periodically poled lithium niobate (PPLN) waveguide based circuits, thanks to the advantages of SOA and PPLN in the aspects of high nonlinearity, strong compactness and wide wavelength operating window.

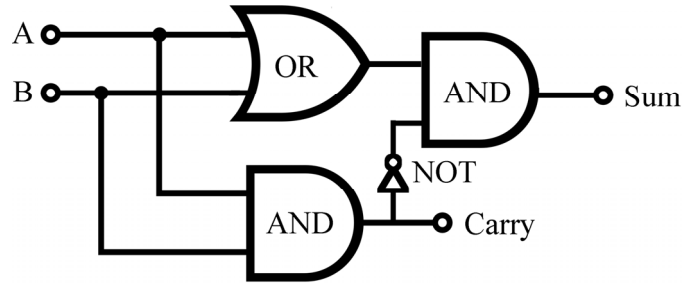


Figure 7.2 Logic diagram of the half-adder in [188].

The initial realization of an all-optical half-adder was presented in [188]. In this scheme, terahertz optical asymmetric demultiplexers (TOAD), which consisted of a nonlinear loop mirror with an SOA, were used as logic gates due to their high switching speed (>40 Gbit/s) [189]. However, it was difficult to achieve XOR logical operation in a single gate. Instead, the approach to obtain XOR logical operation was to logically combine AND and OR logical operations, i.e. $A \oplus B = (A + B)\overline{AB}$. Thus, the scheme was based on an equivalent logical diagram, as shown in Fig. 7.2. OR logic gate was simply realized by a power coupler. Besides, three TOAD switches were used. Two TOADs functioned as two AND logic gates and one was used for wavelength conversion. The operating speed was 1 Gbit/s. The complicated configuration of the TOADs increased the complexity of the half-adder, which was not suitable for compact arithmetic modules.

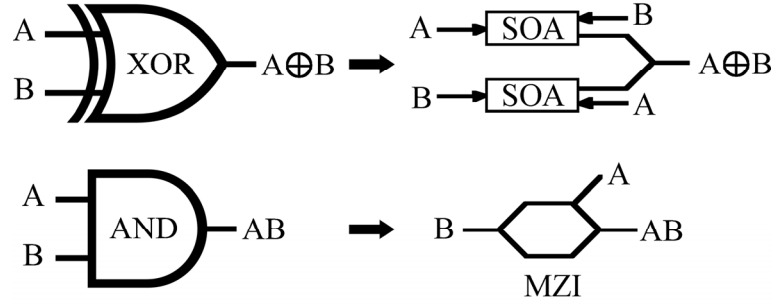


Figure 7.3 Schematic diagram of two SOAs based an XOR logic gate and an MZI and an AND logic gate in [190].

Then, a half-adder was demonstrated at data rate of 10 Gbit/s [190]. This scheme was based on the logic diagram in Fig. 7.1(a). Two SOAs were used to generate Boolean $A \oplus B$ and a Mach-Zehnder interferometric switch was utilized as a XPM wavelength converter to obtain AB . Fig. 7.3 shows the structures of the all-optical XOR and AND logic gates. However, the XPM wavelength conversion in the Mach-Zehnder switch was data pattern dependent, which resulted in the degradation of the signal quality.

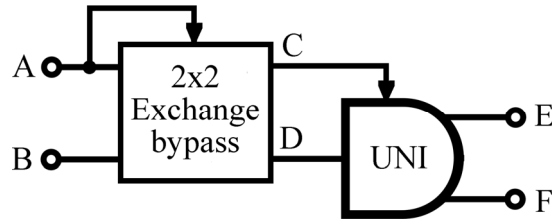


Figure 7.4 Schematic diagram of the half-adder in [191].

Table 7.2 Truth table of the single-rail half-adder.

A	B	C	D	E	F
0	0	0	0	0	0
0	1	0	1	1	0
1	0	0	1	1	0
1	1	1	1	0	1
		AND	OR	Sum	Carry

To achieve resilience to data pattern effects, a single-rail half-adder was proposed [191]. Two cascaded SOA based ultrafast nonlinear interferometers (UNI) were applied for the constitution of a 10 Gbit/s half-adder. The optical schematic and the truth table are shown in Fig. 7.4 and Table 7.2. Compared to the traditional dual-rail half-adder, the single-rail structure had different operating procedure. The input signals A and B were not directly manipulated in the logical operations of XOR and AND. Instead, the input signals were firstly processed by a 2x2 exchange bypass switch. The control signal of the switch was identical to one of the input signals. When the control signal was logic '0', input signals (A and B) passed over to the corresponding output ports (signals C and D). Whenever a control signal was present, the switch operated in the cross state and the input signals appeared switched over at the output ports (signals D and C). As a result, the signals C and D were the outputs of AND and OR logical operations of the signals A and B. Then, the second UNI conducted XOR and AND logical operations of signals C and D, yielding XOR and AND logical operations of initial signals A and B, i.e. sum and carry. Besides data pattern independence, the scheme exhibited very low switching energy (sub-fJ). Nevertheless, it required a precise polarization control for the signal processing in the two UNIs.

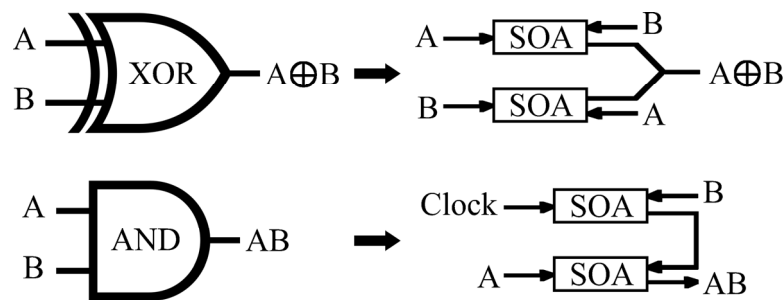


Figure 7.5 Schematic diagram of four SOAs based on XOR and an AND logic gates in [192].

A 10 Gbit/s half-adder was realized by employing XGM in the four SOAs [192]. Two SOAs were employed to form an XOR logic gate and the other two were built as an AND logic gate, as shown in Fig. 7.5. The configuration was straightforward but too

many active devices were used.

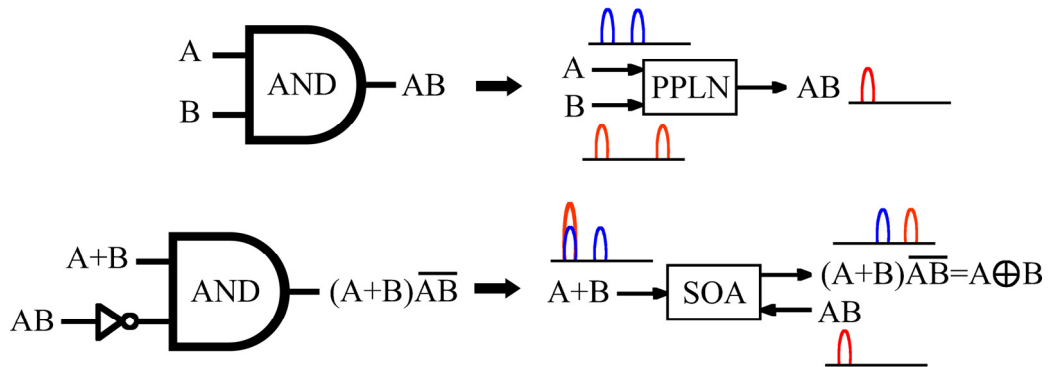


Figure 7.6 Schematic diagram of a PPLN and an SOA based two AND logic gates in [193].

In [193], an all-optical half-adder was demonstrated at the repetition rate of 5 Gbit/s for a simplified structure. This scheme was also based on the logic diagram in Fig. 7.2. Two AND logic gates were realized by an SOA and a PPLN, separately. The carry signal was generated through difference frequency generation (DFG) in the PPLN. Then, the carry signal was injected into the SOA as a pump signal. Whenever the carry as '1', it squelched the gain of the SOA and the corresponding input pulses passing through the SOA were suppressed. Only those pulses, which did not have a corresponding pulse of the carry, emerged at the SOA output. Fig. 7.6 shows that SOA and PPLN function as two AND logic gates.

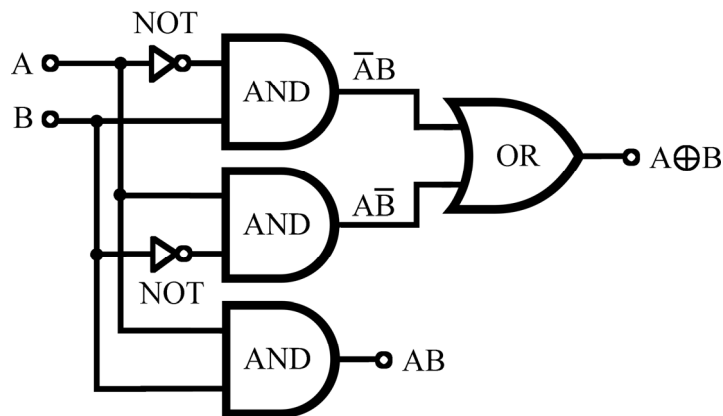


Figure 7.7 Logic diagram of simultaneous half-addition and half-subtraction scheme.

According to the logic diagram in Fig. 7.1 and the truth table in Table 7.1, both half-addition and half-subtraction modules need XOR logic operation of two input signals. If both modules are developed in one device sharing the same XOR logic gate, the scheme is more powerful and efficient. Furthermore, the XOR logic operation can be realized by adding $A\bar{B}$ and $\bar{A}B$ together ($A \oplus B = A\bar{B} + \bar{A}B$), where $A\bar{B}$ or $\bar{A}B$ is borrow in the half-subtraction. It indicates that to realize half-addition and half-subtraction simultaneously, the most straightforward way is to generate $A\bar{B}$, $\bar{A}B$ and AB and then combine $A\bar{B}$ and $\bar{A}B$ together. The logic diagram of simultaneous half-addition and half-subtraction is depicted in Fig. 7.7. The final implementation requires six logic gates: three AND gates, one OR gate and two inverters.

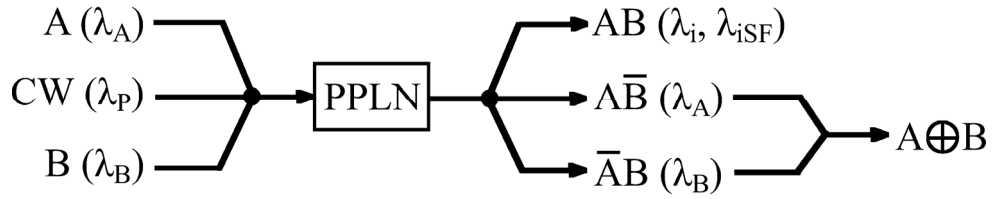


Figure 7.8 Schematic diagram of single-PPLN based half-adder and half-subtractor in [194].

The first simultaneous half-addition and half-subtraction scheme was proposed in [194]. The scheme was based on the cascaded sum (SFG) and DFG using only one PPLN waveguide, as shown in Fig. 7.8. The principle can be briefly explained as follows. Two data signals A and B at λ_A and λ_B together with a CW pump at λ_P are launched into the PPLN waveguide. The SFG interaction converts one photon from signal A and another photon from signal B into one sum-frequency photon, resulting an output AB at λ_{SF} , which is simultaneously transformed into one photon of the pump and the other photon of the new generated idler signal λ_i through the subsequent DFG process. Thus, both signals A and B are depleted during the generation of the sum-frequency and idler signals. If the input signal A is '1', the output of signal B is '0'

in spite of input signal B with any value ('1' or '0'). The output of signal B is equal to '1', only when input signals A and B are '0' and '1' respectively. Therefore, the output at λ_B is $\bar{A}B$. Similarly, the output at λ_A is $A\bar{B}$. In the simulation, a 40 Gbit/s arithmetic operation was achieved. The pity is that this scheme only stays in the numerical analysis.

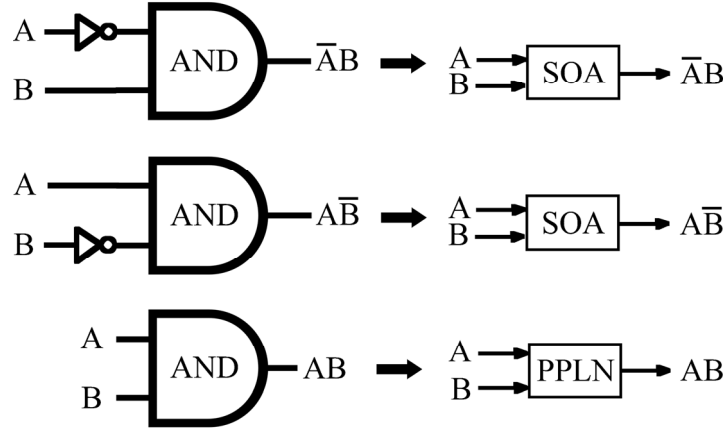


Figure 7.9 Schematic diagram of two SOAs and a PPLN based three AND logic gates in [186].

In [186], a 5 Gbit/s simultaneous half-addition and half-subtraction was experimentally demonstrated. The scheme employed two SOAs and a PPLN waveguide. The two parallel SOAs were used to generate $A\bar{B}$ and $\bar{A}B$ and the PPLN was to perform as an AND logic gate, as shown in Fig. 7.9. A power coupler following the two SOAs was to combine $A\bar{B}$ and $\bar{A}B$ and generated $A \oplus B$.

The optimized design of an all-optical arithmetic operation circuit needs to take into consideration of the number of active devices used, the power consumed, the number of assist light sources needed, the number of functions realized, the operating speed achieved as well as the signal quality obtained.

7.2 Simultaneous half-adder and half-subtractor

In this section, a 10 Gbit/s all-optical simultaneous half-addition and half-subtraction scheme, employing two SOAs and without any assist light source, is

demonstrated.

7.2.1 Operation principle

In the proposed simultaneous half-addition and half-subtraction scheme, two SOAs are employed to perform three AND logical operations. One is to generate $\overline{A}B$ using XGM and the other is to generate $A\overline{B}$ and AB using XGM and FWM, as shown in Fig. 7.10.

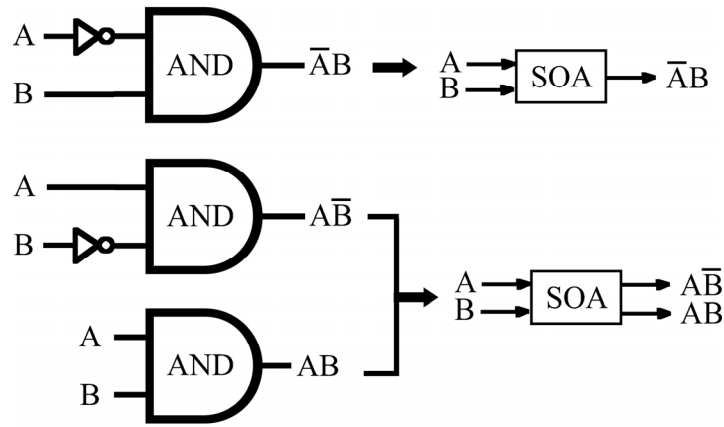


Figure 7.10 Schematic diagram of two SOAs based three AND logic gates.

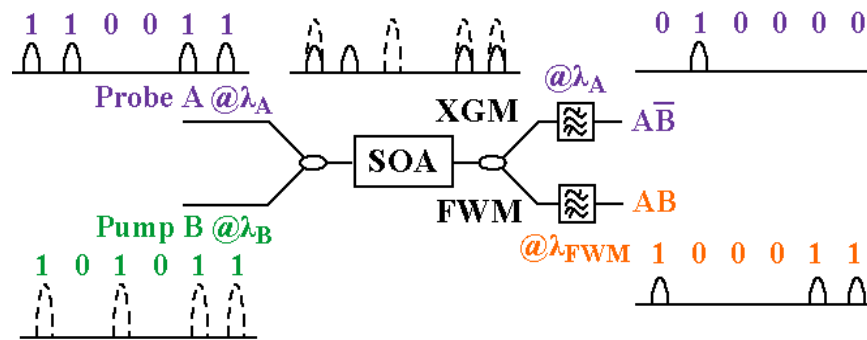


Figure 7.11 The operation principle of the proposed scheme.

The working principle of the SOA is illustrated in Fig. 7.11. Two input signals (A and B) in OOK format are centered at two different wavelengths (λ_A and λ_B). The two signals have different powers. Signal A has lower power, acting as probe, and signal B

has higher power, acting as pump. The optical pulses of the two signals are temporally overlapped to each other and are injected into the SOA synchronously.

The operation is based on XGM and FWM in the SOA. When both data bits of signal A and signal B are logic '1's, the SOA is saturated by the high-intensity pulse of signal B, due to the carrier depletion, and XGM effect occurs. The low-intensity pulse of signal A is suppressed and there is no output at the wavelength of λ_A . In addition, FWM effect occurs with the coexistence of both pulses of signal A and signal B and a new signal is generated at λ_{FWM} ($\lambda_{FWM} = 2\lambda_A - \lambda_B$), which realizes the function of AB . If the data bit of signal A is logic '1' and the data bit of signal B is logic '0', the low-intensity pulse of signal A is amplified and output at the wavelength of λ_A , where the function of \overline{AB} is achieved. With the same setup but reversed roles of the two signals, the function of \overline{AB} can be obtained at the wavelength of λ_B . Finally, the function of $A \oplus B$ can be easily attained through the combination of both \overline{AB} and \overline{AB} by a power coupler.

7.2.2 Experimental demonstration

Figure 7.12 shows the experiment setup of the proposed half-adder and half-subtractor. Two MLLD were used to produce two 2.6 ps (FWHM) Gaussian shaped optical pulse trains at 1547 nm (signal A) and 1553 nm (signal B). The pulse trains were modulated by two IMs with 10 Gbit/s $2^{15}-1$ PRBS data and $\overline{\text{data}}$, separately. In one branch, a 20 m SMF was added after the modulation to mismatch the data pattern between the two branches. Then, the two modulated pulse trains were combined for the amplification.

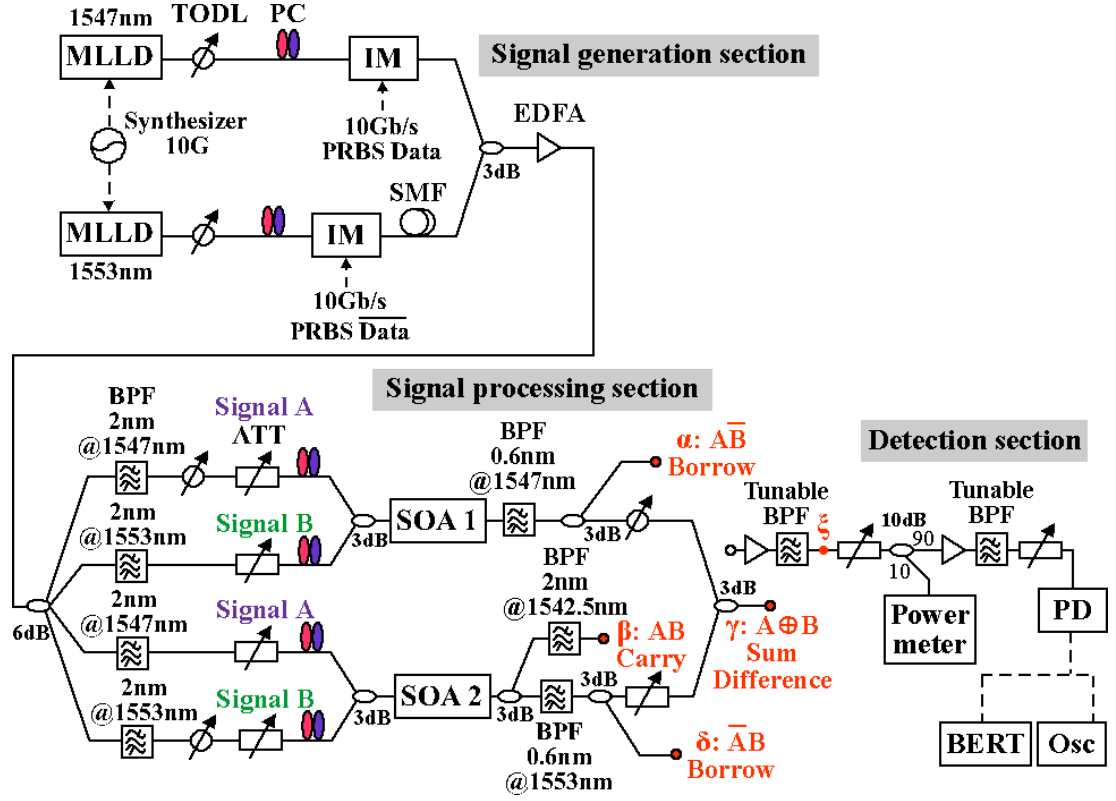


Figure 7.12 The experiment setup of 10 Gbit/s half-adder and half-subtractor.

After that, a 1x4 coupler was used to split the signal into four branches. In these four branches, four 2 nm BPF, two tunable optical delay lines and four attenuators were used to extract the target data, align the time difference and control the powers. The signals in the first two branches were coupled into SOA 1 after optimized polarization control. The average power of signal A was attenuated to -7.52 dBm (peak power of 8.33 dBm), while signal B had the average power of 1.67 dBm (peak power of 17.52 dBm), which was used as a pump signal. XGM, which was insensitive to polarization, occurred with the existence of signal B and the function of \overline{AB} was achieved, which was extracted by a 0.6 nm BPF centered at 1547 nm. The output spectrum before filtering is shown in Fig. 7.13(a).

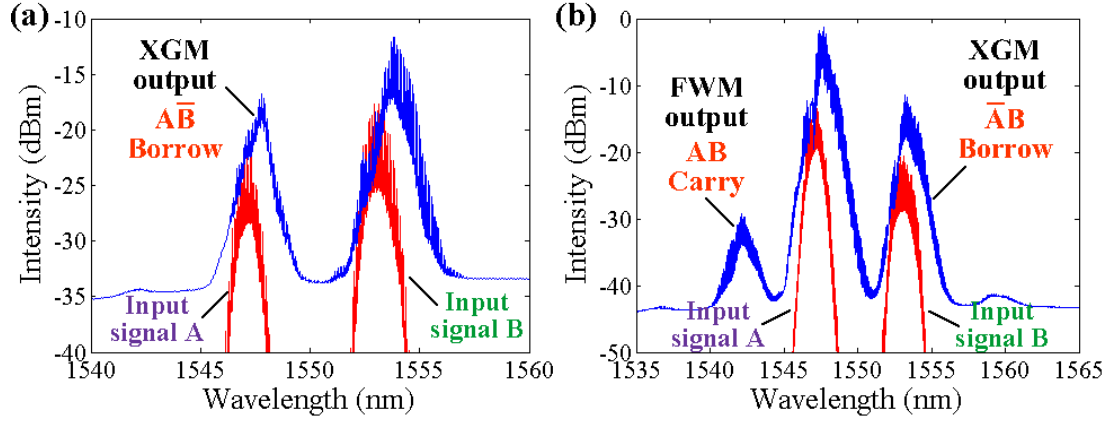


Figure 7.13 (a) and (b) The input and output spectra, measured before and after SOA 1 and SOA 2. (Resolution: 0.01 nm).

The signals in the other two branches were coupled into SOA 2 after the individual polarization control, since the generation of FWM in the SOA was polarization dependent. The average powers of signal A and signal B were adjusted to 4.28 dBm and -5.31 dBm (peak powers of 20.13 dBm and 10.53 dBm), respectively. In this case, signal A was used as a pump signal and the function of \overline{AB} was filtered out by a 0.6 nm BPF at 1553 nm. Besides, a new signal was generated when both input signals were '1', i.e. AB , resulted from the FWM effect in SOA 2. Since the wavelengths of the input signals were red-shifted, due to SPM and XGM effects in the SOA, the signal of AB was extracted at 1542.5 nm by a 2 nm BPF. The output spectra of \overline{AB} and AB before filtering were shown in Fig. 7.13(b). After balancing the power by an optical attenuator and aligning the time by an optical delay line, the signals of \overline{AB} and \overline{AB} were combined by a 3 dB coupler to produce the logical function of $A \oplus B$. The average powers of \overline{AB} , \overline{AB} , AB and $A \oplus B$ at points α , δ , β and γ were -15.93, -14.02, -17.56 and -15.31 dBm, respectively. In the experiment, SOA 1 and SOA 2 were biased at 389 mA and 423 mA and their 10-90% gain recovery time were about 25 ps and 30 ps, respectively. The data rate was limited by SOA 2. To achieve a higher data rate and guarantee a good performance, we appeal to use SOAs with fast gain recovery.

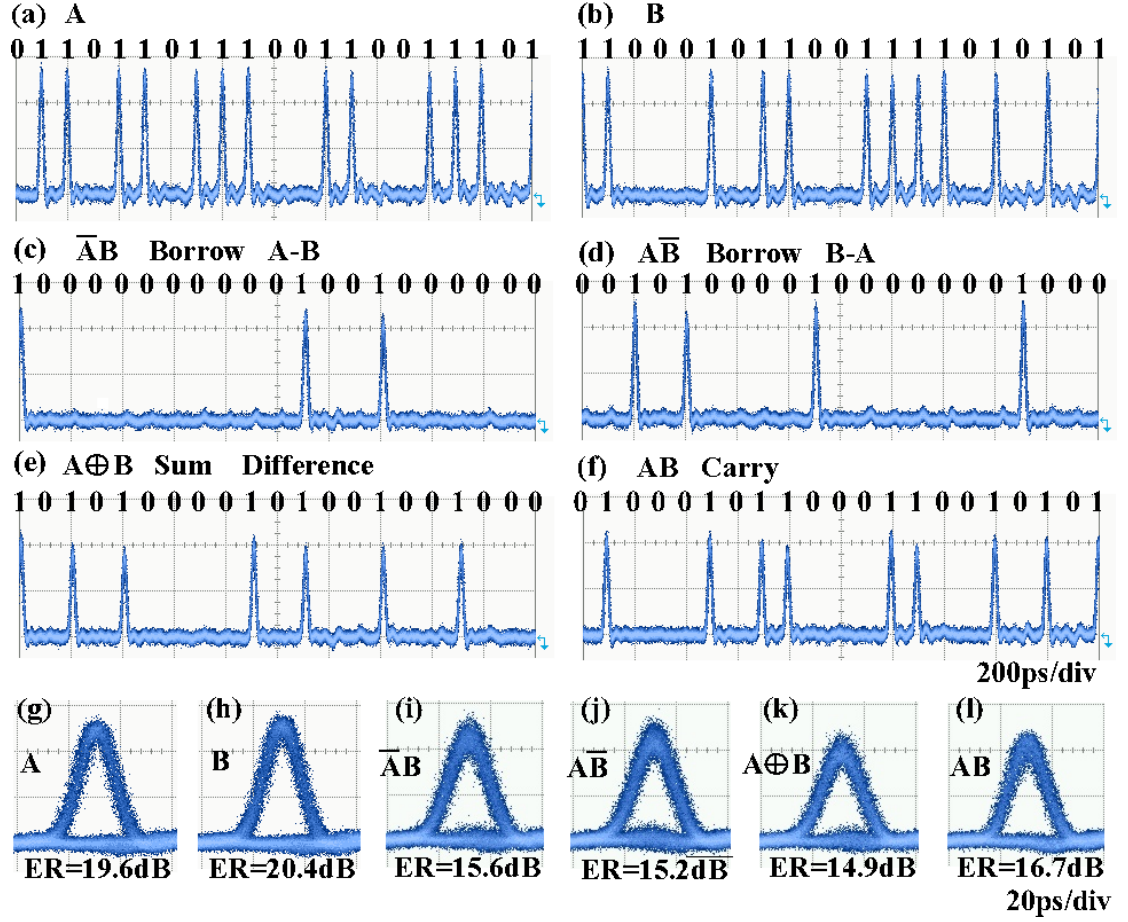


Figure 7.14 Waveforms of (a) and (b) input signals and (c)–(f) output signals. (g)–(l) Corresponding eye diagrams. (Output signals are measured at point ξ).

Figure 7.14 shows waveforms and eye diagrams of the input signals A and B and the output signals of borrows, difference, sum and carry. The output signals were measured at point ξ . The binary data are labelled above the waveforms. In the borrow, there is an output pulse only when the data bit of signal A is logic ‘1’ and the data bit of signal B is logic ‘0’ for the case of $A-B$, and vice versa. The outputs of sum and difference are corresponding to the logic function of $A \oplus B$, where either the data bit of signal A or the data bit of signal B is logic ‘1’. Additionally, the carry is achieved when both input signals A and B are logic ‘1’. Open and clear eye diagrams are obtained for all outputs. Based on the experimental observation, the qualities of the input signals have small influence on the XGM outputs but affect the FWM output significantly. In the experiment, the extinction ratios (ER) of the output signals are all larger than 14 dB.

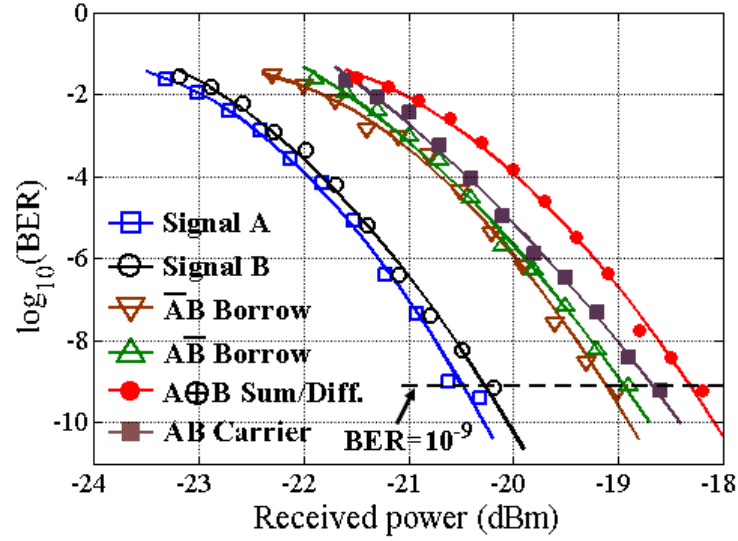


Figure 7.15 BER performances for the input and output signals.

BER performance is depicted in Fig. 7.15. Error-free operations are all achieved. Compared to the original signal A and B, which were measured directly after the intensity modulations, the outputs of borrows (\overline{AB} and \overline{AB}) show about 1.5 dB power penalty at BER of 10^{-9} . The function of $A \oplus B$ for sum and difference exhibits a 2 dB power penalty. In addition, the output of carry has a power penalty of about 1.8 dB.

7.3 Summary

In this chapter, an all-optical half-addition and half-subtraction scheme is demonstrated. The half-addition and half-subtraction of two 10 Gbit/s RZ-OOK signals with the data of pattern length of $2^{15}-1$ are realized simultaneously in the same setup. Only two SOAs are employed and no assist light source is needed. Error-free operations are all achieved. Due to the multi-functions and the use of integrable components, the proposed scheme has the potential to be applied to the future optical systems, such as ALU and encryption/decryption device.

Chapter 8

All-Optical Modulation Format Conversion

With the rapid development of optical communications, optical network structures become miscellaneous to realize high-transmission-capacity, high-spectral-efficiency, high-data-rate and high-energy-efficiency transmissions for the growing demands of future applications, such as high-speed internet, broadcasting video and massive telepresence. These various and sundry optical networks have different layouts, depending on network scaling, transmission rate and capacity, power consumption and communication security [195, 196]. To satisfy the requirements of these optical networks, a variety of modulation formats have been proposed, which have their own unique benefits. For example, since optical signals using non-return-to-zero on-off-keying (NRZ-OOK) modulation format have a good resilience to chromatic dispersion due to narrow spectrum bandwidth and a high tolerance to timing jitter due to flat tops, NRZ-OOK modulation format is very suitable in the high-speed optical time-division multiplexing access (OTDMA) network [197]. Thus, modulation formats with distinct advantages should be selectively employed in the different types of networks. Besides, it is also important to achieve all-optical modulation format conversions in the interconnection of networks to reduce costs of complicated electrical circuits, such as high-speed optical-to-electrical (O/E) and electrical-to-optical (E/O) converters, and simplify the conversion system.

In this chapter, two modulation format conversion schemes are presented. The first one is NRZ-OOK to PSK-Manchester format conversion using an SOA based Mach-Zehnder interferometer (MZI). The second one is return-to-zero-OOK (RZ-OOK) to DQPSK format conversion using a SC based threshold.

8.1 NRZ-OOK to PSK-Manchester format conversion

Many researches have investigated generations and applications of Manchester coding format, which has advantages of simple timing extraction, self-clocking and

simple error detection. In [198], amplitude-shift keying (ASK) Manchester coding format was used with a burst-mode optical packet receiver in a PON system. However, ASK-Manchester coding format is not robust to beat interference noise (BIN). Then, phase-shift keying (PSK) Manchester coding format was proposed for the stronger tolerance to BIN and was suggested to be used in a WDM-PON [199]. Besides, Manchester coding format incorporating duobinary coding was evaluated and it presented an improved chromatic dispersion tolerance by nearly three times compared with ASK-Manchester coding format [200]. The generation of Manchester-duobinary format signal using a directly modulated chirp managed laser was experimentally demonstrated at 10 Gbit/s and the enhanced tolerance to chromatic dispersion was also achieved [201]. Besides generation of Manchester coding format, it is necessary to realize modulation format conversions from/to Manchester coding format to suit the preferences of different networks. In [202], 10 Gbit/s NRZ-OOK to ASK-Manchester modulation format conversion was demonstrated employing nonlinear polarization rotation in a 1 km HNLF.

In this section, we demonstrate all-optical NRZ-OOK to PSK-Manchester modulation format conversion.

8.1.1 Operation principle

The NRZ-OOK to PSK-Manchester modulation format converter functions like an XOR logic gate. A clock signal is ‘1’ in the first half bit duration and ‘0’ in the second half bit duration. The XOR logic gate operates at the double repetition rate of a NRZ-OOK signal. When the NRZ-OOK signal is bit ‘1’, the output within this bit duration is ‘01’, since in the first half bit duration, two inputs to the XOR logic gate are ‘1’s, and in the second half bit duration, two inputs become ‘1’ and ‘0’. When the NRZ-OOK signal is bit ‘0’, the output is ‘10’.

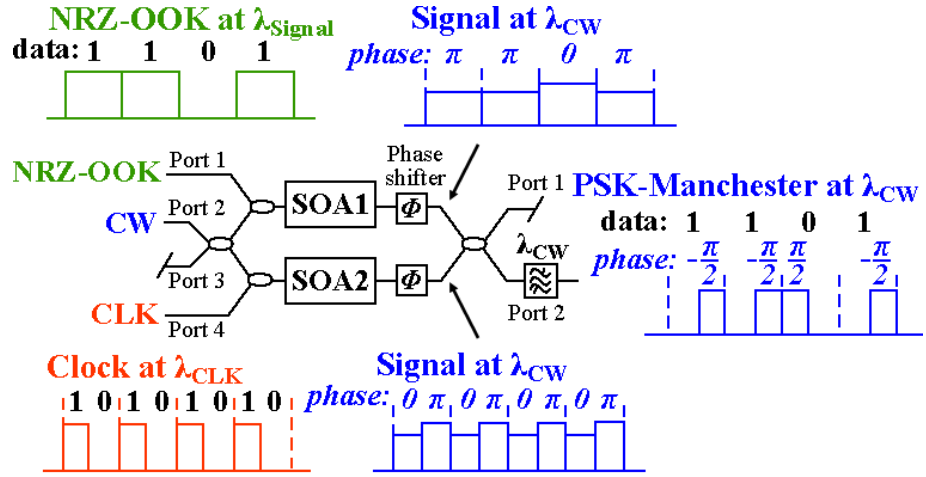


Figure 8.1 Operation principle of NRZ-OOK to PSK-Manchester modulation format conversion.

The function of XOR logic gate is realized by an SOA-MZI, as illustrated in Figure 8.1. A NRZ-OOK signal, a probe light and a clock signal are injected into input ports 1, 2 and 4, respectively. The NRZ-OOK signal and the probe light are coupled into the upper branch. When the NRZ-OOK signal is bit ‘1’, the probe light experiences a phase shift and a gain modulation due to XPM and XGM in the SOA 1. In the SOA 2, the probe light is modulated with the clock signal every half bit. Two phase shifters are used for optimizing in-phase condition, under which the probe light has a constructive interference in the output port 2. It is straightforward to show a mathematical expression of the output optical field as follows.

$$E_{out}(\theta) = \frac{A}{2} j [\exp(-\alpha_1 + j(\theta_1 + \varphi_1)) + \exp(-\alpha_2 + j(\theta_2 + \varphi_2))] \exp(j\omega_c t) \quad (8.1)$$

where A and ω_c is the amplitude and angular frequency of probe light, α_1 and α_2 are the XGM coefficient, θ_1 and θ_2 are the XPM phase shifts, and φ_1 and φ_2 are the phase shifts introduced by the two phase shifters. When gain modulation depths are same in the two SOAs, i.e. $\alpha_1 = \alpha_2$, intensities and phases of the output optical field are listed in Table 1. When the NRZ-OOK signal is bit ‘0’, there is an output only in the first half bit duration and the phase of the output is $\pi/2$. If the NRZ-OOK signal is bit ‘1’, the output is only in the second half bit duration and the phase is $-\pi/2$. The NRZ-OOK signal is converted into a format with binary phase shift and binary pulse position, i.e. PSK-Manchester format.

Table 8.1 Output of probe light with a set of representative parameters.

NRZ-OOK	Clock (half bit)	α_1	α_2	$\theta_1+\phi_1$ (rad)	$\theta_2+\phi_2$ (rad)	Output phase θ (rad)	Output Intensity $ E ^2$
0	0	0	0	0	π	0	0
0	1	0	α_1	0	0	$\pi/2$	$A^2(1+\exp(-\alpha_1))^2/4$
1	0	α_1	0	π	π	$-\pi/2$	$A^2(1+\exp(-\alpha_1))^2/4$
1	1	α_1	α_1	π	0	0	0

8.1.2 Experimental demonstration

Figure 8.2 shows the experimental setup. Three CW light sources at different wavelengths were used. The 1547 nm CW light was modulated with a 2.5 Gbit/s $2^{15}-1$ PRBS data by an IM. The 1553 nm CW light was modulated with a 2.5 GHz sinusoidal clock signal and controlled by a delay line for temporal alignment with the NRZ-OOK signal. The 1550 nm CW light was used as a probe light. The average powers of the probe light, NRZ-OOK and clock signals were 1.1, 0.18 and -0.32 dBm, respectively. An output was obtained from output port 2 and filtered out by a 2 nm BPF centered at 1550 nm. After that, the signal was transmitted to a photodiode for detection through a 50 km transmission.

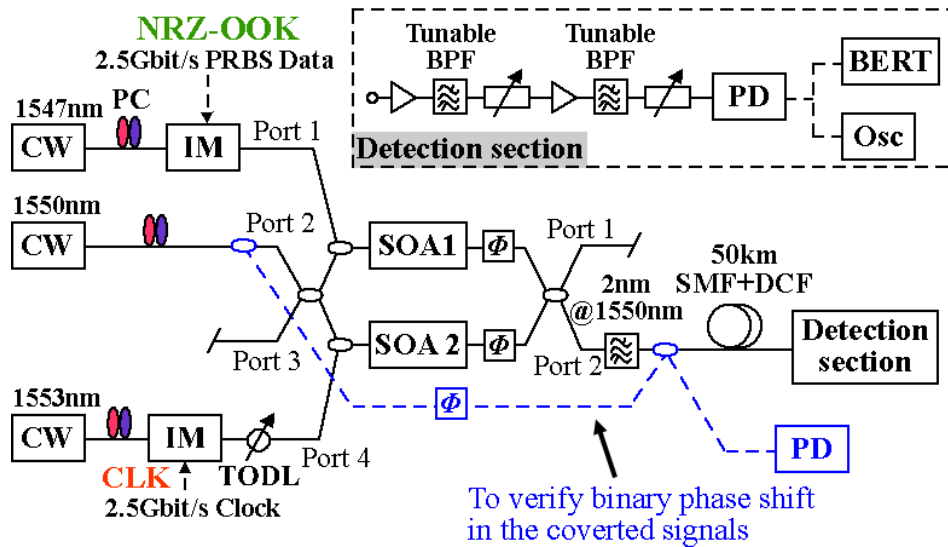


Figure 8.2 Experimental setup of the proposed scheme.

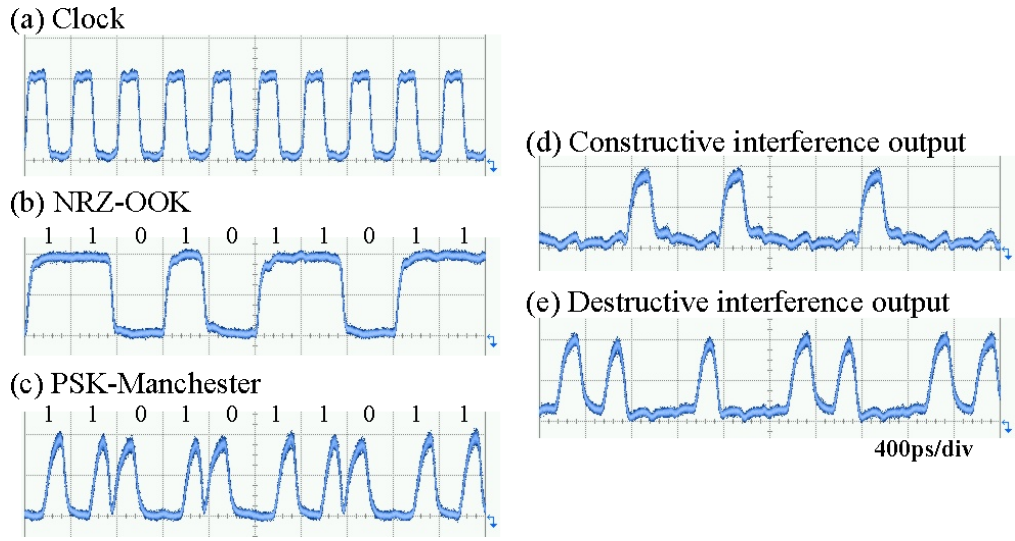


Figure 8.3 Experimental setup of the proposed scheme. (a) and (b) Input clock and NRZ-OOK signals. (c) Converted PSK-Manchester signal. (d) and (e) Interference outputs.

The waveforms of the input and converted PSK-Manchester signals are illustrated in Figs. 8.3(a)-(c). In the PSK-Manchester signal, pulses, representing bit ‘0’, appear in the first half bit duration and pulses for bit ‘1’ are in the second half bit duration, which conforms the theoretical analysis. Besides the characteristic of binary pulse position, binary phase shift of the converted signal is verified by interfering with the original CW light. The signal quality is affected by the speed of the phase recovery of the SOAs. A blue dashed line connected between input and output forms an interferometer as shown in Fig. 8.2. Figs. 8.3(d) and (e) show the outputs of interference conditions. Under the constructive interference condition, pulses for bit ‘0’ are obtained, while pulses for bit ‘1’ appear only under the destructive interference condition. It indicates that there is a π -phase shift between bit ‘0’ and ‘1’, which is consistent with the theoretical analysis as well.

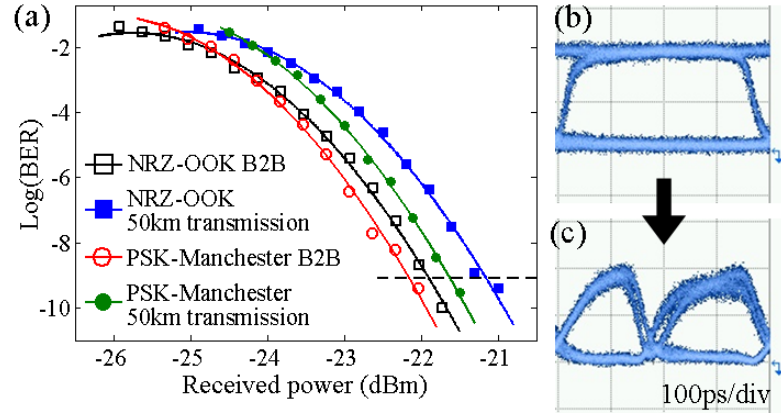


Figure 8.4 (a) Measured BER performances. (b) and (c) Eye diagrams of NRZ-OOK and PSK-Manchester signals without transmission at $\text{BER}=10^{-9}$.

Bit error rate (BER) for both NRZ-OOK and converted PSK-Manchester signals are depicted in Fig. 8.4(a). The converted PSK-Manchester signal has better performances and when $\text{BER}=10^{-9}$ there is 0.3 and 0.6 dB improvement in the back-to-back situation and after 50 km transmission. The signal quality of PSK-Manchester signal is degraded, which can be observed from eye diagrams as shown in Figs. 8.4(b) and (c). Since the signal with Manchester format consumes only half energy compared to that with NRZ-OOK format, this enhanced energy efficiency makes up the degradation.

8.1.3 Improvement in operating speed

It is worth noting that the data rate is limited by the slow phase recovery of the SOAs ($>120\text{ps}$). In the calculation, we investigate the conversion at the data rate of 40 Gbit/s using two SOAs with 10-90% phase recovery of about 40 ps, as shown in Fig. 8.5(a). Figs. 8.5(b) and (c) illustrate clear eye diagrams of the NRZ-OOK and converted PSK-Manchester signals. Error-free ($\text{BER}<10^{-9}$) conversion in the calculation indicates that it has the potential to improve the operating speed if SOAs with fast phase recovery are employed in the proposed scheme.

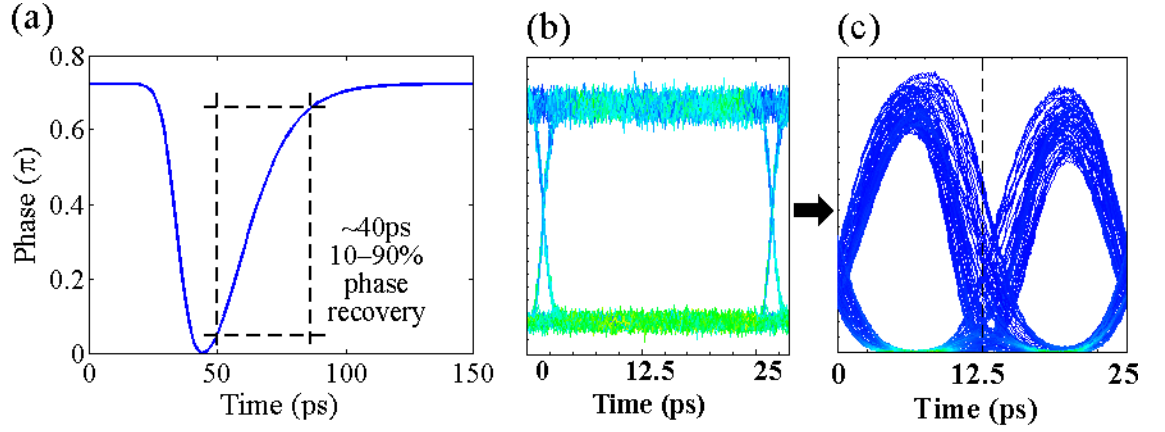


Figure 8.5 (a) Calculated phase recovery of the SOAs. (b) and (c) Eye diagrams of calculated 40 Gbit/s NRZ-OOK and converted PSK-Manchester signals.

8.2 DQPSK to OOK format conversion

In the past few years, various kinds of all-optical modulation format conversion schemes have been investigated, among which considerable schemes focused on the conversions from OOK to PSK modulations. These schemes were based on the different types of techniques, e.g. from NRZ-OOK to RZ-BPSK, QPSK and 8PSK using optical HNLF [203], from NRZ-OOK to RZ-BPSK and RZ-QPSK using SOA-MZI wavelength converter [204], and NRZ to BPSK and QPSK using cascaded MRRs [205].

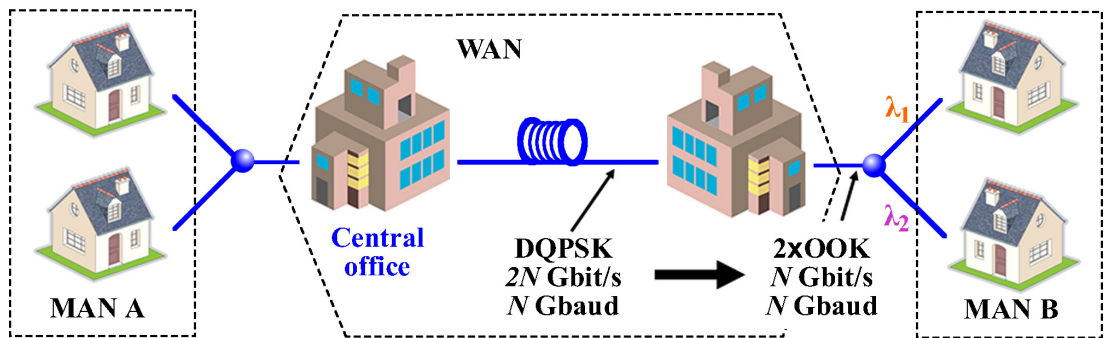


Figure 8.6 Proposed scheme in the network structure.

It is also important to achieve the modulation format conversion from PSK to OOK in order to realize the transparent downlink connection between two different networks. For instance, wide area network (WAN) supports long-distance and high-capacity communication, in which PSK modulation formats, such as DPSK, DQPSK, BPSK and

QPSK, are preferably adopted due to their high transmission capacity, high spectral efficiency and high tolerance in the long-haul transmission, as shown in Fig. 8.6. On the other hand, in the metropolitan area network (MAN), OOK modulation format is suitable because of its simplicity in system structure and high cost-effectiveness. In [206], NRZ-DPSK to RZ-OOK format conversion scheme using optical delay line interferometer and SOA was demonstrated. Furthermore, it is necessary to perform advanced PSK (DQPSK, QPSK and 8PSK etc.) to OOK modulation format conversion to satisfy different preference of a variety of networks.

In this section, we demonstrate all-optical RZ-DQPSK to RZ-OOK modulation format conversion.

8.2.1 Operation principle

The operation principle of the proposed scheme is shown in the Fig. 8.7. The DQPSK data is firstly demodulated by an MZI, which is incorporated with a delay of one-symbol duration and $\pm\pi/4$ phase shifts. After the demodulation, two sequences of pulses are generated in the OOK format, at points α and β in Fig. 8.7. However, the extinction ratio (ER) is only 7.66 dB, due to the incomplete in-phase and out-of-phase interference, and these signals with low ER are not suitable for further transmission. To suppress the unwanted low-intensity pulses and separate two channels (I and Q channels of DQPSK data), a supercontinuum (SC) based optical thresholding scheme is employed, which consists of an erbium doped fiber amplifier (EDFA), a DFF and a BPF [116]. The pulses with high intensity can generate SC in the DFF, while the unwanted low-intensity pulses are unable to produce SC. The followed filters centered at two different wavelengths allow the SC generated by the high-intensity pulses pass through and make a separation of the two channels. The signals after the thresholder are shown at points γ and δ in Fig. 8.7. The high-intensity pulses remain while the low-intensity pulses are removed.

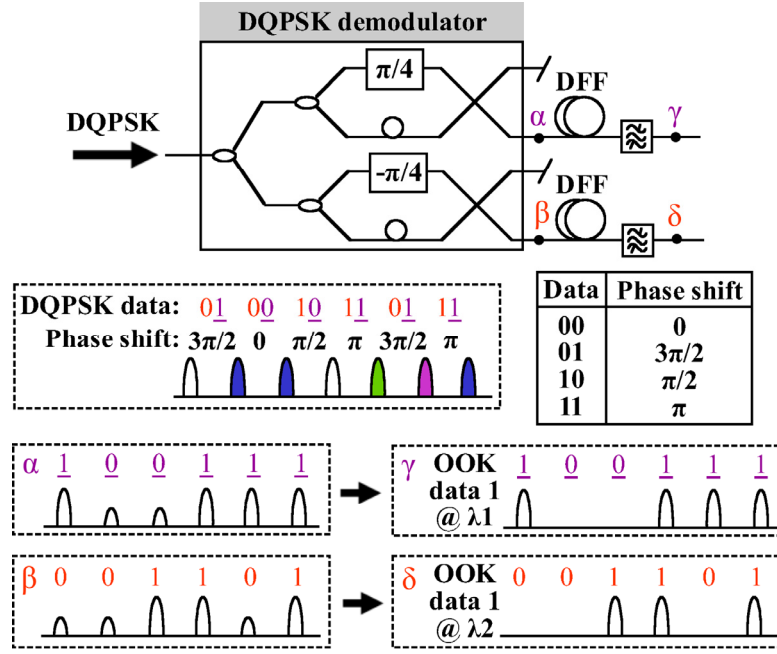


Figure 8.7 The operation principle of DQPSK to OOK modulation format conversion.

8.2.2 Experimental demonstration

The characteristics of a SC based optical thresholder are analyzed by using filters with different bandwidth ($\Delta\lambda=1, 2$ and 5 nm). The two filters were centered at 1545 nm and 1555 nm, as shown in Fig. 8.8(a). A 2.4 ps (FWHM) optical pulse train at the repetition rate of 10 GHz was used. The measured power transfer function is depicted in Fig. 8.8(b). The measured operation power of the thresholder was about 25 mW in average, which meant the peak power is about 1 W (or 2.5 pJ/bit). When the filter was centered in the 1555 nm, it could achieve higher output power, since the SC was generated more efficiently on the right side of 1550 nm, due to the characteristics of the DFF. The optical thresholder using wide bandwidth filter had high power conversion efficiency (the ratio between output power and input power). To avoid the increase of the pulse intensity fluctuation, a flat power transfer function is desirable. Thus, the flatness of the transfer function was studied by measuring the range of the input power when the output power changes 10% of the maximum output power, as labeled in Fig. 8.8(b). The optical thresholder using narrow bandwidth filter had flatter transfer function. Therefore, there was a tradeoff in choosing BPF in the optical thresholder. The narrow bandwidth filter was preferred in terms of the flatness of the transfer function

and the spectrum utilization efficiency, while the optical thresholder using wide bandwidth filter had higher power conversion efficiency.

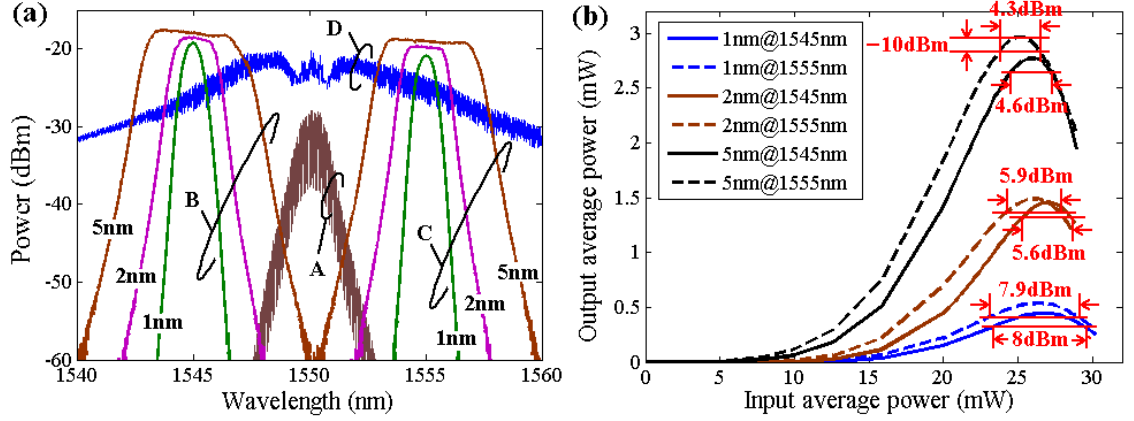


Figure 8.8 (a) Measured spectra of A: demodulated DQPSK signal, B: filter response at 1545 nm, C: filter response at 1555nm and D: generated SC. (b) Power transfer function of the SC based optical thresholder.

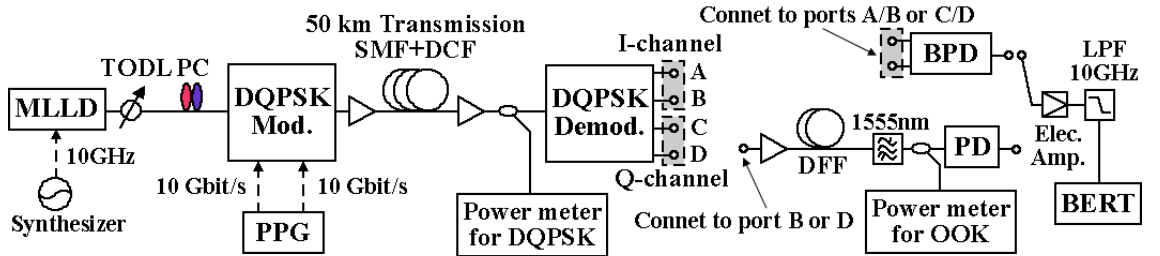


Figure 8.9 Experiment setup of DQPSK to OOK modulation format conversion.

Figure 8.9 shows the experimental setup for the demonstration of the DQPSK to OOK modulation conversion. A sequence of 2.4 ps Gaussian shaped pulses at the repetition rate of 10 GHz were modulated with two pre-coded 10 Gbit/s data sequences with the length of 2^9-1 . After that, the modulated pulse train was transmitted to the receiving side. In the transmission line, chromatic dispersion in the optical signals was compensated by a dispersion compensation fiber and the total transmission distance was 50 km. The pulses were broadened to 2.9 ps after the transmission due to the residual chromatic dispersion.

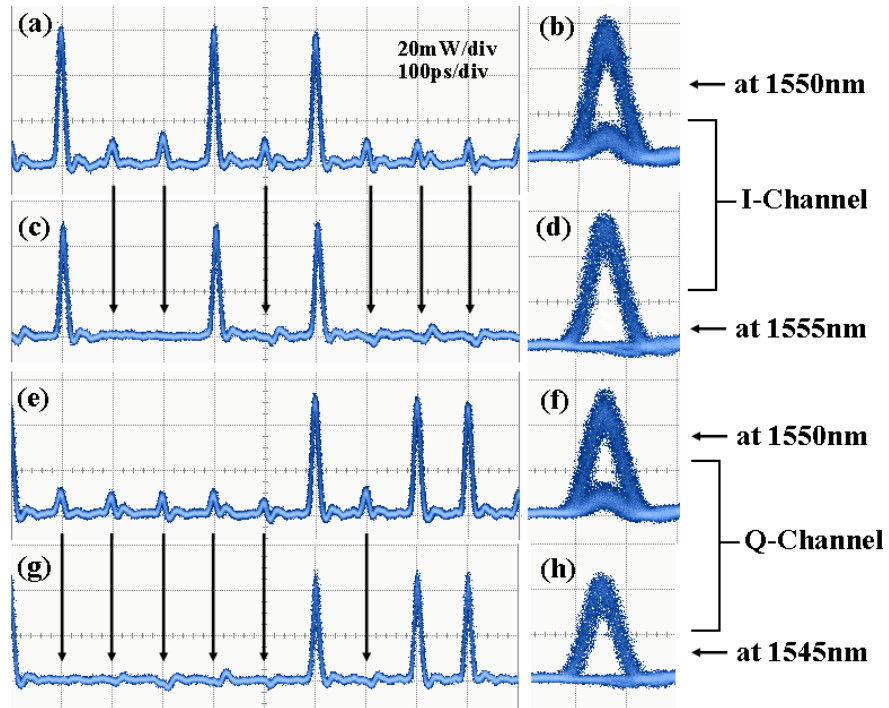


Figure 8.10 (a) Demodulated signals and (b) eye diagram for I-channel. (c) Signals after optical threshold and (d) eye diagram for I-channel. (e) Demodulated signals and (f) eye diagram for Q-channel. (g) Signals after optical threshold and (h) eye diagram for Q-channel.

In the receiving side, a DQPSK demodulator was used to recover the data of I- and Q-channels. The demodulated signals were in OOK format, as illustrated in Figs. 8.10(a) and (e). Nonetheless, the existence of the unwanted low-intensity pulses degraded the eye diagrams (Figs. 8.10(b) and (f)). Then, the demodulated signals were processed by the optical thresholder. The input power was well controlled to the optimum point. The signals after the optical thresholder using 2 nm filter are shown in Fig. 8.10(c) and (g). The low-intensity pulses were efficiently suppressed and clear open eyes could be observed. Besides, the data on the I- and Q-channels were allocated into 1555 nm and 1545nm, separately.

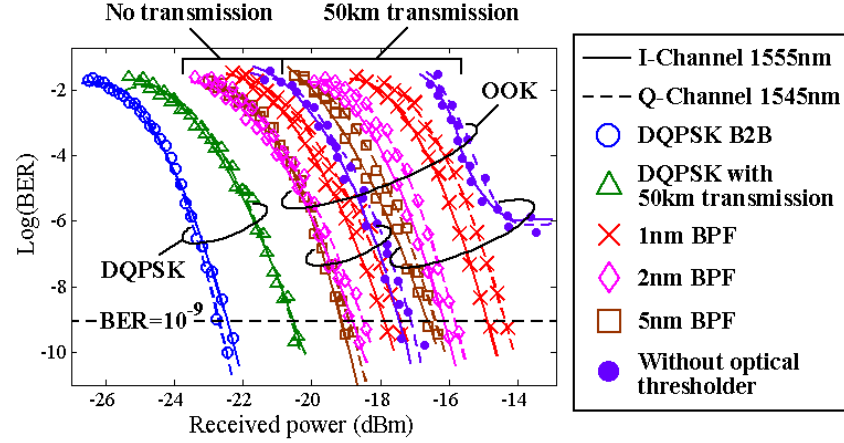


Figure 8.11 BER performances for DQPSK and OOK data using different filters with and without 50 km transmission.

The measured BER performances are depicted in Fig. 8.11. In the case of back-to-back transmission, the modulation format conversions from DQPSK to OOK have power penalties of about 3.2 to 4.3 dB at BER of 10^{-9} . After 50 km transmission, in the case without the assistance of the optical thresholding scheme, an error-floor is observed (the most right two curves in Fig. 8.11). When the optical thresholding scheme is employed, error free transmissions ($\text{BER} < 10^{-9}$) are achieved for all cases. The power penalties become 3.7 to 5 dB. In these power penalties, the amount of 3 dB is attributed to the discrepancy in the receiving sensitivity of the direct detection and the balanced detection. In addition, it has better BER performances when the filters of 2 nm and 5 nm bandwidth are used, since the higher power conversion can be achieved in the optical thresholder, compared to that when the filter of 1 nm bandwidth is used.

8.3 Summary

In this chapter, two all-optical modulation format conversion schemes are demonstrated.

The first modulation format scheme is a NRZ-OOK to PSK-Manchester modulation format conversion. The operation principle is theoretically analyzed. The scheme uses an SOA-MZI based XOR logic gate. In the experiment, an error-free conversion from NRZ-OOK to PSK-Manchester format is achieved and the characteristics of binary

pulse position and binary phase shift of the converted PSK-Manchester signal are investigated. According to the calculation results, the proposed scheme has the potential to operate at a high data rate. This SOA-MZI based modulation format conversion scheme allows photonic integration.

In the second scheme, an all-optical RZ-DQPSK to RZ-OOK modulation format conversion is demonstrated. The scheme uses the SC based optical thresholder, which is widely used to suppress the MAI noises in the OCDMA systems. The optical thresholder is investigated by changing the BPFs with different bandwidths. Thanks to the regeneration of high-intensity pulses and the suppression of low-intensity pulses, error-free transmissions ($\text{BER} < 10^{-9}$) are achieved for the converted OOK signals after a 50 km DQPSK transmission at 10 Gbaud. Meanwhile, the modulation format conversion allocates the data on the two DQPSK channels into two different wavelengths, realizing the wavelength division.

The modulation format conversion schemes cater to the preferences of the networks employing different modulation formats and multiplexing techniques and they are promising techniques for future diversified networks.

Chapter 9

Conclusions and Future Research Directions

We have developed OCDMA systems in the various aspects including coding devices, security vulnerability, advanced modulation format as well as PON structure. In addition, inspired by the techniques of nonlinear signal processing in the OCDMA systems, we have conducted some researches on signal processing in the field of waveform generation, arithmetic operation and modulation format conversion. In this chapter, we summarize our researches in detail and then propose some possible research opportunities based on our present work.

9.1 Conclusion

Our researches presented in this thesis are summarized as follows.

- FBG based optical coding device

Optical coding devices are key components in the OCDMA systems, which are able to provide security for transmitted signals. However, this plausible fact needs a deep discussion. We have found that the code information can be extracted from the signals encoded by the conventional $0/\pi$ -SSFBG en/decoders, which results in serious security vulnerability. To improve the security, we have proposed $\pm\pi/2$ -SSFBG en/decoders, which can conceal code information in the encoded signal very well, especially using short pulse (pulse width $<$ chip duration) as an input signal. Besides the improvement in security, we have investigated the hybrid use of $0/\pi$ -SSFBG and $\pm\pi/2$ -SSFBG en/decoders in the OCDMA systems with both intensity and phase modulations. $\pm\pi/2$ -SSFBG en/decoders can be simultaneously employed with $0/\pi$ -SSFBG en/decoders in the same system due to their good correlation properties. This capability makes it possible to reutilize the same codes from the limited code space.

We have also designed another FBG based coding device, which can realize code recognition and chromatic dispersion compensation at the same time, using layer-peeling synthesis method. We have calculated the tolerance of the phase shifts in

the fabrication. According to our simulation results, DC-FBG decoders can correctly decode the signals after a dispersive transmission. Compared to conventional decoding devices, DC-FBG decoders present a better performance in the OCDMA systems without dispersion compensation, especially at a high data rate.

- Eavesdropping schemes

We have demonstrated two eavesdropping schemes to attack single-user DPSK-OCDMA and CSK-OCDMA systems. The one-bit delay interference detection can figure out the difference in phase between two adjacent encoded signals, while the differential detection can distinguish the discrepancy in waveform between any two encoded signals. Eavesdroppers can easily intercept confidential data from encoded signals in the DPSK-OCDMA and CSK-OCDMA systems using the one-bit delay interference detection and attack CSK-OCDMA system using the differential detection without any knowledge of code. It reveals the vulnerability of both OCDMA systems and requires strengthening the secure optical transmission systems to avoid eavesdropping from the both unauthorized detections.

- Orthogonal DPSK/CSK modulation

To increase transmission capacity and improve security, we have presented an orthogonal modulation format based on DPSK and CSK. In the experiment, we have achieved a 2 bit/symbol 10 Gsymbol/s error-free transmission using the orthogonal modulation. We have also evaluated the security of this new system. The security vulnerability of CSK data still occurs if the system is attacked by using the differential detection, while fortunately DSPK data is well submerged in the encoded signals against the attack from the one-bit delay interference detection. Furthermore, the system allows the use of advanced multi-level modulation in both DPSK and CSK modulation formats and it implies that the transmission capacity can be further improved.

- Source-free-ONU OCDMA-PON

We have proposed a full-asynchronous gigabit-symmetric OCDMA-PON, in which

a remodulation scheme is used, allowing ONUs source-free, and a self-clocked time gate is employed to extract the decoded signals. The duplex transmission is based on DPSK downstream and remodulated OOK upstream transmissions. In the upstream transmission, no light sources are needed because the upstream data is directly modulated to the same optical carrier of the downstream. The reuse of optical carrier reduces the cost of each ONU and simplifies the system structure. Another remarkable technique used in this OCDMA-PON is a self-clocked time gate. The clock signal can be regenerated from the decoded signals by using SC based thresholder. Then, the target decoded signal can be extracted by using FWM based time gating. With the help of this self-clocked time gate, we can improve the signal quality of decoded signal and realize asynchronization of the duplex transmission. In the experimental demonstration, we have achieved 4-user 10 Gbit/s/user OCDMA-PON over 50 km transmission.

- Various waveform generation

We have proposed and demonstrated a waveform generation scheme which only employs a single-stage DD-MZM and a first-order dispersive element. Besides, we have built a theoretical model, derived mathematical expressions of the scheme and developed an algorithm to predict the waveform generation. According to the theoretical analysis, we have found that there are four variables contributing to the waveform generation. By using different combinations of these four variables, various waveforms have been theoretically and experimentally generated at 10 GHz including short pulse, trapezoidal, triangular and sawtooth waveforms and doublet pulse. Furthermore, we have investigated the characteristics of these waveforms by calculating the gradient and the instantaneous frequency. Last but not least, the scheme has two beneficial features, tunable repetition rate and adjustable optical center wavelength.

- All-optical half-adder and half-subtractor

We have demonstrated an all-optical simultaneous half-addition and half-subtraction scheme. In this scheme, only two SOAs are used and no additional assist light source is needed. We have successfully achieve the error-free half-addition

and half-subtraction operations of two 10 Gbit/s RZ-OOK signals with the pattern length of $2^{15}-1$. No data pattern dependence phenomenon is observed. Due to the use of SOAs, this multi-functional arithmetic scheme has the potential to be developed into an integrated device.

- Modulation format conversion

To satisfy the diversity of the optical communication network, we have carried out the researches on two modulation format conversion schemes.

We firstly demonstrated NRZ-OOK to PSK-Manchester modulation format conversion. NRZ-OOK format has good resilience to chromatic dispersion and high tolerance to timing jitter, while PSK-Manchester format presents a strong tolerance to beat interference noises. Thus, these two kinds of modulation formats are suitable to different situations. For example, NRZ-OOK format is widely used in the high-speed OTDM network, and PSK-Manchester format is suggested to be used in the WDM network. We have accomplished a 2.5 Gbit/s NRZ-OOK to PSK-Manchester format conversion using an SOA-MZI based XOR gate. The theoretical analysis indicates that the operating speed can be further improved by employing SOAs with fast phase recovery.

We have also conducted the research on RZ-DQPSK to RZ-OOK modulation format conversion. These two kinds of modulation formats are suitable for the network with different capacity. RZ-DQPSK is suitable for a WAN which supports high capacity and long distance communication, while RZ-OOK is adequate to a MAN where low cost and simple system are preferred by end users. In the demonstration, we have used a SC based threshold, which is often used in the OCDMA systems, to realize a 10 Gbaud conversion after a 50 km RZ-DQPSK transmission to RZ-OOK format. The RZ-OOK signals after the conversion are allocated at two wavelengths.

9.2 Future Research Directions

Some research opportunities are summarized as below.

- In Chapter 2, two novel FBG based coding devices are proposed. The hybrid use of

$0/\pi$ -SSFBG and $\pm\pi/2$ -SSFBG en/decoders enables an efficient use of available codes. Besides, DC-FBG en/decoders have been realized in the later research work [122]. A well-designed network is preferred to efficiently utilize these coding devices to optimize the use of their unique properties.

- It is a challenge but also very necessary to build an optical communication system with high security. An in-depth consideration should be made before the design of secure optical communication systems. It should be kept in mind that the systems should be immune to all kinds of eavesdropping methods including energy detection, one-bit delay interference detection as well as differential detection.
- To be competitive with other candidates in the access networks, OCDMA systems should significantly improve the transmission capacity. A lot of aspects should be improved. For example, some advanced modulation formats such as QAM techniques can be used in the systems. Besides, the developments of optical codes with good aperiodic correlation properties as well as coding devices with the ability to handle long codes are essential.
- As a photonic-assisted waveform generator, the proposed various waveform generation scheme has significant latent capacity. Firstly, it has potential to generate more useful waveforms. According to our analysis, there are only four variables affecting the waveform generation, but these four variables can be changed not only in magnitude but also in formats, which results in more combinations. For example, in our work, the RF signal is a sinusoidal wave. If the RF signal is changed to other formats, triangular or square wave, the scheme may produce more varieties of waveforms. Secondly, the repetition rate can be further increased. At a conservative estimation based on the characteristics of the device, the scheme can generate waveforms at a repetition rate up to 18 GHz. Thirdly, the scheme may simultaneously generate waveforms at two different wavelengths if two CW lights at two wavelengths are used as input signals.

List of References

- [1] P. Prucnal, M. Santoro, F. Ting, "Spread spectrum fiber-optic local area network using optical processing," *J. Lightwave Technology*, vol. 4, pp. 547–554, 1986.
- [2] A. M. Weiner, J. P. Heritage, J. A. Salehi, "Encoding and decoding of femtosecond pulses," *Optics Letters*, vol. 13, pp. 300–302, 1988.
- [3] J.A. Salehi, "Code division multiple-access techniques in optical fiber networks. I. Fundamental principles," *J. Lightwave Technol.*, vol. 37, pp. 824–833, Aug. 1989.
- [4] J. A. Salehi, A. M. Weiner, and J. P. Heritage, "Coherent ultrashort light pulse code-division multiple access communication systems," *J. Lightwave Technol.*, vol. 8, pp. 478–491, Mar. 1990.
- [5] D. Zaccarin and M. Kavehrad, "An optical CDMA system based on spectral encoding of LED," *Photon. Technol. Lett.*, vol. 5, pp. 479–482, Apr. 1993.
- [6] R. A. Griffin, D. D. Sampson, and D. A. Jackson, "Coherence coding for photonic code-division multiple access networks," *J. Lightwave Technol.*, vol. 13, pp. 1826–1837, Sep. 1995.
- [7] H. P. Sardesai, C.-C. Chang, and A. M. Weiner, "A femtosecond code division multiple access communication system test-bed," *J. Lightwave Technol.*, vol. 16, pp. 1953–1964, Nov. 1998.
- [8] H. Tsuda, H. Takenouchi, T. Ishii T, K. Okamoto, T. Goh, K. Sato, A. Hirano, T. Kurokawa, C. Amano, "Spectral encoding and decoding of 10 Gbit/s femtosecond pulses using high resolution arrayed-waveguide grating," *Electron. Lett.*, vol. 35, pp. 1186–1188, July 1999.
- [9] N. Wada, K. Kitayama, "A 10 Gb/s optical code division multiplexing using 8-chip optical bipolar code and coherent detection," *J. Lightwave Technol.*, vol. 17, pp. 1758–1765, Oct. 1999.
- [10] A. Grunnet-Jepsen , A. E. Johnson, E. S. Maniloff, T. W. Mossberg, M. J. Munroe, J. N. Sweetser, "Fibre Bragg grating based spectral encoder/decoder for lightwave CDMA," *Electron. Lett.*, vol. 35, pp. 1096–1097, June 1999.
- [11] M. R. Mokhtar, M. Ibsen, P. C. Teh, D. J. Richardson, "Reconfigurable multilevel phase-shift keying encoder-decoder for all-optical networks," *Photon. Technol. Lett.*, vol. 15, pp. 431–433, Mar 2003.
- [12] P. C. Teh, M. Ibsen, D. J. Richardson, "Demonstration of a full-duplex bidirectional spectrally interleaved OCDMA/DWDM system," *Photon. Technol. Lett.*, vol. 15, pp. 482–484, Mar 2003.
- [13] P. C. Teh, M. Ibsen, J. H. Lee, P. Petropoulos, D. J. Richardson, "Demonstration of a four-channel WDM/OCDMA system using 255-chip 320-Gchip/s quarternary phase coding gratings," *Photon. Technol. Lett.*, vol. 14, pp. 227–229,

Feb. 2002.

- [14] V. Baby, I. Glesk, R. J. Runser, R. Fischer, Y. K. Huang, C. S. Bres, W. C. Kwong, T. H. Curtis, and P. R. Prucnal, "Experimental demonstration and scalability analysis of a four-node 102-Gchip/s fast frequency-hopping time-spreading optical CDMA network," *Photon. Technol. Lett.*, vol. 17, no. 1, pp. 253–255, Jan. 2005.
- [15] H. Sotobayashi, W. Chujo, and K. Kitayama, "Highly spectral-efficient optical code-division multiplexing transmission system," *J. Select. Topics Quantum Electron.*, vol. 10, pp. 250–258, Mar./Apr. 2004.
- [16] K. Kitayama, X. Wang and N. Wada, "OCDMA over WDM PON -A Solution Path to Gigabit-Symmetric FTTH-", *IEEE J. Lightwave Technol.* Vol.24, pp.1654-1662, Apr. 2006.
- [17] X. Wang, N. Wada, G. Cincotti, T. Miyazaki, and K. Kitayama, "Demonstration of Over 128Gbps-capacity (12-user x 10.71 Gbps/user), Truly Asynchronous OCDMA Using FEC and AWG-based Multi-port Optical Encoder/decoders", *Photonic Technol. Lett.*, vol. 18, pp.1603–1605, Aug. 2006.
- [18] X. Wang and N. Wada, "Experimental demonstration of OCDMA traffic over optical packet switching network with hybrid PLC and SSFBG en/decoders", *J. Lightwave Technol.*, vol. 24, pp.3012–3020, Aug. 2006.
- [19] W. Cong, C. Yang, R. P. Scott, V. J. Hernandez, N. K. Fontaine, B. H. Kolner, J. P. Heritage, and S. J. B. Yoo, "Demonstration of 160- and 320-Gb/s SPECTS O-CDMA network testbeds," *Photon. Technol. Lett.*, vol. 18, pp. 1567–1569, Aug. 2006.
- [20] X. Wang, N. Wada, T. Miyazaki, G. Cincotti and K. Kitayama, "Field Trial of Asynchronous WDM/DPSK-OCDMA Using Hybrid E/D," *J. Lightwave Technol.*, vol. 25, pp. 207–215, Jan. 2007.
- [21] V. J. Hernandez, W. Cong, J. Hu, C. Yang, N. K. Fontaine, R. P. Scott, B. H. Kolner, J. P. Heritage, and S. J. B. Yoo, "A 320-Gb/s capacity (32-user \times 10 Gb/s) SPECTS O-CDMA network testbed with enhanced spectral efficiency through forward error correction," *J. Lightwave Technol.*, vol. 25, pp. 79–86, Jan. 2007.
- [22] C. Yang, R. P. Scott, D. J. Geisler, N. K. Fontaine, J. P. Heritage, and S. J. B. Yoo, "Four-State Data Encoding for Enhanced Security Against Upstream Eavesdropping in SPECTS O-CDMA," *J. Lightwave Technology*, vol. 29, no. 1, pp. 62–68, Jan. 2011.
- [23] Z. Gao, B. Dai, X. Wang, N. Kataoka and N. Wada, "Transparent transmission of secure time domain spectral phase encoding DPSK-OCDM signal over DWDM network," *J. Optical Communications and Networking*, vol. 3, no. 5, pp. 404–410, 2011.
- [24] T. Kodama, N. Kataoka, N. Wada, G. Cincotti, X. Wang, and K. Kitayama, "4096-Ary OCDM/OCDMA System Using Multidimensional PSK Codes

Generated by a Single Multiport En/Decoder,” J. Lightwave Technol., vol. 29, pp. 3372–3380, 2011.

- [25] X. Wang, K. Matsushima, A. Nishiki, N. Wada, and K. Kitayama, “High reflectivity superstructured FBG for coherent optical code generation and recognition,” Opt. Express, vol. 12, pp. 5457–5468, 2004.
- [26] K. Kitayama, “Novel spatial spread spectrum based fiber optic CDMA networks for image transmission,” J. Select. Areas Commun., vol. 12, pp. 762–772, 1994.
- [27] K. Kitayama, M. Nakamura, Y. Igasaki and K. Kaneda, “Image fiber-optic two-dimensional parallel links based upon optical space-CDMA: Experiment,” J. Lightwave Technol., vol. 15, pp. 201–212, 1997.
- [28] G. C. Yang and W. C. Kwong, “Performance comparison of the multiwavelength CDMA and WDMA+CDMA for fiber-optic networks,” Trans. Commun., vol. 45, pp. 1426–1434, 1997.
- [29] K. Yu and N. Park, “Design of new family of two-dimensional wavelength-time spreading codes for optical code division multiple access networks,” Electron. Lett., vol. 35, pp. 830–831, 1999.
- [30] N. Wada, H. Sotobayashi and K. Kitayama, “2.5Gbit/s time-spread/wavelength-hop optical code division multiplexing using fibre Bragg grating with supercontinuum light source,” Electron. Lett., vol. 36, pp. 815–817, 2000.
- [31] Z. Gao, B. Dai, X. Wang, N. Kataoka and N. Wada, “2D Time Domain Spectral Phase Encoding/Wavelength hopping coherent DPSK-OCDMA system Using Fiber Bragg Gratings and Phase Modulator,” Asia Communications and Photonics Conference and Exhibition (ACP '10), Shanghai, China, Dec. 2010, Paper FO7.
- [32] J. G. Zhang and G. Pichi, “Tunable prime-code encoder/decoder for all-optical CDMA applications,” Electron. Lett., vol. 29, pp. 1211–1212, 1993.
- [33] D. D. Sampson, R. A. Griffin and D. A. Jackson, “Photonic CDMA by coherent matched filtering using time-addressed coding in optical ladder networks,” J. Lightwave Technol., vol. 12, pp. 502–511, 1994.
- [34] J. G. Zhang, L. K. Chan, W. C. Kwong, K. W. Cheung and A. B. Sharma, “Experiments on high-speed all-optical code-division multiplexing systems using all-serial encoders and decoders for 2^n prime code,” J. Select. Topics Quantum Electron., vol. 5, pp. 368–375, 1999.
- [35] A. M. Weiner, “Femtosecond pulse shaping using spatial light modulators,” Rev. Sci. Instrum., vol. 71, pp. 1929–1960, 2000.
- [36] V. J. Hernandez, Y. Du, W. Cong, R. P. Scott, K. Li, J. P. Heritage, Z. Ding, B. H. Kolner, and S. J. Ben Yoo, “Spectral Phase-Encoded Time-Spreading (SPECTS) Optical Code-Division Multiple Access for Terabit Optical Access Networks”, J.

Lightwave Technol., vol. 22, pp. 2671–2679, 2004.

- [37] J. -F. Huang, D. -Z. Hsu, “Fiber-Grating-Based Optical CDMA Spectral Coding with Nearly Orthogonal M-Sequence Codes,” *Photon. Tech. Lett.*, vol. 12, pp. 1252–1254, 2000.
- [38] Z. Wei, H. M. H. Shalaby, H. Ghafouri-Shiraz, “Modified Quadratic Congruence Codes for Fiber Bragg-Grating-Based Spectral-Amplitude-Coding Optical CDMA Systems,” *J. Lightw. Technol.*, vol. 19, pp. 1274–1281, 2001.
- [39] L. R. Chen, P. W. E. Smith, and C. Martijn de Sterke, “Wavelength-encoding/temporal-spreading optical code division multiple-access system with in-fiber chirped moiré gratings,” *Appl. Opt.*, vol. 38, pp. 4500–4508, 1999.
- [40] L. R. Chen, and P. W. E. Smith, “Demonstration of Incoherent Wavelength-Encoding/Time-Spreading Optical CDMA Using Chirped Moiré Gratings,” *Photon. Technol. Lett.*, vol. 12, pp. 1281–1283, 2000.
- [41] I. Fsaifes, A. Millaud, S. Cordette, C. Lepers, M. Douay, and C. Ware, "Spectral Phase OCDMA Encoder/Decoder Using Travelling Interference Fringe Photo-Writing Technique," in *Proc. Asia Communications and Photonics Conference and Exhibition (ACP '09)*, Shanghai, China, 2009, paper TuY3.
- [42] A. Grunnet-Jepsen, A. E. Johnson, E. S. Maniloff, T. W. Mossberg, M. J. Munroe, and J. N. Sweetser, “Demonstration of All-Fiber Sparse Lightwave CDMA Based on Temporal Phase Encoding,” *Photon. Technol. Lett.*, vol. 11, pp. 1283–1285, 1999.
- [43] H. P. Sardesai, C. C. Chang, and A. M. Weiner, “A Femtosecond Code-Division Multiple-Access Communication System Test Bed,” *J. Lightw. Technol.*, vol. 16, pp. 1953–1964, 1998.
- [44] X. Fang, D. -N. Wang, S. Li, “Fiber Bragg grating for spectral phase optical code-division multiple-access encoding and decoding,” *J. Opt. Soc. Am. B.*, vol. 20, pp. 1603–1610, 2003.
- [45] P. C. Teh, P. Petropoulos, M. Ibsen, and D. J. Richardson, “A comparative study of the performance of seven- and 63-chip optical code-division multiple-access encoders and decoders based on superstructured fiber Bragg gratings,” *J. Lightw. Technol.*, vol. 19, pp. 1352–1365, 2001.
- [46] X. Wang, K. Matsushima, K. Kitayama, A. Nishiki, N. Wada, and F. Kubota, “High-performance optical code generation and recognition by use of a 511-chip, 640-Gchip/s phase-shifted superstructured fiber Bragg grating,” *Opt. Lett.*, vol. 30, pp. 355–357, 2005.
- [47] Y. Dai, X. Chen, Y. Zhang, J. Sun, and S. Xie, “Phase-error-free, 1023-chip OCDMA en/de-coders based on reconstruction equivalent chirp technology and error-correction method,” in *Proc. Opt. Fiber Commun. Conf. (OFC 06)*, paper JWA28, Anaheim, USA, 2006.

- [48] B. Dai and X. Wang, "Security Improvement Using $\pm\pi/2$ -Phase-Shifted SSFBG En/Decoder in Time-Spreading OCDMA", *Photon. Technol. Lett.*, vol. 22, no. 12, pp. 881–883, Jun. 2010.
- [49] B. Dai, Z. Gao, X. Wang, N. Kataoka and N. Wada, "Performance Comparison of $0/\pi$ - and $\pm\pi/2$ -Phase-Shifted Superstructured Fiber Bragg Grating En/decoder," *Opt. Express*, vol. 19, no. 13, pp. 12248–12260, Jun. 2011.
- [50] H. Tsuda, H. Takenouchi, T. Ishii, K. Okamoto, T. Goh, K. Sato, A. Hirano, T. Kurokawa, and C. Amano, "Spectral encoding and decoding of 10 Gbit/s femtosecond pulses using high resolution arrayed-waveguide grating," *Electron. Lett.*, vol. 35, pp. 1186–1188, 1999.
- [51] R. G. Broeke, J. Cao, N. K. Fontaine, C. Ji, N. Chubun, F. Olsson, S. Lourdudoss, B. H. Kolner, J. P. Heritage, and S. J. B. Yoo, "Phase characterization of an InP based optical-CDMA encoder using frequency resolved optical gating (FROG)," in *Proc. 18th Annu. Meeting IEEE Lasers Electro-Opt. Soc. (LEOS 05)*, pp. 140–141, 2005.
- [52] S. Yegnanarayanan, A. S. Bhushan, and B. Jalali, "Fast Wavelength-Hopping Time-Spreading Encoding/Decoding for Optical CDMA," *Opt. Lett.*, vol. 12, pp. 573–575, 2000.
- [53] K. Yu, J. Shin, and N. Park, "Wavelength-Time Spreading Optical CDMA System Using Wavelength Multiplexers and Mirrored Fiber Delay Lines," *Photon. Technol. Lett.*, vol. 12, pp. 1278–1280, 2000.
- [54] G. Cincotti, N. Wada, and K. Kitayama, "Characterization of a full encoder/decoder in the AWG configuration for code-based photonic routers — part I: modeling and design," *J. Lightw. Technol.*, vol. 24, pp. 103–112, 2006.
- [55] N. Wada, G. Cincotti, S. Yoshima, N. Kataoka, and K. Kitayama, "Characterization of a Full Encoder/Decoder in the AWG Configuration for Code-Based Photonic Routers — Part II: Experiments and Applications," *J. Lightw. Technol.*, vol. 24, pp. 113–121, 2006.
- [56] G. Cincotti, G. Manzacca, X. Wang, T. Miyazaki, N. Wada, and K. Kitayama, "Reconfigurable Multiport Optical Encoder/Decoder With Enhanced Auto-Correlation," *Photon. Technol. Lett.*, vol. 20, pp. 168–170, 2008.
- [57] A. Agarwal, P. Toliver, R. Menendez, S. Etemad, J. Jackel, J. Young, T. Banwell, B. E. Little, S. T. Chu, W. Chen, W. Chen, J. Hryniewicz, F. Johnson, D. Gill, O. King, R. Davidson, K. Donovan and P. J. Delfyett, "Fully Programmable Ring-Resonator-Based Integrated Photonic Circuit for Phase Coherent Applications," *J. Lightw. Technol.*, vol. 24, pp. 77–87, 2006.
- [58] X. Wang, and Z. Gao, "Novel Reconfigurable Two-Dimensional Coherent Optical En/Decoder Based on Coupled Micro-Ring Reflector", *Photon. Technol. Lett.*, vol. 23, pp. 591–593, 2011.
- [59] K. O. Hill, Y. Fujii, D. C. Johnson, and B. S. Kawasaki, "Photo-sensitivity in

- optical fiber waveguides: application to reflection filter,” *Appl. Phys. Lett.*, vol. 32, pp. 647–649, 1978.
- [60] B. S. Kawasaki, K. O. Hill, D. C. Johnson, and Y. Fujii, “Narrow-band Bragg reflectors in optical fibers,” *Opt. Lett.*, vol. 3, pp. 66–68, 1978.
 - [61] K. O. Hill and G. Meltz, “Fiber Bragg grating technology fundamentals and overview,” *J. Lightw. Techn.*, vol. 15, pp. 1263–1276, 1997.
 - [62] T. Erdogan, “Fiber grating spectra,” *J. Lightw. Techn.*, vol. 15, pp. 1277–1294, 1997.
 - [63] K. O. Hill, “Aperiodic distributed-parameter waveguides for integrated optics,” *Appl. Opt.*, vol. 13, pp. 1853–1856, 1974.
 - [64] K. O. Hill, S. Thériault, B. Malo, F. Bilodeau, T. Kitagawa, D. C. Johnson, J. Albert, K. Takiguchi, T. Kataoka, and K. Hagimoto, “Chirped in-fiber Bragg grating dispersion compensators: linearization of the dispersion characteristic and demonstration of dispersion compensation in a 100km, 10Gbit/s optical fiber link,” *Electron. Lett.*, vol. 30, pp. 1755–1756, 1994.
 - [65] J. A. R. Williams, I. Bennion, K. Sugden, and N. J. Doran, “Fiber dispersion compensation using a chirped in-fibre Bragg grating,” *Electron. Lett.*, vol. 30, pp. 985–987, 1994.
 - [66] K. O. Hill, F. Bilodeau, B. Malo, T. Kitagawa, S. Thériault, D. C. Johnson, J. Albert, and K. Takiguchi, “Chirped in-fiber Bragg grating for compensation of optical-fiber dispersion,” *Opt. Lett.*, vol. 19, pp. 1314–1316, 1994.
 - [67] R. Kashyap, R. Wyatt, and P. F. McKee, “Wavelength flattened saturated erbium amplifier using multiple side-tap Bragg gratings,” *Electron. Lett.*, vol. 29, pp. 1025–1026, 1993.
 - [68] J. Capmany, D. Pastor, and J. Marti, “EDFA gain equalizer employing linearly chirped apodized fiber gratings,” *Microw. and Opt. Technol. Lett.*, vol. 12, pp. 158–160, 1996.
 - [69] C. R. Giles, T. Erdogan, and V. Mizrahi, “Simultaneous wavelength stabilization of 980-nm pump lasers,” *Photon. Technol. Lett.*, vol. 6, pp. 907–909, 1994.
 - [70] K. Hogari, Y. Miyajima, S. Furukawa, N. Tomita, K. Tomiyama, and M. Ohashi, “Wideband and highly reflective step-chirped fiber grating filter embedded in an optical fiber connector,” *Electron. Lett.*, vol. 32, pp. 1230–1232, 1996.
 - [71] G. A. Ball and W. W. Morey, “Efficient integrated Nd^{3+} fiber laser,” *Photon. Technol. Lett.*, vol. 3, pp. 1077–1078, 1991.
 - [72] G. A. Ball and W. H. Glenn, “Design of a single-mode linear-cavity erbium fiber laser utilizing Bragg reflectors,” *J. Lightw. Technol.*, vol. 10, pp. 1338–1343, 1992.
 - [73] G. A. Ball, W. W. Morey, and W. H. Glenn, “Standing-wave monomode erbium

- fiber laser,” *Photon. Technol. Lett.*, vol. 3, pp. 613–615, 1991.
- [74] M. Sejka, P. Varming, J. Hubner, and M. Kristensen, “Distributed feedback Er^{3+} -doped fiber laser,” *Electron. Lett.*, vol. 31, pp. 1445–1446, 1995.
 - [75] G. A. Ball and W. W. Morey, “Compression-tuned single-frequency Bragg fiber laser,” *Opt. Lett.*, vol. 19, pp. 1979–1981, 1994.
 - [76] A. Galvanauskas, P. A. Krug, and D. Harter, “Nanosecond-to-picosecond pulse compression with fiber gratings in a compact fiber-based on pulse width control with chirped fiber Bragg gratings,” *Opt. Lett.*, vol. 20, pp. 172–174, 1995.
 - [77] A. D. Kersey, “A review of recent developments in fiber optic sensor technology,” *Opt. Fiber Technol.*, vol. 2, pp. 291–317, 1996.
 - [78] G. Meltz, “Overview of fiber grating-based sensors,” in *Proc. SPIE, Distributed and Multiplexed Sensor VI*, SPIE-2838, pp. 2–23, 1996.
 - [79] A. D. Kersey, M. A. Davis, T. A. Berkoff, D. G. Bellemore, K. P. Koo, and R. T. Jones, “Progress toward the development of practical fiber Bragg grating instrumentation systems,” in *Proc. SPIE, Fiber Optic and Laser Sensors XIV*, vol. SPIE-2839, pp. 40–64, 1996.
 - [80] W. W. Morey, G. Meltz, and J. M. Weiss, “Evaluation of a fiber Bragg grating hydrostatic pressure sensor,” in *Proc. 8th Opt. Fiber Sensor Conf.* paper PD4, 1992.
 - [81] R. Feced, M. N. Zervas, and M. A. Muriel, “An efficient inverse scattering algorithm for the design of nonuniform fiber Bragg gratings,” *J. Quant. Electron.*, vol. 35, pp. 1105–1115, 1999.
 - [82] J. Skaar, L. Wang, and T. Erdogan, “On the synthesis of fiber Bragg gratings by layer peeling,” *J. Quant. Electron.*, vol. 37, pp. 165–173, 2001.
 - [83] B. Glance, J. M. Wiesenfeld, U. Koren, A. H. Gnauck, H. M. Presby, and A. Jourdan, “High performance optical wavelength shifter,” *Electron. Lett.*, vol. 28, pp. 1714–1715, 1992.
 - [84] T. Durhuus, R. J. S. Pedersen, B. Mikkelsen, K. E. Stubkjaer, M. Oberg, and S. Nilson, “Optical wavelength conversion over 18 nm at 2.5 Gb/s by DBR laser,” *Photon. Technol. Lett.*, vol. 5, no. 1, pp. 86–88, 1993.
 - [85] C. Joergensen, T. Durhuus, C. Braagaard, B. Mikkelsen, and K. E. Stubkjaer, “4 Gb/s optical wavelength conversion using semiconductor optical amplifiers,” *Photon. Technol. Lett.*, vol. 5, no. 6, pp. 657–660, 1993.
 - [86] R. Schnabel, W. Pieper, M. Ehrhardt, M. Eiselt, and H. G. Weber, “Wavelength conversion and switching of high speed data signals using semiconductor laser amplifiers,” *Electron. Lett.*, vol. 29, pp. 2047–2048, 1993.
 - [87] T. Durhuus, C. Joergensen, B. Mikkelsen, R. J. S. Pedersen, and K. E. Stubkjaer, “All optical wavelength conversion by SOAs in a Mach–Zehnder

- configuration,” *Photon. Technol. Lett.*, vol. 6, no. 1, pp. 53–55, 1994.
- [88] A. E. Willner and W. Shieh, “Optimal spectral and power parameters for all-optical wavelength shifting: Single stage, fan-out, and cascability,” *J. Lightw. Technol.*, vol. 13, no. 5, pp. 771–781, 1995.
 - [89] T. Durhuus, B. Mikkelsen, C. Joergensen, S. L. Danielsen, and K. E. Stubkjaer, “All-optical wavelength conversion by semiconductor optical amplifiers,” *J. Lightw. Technol.*, vol. 14, no. 6, pp. 942–954, 1996.
 - [90] M. Asghari, I. H. White, and R. V. Panty, “Wavelength conversion using semiconductor optical amplifiers,” *J. Lightw. Technol.*, vol. 15, no. 7, pp. 1181–1190, 1997.
 - [91] A. Matsumoto, K. Nishimura, K. Utaka, and M. Usami, “Operational design on high-speed semiconductor optical amplifier with assist light for application to wavelength converters using cross-phase modulation,” *J. Quan. Electron.*, vol. 42, no. 3, 2006.
 - [92] G. Contestabile, M. Presi, R. Proietti, E. Ciaramella, “Optical Reshaping of 40-Gb/s NRZ and RZ Signals Without Wavelength Conversion,” *Photon. Technol. Lett.*, vol. 20, pp. 1133–1135, 2008.
 - [93] G. Contestabile, R. Proietti, M. Presi, S. Gupta, E. Ciaramella, “All-optical 40 Gbits/s packet regeneration by means of cross-gain compression in a semiconductor optical amplifier,” *Opt. Lett.*, vol. 33, pp. 1470–1472, 2008.
 - [94] G. Contestabile, A. Maruta, S. Sekiguchi, K. Morito, M. Sugawara, and K. Kitayama “Regenerative Amplification by using Self Phase Modulation in a Quantum Dot SOA,” *Photon. Technol. Lett.*, vol. 22, pp. 492–494, 2010.
 - [95] M. Shin, P. S. Devgan, V. S. Grigoryan, and P. Kumar, “SNR Improvement of DPSK Signals in a Semiconductor Optical Regenerative Amplifier,” *Photon. Technol. Lett.*, vol. 18, no. 1, pp. 49–51, 2006.
 - [96] V. S. Grigoryan, M. Shin, P. Devgan, J. Lasri, and P. Kumar, “SOA-Based Regenerative Amplification of Phase-Noise-Degraded DPSK Signals: Dynamic Analysis and Demonstration,” *J. Lightw. Technol.*, vol. 24, no. 1, pp. 135–142, 2006.
 - [97] X. Huang, Z. Zhang, C. Qin, Y. Yu, and X. Zhang, “Optimized Quantum-Well Semiconductor Optical Amplifier for RZ-DPSK Signal Regeneration,” *J. Quant. Electron.*, vol. 47, no. 6, pp. 819–826, 2011.
 - [98] R.P. Webb, R.J. Manning, G.D. Maxwell and A.J. Poustie, “40 Gbit/s all-optical XOR gate based on hybrid-integrated Mach-Zehnder interferometer,” *Electron. Lett.*, vol. 39, no. 1, pp. 79–81, 2003.
 - [99] H. Sun, Q. Wang, H. Dong and N. K. Dutta, “XOR performance of a quantum dot semiconductor optical amplifier based Mach-Zehnder interferometer,” *Opt. Express*, vol. 13, no. 6, pp. 1892–1899, 2005.

- [100] H. Sun, Q. Wang, H. Dong, Z. Chen, N. K. Dutta, J. Jaques, and A. B. Piccirilli, "All-Optical Logic XOR Gate at 80 Gb/s Using SOA-MZI-DI," *J. Quant. Electron.*, vol. 42, no. 8, pp. 747–751, 2006.
- [101] I. Kang, M. Rasras, L. Buhl, M. Dinu, S. Cabot, M. Cappuzzo, L. T. Gomez, Y. F. Chen, S. S. Patel, N. Dutta, A. Piccirilli, J. Jaques, and C. R. Giles, "All-optical XOR and XNOR operations at 86.4 Gb/s using a pair of semiconductor optical amplifier Mach-Zehnder interferometers," *Opt. Express*, vol. 17, no. 21, pp. 19062–19066, 2009.
- [102] J. Xu, X. Zhang, Y. Zhang, J. Dong, D. Liu, and D. Huang, "Reconfigurable All-Optical Logic Gates for Multi-Input Differential Phase-Shift Keying Signals: Design and Experiments," *J. Lightw. Technol.*, vol. 27, no. 23, pp. 5268–5275, 2009.
- [103] Y. Aikawa, S. Shimizu, and H. Uenohara, "Demonstration of All-Optical Divider Circuit Using SOA-MZI-Type XOR Gate and Feedback Loop for Forward Error Detection," *J. Lightw. Technol.*, vol. 29, no. 15, pp. 2259–2266, 2011.
- [104] N. K. Dutta, Q. Wang, "Semiconductor optical amplifiers," World Scientific Pub., 2006.
- [105] G. P. Agrawal, "Fiber-Optic Communication Systems", John Wiley & Sons Inc., 1997.
- [106] G. P. Agrawal and N. A. Olsson, "Self phase modulation and spectral broadening of optical pulses in semiconductor laser amplifiers," *J. Quantum Electron.*, vol. 25, no. 11, pp. 2297–2306, 1989.
- [107] P. P. Baveja, D. N. Maywar, A. M. Kaplan, and G. P. Agrawal, "Self-Phase Modulation in Semiconductor Optical Amplifiers: Impact of Amplified Spontaneous Emission," *J. Quant. Electron.*, vol. 46, no. 9, pp. 1396–1403, 2010.
- [108] A. Mecozzi, "Small-signal theory of wavelength converters based on cross-gain modulation in semiconductor optical amplifiers," *Photon. Technol. Lett.*, vol. 8, pp. 1471–1473, 1996.
- [109] K. Obermann, S. Kindt, D. Breuer, and K. Petermann, "Performance analysis of wavelength conversion based on cross-gain modulation in the semiconductor-optical amplifiers," *J. Lightwave Technol.*, vol. 16, pp. 78–85, 1998.
- [110] H. Lee, H. Yoon, Y. Kim, and J. Jeong, "Theoretical Study of Frequency Chirping and Extinction Ratio of Wavelength-Converted Optical Signals by XGM and XPM Using SOA's," *J. Quant. Electron.*, vol. 35, no. 8, pp. 1213–1219, 1999.
- [111] R. S. Grant, G. T. Kennedy, W. Sibbet, "Cross-phase modulation in semiconductor optical amplifier," *Electron. Lett.*, vol. 27, no. 10, pp. 801–803, 1991.

- [112] G. P. Agrawal, "Population pulsations and nondegenerate four-wave mixing in semiconductor lasers and amplifiers," *J. Opt. Soc. Am. B*, vol. 5, no. 1, pp. 147–159, 1988.
- [113] A. Mecozzi, S. Scotti, A. D'Ottavi, E. Iannone, and P. Spano, "Four-Wave Mixing in Traveling-Wave Semiconductor Amplifiers," *J. Quant. Electron.*, vol. 31, no. 4, pp. 689–699, 1995.
- [114] X. Wang, K. Matsushima, K. Kitayama, A. Nishiki, N. Wada and F. Kubota, "High performance optical code generation and recognition by use of a 511-chip, 640-Gchip/s phase-shifted superstructured fiber Bragg grating," *Opt. Lett.*, vol. 30, pp. 355–357, 2005.
- [115] Z. Si, F. Yin, M. Xin, H. Chen, M. Chen and S. Xie, "Code extraction from encoded signal in time-spreading optical code division multiple access," *Opt. Lett.*, vol. 35, pp. 229–231, 2010.
- [116] X. Wang, T. Hamanaka, N. Wada and K. Kitayama, "Dispersion-flattened-fiber based optical thresholder for multiple-access-interference suppression in OCDMA system," *Opt. Express*, vol. 13, pp. 5499–5505, 2005.
- [117] N. Wada, H. Sotobayashi and K. Kitayama, "Error-free 100km transmission at 10Gbit/s in optical code division multiplexing system using BPSK picosecond-pulse code sequence with novel time-gating detection," *Electron. Lett.*, vol. 35, pp. 833–834, 1999.
- [118] V. J. Hernandez, W. Cong, R. P. Scott, C. Yang, N. K. Fontaine, B. H. Kolner, J. P. Heritage and S. J. B. Yoo, "320-Gb/s Capacity (32 Users \times 10 Gb/s) SPECTS O-CDMA Local Area Network Testbed," in *Proc. Opt. Fiber Commun. Conf. (OFC' 06)*, Anaheim, USA, paper PDP45, 2006.
- [119] P. Petropoulos, N. Wada, P. C. Teh, M. Ibsen, W. Chujo, K. Kitayama, D. J. Richardson, "Demonstration of a 64-chip OCDMA system using superstructured fiber gratings and time-gating detection," *Photon. Technol. Lett.*, vol. 13, pp. 1239–1241, 2001.
- [120] N. Kataoka, N. Wada, G. Cincotti, and K. Kitayama, "Dispersion-compensation-free, long-reach OCDMA-PON system with passive remote node at arbitrary position using single multi-port encoder/decoder," in *Conference on Lasers and Electro-Optics*, San Jose, CA, paper CThC6, 2010.
- [121] X. Wang and K. Kitayama, "Analysis of Beat Noise in Coherent and Incoherent Time-spreading OCDMA," *J. Lightw. Technol.*, vol. 22, no. 10, pp. 2226–2235, 2004.
- [122] R. Baños, D. Pastor, W. Amaya, and V. Garcia-Munoz, "Chromatic dispersion compensation and coherent direct-sequence OCDMA operation on a single super structured FBG," *Opt. Express*, vol. 20, no. 13, pp. 13966–13976, 2012.
- [123] T. H. Shake, "Security performance of optical CDMA against eavesdropping," *J. Lightw. Technol.*, vol. 23, pp. 665–670, 2005.

- [124] Z. Jiang, D. S. Seo, S. D. Yang, D. E. Leaird, R. V. Roussev, C. Langrock, M. M. Fejer, and A. M. Weiner, "Four user, 2.5 Gb/s, spectrally coded O-CDMA system demonstration using low power nonlinear processing," *J. Lightw. Technol.*, vol. 23, no. 1, pp. 143–158, 2005.
- [125] X. Wang, N. Wada, T. Miyazaki, and K. Kitayama, "Coherent OCDMA system using DPSK data format with balanced detection," *Photon. Tech. Lett.*, vol. 18, pp. 826–828, 2006.
- [126] X. Wang, N. Wada, T. Miyazaki, G. Cincotti, and K. Kitayama, "Asynchronous multiuser coherent OCDMA system with code-shift-keying and balanced detection," *J. Select. Topics in Quantum Electron.*, vol. 13, pp. 1463–1470, 2007.
- [127] A. M. Weiner, Z. Jiang, and D. E. Leaird, "Spectrally phase-coded O-CDMA," *J. Opt. Netw.*, vol. 6, pp. 728–755, 2007.
- [128] P. Toliver, A. Agarwal, T. Banwell, R. Menendez, J. Jackel, and S. Etemad, "Demonstration of High Spectral Efficiency Coherent OCDM Using DQPSK, FEC, and Integrated Ring Resonator-Based Spectral Phase Encoder/Decoders," in *Proc. the Optical Fiber Communication Conference and Exposition (OFC)*, CA, paper PDP7, 2007.
- [129] R. Menendez, A. Agarwal, P. Toliver, J. Jackel, and S. Etemad, "Direct optical processing of M-ary code-shift-keyed spectral-phase-encoded OCDMA," *J. Opt. Netw.*, vol. 6, pp. 442–450, 2007.
- [130] T. Kodama, N. Kataoka, N. Wada, G. Cincotti, X. Wang, T. Miyazaki, and K. Kitayama, "High-security 2.5 Gbps, polarization multiplexed 256-ary OCDM using a single multi-port encoder/decoder," *Opt. Express*, vol. 18, pp. 21376–21385, 2010.
- [131] T. Koonen, G. Morthier, J. J. Jennen, H. de Waardt, and P. Demeester, "Optical packet routing in IP-over-WDM networks deploying two-level optical labeling," in *27th Eur. Conf. Optical Comm. (ECOC)*, vol. 4, 2001, pp. 608–609, 2001.
- [132] J. Zhang, N. Chi, P. Holm-Nielsen, C. Peucheret and P. Jeppesen, "A novel optical labeling scheme using a FSK modulated DFB laser integrated with an EA modulator," in *Proc. OFC 2003*, GA, TuQ5.
- [133] K. Vlachos, J. Zhang, J. Cheyns, Sultur, N. Chi, E. V. Breusegem, I. Tafur Monroy, J. G. L. Jennen, P. V. Holm-Nielsen, C. Peucheret, R. O'Dowd, P. Demeester, and A. M. J. Koonen, "An Optical IM/FSK Coding Technique for the Implementation of a Label-Controlled Arrayed Waveguide Packet Router," *J. Lightw. Technol.*, vol. 21, pp. 2617–2628, 2003.
- [134] C. W. Chow, C. S. Wong, and H. K. Tsang, "Optical packet labeling based on simultaneous polarization shift keying and amplitude shift keying," *Opt. Lett.*, vol. 29, pp. 1861–1863, 2004.
- [135] P. J. Winzer, A. H. Gnauck, C. R. Doerr, M. Magarini, L. L. Buhl, "Spectrally

efficient long-haul Optical networking using 112-Gb/s polarization-multiplexed 16-QAM,” *J. Lightw. Technol.*, vol. 28, pp. 547–556, 2010.

- [136] M. Nakazawa, “Optical quadrature amplitude modulation (QAM) with coherent detection up to 128 states,” in *Proc. OFC 2009, CA, OThG1*.
- [137] Z. A. El-Sahn, B. J. Shastri, Z. Ming, N. Kheder, D. V. Plant, and L. A. Rusch, “Experimental demonstration of a SAC-OCDMA PON with burst-mode reception: local versus centralized sources,” *J. Lightw. Technol.*, vol. 26, pp. 1192–1203, 2008.
- [138] N. Kataoka, N. Wada, X. Wang, G. Cincotti, A. Sakamoto, Y. Terada, T. Miyazaki, and K. Kitayama, “Field trial of duplex, 10 Gbps x 8-user DPSK-OCDMA system using a single 16x16 multi-port encoder/decoder and 16-level phase-shifted SSFBG encoder/decoders,” *J. Lightw. Technol.*, vol. 27, pp. 299–305, 2009.
- [139] J. Liu, D. Zeng, C. Guo, L. Xu, and S. He, “OCDMA PON supporting ONU inter-networking based on gain-switched Fabry–Pérot lasers with external dual-wavelength injection,” *Opt. Express*, vol. 18, pp. 22982–22987, 2010.
- [140] P. J. Urban, B. Huiszoon, R. Roy, M. M. de Laat, F. M. Huijskens, E. J. Klein, G. D. Khoe, A. M. J. Koonen, and H. de Waardt, “High-bit-rate dynamically reconfigurable WDM-TDM access network,” *J. Opt. Commun. Netw.*, vol. 1, pp. A143–A159, 2009.
- [141] G. Cincotti, N. Kataoka, N. Wada, X. Wang, T. Miyazaki, and K. Kitayama, “Demonstration of asynchronous, 10Gbps OCDMA PON system with colorless and sourceless ONUs,” in *35th European Conference and Exhibition on Optical Communication (ECOC 2009)*, Vienna, Austria, paper 6.5.7, 2009.
- [142] W. Hung, C. K. Chan, L. K. Chen, and F. Tong, “An optical network unit for WDM access networks with downstream DPSK and upstream remodulated OOK data using injection-locked FP laser,” *Photon. Technol. Lett.*, vol. 15, pp. 1476–1478, 2003.
- [143] L. Y. Chan, C. K. Chan, D. T. K. Tong, S. Y. Cheung, F. Tong, and L. K. Chen, “Upstream traffic transmitter using injection-locked Fabry-Perot laser diode as modulator for WDM access networks,” *Electron. Lett.*, vol. 38, pp. 43–45, Jan. 2002.
- [144] C. W. Chow, “Wavelength remodulation using DPSK down-and-upstream with high extinction ratio for 10-Gb/s DWDM-passive optical networks,” *Photon. Technol. Lett.*, vol. 20, pp. 12–14, 2008.
- [145] J. Yu, M. F. Huang, D. Qian, L. Chen, and G. K. Chang, “Centralized lightwave WDM-PON employing 16-QAM intensity modulated OFDM downstream and OOK modulated upstream signals,” *Photon. Technol. Lett.*, vol. 20, pp. 1545–1547, 2008.
- [146] H. P. Sardesai, and A. M. Weiner, “Nonlinear fibre-optic receiver for ultrashort

- pulse code division multiple access communications,” *Electron. Lett.*, vol. 33, pp. 610–611, 1997.
- [147] J. H. Lee, P. C. Teh, Z. Yusoff, M. Ibsen, W. Belardi, T. M. Monro, and D. J. Richardson, “A holey fiber-based nonlinear thresholding device for optical CDMA receiver performance enhancement,” *Photonics Technol. Lett.*, vol. 14, pp. 876–878, 2002.
 - [148] R. P. Scott, W. Cong, K. Li, V. J. Hernandez, B. H. Kolner, J. P. Heritage, and S. J. Ben Yoo, “Demonstration of an Error-Free 4 × 10 Gb/s Multiuser SPECTS O-CDMA Network Testbed,” *Photon. Technol. Lett.*, vol. 16, pp. 2186–2188, 2004.
 - [149] H. Sotobayashi and K. Kitayama, “All-optical simultaneous code and wavelength conversion of 10 Gbit/s BPSK codes by four-wave mixing in semiconductor optical amplifier for optical code division multiplexing,” *Electron. Lett.*, vol. 35, pp. 1091–1093, 1999.
 - [150] R. P. Scott, W. Cong, V. J. Hernandez, K. Li, B. H. Kolner, J. P. Heritage, S. J. B. Yoo, “An eight-user time-slotted SPECTS O-CDMA testbed: demonstration and simulations,” *J. lightw. Technol.*, vol. 23, no. 10, pp. 3232–3240, 2005.
 - [151] K. E. Stubkjaer, “Semiconductor optical amplifier-based all-optical gates for high-speed optical processing,” *J. Sel. Top. Quant. Electron.*, vol. 6, pp. 1428–1435, 2000.
 - [152] K. L. Deng, I. Glesk, K. I. Kang, and P. R. Prucnal, “Unbalanced TOAD for optical data and clock separation in self-clocked transparent OTDM networks,” *Photon. Technol. Lett.*, vol. 9, pp. 830–832, 1997.
 - [153] N. Wada, H. Sotobayashi, and K. Kitayama, “Error-free 100km transmission at 10Gbit/s in optical code division multiplexing system using BPSK picosecond-pulse code sequence with novel time-gating detection,” *Electron. Lett.*, vol. 35, pp. 833–834, 1999.
 - [154] R. Elschner, C.-A. Bunge, and K. Petermann, “System impact of cascaded all-optical wavelength conversion of D(Q)PSK signals in transparent optical networks,” *J. Netw.*, vol. 5, pp. 219–224, 2010.
 - [155] I. Widjaja, “Performance analysis of burst admission-control protocols,” *IEE P. Commun.*, vol. 142, pp. 7–14, 1995.
 - [156] Y. Ma, Y. Qian, G. Peng, X. Zhou, X. Wang, J. Yu, Y. Luo, X. Yan, and F. Effenberger, “Demonstration of a 40Gb/s time and wavelength division multiplexed passive optical network prototype system,” in *Optical Fiber Communication Conference (OFC)*, Los Angeles, California, paper PDP5D, 2012.
 - [157] W. S. Warren, H. Rabitz, and M. Dahleh, “Coherent control of quantum dynamics: the dream is alive,” *Science*, vol. 259, pp. 1581–1589, 1993.

- [158] G. J. Tearney, M. E. Brezinski, B. E. Bouma, S. A. Boppart, C. Pitris, J. F. Southern, and J. G. Fujimoto, "In Vivo Endoscopic Optical Biopsy with Optical Coherence Tomography," *Science*, vol. 276, pp. 2037–2039, 1997.
- [159] A. M. Weiner, "Femtosecond pulse shaping using spatial light modulators," *Rev. Sci. Instrum.*, vol. 71, pp. 1929–1960, 2000.
- [160] H. Chi, F. Zeng, and J. Yao, "Photonic generation of microwave signals based on pulse shaping," *Photon. Tech. Lett.*, vol. 19, pp. 668–670, 2007.
- [161] X. Zhou, X. Zheng, H. Wen, H. Zhang, Y. Guo, and B. Zhou, "Optical Frequency Comb Based on Cascading Intensity Modulation for Optical Arbitrary Waveform Generation," *Asia Communications and Photonics Conference and Exhibition (ACP'10)*, Shanghai, China, Paper SuG4, 2010.
- [162] T. Yamamoto, T. Komukai, K. Suzuki, and A. Takada, "Multicarrier Light Source With Flattened Spectrum Using Phase Modulators and Dispersion Medium," *J. Lightw. Technol.*, vol. 27, pp. 4297–4305, 2009.
- [163] M. Fujiwara, M. Teshima, J. Kani, H. Suzuki, N. Takachio, and Katsumi Iwatsuki, "Optical Carrier Supply Module Using Flattened Optical Multicarrier Generation Based On Sinusoidal Amplitude and Phase Hybrid Modulation," *J. Lightw. Technol.*, vol. 21, pp. 2705–2714, 2003.
- [164] R. Wu, V. R. Supradeepa, C. M. Long, D. E. Leaird, and A. M. Weiner, "Generation of very flat optical frequency combs from continuous-wave lasers using cascaded intensity and phase modulators driven by tailored radio frequency waveforms," *Opt. Lett.*, vol. 35, pp. 3234–3236, 2010.
- [165] N. K. Fontaine, R. P. Scott, J. Cao, A. Karalar, W. Jiang, K. Okamoto, J. P. Heritage, B. H. Kolner, and S. J. B. Yoo, "32 phase x 32 amplitude optical arbitrary waveform generation," *Opt. Lett.*, vol. 32, pp. 865–867, 2007.
- [166] T. Sakamoto, T. Kawanishi, and M. Izutsu, "Asymptotic formalism for ultraflat optical frequency comb generation using a Mach-Zehnder modulator," *Opt. Lett.*, vol. 32, pp. 1515–1517, 2007.
- [167] T. Sakamoto, T. Kawanishi, and M. Tsuchiya, "10 GHz, 2.4 ps pulse generation using a single-stage dual-drive Mach-Zehnder modulator," *Opt. Lett.*, vol. 33, pp. 890–892, 2008.
- [168] I. Morohashi, T. Sakamoto, H. Sotobayashi, T. Kawanishi, I. Hosako, and M. Tsuchiya, "Widely repetition-tunable 200fs pulse source using a Mach-Zehnder-modulator based flat comb generator and dispersion-flattened dispersion decreasing fiber," *Opt. Lett.*, vol. 33, pp. 1192–1194, 2008.
- [169] A. M. Weiner, J. P. Heritage, and E. M. Kirschner, "High resolution femtosecond pulse shaping," *J. Opt. Soc. Am. B*, vol. 5, pp. 1563–1572, 1988.
- [170] F. Parmigiani, M. Ibsen, T.T. Ng, L. Provost, P. Petropoulos, D. J. Richardson, "An Efficient Wavelength Converter Exploiting a Grating-Based Saw-Tooth

Pulse Shaper”, *Photon. Technol. Lett.*, vol. 20, pp. 1461–1463, 2008.

- [171] P. Petropoulos, M. Ibsen, A. D. Ellis, and D. J. Richardson, “Rectangular pulse generation based on pulse reshaping using a superstructured fiber Bragg grating,” *J. Lightw. Tech.*, vol. 19, pp. 746–752, 2001.
- [172] T. Kurokawa, H. Tsuda, K. Okamoto, K. Naganuma, H. Takenouchi, Y. Inoue, and M. Ishii, “Time-space-conversion optical signal processing using arrayed-waveguide grating,” *Electron. Lett.*, vol. 33, pp. 1890–1891, 1997.
- [173] H. Takenouchi, H. Tsuda, K. Naganuma, T. Kurokawa, Y. Inoue, and K. Okamoto, “Differential processing of ultrashort optical pulses using arrayed-waveguide grating with phase-only filter,” *Electron. Lett.*, vol. 34, pp. 1245–1246, 1998.
- [174] D. E. Leaird, A. M. Weiner, S. Kamei, M. Ishii, A. Sugita, and K. Okamoto, “Generation of flat-topped 500-GHz pulse bursts using loss engineered arrayed waveguide gratings,” *Photon. Technol. Lett.*, vol. 14, pp. 816–818, 2002.
- [175] Z. Jiang, D. S. Seo, D. E. Leaird and A. M. Weiner, “Spectral line-by-line pulse shaping,” *Opt. Lett.*, vol. 30, pp. 1557–1559, 2005.
- [176] Z. Jiang, C.-B. Huang, D. E. Leaird, and A. M. Weiner, “Optical arbitrary waveform processing of more than 100 spectral comb lines,” *Nature Photonics*, vol. 1, pp. 463–467, 2007.
- [177] R. E. Saperstein, D. Panasenکو, and Y. Fainman, “Demonstration of a microwave spectrum analyzer based on time-domain optical processing in fiber,” *Opt. Lett.*, vol. 29, pp. 501–503, 2004.
- [178] R. E. Saperstein, N. Alic, D. Panasenکو, R. Rokitski, and Y. Fainman, “Time-domain waveform processing by chromatic dispersion for temporal shaping of optical pulses,” *J. Opt. Soc. Am. B*, vol. 22, pp. 2427–2436, 2005.
- [179] J. C. Cartledge, “Performance of 10 Gb/s Lightwave Systems Based on Lithium Niobate Mach-Zehnder Modulators with Asymmetric Y-Branch Waveguides,” *Photon. Technol. Lett.*, vol. 7, pp. 1090–1092, 1995.
- [180] G. J. Meslener, “Chromatic Dispersion Induced Distortion of Modulated Monochromatic Light Employing Direct Detection,” *J. Quantum Elect.*, vol. QE-20, pp. 1208–1216, 1984.
- [181] M. Govind and T. N. Ruckmongathan, “Trapezoidal and Triangular Waveform Profiles for Reducing Power Dissipation in Liquid Crystal Displays,” *J. Display Technol.*, vol. 4, pp. 166–172, 2008.
- [182] Federal Communications Commission, “Revision of part 15 of the commissions rules regarding ultra-wideband transmission systems,” 2002.
- [183] J. Qiu, K. Sun, M. Rochette and L. R. Chen, “Reconfigurable All-Optical Multi logic Gate (XOR, AND, and OR) Based on Cross-Phase Modulation in a Highly Nonlinear Fiber,” *Photon. Technol. Lett.*, vol. 22, no. 16, pp. 1199–1201, 2010.

- [184] J. Wang, G. Meloni, G. Berrettini, L. Potì and A. Bogoni, "All-optical binary counter based on semiconductor optical amplifiers," *Opt. Lett.*, vol. 34, no. 22, pp. 3517–3519, 2009.
- [185] B. Tian, W. V. Etten and W. Beuwer, "Ultrafast All-Optical Shift Register and Its Perspective Application for Optical Fast Packet Switching," *J. Sel. Top. Quant. Electron.*, vol. 8, no. 3, pp. 722–728, 2002.
- [186] J. E. McGeehan, S. Kumar, and A. E. Willner, "Simultaneous optical digital half-subtraction and -addition using SOAs and a PPLN waveguide," *Opt. Express*, vol. 15, no. 9, pp. 5543–5549, 2007.
- [187] J. E. McGeehan, S. Kumar, D. Gurkan, S. M. R. M. Nezam, A. E. Willner, K. R. Parameswaran, M. M. Fejer, J. Bannister and J. D. Touch, "All-optical decrementing of a packet's time-to-live (TTL) field and subsequent dropping of a zero-TTL packet," *J. Lightw. Technol.*, vol. 21, no. 11, pp. 2746–2752, 2003.
- [188] A. J. Poustie, K. J. Blow, A. E. Kelly, and R. J. Manning, "All-optical binary half-adder," *Opt. Commun.*, vol. 156, no. 12, pp. 22–26, Nov. 1998.
- [189] J. P. Sokoloff, P. R. Prucnal, I. Glesk, and M. Kane, "A terahertz optical asymmetric demultiplexer (TOAD)," *Photon. Technol. Lett.*, vol. 5, pp. 787–790, 1993.
- [190] J. H. Kim, Y. T. Byun, Y. M. Jhon, S. Lee, D. H. Woo, S. H. Kim, "All-optical half-adder using semiconductor optical amplifier based devices," *Opt. Commun.*, vol. 218, pp. 345–349, Apr. 2003.
- [191] D. Tsiokos, E. Kehayas, K. Vysokinos, T. Houbavlis, L. Stampoulidis, G. T. Kanellos, N. Pleros, G. Guekos, and H. Avramopoulos, "10-Gb/s all-optical half-adder with interferometric SOA gates," *Photon. Technol. Lett.*, vol. 16, no. 1, pp. 284–286, 2004.
- [192] S. H. Kim, J. H. Kim, J. W. Choi, C. W. Son, Y. T. Byun, Y. M. Jhon, S. Lee, D. H. Woo, and S. H. Kim, "All-optical half adder using cross gain modulation in semiconductor optical amplifiers," *Opt. Express*, vol. 14, no. 22, pp. 10693–10698, 2006.
- [193] S. Kumar, A. E. Willner, D. Gurkan, K. R. Parameswaran and M. M. Fejer, "All-optical half adder using an SOA and a PPLN waveguide for signal processing in optical networks," *Opt. Express*, vol. 14, no. 22, pp. 10255–10260, 2006.
- [194] J. Wang, J. Sun, Q. Sun, "Single-PPLN-based simultaneous half adder, half-subtractor, and OR logic gate: proposal and simulation," *Opt. Express*, vol. 15, no. 4, pp. 1690–1699, 2007.
- [195] J. Baliga, R. Ayre, K. Hinton, W. V. Sorin and R. S. Tucker, "Energy Consumption in Optical IP Networks," *J. Lightw. Technol.*, vol. 27, pp. 2391–2403, 2009.

- [196] R. W. Tkach, "Scaling Optical Communications for the Next Decade and Beyond," *Bell Labs Tech. J.*, vol. 14, no. 4, pp. 3–10, 2010.
- [197] Y. Ding, H. Hu, M. Galili, J. Xu, L. Liu, M. Pu, H. C. H. Mulvad, L. K. Oxenløwe, C. Peucheret, P. Jeppesen, X. Zhang, D. Huang, and H. Ou, "Generation of a 640 Gbit/s NRZ OTDM signal using a silicon microring resonator," *Optics Express*, vol. 19, pp. 6471–6477, 2011.
- [198] H. Nishizawa, Y. Yamada, K. Habara and T. Ohyama, "Design of a 10-Gb/s Burst-Mode Optical Packet Receiver Module and Its Demonstration in a WDM Optical Switching Network," *J. Lightw. Technol.*, vol. 20, pp. 1078–1083, 2002.
- [199] Z. Li, Y. Dong, Y. Wang and C. Lu, "A Novel PSK-Manchester Modulation Format in 10-Gb/s Passive Optical Network System With High Tolerance to Beat Interference Noise," *Photon. Technol. Lett.*, vol. 17, pp. 1118–1120, 2005.
- [200] Y. Dong, Z. Li, C. Lu, Y. Wang, Y. J. Wen, T. H. Cheng and W. Hu, "Improving Dispersion Tolerance of Manchester Coding by Incorporating Duobinary Coding," *Photon. Technol. Lett.*, vol. 18, pp. 1723–1725, 2006.
- [201] Z. Liu and C.-K. Chan, "Generation of Dispersion Tolerant Manchester-Duobinary Signal Using Directly Modulated Chirp Managed Laser," *Photon. Technol. Lett.*, vol. 23, pp. 1043–1045, 2011.
- [202] Y.-W. Song, K. T. Dinh and S. Yamashita, "Generation of all-fiber optical Manchester code using nonlinear polarization rotation," *Optics Express*, vol. 14, pp. 63–68, 2006.
- [203] K. Mishina, S. Kitagawa and A. Maruta, "All-optical modulation format conversion from on-off-keying to multiple-level phase-shift-keying based on nonlinearity in optical fiber," *Opt. Express*, vol. 15, pp. 8444–8453, 2007.
- [204] K. Mishina, S. M. Nissanka, A. Maruta, S. Mitani, K. Ishida, K. Shimizu, T. Hatta, and K. Kitayama, "All-optical modulation format conversion from NRZ-OOK to RZ-QPSK using parallel SOA-MZI OOK/BPSK converters," *Opt. Express*, vol. 15, pp. 7774–7785, 2007.
- [205] Y. Lu, F. Liu, M. Qiu and Y. Su, "All-optical format conversions from NRZ to BPSK and QPSK based on nonlinear responses in silicon microring resonators," *Opt. Express*, vol. 15, pp. 14275–14282, 2007.
- [206] E. Lazzeri, A. T. Nguyen, G. Serafino, N. Kataoka, N. Wada, L. Ascari, A. Bogoni and L. Potì, "All-optical NRZ-DPSK to RZ-OOK format conversion using optical delay line interferometer and semiconductor optical amplifier," *Photonics in Switching (PS' 10)*, Monterey, CA, paper JTUB45, 2010.